Noise, coherent activity and network structure in neuronal cultures

JAVIER GÓMEZ ORLANDI

– Ph.D. thesis –

Ph.D. advisor:

JAUME CASADEMUNT VIADER

Barcelona, September 2015

Programa de Doctorat en Física
Departament d'Estructura i Constituents de la Matèria
Facultat de Física

Universitat de Barcelona

Javier G. Orlandi
Departament d'Estructura i Constituents de la Matèria
Facultat de Física
Universitat de Barcelona
Barcelona, E-08028
Spain
orlandi@ecm.ub.edu
http://www.javierorlandi.com

Noise, coherent activity and network structure in neuronal cultures
Ph.D. thesis
Programa de Doctorat en Física
Línia de recerca en Física de la matèria condensada
Memòria presentada per a optar al títol de Doctor en Física
Barcelona, June 2015

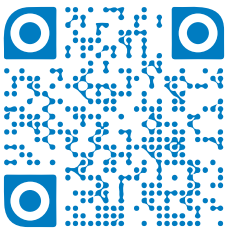

Scan for updates and supplementary material

Centuries are needed to nurture the tree of science and make it grow, but one blow from the hatchet of destruction cuts it down.

– Bernard Germain de Lacépède, 1801

Acknowledgements

I find myself writing these lines at the last moment. In less than 24h this will all be over. The thesis, that is. All the work I have performed in the past four (five? six?) years reduced to a single document. A file. 60 Mbs. A little less than half a billion ones and zeros in sequence. And yet, it was worth it. These years have been the most beautiful of my life (so far). To be able to work in what I love, and to make a contribution to the collective scientific knowledge (albeit small, and probably soon to be forgotten), was worth the effort. These years have not been easy, specially the last few months, and I am extremely grateful to all the people that have been present in my life. This thesis would not have been possible without them.

A en Jaume, que va veure alguna cosa en mi i em va donar aquesta oportunitat. Sense ell molt probablement mai hagués acabat aquí. Encara recordo aquell dia, després d'una presentació a classe de biofísica cel·lular, on vaig mostrar un treball sobre la motilitat de la listèria. Qui hauria de dir que aquella bactèria decidiria el meu futur. Gràcies Jaume. Sempre hi has estat quan t'he necessitat, he aprés moltíssim amb tu, i també m'has permès gaudir de tota la llibertat i independència que he requerit. Desitjo que continuem el que aquí hem començat, tenim idees per dues tesis més!

A Jose María, mi padrino científico, con él empecé en esto. Ya durante el máster de biofísica me introdujo en la investigación de verdad, y con él llegó mi primera publicación. Gracias! Siempre has estado presente, no había día que no pasaras a verme al despacho, no sólo cuando lo compartía con Rubén y María.

A en Jordi, la seva arribada a Barcelona va ser clau en aquesta tesi. No hagués tocat la neurociència si no hagués estat per ell. Ja des del primer viatge junts a Alemanya vaig tenir clar quin seria el meu camí. Gràcies Jordi. Has estat pràcticament un segon director per a mi i un model a seguir. I per sobre de tot, un gran amic.

I am also extremely grateful to the people from the Max Planck Institute in Göttingen, who treated me as one of them from day one. Although my stay was short, it was extremely enlightening. There is a brilliant group of people there. Thanks Theo, you have always welcomed us in Germany, I know you have a special place in your heart for Barcelona. Thank you Demian, I have been able to learn a lot from you, specially in bringing order from chaos. And last but not least, Olav. Thank you! You have been both a peer and a mentor, not only in science, but also in life. You have been a true friend.

Gràcies també a tota la gent del grup de no lineal i del consolider, hem passat molts bon moments junts. A la Marta, a qui considero un altre referent científic i també personal. Al Jordi, que sempre ha tingut la porta oberta per parlar de tot, en especial de política científica i de la universitat. També a la resta de gent del departament, i a la Dolors, la Rosa, la Mònica i la Pilar, que fan la nostra vida molt més fàcil.

To all the people from the BARCSYN community, you all are building something great in here. And specially to Alex, Albert, Mavi, and all the people that have been there form the beginning. També a la gent del grup experimental de neurofísica, Núria, Mary, Sara, Eli i Lluís. Sobretot a tu Sara, amb qui he compartit un munt de bons moments. Gracies també a tu Enric la teva feina també ha estat imprescindible per aquesta tesi i ens ho hem passat la mar de bé.

A todos los que han pasado por el 606. Dani, María, Pau, Rubén, Sara (aunque no le hayamos visto el pelo) y sobre todo ahora a Claudia, sin ella estos últimos meses habrían sido terribles. A todos, lo bien que nos lo hemos pasado! Gracias Rubén y gracias Pau, los dos habéis sido fantásticos y hemos pasado momentos muy buenos juntos. Tanto a nivel científico como personal. Y aún tenemos un artículo pendiente!

A María, a Noemí y a Jose, que ya hace tiempo que se fueron, pero con quien también he compartido grandes momentos de esta tesis. Gracias. A la gente de didra, y totas las comilonas que nos hemos pegado. També a tota la gent del màster de Biofísica, una llàstima que ja no hi sigui.

A tota la gent del bus, amb qui he viscut tants viatges. Qui ho diria que formaríem un grup tan maco i heterogeni! Gràcies també per ser una dosi diària de realitat. Gràcies Gerard, Anna, Esther, Gonzalo, Montse, Berta, Sergi, i els que em deixo.

A mis compañeros de la FJI y de D-Recerca, con quien he compartido muchísimas horas durante esta tesis, seguramente más de las que debería. Espero que nuestro trabajo haya servido para algo. Sino ya para nosotros, para los que ahora llegan. Gràcies Vane, Naiara, Agnese, Paolo, quina marxa que teniu! Gràcies també Jose María, tu em vas contagiar l'amor pel BOEs. Gracias Noe, Elena, Pablo, Ester, vaya grupito que nos montamos! Sois los mejores.

A mi familia, que ha estado siempre a mi lado y me ha apoyado en todo momento. Gracias Papá. Gracias Eva y gracias Manel. Y sobretodo a ti Mamá, sin ti esto no habría sido posible. También un especial recuerdo para los que nos dejaron durante el transcurso de esta tesis, mi yaya Montserrat y mi abuelo Marino, que siempre fue un modelo a seguir para mi.

Y como no, gracias Pili. Llegaste cuando menos te esperaba, pero llegaste para quedarte. Y aquí sigues! Por muy lejos que te encuentres, ya sean los 9.600 km que ahora nos separan, o los 690 km de cuando nos conocimos, en realidad siempre estás aquí conmigo, te llevo en mi corazón. Gracias sobretodo en estos últimos meses y estos últimos días, no ha tenido que ser nada fácil aguantarme.

This thesis would not have been possible without the financial support provided by the University of Barcelona, under the APIF program (Ajuts de Personal Investigador en Formació) for which I am grateful.

The work presented in this thesis also had financial support from Ministerio de Ciencia e Innovación (Spain) under projects FIS2009-07523, and FIS2010-21924-C02-02, FIS2011-28820-C02-01 and the Generalitat de Catalunya under project 2009-SGR-00014.

A Daniela,

Toda una vida por delante

Contents

0 Outline of the thesis

In this thesis we apply a multidisciplinary approach, based on statistical physics and complex systems, to the study of neuronal dynamics. We focus on understanding, using theoretical and computational tools, how collective neuronal activity emerges in a controlled system, a neuronal culture. We show how the interplay between noise and network structure defines the emergent collective behavior of the system.

Chapter 1 comprises the general introduction. We present a personal view on the fields of complex systems, multidisciplinary physics, and modern neuroscience. As well as our take on how one can benefit from the other. We proceed to describe how neuronal cultures are an extremely useful system to study physics and neuroscience simultaneously. We also include a general review of most of the research topics within neuronal cultures that are relevant to physics, as well as a brief summary of the physiological ingredients required to understand them.

Chapter 2 contains the most salient results of this thesis. We build a simulation framework that takes into account the underlying network structure of neuronal cultures and use an accurate, yet simple, model for the individual neuronal dynamics. We show that the collective behavior of young cultures is dominated by the nucleation and propagations of activity fronts (bursts) throughout the system. These bursts nucleate at specific sites of the culture, called nucleation points, which result in a highly heterogeneous probability distribution of nucleation. We are able to explain theoretically the nucleation process by means of a mechanism of noise propagation and amplification, called *noise focusing*.

Noise, in the form of the spontaneous activity of individual neurons, is characterized by avalanches of activity, which travel and are amplified through the network in well–defined paths. The convergence of these paths of activity is what characterizes the different nucleation sites, i.e., the confluence of amplification paths. These preferred paths also form an effective network, which is a subset of the original structural network that comprise most of the activity. We show how the underlying dynamics are able to transform the structural network, with Gaussian–like degree distributions into effective scale–free networks.

We also present experimental confirmation of the wave–like structure of activity bursts in young cultures and present evidence of the *noise focusing* mechanism.

Chapter 3 further explores the internal structure of activity avalanches by using well–defined regular networks, in which all the neurons have the same connectivity rules (motifs). Within these networks, we are able to associate to the avalanches an effective velocity and topological size and relate it to specific motifs.

In Chapter 4 we devise a continuum description of a neuronal culture at the mesoscale, i.e., we move away from the single neuron dynamics into a coarse–grained description that is able to capture most of the characteristic observables presented in previous chapters.

Chapter 5 is dedicated to studying neuronal cultures within the framework of quorum percolation. We study the effect of network structure within quorum percolation and propose a new model, called *stochastic quorum percolation* that includes dynamics and the effect of internal noise.

In Chapter 6, we use tools from information theory, namely transfer entropy, to show how to reliably infer the connectivity of a neuronal network from its activity, and how to distinguish between different excitatory and inhibitory connections purely from the activity, with no prior knowledge of the different neuronal types. The technique works directly on the fluorescence traces obtained in calcium imaging experiments, without the need to infer the underlying spike trains.

Finally, Chapter 7 summarizes the general results, conclusions and perspectives that are drawn from this thesis.

1 Introduction

The 21st century is giving birth to a new era whose reach is still too early to grasp. Its origins might very well be the invention of new technologies and the geopolitical changes that arose after the cold war. The ways in which we communicate, process and store information, coupled with globalization, free market economies and fading physical and cultural frontiers are all working together towards a new model of society, and science is at its core.

Not only is science the source of new technologies, but it also nourishes from them. With the 'big data' (the ability to record vast amounts of information) and the 'quantification' (measuring everything) revolution that is currently undergoing, traditional scientific disciplines are looking at new ways to understand the world. Physics (and physicists) in particular, might be the best example. Probably the first discipline to use and generate large amounts of data, and quantitative by definition, its reach is now spanning across other disciplines. There has been a constant flow of physicists into other areas of science: biology, chemistry, neuroscience, economics and social sciences to name a few. These other sciences were originally observational and mostly descriptive, but they are evolving. Biology is not about writing a catalog of life anymore; new disciplines like systems biology and bioinformatics are transforming more traditional fields like genetics, cell biology and biochemistry. Chemists are engineering new molecules and compounds *in silico*[1], trying millions of candidates before going to the lab to finally synthesize them. Economists are tracking, analyzing and predicting markets and human interactions in real time, leading to a new understanding of social behavior.

[1] The term *in silico*, i.e., a computer simulation, will be used throughout this thesis.

These multidisciplinary advances have at its core the complexity of the systems under study, made of multiple interconnected and heterogeneous units, interacting in non-deterministic ways. Although all these fields and systems might look unrelated (what does a protein-interaction network, an ecosystem and a financial market have in common?), they all share similarities and possibly some universal properties. By trying to understand them, the new field of complex systems has emerged. Although it began as a branch of statistical physics, i.e., complex networks [Albert 2002], it has quickly gained popularity, where scientists across many different fields are using their concepts and theories.

Although the concept of 'big data' probably began with CERN, it really took off with the Human Genome Project [Lander 2001] (HGP), where many laboratories across the world teamed together to sequence the whole human genome and made the data publicly available. Although these projects spanned large teams and collaborations, they were not truly multidisciplinary or had anything to do with complex systems per se. The amount of data the HGP produced and the need to understand it, however, triggered the interest of many scientists from other disciplines, and subfields like systems biology and bioinformatics flourished.

Concurrently, the seminal works on complex networks by D. J. Watts & S. H. Strogatz [Watts 1998] and A. Barabási & R. Albert [Barabási 1999] appeared, and modern network theory was born. Network theory has become essential for the study of any complex system (its elements interact between them through a network structure), and has spanned its own subfield of complex networks, which coupled with the aforementioned access to 'big data' has heavily influenced new scientists into looking at their research in a different way.

Although many fields quickly embraced this new approach, neuroscience appeared to be falling behind. One of the sciences that could benefit the most from this new approach was evolving slowly. Probably because the technological advances required to obtain 'big data' in neuroscience took longer to develop, and are only starting to become available now (see Figure 1.1).

The change, however, finally arrived in 2013, overshadowing all other disciplines. The coeval announcement of the Human Brain Project (HBP) [Waldrop 2012, Abbott 2013a] by the European Commission and the BRAIN Initiative [Shen 2013] by the U.S. administration triggered a new era in neuroscience [Abbott 2013b]. Although these projects might be ill-conceived, and even backfire (as some have already suggested [Fregnac 2014]), they are going to push neuroscience forward and modernize it to the level of other disciplines. The development of new measuring techniques, new ways to analyze data and coordinated efforts towards well defined goals should compensate any backlash due to these projects not reaching their proposed milestones. These projects have returned neuroscience the attention it deserves, and made understanding the brain the ultimate challenge for the upcoming decades, if not for the whole century.

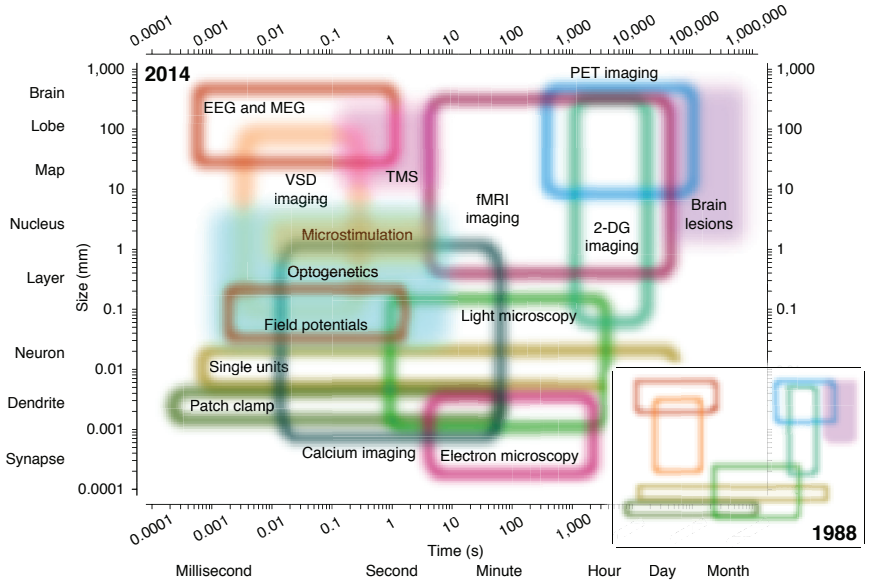

Figure 1.1 | Main methods in neuroscience. Regions of applicability of each modern experimental technique in neuroscience. Open regions denoting measurement techniques and filled regions perturbation ones. Inset, the regions available in 1988. Repr. with perm. [Sejnowski 2014].

1.1 The brain, the challenge of the 21st century

Back in the fifth century B.C., Hippocrates already considered the brain as "the seat of intelligence, sensory perception and motor control", and also as the source of emotions, amongst others (contrary to the Aristotelian view, that believed the heart to be the center of sensation and movement) [Gross 1995, Crivellato 2007]. But it was not until the late nineteenth century and the works by S. Ramón y Cajal (aided by the development of Golgi stains [De Carlos 2007]), that we started to understand the inner workings of the brain, and neuroscience, as we know it, was born. Ramón y Cajal greatest breakthrough came by identifying the neuron as the fundamental unit in the brain, and the synapses as the main component of information transmission; what is now called the 'neuron doctrine' [Cajal 1906]. He even identified the first microcircuits as well as myriads of different neuronal types, and even postulated some sort of synaptic plasticity, in the same lines as D. G. Hebb did many years later, what is nowadays known as Hebbian plasticity [Markram 2012].

Now in the twenty-first century, new theories and technological developments are redefining and even changing the old neuron doctrine. Recent analysis of neuronal activity at the nanoscale [Sjöström 2008] suggests that a more fundamental computational unit that the neuron exists, the dendrites. Each branch of the dendritic tree seems to react in a particular and non–linear way to the received inputs and also

trigger dendritic spikes affecting the whole neuronal behavior[2]. On the other hand, several studies [Grillner 2006] suggest that to understand brain activity and behavior (specially in the more advanced areas like the cortex), we might need to forget about the neuron altogether, and consider the 'microcircuit'[3] as the fundamental computational unit.

These new ways of looking at the brain might trigger a new revolution in neuroscience in the same way as Ramón y Cajal did, and the two are in no way mutually exclusive. Whereas computation might happen at the dendrites, each neuron will surely belong to several microcircuits and the specificity could happen in the dendrites. The neuron acting as a parallel processor, and each branch submitting tasks in parallel.

The two aforementioned projects are also bringing neuroscience into the new century and pushing scientists into novel and unexplored territories. The Human Brain Project, that aims to "achieve a unified, multi–level understanding of the human brain" by generating the most detailed simulation of the human brain to date, is also gathering data at an unprecedented level of detail from the brain. By coordinating across many labs around the globe, the project is also unifying the way in which neuroscience data is recorded and shared, from the molecular level (starting by the gene expression of molecular channels) up to whole-brain activity. Even if the project might not reach its long-term goals [Fregnac 2014], neuroscience as a whole will benefit greatly (as well as other disciplines, like computer science, with the development of novel neuromorphic and neurorobotic technologies inspired by the brain). The other macro project, the BRAIN Initiative, aims to accelerate the development and application of innovative neurotechnologies focusing on brain research. A special emphasis is put into imaging the *in vivo* brain to open new doors to explore how the brain handles information, both in health and in disease. In their own words, "there's a big gap between what we want to do in brain research and the technologies available to take us there".

With the current state of affairs in neuroscience, physicists are in an excellent position to contribute. The announced macro projects as well as the latest developments in technology are evolving neuroscience into a discipline more interdisciplinary and quantitative than ever before, and that is something where physicists excel at. There is also the rising need of new and fundamental theories that can explain brain behavior at a new level of complexity. The extremely high amount of data that is going to be collected in the following years (the mouse connectome is already generating of the other of petabytes worth of data [Lichtman 2014]) is going to become unmanageable soon and reducing it to a convenient level will be required, as well as new theories and ways to work with it.

[2] The importance of the dendrites for computation, however, has been known for a while [Yuste 1996].

[3] The microcircuit has to be understood as a set of neurons and synapses performing a specific task, in a similar fashion as logic gates in electrical circuits.

1.2 Neuronal cultures, at the interface of physics and neuroscience

Physicists are also contributing to neuroscience at a more fundamental level, unraveling universal principles governing all brains (not just the human one) and nervous tissue in general. It is not only the human brain that poses a mystery, it is fair to say that we have not yet solved the inner workings of any "brain", not even the *C. elegans*[4] nervous system.

There are many branches of physics involved in tackling problems in neuroscience: network theory and phase transitions has been used to study the *C. elegans* connectome [Arenas 2009, Nicosia 2013]; self-organized criticality has been able to explain cortical dynamics [Beggs 2003, Beggs 2004]; stochastic processes have shed new light into the brain resting state [Deco 2011], etc. But if there is one platform or device where physics can contribute the most to neuroscience, it has to be neuronal cultures. Neuronal cultures are the harmonic oscillator, the hydrogen atom, of neuroscience. Simple, yet powerful enough, controlled systems to test theories and hypothesis. Not as complex as a brain (or one of its parts), but rich enough to show many different complex behaviors, it might be one of the keys to unravel some of the mysteries of the brain.

Neuronal cultures consist of many neurons (ranging from dozens to millions) grown together in the lab, usually in a petri dish. Typically these neurons come from pre-natal embryos and are dissociated from the original tissue, by either mechanical or chemical manipulation. The neurons are then incubated in growth medium for several days, during which the neurons migrate, grow and try to form connections with their neighbors. These neurons are also electrically active, evolving from an initial stage of silence or individual spontaneous firing to later stages of self–organized collective spontaneous firing or even more complex activity patterns. The neurons in a culture belong to many families of neuronal types, but the two main groups are defined by their excitability and they can be either excitatory or inhibitory; the first promoting activity on their neighbors and the later hindering it.

The term neuronal culture is quite broad, and can lead to confusion if one is not careful. Cultures can come from many different animals (rat, mice, ferret, locust, ...), from different brain areas (spinal cord, cortex, hippocampus, ...), from different preparations (dissociated and organotypic), as well as from different developmental stages (pre and postnatal), and even derived from stem cells. Although they share many similarities, there are also many differences. Spinal cord cultures show the presence of peacemaker cells, whereas cortex and hippocampus do not; organotypic cultures have connectivity profiles similar to those found in the brain[5] whereas dissociated ones do not; cultures derived from stem cells are barely active sponta-

[4] *Caernorhabditis elegans* has one of the simplest nervous systems, composed of only (and exactly) 302 neurons distributed along its body.

[5] But not quite [De Simoni 2003].

neously, etc. Unless otherwise specified, the results presented in this thesis focus on neuronal cultures dissociated from the cortex of Sprague-Dawley rat embryonic brains of 18-19 days of development.

Neuronal cultures are an invaluable tool to study both physics and neuroscience at the same time. For physics, it provides a well-controlled non-equilibrium system that self-organizes and is composed of a complex network of interacting non-linear units. One can use them to study synchronization mechanisms [Baruchi 2008], percolation [Breskin 2006], criticality [Tetzlaff 2010], self-organization during development [Pu 2013], noise [Orlandi 2013], network theory [Teller 2014], network reconstruction [Stetter 2012], and even use them to build neuromorphic devices [Feinerman 2008]. In neuroscience they can be used to study development [Soriano 2008], plasticity [van Pelt 2005], oscillations [Czarnecki 2012], the microconnectome [Shimono 2014], and also use them as a platform for drug development and testing in toxicity [Frega 2012] and neurodegenerative diseases [Huang 2012] (see Figure 1.2 for some illustrative examples). The multidisciplinary use of cultures is quite new however, and a closer look at their history can shed some light on their advantages and shortcomings.

1.3 A brief historical review on neuronal cultures

In the mid 2000s, when terms like interdisciplinary sciences, complex systems and self-organization reached widespread popularity, *in vitro* neuronal cultures emerged as a successful model system of neuronal activity, specially for the physics, biophysics and systems neuroscience communities; general physical principles behind the collective dynamics of neurons have been elucidated within this framework [Beggs 2003, Feinerman 2005, Soriano 2008]. The use of neuronal cultures in classical neuroscience, however, is nothing new, already in the 1950s, cell cultures (both dissociated and organotypical) were being studied, although their utility was always considered marginal, see [Nelson 1975] for a complete review.

Why did it take almost fifty years for neuronal cultures to become widely used and recognized as a useful tool? The answer is already on Nelson's review "[...] The close association and interaction between cells are rigorously interrupted as an integral aspect of the dissociation procedure; this may have some experimentally attractive features, but it is a catastrophic intervention". Classical neuroscience and neurobiology disregarded cultures as a useful tool for understanding brain dynamics and neuronal activity for a long time, they were mainly used to study single or pairwise neuron properties and dynamics; quoting Nelson again "for the study of a number of important anatomical, physiological and biochemical properties of neurobiologic interest".

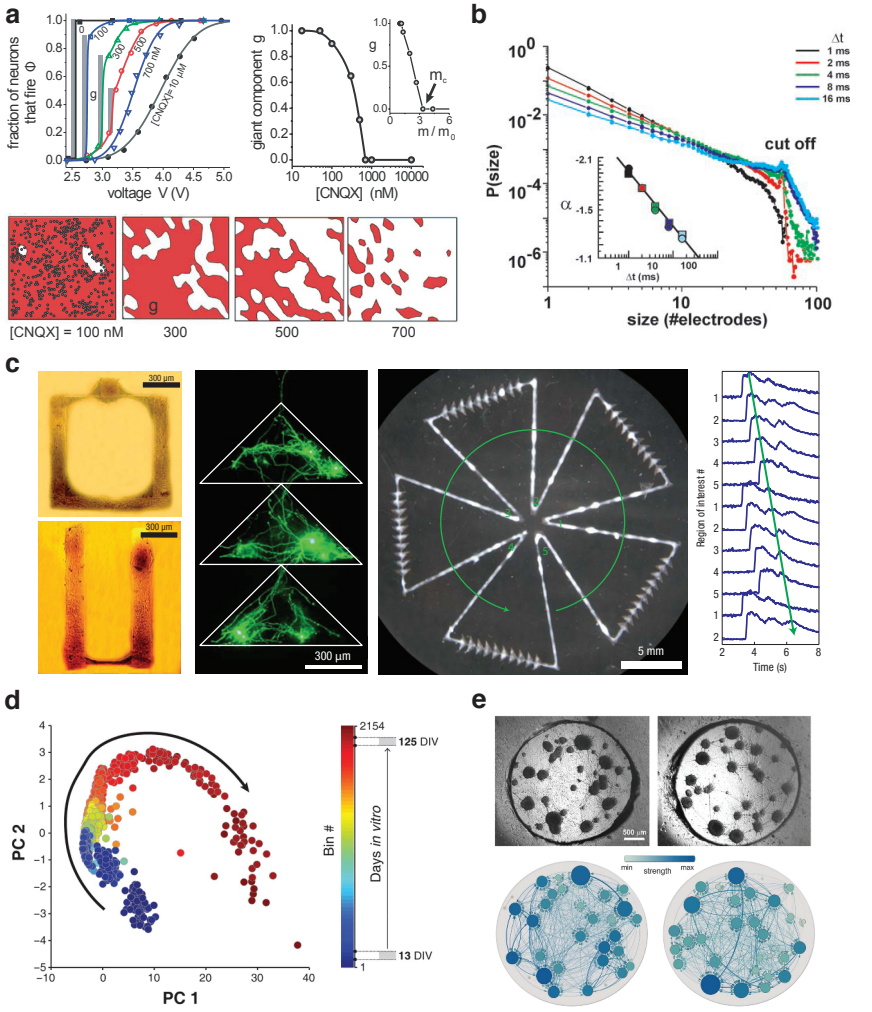

Figure 1.2 | The physics of neuronal cultures. a, Percolation. Fraction of neurons that fire in a culture vs an applied external current for different concentrations of CNQX[a], a drug that debilitates the connections. The giant component forms at a critical value, denoting a phase transition. Repr. with perm. [Soriano 2008]. **b,** Criticality. Probability distribution of avalanche sizes in an organotypic cortical culture for different binning sizes, denoting a sweet spot of critical behavior with a characteristic exponent of $\alpha = 3/2$. Repr. with perm. [Beggs 2003]. **c,** Neuromorphic devices. Equivalent of logic gates built from neuronal tissue. Top left: AND gate. Bottom left: threshold component. Middle: three diodes coupled together. Right: a clock built from many diodes, the signal can only travel counterclockwise. Repr. with perm. [Feinerman 2008]. **d,** Development. Activity patterns analyzed by Principal Component Analysis across more than 100 days of culture development. The system self-organizes and evolves continuously in phase space. Repr. from [Pu 2013] CC BY NC SA. **e,** Network theory. Network reconstruction and characterization through its dynamics in cultures of highly clustered networks. Top: two characteristic examples of the real tissue. Bottom: the reconstructed network. Repr. from. [Teller 2014] CC BY.

[a] 6-cyano-7-nitroquinoxaline-2,3-dione.

It took twenty years since the first studies with cultures, for the development of experimental techniques capable of recording simultaneously activity of many neurons; and twenty more for them to mature and become easily available to interdisciplinary laboratories. Multi–unit recording of neuronal activity in cultures has evolved through two different techniques: multielectrode arrays (MEAs) and calcium imaging, both implemented in the 80s. Before that, most activity recordings were based on the patch–clamp technique, first using on–cell patch mode [Neher 1976] and later as whole–cell recordings [Hamill 1981, Fenwick 1982], e.g. [Hirano 1986].

1.3.1 Multielectrode arrays

The typical MEA preparation for cultures consists of a glass coverslip on which a thin–film microcircuit has been deposited. The microcircuit contains an array of microelectrodes that are directly in contact with the neurons or the medium and are able to record changes in extracellular currents. The first MEA in dissociated cultures can be traced back to [Pine 1980][6] and consisted of 32 electrodes of 8x10 μm in area. The most common MEAs used in the present day[7] remain basically unchanged, consisting of 64 electrodes of 30 μm diameter spaced 200 μm apart, e.g., [Beggs 2003, Jacobi 2007, Czarnecki 2012]. Newer setups, however, are actively being developed, from high–density MEAs with 512 recording sites [Litke 2004, Ito 2014] to multi-transistor arrays based on CMOS[8] technology presenting up to 11,011 [Frey 2009], 16,384 [Lambacher 2011] and 32,768 [Eversmann 2011] recording sites, reaching subcellular resolution with densities between 3,000 and 12,000 transistors/mm^2 (see Figure 1.3).

The electrodes in standard MEAs record the local field potential (LFP) produced by the various neurons in its vicinity and by crossing neurites. Spikes are easily inferred from sharp changes in the LFP, where each electrode is usually able to detect spikes from 1 to 3 neurons via spike sorting algorithms (see [Lewicki 1998] for a review). MEAs recordings accurately detect spikes with sub–millisecond resolution, however, they are only able to record activity from a small subset of the whole population (see Figure 1.3a for a visual estimate of the amount of neurons present between electrodes) and usually only in a small region of the culture, typically in a 2x2 mm area while cultures usually span 13 mm in diameter. Although high–density MEAs and CMOS chips are able to overcome its main limitation (spatial sparsity), its technological development still presents some challenges and we might need another decade for them to become the new standard.

[6] The first MEA, however, was presented in [Thomas 1972] for heart cells.

[7] MultiChannelSystems, Reutlingen, Germany.

[8] Complementary metal-oxide-semiconductor

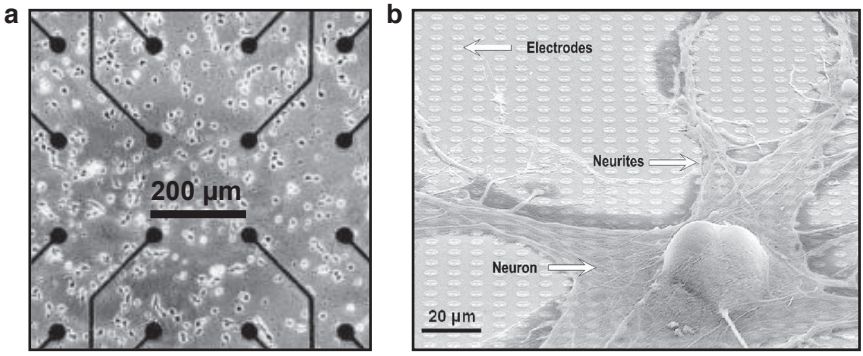

Figure 1.3 | Multielectrode Arrays (MEAs). a, Standard MEA configuration, central view of an 8x8 electrode grid for a high density culture 1 day after plating. Repr. from [Wagenaar 2006a] CC BY. **b,** Snail neuron on a CMOS chip in culture. There is a 200-fold increase in electrode density respect to the standard MEA configuration. Repr. from [Eversmann 2003] ©2003 IEEE.

MEAs have been an extremely successful in the study of collective neuronal activity, specially in culture development [Van Pelt 2004a, Wagenaar 2006a], neuronal avalanches [Beggs 2003, Beggs 2004], self–organized criticality [Pasquale 2008, Tetzlaff 2010], memory [Dranias 2013], and oscillations [Czarnecki 2012] to name a few. They have not been able, however, to shed much light in the precise spatial structure of the activity patterns, and the only studies that dealt with it were either based on acute slices [Tscherter 2001, Compte 2003], one–dimensional systems [Jacobi 2007] or, surprisingly, the first MEAs studies on cultures [Robinson 1993, Maeda 1995], mostly because their "primitive" setups had a much higher intra–electrode distance and were able to observe activity at much larger distances. New studies related to the internal network structure (or the microconnectome) are also starting to appear [Shimono 2014], and go in the same direction as the main results presented in this thesis.

1.3.2 Calcium imaging

Standard calcium imaging techniques in neuroscience are based on the fact that calcium is one of the main signaling molecules in neuronal activity; amongst others, it is involved in spike generation via voltage-gated channels and internal stores, and also in synaptic transmission via AMPA[9] and NMDA[10] receptors, which are calcium-permeable when bound with glutamate (see [Grienberger 2012] for a review). The main idea is to obtain a molecule that when bound to a calcium ion,

[9] α-Amino-3-hydroxy-5-methyl-4-isoxazolepropionic acid.

[10] N-Methyl-D-aspartate.

fluoresces with a characteristic wavelength and is recorded with an external device, like a CCD[11] camera or a photomultiplier.

Although the first calcium indicators date back to the 60s and were based on bioluminescent photoproteins [Shimomura 1962, Ashley 1968], it took 20 years of continuous improvements to achieve an indicator good enough for mainstream use, fura-2 [Grynkiewicz 1985], a chemical indicator. Nowadays there is a wide variety of calcium markers being used in neuroscience, from whole cell chemical indicators, like Fluo-4 [Gee 2000] and Rhod-2 [Minta 1989], to genetically encoded ones, like the GCaMP family [Nakai 2001]. The choice of indicator depends on many factors, but usually on the area of study (culture, single cell, or intracellular) and on the visualization and recording instrument, photodiode array, CCD camera, confocal or two-photon microscope, etc.

Despite the growing complexity in calcium imaging research, its main protocol for *in vitro* neuronal cultures has not changed much in the last decades. A solution containing the fluorescence dye (fura-2 at the beginning, and fluo-4 nowadays) is introduced in the culture well before imaging. After incubation, the culture is transfered to the imaging device (mostly a microscope) for recording. The culture is lit with a light source through a dichroic mirror and the fluorescence response of the molecule is recorded (usually with a CCD camera). During the incubation period, the fluorescence molecules are absorbed by the neurons, and since they already contain calcium, some of the molecules bind to the calcium ions and produce a fluorescence response at rest. When the neuron is actively firing, however, there's a 2-fold increase in calcium concentration inside the cell, which produces a sharp increase in the response signal. One of the interesting things about calcium imaging is that the binding rate of the marker to calcium is much higher than the unbinding rate, so it accurately identifies the time point when a response is triggered and also allows recording at slow speeds, since the unbinding is slow.

This imaging protocol was already being used right after the development of fura-2 to study neuronal excitation in hippocampal cultures, although at the single cell level [Kudo 1986]. The first results on spontaneous activity appeared just a year later [Ogura 1987] (see Figure 1.4a). Almost 30 years later, the recordings are essentially the same (see Figure 1.4b), although current setups allow for much higher recording speeds at bigger areas and with a better fluorescence yield [Stetter 2012, Orlandi 2013].

Beyond the scope of neuronal cultures however, calcium imaging has dramatically changed in the last decade. New imaging technologies, like two-photon [Svoboda 2006] and laser-scanning light-sheet [Keller 2008] microscopy, coupled with new genetically encoded markers allows an unprecedented level of detail in visualizing the brain, both in *in vitro* and *in vivo* preparations. These techniques are non-invasive and capable of recording whole brain activity at the single cell level, the state of the art being more than 80% of all the neurons in the larval zebrafish

[11] Charge–coupled device.

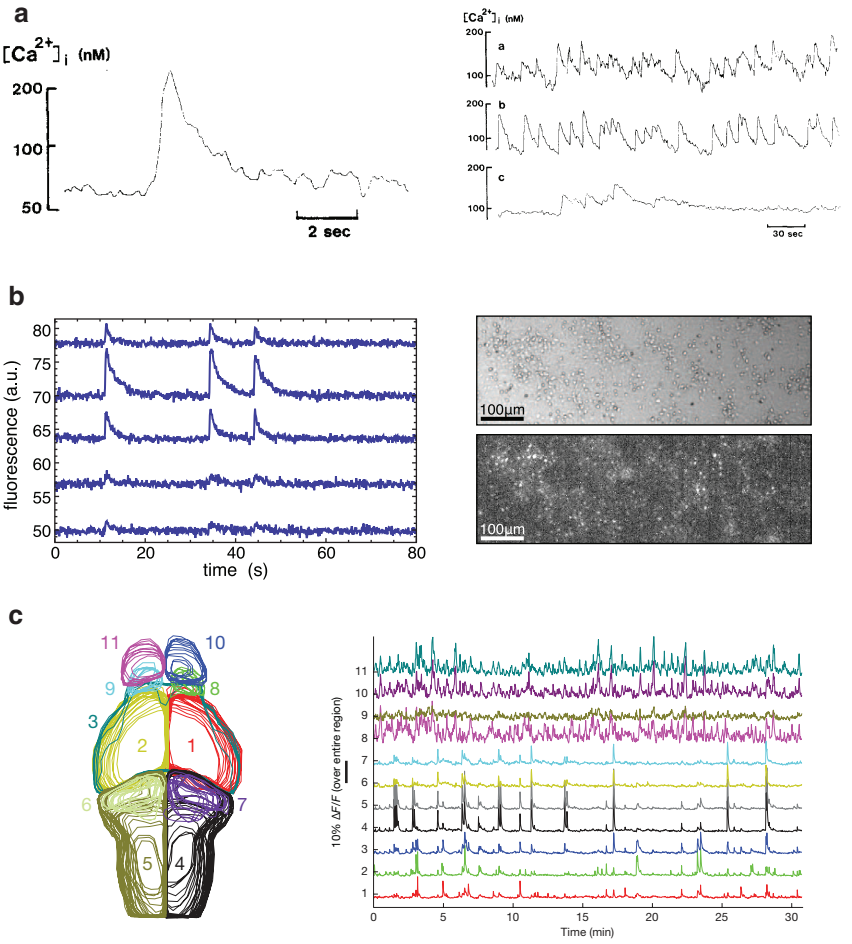

Figure 1.4 | Calcium imaging. a, Left, one of the first calcium traces recorded at the single neuron level showing a burst event, in which the neuron fires multiple times in short succession. The signal shows the characteristic fast amplitude increase when calcium binds to the marker, followed by a slow decay due to the unbinding dynamics. Right, simultaneous recording of three different neurons, showing several coupled, synchronized events. Repr. with perm. [Ogura 1987]. **b,** Left, fluorescence traces recorded more than 20 years later, showing six simultaneous neurons of the hundreds being recorded. Right, area showing a partial view of all the neurons being monitored, (top) bright-field image, (bottom) fluorescence image. Repr. from [Stetter 2012] CC BY. **c,** Whole-brain imaging of the *in vivo* larval zebrafish via high–speed light–sheet microscopy, where more than 80% of all the neurons are recorded. Left, the recorded activity is averaged over different brain areas (numbered). Right, area–averaged traces in a 30 min window. Repr. with perm. [Ahrens 2013].

brain *in vivo* at 0.8Hz [Ahrens 2013] (see Figure 1.4c). They are also the inspiration behind the Brain Initiative, the US funding initiative launched in 2013 to develop novel techniques in brain research [Shen 2013].

1.3.3 Multi–unit recordings of spontaneous activity

The first studies on dissociated cultures focused on morphology and electrophysiology recording two to three neurons at most (see for example [Dichter 1978]), and later expanded to more robust and quantitative studies involving firing patterns of spontaneous activity [Habets 1987] but still monitoring one neuron at a time. Although at the same time calcium imaging was being used to simultaneously record various neurons [Ogura 1987], the results were mostly qualitative. It still took a few years for the first robust results on simultaneous recordings of spontaneous activity to appear, both using calcium imaging [Murphy 1992] and MEAs [Robinson 1993]. By combining early MEAs (4x4 electrodes), calcium imaging and patch–clamp recordings, Robinson and coworkers were able to simultaneously record from different neurons and observe culture–wide periodic bursting, synchronized calcium transients, activity propagation throughout the system and prove that these events had a synaptic origin. This study was later expanded by the same group in a seminal paper [Maeda 1995] that focused on the mechanisms of generation and propagation of synchronized bursting events by using one of the first modern MEA setups (8x8 array) although with a much larger intra–electrode spacing than in current devices.

Maeda and coworkers showed that the activity of developing cultured cortical neurons was dominated by bursting episodes in a narrow frequency band that propagated throughout the system. The localization of the burst onset varied randomly from burst to burst and appeared spontaneously. Their results suggested that the bursting behavior was governed by the level of spontaneous presynaptic firing, the connectivity of the network and the balance between excitability and recovery of the system. It took many years, however, for some of their hypothesis to be verified, both theoretically and experimentally, and is a central focus of attention for this thesis (see Chapters 2 to 5).

Although Maeda and coworkers observed that bursts originated at specific spots of the culture and propagated, almost no other group followed this line of thought, and focused mostly on analyzing the bursts as a synchronization process [Segev 2002, Opitz 2002, Segev 2004, Wagenaar 2006a][12]. The studies that analyzed activity propagation started on one–dimensional cultures, where things are much simpler to understand.

[12] Surprisingly, this might be due to a technological improvement. Their MEA had a much smaller intra–electrode distance than Maeda's original setup and hence were looking at much smaller regions. What appears to be a propagation event can show up as synchronized and unlocalized if the region of observation is small enough.

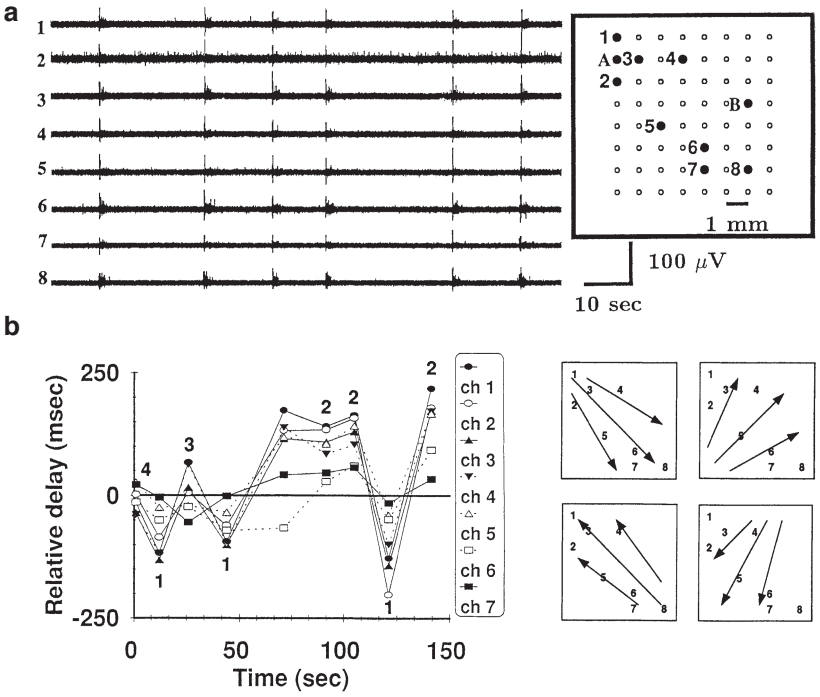

Figure 1.5 | Activity propagation in cultures. a, Left, electrode recordings at eight specific sites from Maeda's original work showing six network bursts. Right, schematic representation of the MEA setup. Notice the 1 mm separation between electrodes, whereas more modern setups have a separation of 0.2 mm (see Figure 1.3a). **b,** Left, relative (to electrode 8) delays on activity onset for different electrodes across nine consecutive bursts. Right, schematic representation of the different propagation patterns across the electrodes. Repr. with perm. [Maeda 1995].

1.3.4 One–dimensional cultures and neuronal models

One–dimensional cultures (1D) consist on neurons grown on a very thin line ($\sim 170\,\mu$m thick), forcing the axons and dendrites to grow in just one possible direction. These lines are created by a combination of chemical coatings and mechanical scratching so that the neurons can only grow in these lines [Feinerman 2003, Feinerman 2005]. With a calcium imaging setup they were able to grow neurons in lines up to 16 mm long (and later up to 8 cm, see Figure 1.6), much longer than the typical axonal length (~ 0.8 mm) in these systems. They were able to observe that activity originated in specific sites of the culture called burst initiation zones (BIZ), usually correlated with high density areas. Activity started by asynchronous firing at slow velocities (~ 20 mm/s), and later developed into a full wave with higher velocities (~ 80 mm/s) propagating throughout the system. There was a clear dependence on propagation velocity and frequency with the number of

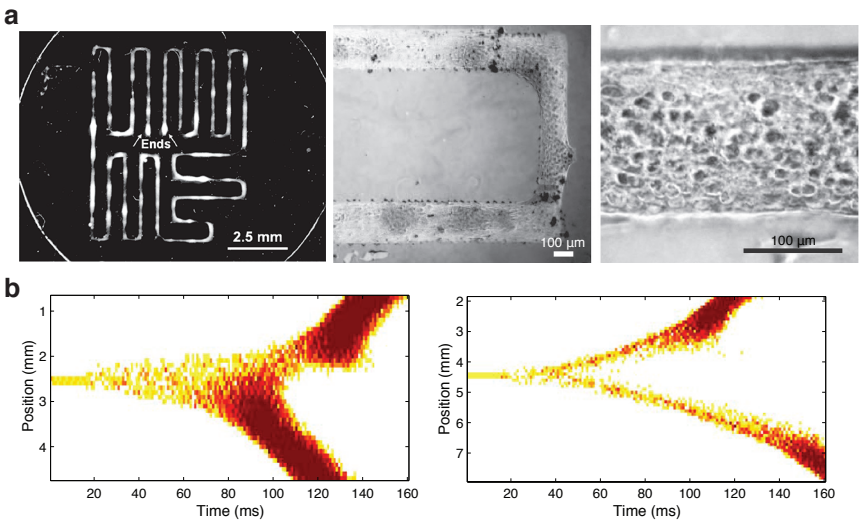

Figure 1.6 | One–dimensional cultures. a, Left, single culture compose of a single thin line 8 cm long. Repr. with perm. [Feinerman 2006]. Middle and right, details of the same line at two levels of detail where the cell bodies can be observed. Repr. with perm. [Eckmann 2007]. **b,** Two examples of propagating waves obtained from the theoretical model that explains the two propagation velocities along an one–dimensional culture. First, a phase of sparse and asynchronous firing (yellow) that starts in a narrow region and later a well-defined traveling wave (red). Color encodes the number of firings per unit area. Repr. with perm. [Alvarez-Lacalle 2009].

excitatory connections and their strength as well as with the excitation–inhibition balance present in the system [Feinerman 2005, Feinerman 2007].

1D cultures were also used to study information transmission and coding. It was shown that these lines act like a chain of Gaussian communication channels although it was found that rate codes could not be reliably transmitted through these network structures [Feinerman 2006]. These lines were later used also as a proof of concept to build neuromorphic devices based on tissue equivalents of logic gates [Feinerman 2008]. By playing with the width and the shape of the lines they were able to build threshold devices, AND gates, diodes and even a clock using a closed sequence of diodes (see Figure 1.2d).

Many of the characteristics of the activity propagation in 1D cultures could be explained by theoretical models of spatially structured activity in integrate–and–fire, synaptically coupled neurons [Pinto 2001, Osan 2004]. These models analyze the propagation of traveling fronts and pulses in neuronal networks by describing the system as an excitable medium. In this description, a potential $u(x,t)$ describes the activity profile for every point x along the line in time t and is governed by the following equation

$$\tau \frac{\partial u(x,t)}{\partial t} = -u(x,t) + \int J(|y-x|) \sum g_{\text{syn}} \exp\left(-\frac{t-t_f^i}{\tau_{\text{syn}}}\right) \Theta(t-t_f^i)\, dy, \quad (1.1)$$

where τ is the membrane time constant, J an arbitrary function describing the connectivity profile that depends only on the relative distance, g_{syn} the synaptic strength, τ_{syn} the synaptic time constant, $\Theta(x)$ the Heaviside step function, t_f^i the time of a presynaptic firing, and the sum goes over all spikes in all synapses. This system can be solved in the linear regime and predicts two different propagating velocities, as in the experiments. The slow velocity however, is an unstable solution, rather than metastable, as the experiments would suggest [Feinerman 2005]. Also, it was shown that a similar system could withstand a complete set of different velocities when a more complex neuron model was considered [Golomb 1997].

With that in mind, Alvarez-Lacalle and coworkers explored discrete neuron models that would be able to explain the experimental data [Alvarez-Lacalle 2009]. They found that the minimal model required to explain the observed 1D dynamics was an adaptive quadratic integrate and fire with depression in the synaptic dynamics. This neuron model is also known as the Izhikevich model [Izhikevich 2003], which in its complete form can be expressed as

$$\begin{aligned} C\dot{v} &= k(v-v_r)(v-v_t) - u + I && \text{if } v \geq v_{\text{peak}}, \text{ then} \\ \dot{u} &= a\{b(v-v_r) - u\} && v \leftarrow c,\ u \leftarrow u+d, \end{aligned} \quad (1.2)$$

where v and u are functions of time that represent the membrane potential and a recovery current respectively. C is the membrane capacitance, v_r the resting membrane potential, v_t the instantaneous threshold potential and I the input currents. k and b are model parameters that can be derived from the rheobase and the input resistance of the neuron (see [Izhikevich 2007] for more information). a is the recovery current time constant, v_{peak} is the spike cutoff value, c the voltage reset value and d describes the total amount of currents activated during the spike and affecting after-spike behavior. The left arrow $\leftarrow$ denotes an instantaneous change of the variables on the left by the right value.

The Izhikevich neuron model is canonical for most real neuronal families, i.e., it can accurately reproduce the behavioral traits of many neurons, and in some cases with a precision comparable to more complex current based models like the Hodgkin Huxley [Izhikevich 2007] (see Figure 1.7). The model only accounts for the neuron response dynamics, and the description of the synaptic dynamics that mediates the coupling between different neurons requires a complementary description.

Neurotransmitters are stored in vesicles at the synapses, and these vesicles can belong to different pools with different availabilities for release. The vesicles of the readily-releasable pool (RRP) fuse with the external cell membrane after an

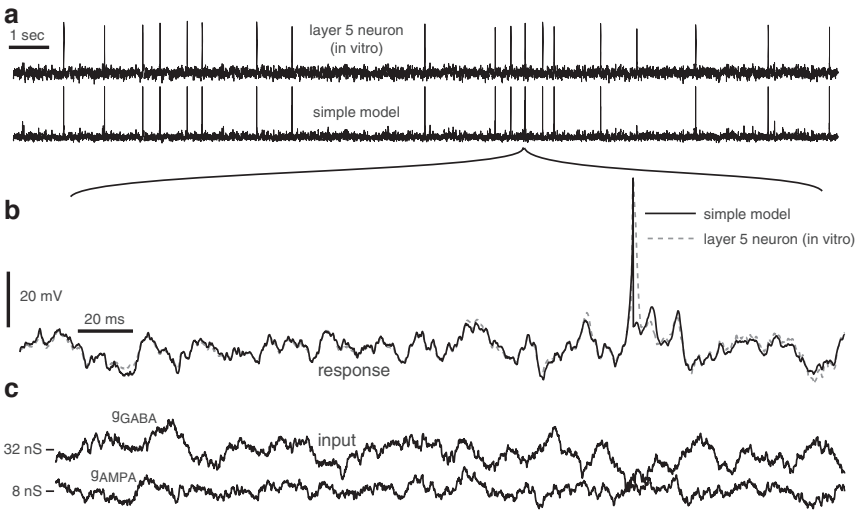

Figure 1.7 | The canonical model. a, Comparison of the activity response of a rat motor cortex layer 5 pyramidal neuron *in vitro* with the model from Section 1.3.4. Excitatory and inhibitory currents for the neuron are generated using an Ornstein-Uhlenbeck stochastic process and applied using the dynamic clamp protocol [Sharp 1993]. Top: the neurons response. Bottom: the simulation response to the exact same input currents. **b,** Magnification of a small region from **a**. The model shows a reasonable fit to the experimental data reproducing over 90% of all the spikes. **c,** The input currents applied to the neuron and the model. Repr. from [Izhikevich 2007] under MIT fair use policy.

action potential (mediated by a calcium signaling pathway) and release the neurotransmitters at the synaptic cleft. These neurotransmitters bind to specific receptors at the postsynaptic terminal producing a signal that travels through the dendritic tree. The kinetics and the dynamics involved in these processes is what is known as synaptic dynamics (see [Stevens 2003, Collingridge 2004, Rizzoli 2005] for more detailed information). In a simplified version the total amount of neurotransmitters available in a synapse is conserved on small time scales, and they can be found in three possible states: recovered (ready to be released), active (bound to the receptor) and inactive (unbound and being recycled).

Regarding synaptic dynamics, it has been observed that short-term synaptic depression (STD) plays a pivotal role in the dynamics of cultures [Cohen 2011], although their importance in slices and *in vivo* during activity is not so clear [Reig 2006]. STD represents the depletion of available neurotransmitters due to repeated activity at the presynaptic terminals. Although there are many models of STD (see [Zucker 2002] for a review on short-term synaptic plasticity), the classical description of STD comes from the seminal work of Tsodyks and Markram [Tsodyks 1997], whose model can be expressed[13] as

[13] Although the original model was a little more complex

$$\dot{R} = \frac{1-R-E}{\tau_R} - U\sum_{t_f} R(t_f)\delta(t-t_f)$$
$$\dot{E} = -\frac{E}{\tau_I} + U\sum_{t_f} R(t_f)\delta(t-t_f), \tag{1.3}$$

where R and E are functions of time for the fraction of neurotransmitters found in the recovered and active states respectively. τ_R and τ_I are the characteristic times of recovery and inactivation respectively, U is the fraction of neurotransmitters that become activated after an action potential[14] and the sum goes over all past spikes t_f. With the synapse at rest, all available neurotransmitters are in the recovered state, but after an action potential a fraction U transitions into the active state inducing a post-synaptic current (PSC) until they become inactivate, and are later recovered. This induced current usually has the form of an alpha function or an exponential for simplicity. Hence, the total current a neuron receives can be seen as directly proportional to the amount of neurotransmitters in the active state E times the synaptic conductance g.

The classical STD description can, however, be simplified into a single depression variable D that models the efficacy of the synapse [Alvarez-Lacalle 2009]. At rest $D = 1$ and after a spike it drops to a value of βD with $\beta < 1$ representing neurotransmitter release. After the drop, the variable recovers exponentially to its resting value or until a new spike, i.e.,

$$\dot{D} = \frac{1}{\tau_D}(1-D) - \sum_{t_f}(1-\beta)D\delta(t-t_f), \tag{1.4}$$

where τ_D is the recovery time constant. The input current a neuron receives from a given presynaptic pair can then be expressed as

$$I(t) = g\sum_{t_f} D(t_f)\exp\left(\frac{t-t_f}{\tau_g}\right)\Theta(t-t_f), \tag{1.5}$$

where τ_g is the characteristic time constant of the synaptic current.

The Izhikevich model with STD is not enough to explain the observed dynamics in 1D cultures by itself. For the model to be complete there are still two missing ingredients: noise and the connectivity profiles. Alvarez-Lacalle and coworkers

[14] We do not consider any form of facilitation, where U would have its own dynamics. In cultures, facilitation plays very little role.

did not consider any noise source, given that they were interested only on activity propagation, and not on spontaneous generation, their protocol manually stimulated the neurons until the activity could be self-sustained. Hence they did not need to consider any of the possible sources of noise in the system.

Regarding connectivity in 1D systems, it is quite straightforward, axons and dendrites can only travel in one direction and the only relevant variable is distance. In their study, they considered only a dependence on axonal length: they established a connection with probability α from neuron i to neuron j if neurons i axon overlapped with neuron j, i.e., $0 < \frac{x_j - x_i}{\pm l} \leq 1$, where the sign denotes if the axon grows towards the positive or the negative axis and l is the axon's length of neuron i (drawn from a Gaussian distribution). For cultures of higher spatial complexity than 1D, the connectivity profiles play an extremely important role, and have to be considered in detail.

1.3.5 Clustered and patterned cultures

Although many interesting results have arisen from 1D studies, their connectivity is too far off from the one encountered in the brain to try to extrapolate the findings to neuroscience; hence several groups have tried to work with cultures with increasing levels of complexity in connectivity, which consist of cultures grown in a two–dimensional substrate but with a constrained topology.

When neurons are cultured without any treatment to the substrate, i.e., the petri dish, at a high enough density, the neurons tend to aggregate to each other and form clusters. Each cluster consists of many neurons (up to several thousands) with their somas touching each other. Each neuron inside the cluster tends to grow its axon in the same direction as their neighbors extending up to other clusters, creating axonal 'highways' that interconnect the clusters and form a network with a topology extremely different from the ones reported in 1D and 2D systems.

The first report from this kind of clusters comes from E. Ben-Jacob's group [Segev 2003]. Their study however, did not focus on connectivity nor in activity. They were interested in the self–organization principles behind clustering formation, involving neuronal migration and growth. The same group also developed techniques to confine neurons in specific geometries, mostly by anchoring the neurons to the substrate with diverse methods, e.g., using poly–D–lysine or carbon nanotubes [Sorkin 2006, Sorkin 2009]; they also looked at activity in clusters and found that as few as 40 neurons were enough to sustain spontaneous collective activity and that activity between clusters propagated with a master/slave asymmetry. At the same time, the group of M. Segal started working with micro–cultures, i.e., cultures consisting of 4–30 neurons and found that those small systems could already develop collective spontaneous activity [Cohen 2011]. J. Soriano's laboratory also

started working with clusters, but with a focus on network theory and the underlying physical principles [Teller 2014] (see Figure 1.2e); although interconnected clusters appeared to fire synchronously, by analyzing the activation sequence with high–speed calcium imaging they were able to resolve the underlying functional network that drives the activity, and found dynamics much richer than master/slave configurations.

In parallel with the development of clustered cultures, several groups started to modify the substrate properties for the homogeneous cultures as well. In fact, a 1D culture is already an example of a patterned culture, and also the neuronal logic devices implemented in E. Moses' group [Feinerman 2007]. The construction of these setups, however, is quite complex and artisan, and does not scale well to more complex patterned structures. The cultures from E. Ben-Jacob's lab also involved patterning; on homogeneous cultures they focused on analyzing master/slave configurations by growing two cultures separated by a physical barrier but interconnected by a narrow bridge [Baruchi 2008]. The group of J. Pine also tried patterning, but with the idea of studying the evolution of very small networks by caging individual neurons [Erickson 2008].

In J. Soriano's laboratory they took a different approach to patterned cultures; they built cultures with patterns inspired by previous experiments with Hele–Shaw flows with quenched disorder [Hernández-Machado 2001, Soriano 2002]. The culture substrate is coated with a photosensitive Polydimethylsiloxane material (PDMS) and a photoresistive mask with the desired disorder pattern is placed on top (initially the pattern consisted of a set of squares distributed randomly, but more complex forms have also been achieved). The sample is then lit with UV light to generate a two–level culture. The bottom level corresponds to the glass coverslip and the top level to the PDMS part that was masked during UV exposure (see Figure 1.8). The result of this technique is that neurons only grow in one of the two possible levels, making the other areas inaccessible. This way it is possible to create custom geometries to study culture dynamics in detail. By using a disordered pattern like the one presented in Figure 1.8 enables the study of the dynamics in the transition between 1D to 2D systems.

1.3.6 Collective dynamics in two–dimensional cultures

In parallel with the studies in confined geometries, several groups directly analyzed both spontaneous and induced activity in homogeneous two–dimensional (2D) cultures with many different approaches, and altogether, a unified view is emerging.

Using percolation theory and electrical stimulation, Soriano and coworkers were able to explain with great detail the developmental stages that undergoes a culture until maturation [Soriano 2008]. When neurons of embryonic brains are placed in

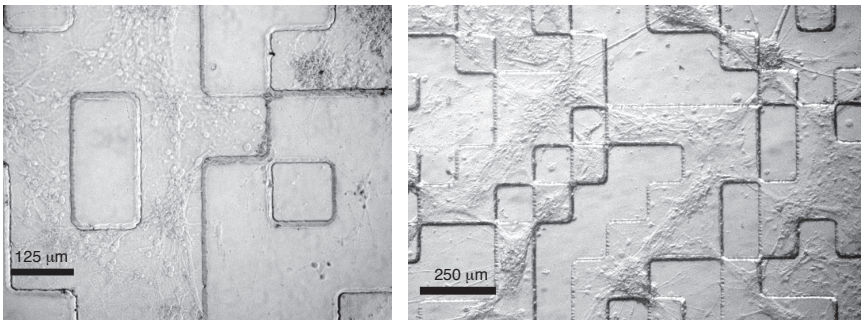

Figure 1.8 | Patterned cultures. Two examples of neuronal cultures patterned with PDMS and random disorder. The neurons grow preferentially in only one of the two levels, although the technique is not perfect. Repr. with perm. [Popiel 2009] ©2009 J. Soriano.

a culture they are not electrically active for the first two days; the neurons, however, start to migrate and grow projections to try and connect with their neighbors. After 2 days in vitro (DIV) a network starts to form and the neurons become responsive to electrical stimulation. At 3 DIV they already show signs of collective behavior after stimulation, and start to respond together, albeit in disconnected clusters; they also become spontaneously active although in this case the firings are still isolated. At day 4 the network is already fully connected and all neurons in the system respond at the same time to stimulation. Although cultures are composed of both excitatory and inhibitory neurons, GABA[15], the main inhibitory neurotransmitter, behaves as excitatory in early stages of development [Ganguly 2001]. It is only after 9 DIV, when the GABA–switch takes place, that inhibition appears.

During the GABA–switch the whole network becomes spontaneously active and is characterized by the presence of network–wide bursts, where all neurons seem to fire together at the same time; the bursts are followed by periods of silence with neurons barely firing. This bursting regime is robust and can last for several weeks; although it is the hallmark of cultures, it is also present in the brain, specially during the development of specific neural circuits, including the cerebellum, the spinal cord, the cochlea and the retina amongst others (see [Blankenship 2010] for a review). For example, during the formation of the ferret's retina, spontaneous activity is key for the development of ocular dominance columns and binocular receptive fields [Huberman 2006] and that blocking retinal waves causes long–term impact on receptive field size [Failor 2015]; in the chick spinal cord spontaneous activity has behavioral implications in motility [Provine 1972] and activity-dependent depression triggers long lasting synaptic reorganization [Fedirchuk 1999].

Van Pelt and coworkers studied the long–term stability of network bursts and observed irregular changes in the dynamics during development, with an increase in burst duration and frequency until 20 DIV, which was followed by a posterior

[15] α-Amino-3-hydroxy-5-methyl-4-isoxazolepropionic acid.

decrease. After 1 month in culture the bursts appeared to be almost instantaneous [van Pelt 2004b, Van Pelt 2004a] and showed activity patterns that resemble cascades of activity, suggesting a possible correspondence to critical behavior. At the same time D. Wagenaar and coworkers performed an extensive study on activity patterns up to 40 DIV with various cell densities, ranging from ultra sparse to dense cultures. They reported an "extremely rich repertoire" of activity patterns with a very high heterogeneity from culture to culture [Wagenaar 2006a] (see Figure 1.9).

Regarding the mechanisms behind burst initiation, the group of S. Marom used MEAs to discover that the sequence of neuronal activation within a burst is non–random and hierarchical, where a small subset of neurons, were consistently active before others [Eytan 2006]. They theorized that an underlying scale–free topology might be behind the underlying process. In a similar direction, a posterior study with data from three different laboratories [Eckmann 2008] also reported the possibility of the presence of leader neurons, with an underlying sub-network that might be activated first and posteriorly recruit neurons in their neighborhoods. This idea was later explored theoretically within the framework of quorum percolation [Eckmann 2010].

1.3.7 Criticality and self–organized criticality

In 2003 and 2004, J. Beggs and D. Plenz published a couple of papers that spanned a new area of research of criticality in neural systems[16] [Beggs 2003, Beggs 2004]. They observed that activity in organotypic cultures and slices from rat cortex were dominated by activity episodes of variable sizes (avalanches). They found that the distribution of sizes followed a power–law behavior with a characteristic exponent of $\alpha = -3/2$ which could be related to the theory of branching processes. The distribution of times also followed a characteristic exponent and a branching parameter σ, could be defined and found to be close to 1, all hallmarks of a system in a critical state. They also found that the spatio–temporal patterns formed by these avalanches formed a characteristic subset and were robust and stable for many hours, being a possible substrate for memory. These avalanches also had the correct structure for information transmission [Beggs 2008]. A later study [Friedman 2012] provided more proof of criticality by showing that the avalanches temporal profiles can be described by a single scaling function, and the different anomalous exponents defined by

$$\begin{aligned} f(S) &\sim S^{-\tau}, \\ f(T) &\sim T^{-\alpha}, \\ \langle S \rangle(T) &\sim T^{1/\sigma \nu z}, \end{aligned} \tag{1.6}$$

[16] Although several authors had already suggested it theoretically for both neural systems and the brain [Corral 1995, Eurich 2002, Chialvo 2004].

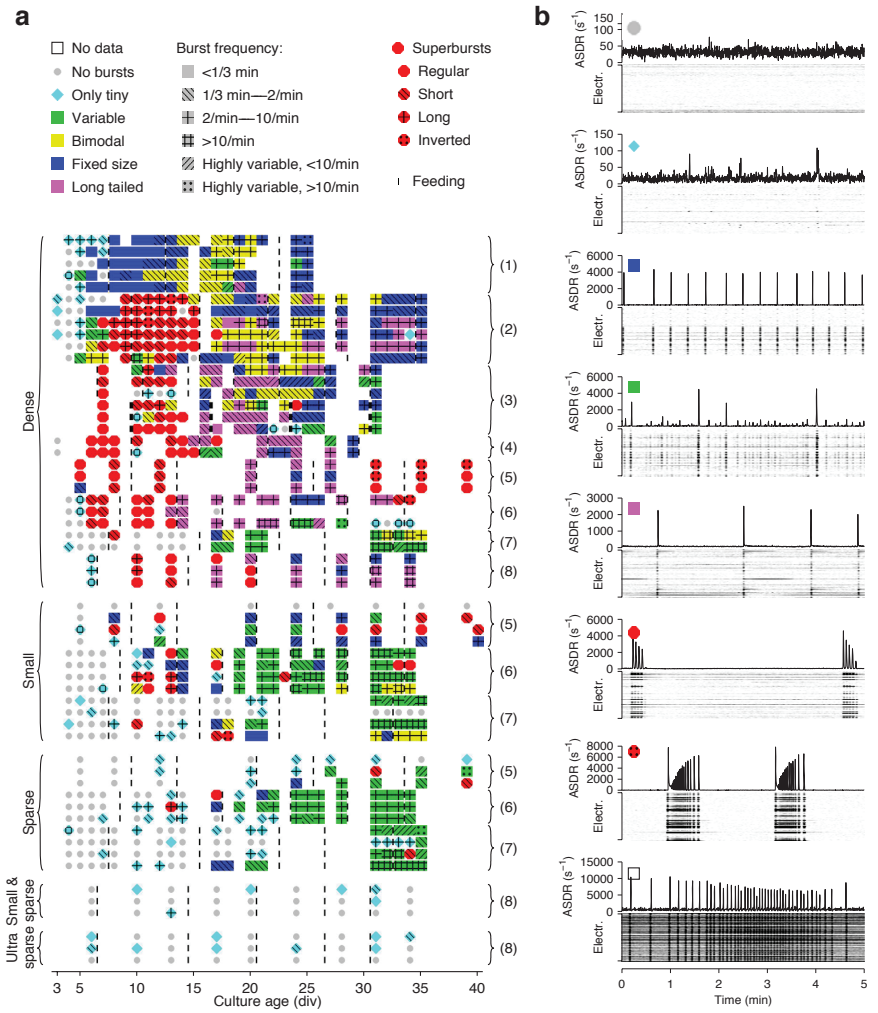

Figure 1.9 | Repertoire of spontaneous activity patterns in 2D cultures. a, Classification of the different activity patterns observed in developing cultures, characterized by their density (y axis) and age (x axis). The patterns are classified by their burst profile and average frequency. A wide variety of patterns coexist with very little correlation, specially in dense cultures. **b,** Examples of various activity patterns, characterized by their average spiking rates (top) and raster plots (bottom) for 5 min samples. The most recurring activity pattern in dense cultures consists of a fixed or variable distribution of bursts with a low frequency, i.e., $< 1/3$ min (blue and green squares). Superbursts, however, also appear quite frequently in dense cultures. In small and sparse cultures, the most recurring activity pattern is either no activity, or bursts with a variable distribution. Repr. from [Wagenaar 2006a] CC BY.

follow the predicted scaling behavior. $f(S)$ and $f(T)$ are the distributions of avalanche sizes and durations respectively and $\langle S\rangle(T)$ the expected avalanche size for a given duration. τ, α, σ, ν and z are the characteristic exponents[17], and they obey the following relationship

$$\frac{\alpha-1}{\tau-1}=\frac{1}{\sigma\nu z}. \tag{1.7}$$

By collapsing the experimental avalanche curves they found the predicted exponent relations and the universal scaling function $\mathscr{F}$ for the datasets that showed signs of criticality (see Figure 1.10).

Probably inspired by these results and also from the results of J. Van Pelt and D. Wagenaar, several groups have been looking for signs of criticality in dissociated cultures. Mazzoni and coworkers showed some power–law distributions on burst size and duration in the leech and hippocampal cultures [Mazzoni 2007], suggesting a critical regime. Simultaneously, V. Pasquale and coworkers analyzed culture maturation under the same perspective [Pasquale 2008], and observed developmental changes from a sub–critical regime to a super–critical and finally a critical one, suggesting that the fate of the culture is "to reach a critical state". Similar results have also been reported from other groups [Tetzlaff 2010, Pu 2013]. Although it is not yet clear what mechanism mediates these developmental changes, it is apparent that the balance between excitation and inhibition in the network is a fundamental aspect, and any disruption in the balance shifts the system away from the critical regime, e.g., blocking NMDA receptors with APV[18] or blocking GABA receptors with bicuculline.

At the same time, several groups have tried to uncover from a theoretical framework the basis of criticality in these systems. They initially correlated some critical exponents to the ones from the theory of branching processes [Harris 1963], and from SOC using the BTW [Bak 1987] and OFC [Olami 1992] models (see also [Pruessner 2012]); but this explanation is nowadays not enough. In a more applied theoretical work, T. Geisel's group introduced the LHG model where dynamical (depressive) synapses in an excitatory network were enough to obtain SOC in neuronal networks with the characteristic $\alpha=-3/2$ exponent when an external drive [Levina 2007] was present; and they later found that they could replace the external drive by introducing facilitation [Levina 2009] in the synapses.

The SOC–description of neuronal avalanches comes from non–conservative models, where an external drive adds energy into the system, which is then released in the form of avalanches with very different time–scales; there is also the presence of an adaptive variable that "tunes" the system and confers it its "self-organization", which in the case of the LHG model is synaptic depression. All these models however, include only excitatory interactions, whereas experimental evidence suggests

[17] The aforementioned α exponent is now called τ to be consistent with the original article.

[18] 2-amino-5-phosphonovaleric acid.

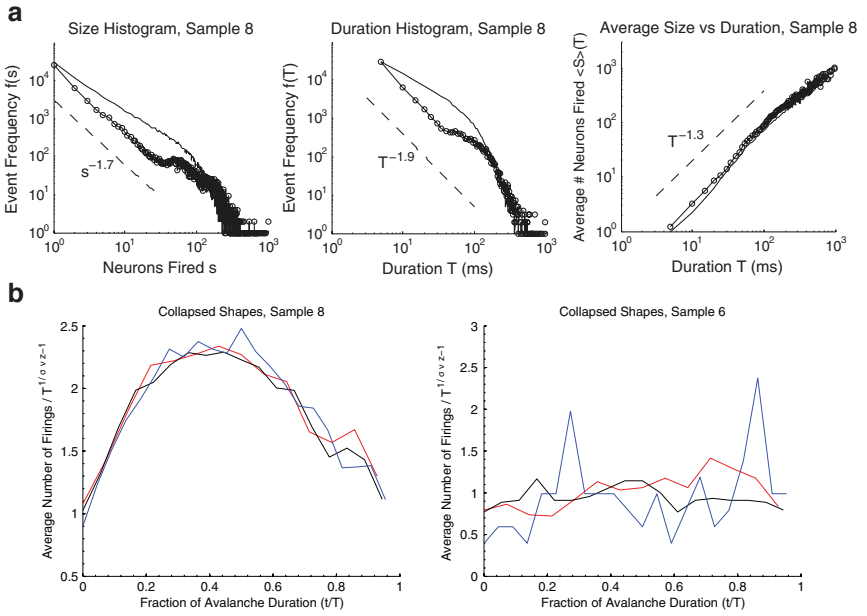

Figure 1.10 | Self–organized criticality in organotypic cultures. a, Distributions of avalanche sizes (left), durations (middle) and its relation, recorded with MEAs in organotypic cultures near the critical regime. **b,** Collapse of the avalanche shapes when rescaled with its characteristic exponents. Each color represents a set of different durations. Repr. with perm. [Friedman 2012].

that inhibition plays a fundamental role in SOC behavior. Evidence of a convincing excitatory–only SOC neuronal system is yet to be found.

Several groups have also developed computational models where inhibition is present [Poil 2012], and some have even tried to establish a relationship between critical systems and to cortical up and down states [Millman 2010, Lombardi 2012], although their relevance is not yet clear, since what is commonly known as cortical up and down states can not really be mapped to a SOC phenomenon [Sanchez-Vives 2010, Ruiz-Mejias 2011]. A theoretical description that takes into account all the experimental observations is still lacking. Developing models with power–law–like behavior is not hard, you only need to know where to look [Stumpf 2012, Schwab 2014].

There has also been progress in the field of SOC in *in vivo* MEA recordings; V. Priesemann and coworkers showed signs of SOC in intracranial depth recordings with varying levels of criticality from wakefulness to deep sleep [Priesemann 2013], and they later suggested that the brain might in fact be in a sub–critical state [Priesemann 2014]. More research is still needed, given that there are still many problems to overcome in these recordings, specially due to finite–size sampling

[Priesemann 2009, Yu 2014]. One has to be extremely skeptic when it comes to critical–behavior in the brain [Beggs 2012].

1.3.8 Advances in cultures

The field of neuronal cultures is evolving rapidly, and the previously mentioned technological advances in MEAs and calcium imaging are generating a new interest on this field from the traditional neuroscience community. While the level of detail that we can achieve with these recording techniques is unprecedented, the capacity of interaction allowed by these techniques is still limited.

The most promising non–invasive technology to modify neuronal activity is optogenetics, which consists of genetically encoding light–sensitive ion channels in the neuron. These channels open when lit with a specific wavelength and trigger neuronal firing, which can be controlled with sub–millisecond precision and is non–invasive, so it can be used both *in vitro* and *in vivo* and for extensive periods of time (see [Yizhar 2011a] for a review). Optogenetics is one of the fastest growing techniques being applied in neuroscience, since it enables an unprecedented level of control at the single neuron level. It is also starting to be used in neuronal cultures, e.g., for the modification of bursting patterns [El Hady 2013].

Another ongoing development is the creation of three–dimensional cultures to better mimic the characteristics of the brain and their environment. The technique is based on the creation of polymeric scaffolds or biocompatible gels where the cells can adhere to and grow [Pampaloni 2007]. Nylon micro meshes, agarose hydrogels and glass microbeads have been used successfully with hippocampal cultures, where the mesh could act as a guide for neurite growth [Yoo 2011, Frega 2014]. There are still several problems to overcome with this technique, mostly regarding recording and visualization, but it is opening new research possibilities, specially in tissue regeneration and on drug delivery studies.

Also promising are the recent developments in neuronal cultures from human cells. Although one cannot harvest cells from living humans, and the use of human embryos for these kind of studies is strictly forbidden, a gate has been opened with stem cells. Until recently, neurons derived from induced pluripotent stem cells (iPSCs) were barely active and could not be used for studies of neuronal dynamics. However, it appears that this issue could finally be overcome by using the appropriate growth medium [Bardy 2015].

1.4 The physiology of neuronal cultures

A neuronal culture, like any living system, is a complex system integrated by a myriad of different components and interactions. While Each of its components is essential for the well functioning of the system, we do not need to characterize each and every one of them to the uttermost detail to be able to understand the system as a whole. In this section we review some of the main concepts and mechanisms from physiology and biology that are needed to understand the behavior of neuronal cultures, specially when it comes to spontaneous activity in two–dimensional cultures.

1.4.1 Connectivity

Understanding the connectivity patterns between neurons is a daunting task (which we will explore in Chapter 6), where each neuron in the living brain can make synapses with thousands of other neurons, sometimes making several connections with the same target. In 1986 researchers completed the full connectivity map (connectome) of *C. elegans* [White 1986], a nematode with only 302 neurons. Its connectivity map, consists of 5000 chemical synapses, 2000 neuromuscular junctions and 600 gap junctions, and although this map is invariant, i.e., the exact connections between neurons are always the same, it proved to be an extremely difficult task. Recent technological advances are making it possible to scale these studies to higher organisms, but there are still many challenges to overcome [Lichtman 2014].

Being able to obtain the full connectome from many organisms and specimens is extremely important [Sporns 2012]. In fact, from a philosophical point of view, the connectome is what gives every one of us our identity, our 'self'. In the words of S. Seung, 'we are our connectome' [Seung 2013]. From a more practical point of view, the data obtained from connectomes is going to greatly improve our understanding of the different wiring mechanisms that give shape to the different brain functions. Even if 'we are our connectome', every one of us is different, and yet, able to function. Unraveling the different universal rules that guide synapse formation and maintenance is the key to understanding brain function. Probably one of the most important tasks for the neuroscience community in the upcoming decades.

In the same direction, several studies have appeared recently trying to untangle the universal principles behind synapse formation. Q. Wen and coworkers observed that most shapes of dendritic arbors are self–similar and can be described by an universal functional form [Wen 2009]. At the same time, several groups have found that the shapes of axonal and dendritic arbors and their connectivity patterns can be described with very few parameters [Snider 2010], and also that a very simple rule is enough to describe neuronal branching [Cuntz 2010], as well as a similar scaling

law for optimal dendritic wiring [Cuntz 2012]. When it comes to particular brain areas, however, things are rather more complicated, e.g., D. Bock and coworkers found that inhibitory neurons in the cortex receive connections from the excitatory neurons with a broad range of orientations, with a lack of specificity [Bock 2011]. At the same time, K. Briggman and coworkers found highly specific connectivity patterns in the retina [Briggman 2011] regarding the computation of direction selectivity.

More specifically in neuronal cultures, Müller and coworkers [Müller 1997] characterized the different populations of excitatory and inhibitory neurons in hypothalamic cultures, and were able to estimate the ratio of inhibitory to excitatory neurons to be 2:3. They also observed that inhibitory neurons formed three times more connections than excitatory ones and also that there was a high number of excitatory–inhibitory reciprocal connections. In the laboratory of M. Segal they have also worked extensively on the physiology of neuronal cultures, and in particular, they characterized how cell density determines the connectivity and morphology of dendrites and spines [Ivenshitz 2010]. They observed an inverse correlation between synaptic strength and cell density, while the strength of spontaneous release remained unchanged. Their results suggest the presence of active mechanisms (plasticity) in the neuron that tune synaptic strength based on its surrounding and their activity.

Given that most neurons in cortical and hippocampal cultures are pyramidal neurons [Spruston 2008], it might be tempting to directly extrapolate from electrophysiological results in these tissues. However, it has to be done with extreme care. For example, it was observed that in layer V of the neocortex, the excitatory post–synaptic potentials (EPSPs) from pyramidal neurons show strong attenuation based on distance [Williams 2002], i.e., the amplitude of the EPSP decayed as it traveled from the synapse to the soma. On the other hand, this attenuation is not present in CA1 hippocampal pyramidal neurons [Magee 2000], where the neurons appear to have developed mechanisms of 'synaptic scaling', so that they can correct the amplitude decay.

1.4.2 Synapse formation and plasticity

The formation and development of connections during maturation in a neuronal culture is an intricate process that involves many different factors (see [Marom 2002] for a review). Neurons in culture start to develop neurites right after plating, and as soon as the cells become spontaneously active, there is a rapid increase in synapse formation, promoted by this activity. The number of total synapses, however, starts to decrease after a few weeks, although the specific time at which this process starts varies greatly between preparations of different laboratories.

The development of synapses is strongly coupled to the activity, e.g., a reduction in activity induces neurite outgrowth, whereas an increase in activity has the opposite effect [Van Huizen 1987]. Also, all synapses appear to be chemical, with no gap junctions present [Nakanishi 1998], although this might be related to the cell densities used in the studies. The development of connections is also coupled to other biological mechanisms, like the presence of neurotrophic factors. It has been shown that the presence of BDNF[19] triggers excitatory synapse formation twofold and also speeds up culture maturation [Jacobi 2009].

In the previous section we reported that the strength of the connections depends on cell density [Ivenshitz 2010], but it also changes during development. One week after plating the distribution of connection strengths is quite narrow, but it broadens after two weeks [Lin 2002]. The strength of the synapses also changes with the levels of activity, where long periods of inactivity increases neurotransmitter release and synapse size [Murthy 2001]. Not only that, but inactivity might also affect the neuron sensitivity to current input by regulating its ionic conductances [Desai 1999].

These mechanisms are related to homeostatic plasticity, which plays a very important role during the development of the nervous system [Turrigiano 2004, van Ooyen 2011] and posterior circuit refinement [Turrigiano 2011]. In a similar direction, there has been interest in trying to induce long–lasting plasticity effects via external stimulation (usually with electrodes). The idea is to try to elicit a non–homogeneous plasticity response by a different mechanism, e.g., spike timing–dependent plasticity [Caporale 2008, Watt 2010]. The results, however, have been mixed. Although there has been several reports of activity–induced plasticity in cultures [Maeda 1998, Jimbo 1999, Shahaf 2001], in most cases it appears to be a non–lasting effect[20]. A thorough study by D. Wagenaar and coworkers tried to induce functional plasticity in cultures with several different protocols and were unable to observe any significant effects [Wagenaar 2006b].

1.4.3 Short–term synaptic depression

Short–term synaptic depression (STD) can also be considered as another type of synaptic plasticity, but on a much shorter time scale. The effects of STD on the activity of neuronal cultures have been reported in numerous studies. We have already shown some of them in Section 1.3.4 from a modeling perspective. STD accounts for the reduction of synaptic efficacy after repetitive stimulation caused by the exhaustion of vesicle pools at the terminals (see [Zucker 2002] for a review). There are many reports of STD in cortical [Boudreau 2005] and hippocampal [Deuchars 1996, Staley 1998] slices, although with different effects

[19] Brain–Derived Neurotrophic Factor.

[20] Soriano, J. (2012) Private communication.

[Virmani 2006]. *In vivo*, however, it could very well be that it has a much smaller importance [Reig 2006].

In dissociated cultures the effect of STD is clear. Different results [Maeda 1995, Tabak 2001, Opitz 2002] already pointed in the direction that STD might play a determinant role in burst termination and distribution. And later, M. Segal group showed unequivocally the role of STD in hippocampal dissociated cultures [Cohen 2011] by directly modifying the dynamics of vesicle recycling.

The current model of synaptic dynamics is characterized by the interplay between three different vesicle pools that exists in the synapses. There exists a small vesicle pool, called the readily releasable pool (RRP) that is located at the synaptic bouton, almost touching (kissing) the membrane [Zhang 2009]. The RRP has very few vesicles (~ 10 in a rat hippocampal synapse), which are ready to be released as soon as a signal (an axon potential) arrives. These vesicles are so close to the membrane that they can also spontaneously fuse REF. After these vesicles fuse with the membrane and release the neurotransmitters in the synaptic cleft, they undergo a slow recycling process which replenishes them and moves them to the recycling pool. The recycling pool is bigger (~ 20 vesicles) and supplies new vesicles to the RRP with a time scale of a few seconds. The third vesicle pool is much bigger (~ 200 vesicles) is called the reserve pool, and is often shared between various boutons. Its main task is to supply the recycle pool with new vesicles, however, it only becomes active after heavy stimulation and its dynamics are extremely slow (see [Rizzoli 2005] for a full review).

The combination of the timescales associated to vesicle recycling and mobilization, specially in the RRP and the recycling pool is what gives STD its characteristic timescales. The timescale associated to STD varies greatly from culture to culture and usually has various components. Garcia-Perez and coworkers [Garcia-Perez 2008] found that the replenishment of the RRP can have two different timescales, a fast one $\sim 7\,\mathrm{s}$ and a slow one $\sim 1\,\mathrm{min}$ which is switched on under heavy use. The strength of depression might also strongly depend on the number of vesicles at each pool. This variability in the STD timescales and pool sizes might explain the wide distribution of bursting activity patterns observed in cultures [Opitz 2002, Wagenaar 2006a].

1.4.4 Spontaneous activity

We have already reviewed in Section 1.3 many of the different dynamical regimes of activity observed in cultures. Here we will focus on the different mechanisms that are involved in the emergence of collective spontaneous activity in cultures, specially in 2D cultures, characterized by the presence of network–wide episodes of collective activity.

1.4.4.1 Noise sources

The collective bursts of activity observed in two–dimensional cultures have a synaptic origin, already shown by H. Robinson and coworkers in one of the first studies of network activity in cultures [Robinson 1993]. They observed that network bursts were completely suppressed after the blockage of excitatory currents by application of CNQX (an AMPA antagonist) and APV (an NMDA antagonist).

Although the propagation of spontaneous firing of individual neurons is necessary to trigger bursts, the determinants of individual spontaneous firings are not so clear. Several reports show that neuronal activity is completely suppressed by the application of CNQX and APV (not only network bursts) [Cohen 2008, Serra 2010]. Many groups have also described that there are no pacemaker or endogenously active cells in hippocampal and cortical cultures [Opitz 2002, Marom 2002], although endogenously active cells are present in spinal cord cultures [Latham 2000], and this effect might depend strongly on the extracellular medium [Su 2001].

Similarly, miniature post–synaptic currents (minis) might play an important role in spontaneous activity and be one of the main sources of noise in these systems [Otsu 2003]. Minis are caused by the spontaneous fusing of synaptic vesicles with the membrane and the subsequent release of neurotransmitters. It has been observed that minis have a functional role in the nervous system, from maintaining synaptic structures [McKinney 1999] to protein synthesis [Sutton 2007] (see [Kavalali 2015] for a review). In cultures, minis are also observed [Serra 2010], and in the case of dense cultures their amplitudes are comparable to the ones from evoked release [Ivenshitz 2010]. Minis might also explain why single neuron activity is also blocked after CNQX and APV application, since they still require free synaptic receptors to trigger any response. Their frequency, however, might be too small to trigger single neuron firing, although they could trigger dendritic spikes instead [Golding 1998, Gasparini 2004].

1.4.4.2 Synaptic currents and other effects

There are two main neurotransmitters involved in synaptic transmission in cortical and hippocampal dissociated cultures, namely glutamate for excitatory connections, and GABA for inhibitory connections (see [Hammond 2001, Hammond 2008] for more details). Glutamate acts primarily in two different receptors, AMPA and NMDA. AMPA plays a major rule in burst generation, whereas the effect of NMDA is mostly associated to burst maintenance and long–lasting plasticity effects [Cohen 2009]. NMDA–induced currents have a much smaller amplitude than AMPA ones, and although they last longer, they are also modulated by the membrane potential of the post–synaptic neuron, having almost no effect if the post–synaptic neuron is not firing (hence its importance in plasticity, as it is only active

when both the pre– and post–synaptic neurons are firing). Among the different GABA receptors, $GABA_A$ is the predominant one. It also plays a major role in burst termination and regulation, but it is not involved in burst initiation. Indeed, given its inhibitory role, it would be surprising if it did.

There are several other mechanisms that might affect spontaneous activity. One that we have already mentioned is the growing medium. Differences ionic concentrations and the presence of specific growth factors might have a big impact on the system dynamics and must be carefully considered from an experimental point of view. Another important factor is temperature, which we have considered in Chapter 2, where we find that the bursting dynamics are present at both room and physiological temperatures. Last but not least, it is worth remarking the presence of astrocites in the culture. Astrocites play very important role in the nervous system [Welberg 2010, Hamilton 2010], and they has been observed to promote activity in cultures [Serra 2010], even though they are not an essential component, since many cultures are grown in the absence of glial cells.

1.5 Connectomics

Important advances in the last decade have provided unprecedented detail on the structure and function of brain circuits [Power 2011, Bullmore 2009] and even programs aiming at an exhaustive mapping of the brain connectome(s) have been announced [Alivisatos 2013, Alivisatos 2012, Abbott 2013a, Chicurel 2000]. First, the combination of invasive and non-invasive techniques such as high-resolution optical imagery and diffusion-based tractography have revealed the major architectural traits of brain circuitry [Hagmann 2008]. Second, functional imaging has provided non-invasive measures of brain activity, both at rest [Deco 2011] and during the realization of specific tasks [Power 2011]. These efforts have opened new perspectives in neuroscience and psychiatry, for instance to identify general principles underlying interactions between multi-scale brain circuits [Raizada 2003, Varela 2001], to probe the implementation of complex cognitive processes [Corbetta 2008, Gaillard 2009], and to design novel clinical prognosis tools by linking brain pathologies with specific alterations of connectivity and function [Lynall 2010, Seeley 2009, Zhou 2012]. At the same time, tremendous technological advancements in serial-section electron microscopy are making the systematic investigation of synaptic connectivity at the level of detail of cortical microcircuits accessible [Bock 2011].

Despite continuous progresses, the understanding of inter-relations between the observed functional couplings and the underlying neuronal dynamics and circuit structure is still a major open problem. Several works have shown that functional connectivity [Friston 2011] at multiple scales is reminiscent of the underlying structural architecture [Deco 2011, Honey 2009, Wang 2013]. This structure-to-

function correspondence is, however, not direct and is rather mediated by interaction dynamics. On one side ("functional multiplicity"), structural networks generating a large reservoir of possible dynamical states can give rise to flexible switching between multiple functional connectivity networks [Battaglia 2012, Deco 2012]. On the other ("structural degeneracy"), very different structural networks giving rise to analogous dynamical regimes may generate qualitatively similar functional networks [Stetter 2012]. Therefore, particular care is required when interpreting data originating from non-invasive functional data-gathering approaches such as fMRI [Logothetis 2008]. Altogether, these arguments call for highly controllable experimental frameworks in which the results and predictions of different functional connectivity analysis techniques can be reliably tested in different dynamic regimes. One of the best experimental platforms for this kind of analysis are neuronal cultures, and this is explored in detail in Chapter 6. In there, we study the reconstruction of connectivity of simulated neuronal networks by directly analyzing calcium imaging time series, with an approach based on information theory called Generalized Transfer Entropy (GTE) [Stetter 2012].

1.5.1 Network inference techniques

There is a rich literature on methods of network structure reconstruction from observed time series, not only stemming from research in neuroscience, but also machine learning and econometrics, which have fueled the area of causal inference from temporal data with numerous novel techniques [Popescu 2013]. Briefly, despite the 20th century rise to prominence of statistics, initially intended to resolve causal quandaries in agricultural and industrial process refinement, the field of statistical causal inference is relatively young. Although its pioneers have received wide praise (Clive Granger receiving the Nobel Prize and Judea Pearl receiving the ACM Turing Award), the methods they have developed are not yet widely known and are still subject to refinement. Even though one of the least controversial necessary criterion of establishing a cause-effect relationship is temporal precedence, many causal inference algorithms do not require time information and establish possible causal relations among observations on other grounds, based on conditional independence testing [Pearl 2000], or, more recently, based on statistics of the joint distribution of pairs of variables. The work of Clive Granger, built upon the 20th century development of time series modeling in engineering and economics, with some input from physiology, lead to a framework which admittedly does not allow us to identify causality unequivocally, but has received a lot of attention because of the simplicity of the method and practical successes obtained in econometrics and neuroscience [Popescu 2013].

The basic idea behind Granger causality is to test whether observations of time series of two variables A and B are symptomatic of an underlying process "A causes

B" rather than “B causes A", is to fit various predictive models A(present time) and B(present time) as a function of A(past times) and B(past times). Clues are obtained if A can be predicted better from past values of A and B rather than from A itself, but B cannot be predicted better from past values of A and B rather than from B itself. Numerous improved methods have been derived, incorporating, for instance, frequency domain analysis in lieu of time domain analyses [Nolte 2010]. One recent idea is to add contemporaneous values of B to predict A, and vice versa, to take into account instantaneous causal effects, due for instance to insufficient time resolution [Moneta 2005].

Another approach, which is not limited to statistics of pairs of variables, is to use score-based methods, by performing a search in the space of all possible architectures, guided by an objective function assessing the goodness of signal reconstruction (possibly penalized to favor sparse connectivity). Such methods include Bayesian approaches such as Dynamical Causal Modeling (DCM) [Friston 2003], which compare data generating models formulated in terms of differential equations (modeling the dynamics of hidden states in the nodes of a probabilistic graphical model), where conditional dependencies are parameterized in terms of directed effective connections. Other related methods include L1 and/or L2 penalized regression methods [Ryali 2012].

These kinds of multivariate approaches very easily reach the “curse of dimensionality”, where there is never enough data to establish statistical significance. On the other hand, in neuroscience, simple linear auto-regressive (AR) models underlying Granger causality do not capture well the complexity of neuronal signals. But not everything is lost, Granger causality is only a special case of a more general form of information theoretic measures. More general ones, like Transfer Entropy (TE) [Kaiser 2002, Schreiber 2000] can capture linear and non-linear interactions between any pair of neurons in the network. TE does not require any specific interaction model between the elements, and therefore it is attracting a growing interest as a tool for investigating functional connectivity in imaging or electrophysiological studies [Gourévitch 2007, Besserve 2010, Wibral 2011, Vicente 2011]. The independence of TE from assumptions about interaction models has made it adequate to deal with different neuronal data, typically spike trains from simulated networks [Kobayashi 2013], multi-electrode recordings [Bettencourt 2007, Garofalo 2009, Ito 2011, Marconi 2012, Shimono 2014] or calcium imaging fluorescence data [Stetter 2012]. TE has proved to be successful in describing topological features of functional cortical cultures [Bettencourt 2007, Garofalo 2009, Marconi 2012], and in reconstructing structural network connectivity from activity [Ito 2011, Stetter 2012].

2

Noise focusing: the emergence of coherent activity in neuronal cultures

The spontaneous activity of neuronal tissues is the ultimate paradigm of complex emergent behavior. Understanding the role of network structure on neuronal dynamics and function is a major challenge that often benefits from modern perspectives in statistical physics and complex networks dynamics [Bullmore 2009, Chialvo 2010]. One of the primary questions one should address is how the spontaneous activity of neuronal networks is generated. In the mammalian brain, spontaneous activity is related to the default, resting–state [Deco 2011], characterized by several oscillatory patterns that cover a wide range of frequencies (the so-called brain rhythms), which play a fundamental role in brain development [Spitzer 2006, Blankenship 2010], synchronization and communication of distant brain areas [Buzsáki 2004].

Although the spontaneous oscillatory activity of neuronal assemblies depends on both intrinsic neuronal properties and network architecture, the robustness of spontaneous activity hints at the existence of general principles that govern its initiation and maintenance. Brain sections in the form of cortical slices preserve many dynamical traits of the original tissue [Sanchez-Vives 2000, Ruiz-Mejias 2011], and organotypical cultures from areas as diverse as the retina [Soto 2012] and the spinal cord [Tscherter 2001] display a rich repertoire of spontaneous activity patterns. Even cultures from dissociated neurons [Eckmann 2007] develop spontaneous activity patterns that resemble those of the brain during development. In fact, in recent years *in vitro* neuronal cultures have been recognized as a successful model system of neuronal activity and general physical principles behind

the collective dynamics of neurons have been elucidated within this framework [Soriano 2008, Feinerman 2008, Cohen 2010].

As we have reviewed in Chapter 1, early stages of activity in cultures are characterized by robust, nearly periodic, episodes of collective neuronal firing (bursts) [Maeda 1995, Opitz 2002, Marom 2002, Wagenaar 2006a, Cohen 2008, Ham 2008], but the mechanisms underlying its generation and maintenance are still poorly understood. Some studies have identified burst initiation areas [Feinerman 2007] or interactions at the population level [Eytan 2006] as triggers of network activity; others have proposed the existence of subnetworks of leader neurons that would control the burst initiation by a recruitment process [Eckmann 2008, Eckmann 2010]; and some have also suggested synchronization through different neuronal types and network structures [Segev 2004, Baruchi 2008].

In this chapter, we unveil a new scenario that shows how the interplay between network topology and intrinsic neuronal dynamics suffice to explain the initiation of collective spontaneous activity as a noise-driven phenomenon. We will prove computationally and experimentally that the global firing of the culture is controlled by a pulse of activity that is randomly nucleated and that propagates throughout the system, and we will expose a mechanism of anisotropic noise amplification that we call *noise focusing*, a phenomenon of implosive, highly heterogeneous concentration of spontaneous activity. This mechanism explains the fast nucleation time scale that is required to reconcile the stochastic alternation of nucleation sites with the nearly periodic bursting.

2.1 Theoretical and computational description of neuronal cultures

To tackle the emergence of spontaneous activity in *in vitro* cultures there are two fundamental aspects that need to be addressed. First, the dynamics governing activity at the single neuron level and their interactions; and second, the underlying network that identifies the connected neuronal pairs. Much is known from the first as neuroscientists and physiologists have spent decades decoding the neuron; but a lot of work is still needed on the network part. Neurons and their activity can easily be probed and visualized in the laboratory, but the connections are much harder to resolve; not only are they much smaller (the typical synapse is below $1\,\mu$m) but their number is vast. There are over 1,000 synapses for every neuron in the brain, and probing every single synapse is infeasible, even with purely observational tools; different strategies are thus required to unveil the network structure on the living brain.

2.1.1 Neuron model

To accurately describe the single neuron dynamics we have to account for both the generation of action potentials in the soma and for the currents involved in neuron–neuron interactions (synaptic dynamics). Following [Alvarez-Lacalle 2009, Izhikevich 2003, Izhikevich 2007] we model the soma dynamics and the generation of action potentials by a quadratic integrate and fire model with adaptation. This description leads to a set of two coupled non-linear ordinary differential equations that, in their reduced form, reads

$$C\dot{v} = k(v - v_r)(v - v_t) - u + I + \eta \tag{2.1}$$

$$\tau_a \dot{u} = b(v - v_r) - u \tag{2.2}$$

$$\text{if} \quad v \geq v_p, \quad \text{then} \quad v \leftarrow v_c, \leftarrow u + d. \tag{2.3}$$

Equation (2.1) describes the dynamics of the soma membrane potential $v(t)$. v_r and v_t are the resting and threshold potentials respectively. C is the normalized leaky membrane capacitance and u is an inhibitory current that accounts for the internal slow currents generated by the activation of ion channels. I contains the synaptic inputs from other neurons and η is a noise term. Equation (2.2) represents effectively the combined effect of the slow currents. τ_a, b and d are parameters that control the adaptation and recovery of the neurons.

In this description, the membrane potential changes from its resting value v_r as it receives inputs from other neurons or noise. Above v_t, the potential grows very rapidly up to a peak value v_p that is associated to the generation of a spike. The potential is then manually reset to $v_c < v_t$ and the inhibitory current u increased. This model accurately describes the generation of the action potential but omits the after–spike dynamics by manually resetting the membrane potential and including an effective refractory time. This omission makes the model very computationally–efficient without sacrificing accuracy, since the after–spike dynamics play very little role in culture dynamics.

The last term of Equation (2.1) accounts for the noise present in the system. The main source of intrinsic noise in our system is a shot noise representing the spontaneous release of neurotransmitters in the presynaptic terminals [Cohen 2009]. This spontaneous release generates small currents (*minis*) in the post-synaptic terminal that travel down the dendritic tree to the soma, in the same way as evoked currents from other firings. In the model, the only difference between spontaneous and evoked currents is their amplitude. Given this choice of noise, most of the presented results can be easily generalized to other neuronal assemblies where the system receives an external and uncorrelated input in the form of a Poisson process. A small Gaussian white noise is also added to the system to account for intrinsic membrane potential fluctuations.

This model reproduces the spiking behavior of most cortical neurons, but given that in cortical networks several types of neurons coexist, we have tested the influence of neuronal variability in the dynamics of the network with no significant changes observed in the overall behavior. For instance, we have studied the influence of subpopulations of low and high threshold spiking neurons (LTSN and HTSN, respectively). We introduced 10% of HTSN (with $v_c = -45$ mV and $d = 50$) [Izhikevich 2003] and 10% of LTSN (divided in two groups, 5% with $v_c = -40$ mV, $d = 55$, and 5% with $v_c = -35$ mV, $d = 60$), and found no significant differences. Consequently, ew restricted most of our numerical simulations to populations of regular spiking neurons. Also, for most of our numerical analyses we have considered fully excitatory networks, although most of the results remain essentially unaffected under the presence of weak inhibition, as is the case for young cultures [Soriano 2008].

The list of parameters used to describe the dynamic behavior of the spiking neurons are listed in Table 2.1.

2.1.2 Synapse model

Each connection between two neurons is associated to a chemical synapse with its own dynamics[1]. For simplicity we consider that when a neuron generates an action potential, all its presynaptic terminals release neurotransmitters at the same time with probability $p = 1$.

Let us consider the dynamics of a synapse that connects neuron i with neuron j ($i \to j$). When the neuron i generates a spike at time t_m it triggers the release of neurotransmitters at the synapse and induces a post-synaptic current at neuron j. This current travels from the synapse to the soma and depolarizes the membrane, facilitating the generation of an action potential at neuron j. The total input currents on neuron j is then

$$I_j(t) = \sum_{i=1}^{k_j^{\text{in}}} \sum_{t_m<t} E_i(t,t_m), \tag{2.4}$$

where $E_i(t,t_m)$ is the current induced by neuron i at time t as a result of the action potential generated at time t_m. The first summation comprises all input connections k_j^{in} on neuron j, and the second one all spikes previously generated. Note that the subset t_m is in general different from neuron to neuron, and can be viewed as the spike history of neuron i.

[1] Electrical synapses play very little role in homogeneous cultures.

Each of the post-synaptic currents is modeled as a sudden increase in intensity at the time of action potential t_m and an exponential decay afterwards. We do not consider any transmission delay given the typical dimensions of cultures. For our excitatory currents we consider only the effect of AMPA receptors since they are the main source of activity in network bursts[2]. The post-synaptic currents due to the firing of neuron i can be expressed as

$$E_i(t,t_m) = g_A D_i(t_m) \exp\left(-\frac{t-t_m}{\tau_A}\right) \theta(t-t_m), \tag{2.5}$$

where g_A is the strength of the synapse (associated to the receptor density at the post-synaptic terminal) and τ_A the characteristic decay time of the post-synaptic current. $D(t)$ accounts for short-term depression, a mechanism in which synapses reduce their efficacy due to depletion of neurotransmitters in their presynaptic vesicles [Golomb 1997]. Short-term depression acts on a fast time scale and therefore affects the spontaneous bursting activity.

Depression is modeled as an internal variable D that describes the efficacy of the neuron presynaptic terminals. D has a resting value of 1 and relaxes exponentially as [Tsodyks 1997, Tsodyks 2000, Alvarez-Lacalle 2009]

$$\dot{D} = \frac{1}{\tau_D}(1-D) - (1-\beta)D\delta(t-t_m), \tag{2.6}$$

where τ_D is the characteristic recovery time associated to the recycling of synaptic vesicles [Garcia-Perez 2008, Cohen 2011]. This recovery time is highly variable from culture to culture and DIV, and is the time scale that controls the inter burst intervals. It is typically in the range $0.5-20\,$s. The release of neurotransmitters at the synapse as a consequence of firing results in a reduction of D to βD, with $\beta < 1$. Subsequent action potentials will induce post-synaptic currents, gradually with lower strength, resulting in a reduced efficacy to generate a spike in the post-synaptic neuron unless the synapse has had enough time to recover.

2.1.3 Metric construction of the network

To construct the neuronal network we model pyramidal neurons (which account for most of the neuronal types found in cultures) as circular cell bodies (somas) with fixed diameter $\phi_s = 15\,\mu$m. The cell bodies are then randomly placed on a bi–dimensional area described by the coordinates (x,y), and without any overlap between cell bodies. The total number N of neurons is given by the density ρ.

[2] We have also tested the effect of NMDA currents, and their major role during bursts is to lengthen their duration, and play almost no role during burst formation.

Table 2.1 | Dynamical parameters. List of parameters used to simulate the neuronal dynamics.

Dynamics Parameters	Value
Soma parameters	
Resting membrane potential	$v_r = -60\,\mathrm{mV}$
Threshold membrane potential	$v_t = -45\,\mathrm{mV}$
Peak membrane potential	$v_p = 35\,\mathrm{mV}$
Reset membrane potential	$v_c = -50\,\mathrm{mV}$
Normalized membrane capacitance	$C = 50\,\mathrm{ms}$
	$k = 0.5\,\mathrm{mV}^{-1}$
	$\tau_a = 50\,\mathrm{ms}$
	$b = 0.5$
	$d = 50\,\mathrm{mV}$
Synapse parameters	
Depression recovery time	$\tau_D = 5 \cdot 10^2 - 2 \cdot 10^4\,\mathrm{ms}$
Depression decay	$\beta = 0.8$
AMPA current strength	$g_A = 10 - 50\,\mathrm{mV}$
AMPA current decay time	$\tau_A = 10\,\mathrm{ms}$
$\mathrm{GABA_A}$ current strength	$g_G = 20 - 100\,\mathrm{mV}$
ycurrent decay time	$\tau_G = 20\,\mathrm{ms}$
Noise parameters	
White noise strength	$g_s = 3 \cdot 10^2\,\mathrm{mV^2 ms}$
White noise auto-correlation	$\langle \eta(t)\eta(t')\rangle = 2g_s\delta(t-t')$
Shot noise frequency	$\lambda = 0.01 - 0.05\,\mathrm{ms}^{-1}$
Shot noise strength (minis)	$g_m = 10 - 50\,\mathrm{mV}$
Shot noise decay time	$\tau_m = \tau_A$
Simulation parameters	
Algorithm	Forward Euler
Time step	$\Delta t = 0.01 - 0.1\,\mathrm{ms}$
Typical Run time	$10^4\,\mathrm{s}$

We consider densities in the range $250 - 1000\,\mathrm{neurons/mm^2}$ to match the values observed experimentally.

From each soma on the substrate an axon grows in a random direction following a quasi–straight path, as described below, and with a final length that is given by a Rayleigh distribution of the form

$$p(\ell) = \frac{\ell}{\sigma_\ell^2} \exp\left(\frac{-\ell^2}{2\sigma_\ell^2}\right), \tag{2.7}$$

where $\sigma_\ell^2 = 900\,\mu\mathrm{m}$ is the variance of the distribution and its value is chosen so that the average axonal length matches the value $\langle \ell \rangle \sim 1.1\,\mathrm{mm}$ measured in our experiments. The choice of a Rayleigh distribution corresponds to a Gaussian isotropic distribution at the axon's tip. If the X and Y coordinates of the axon tip are uncoupled and both follow a Gaussian distribution with variance σ^2, the resulting length is described by a Rayleigh distribution.

Experimental observations show that axons grow mostly straight but with a persistence length of a few hundred microns. To mimic this condition realistically, we apply the following algorithm to position each axon. We initially divide the total length ℓ into small segments $\Delta\ell = 10\,\mu$m long. The first segment is placed at the end of the neuron cell body, and with an orientation that follows an uniform angular distribution

$$p(\theta_0) = \frac{1}{2\pi}. \tag{2.8}$$

The i-th segment is then placed at the end of the previous one, and oriented following a Gaussian distribution around the previous segment given by

$$p(\theta_i) = \frac{1}{\sqrt{2\pi\sigma_\theta^2}} \exp\left(-\frac{(\theta_i - \theta_{i-1})^2}{2\sigma_\theta^2}\right), \tag{2.9}$$

where θ_{i-1} is the angle between the segment $i-1$ and the origin. σ_θ is chosen to obtain the desired persistence length (typically $\sigma_\theta \sim 15°$). The growing process is then repeated until all segments are laid down.

To complete the description of the network we set up the dendritic tree. Based on [Wen 2009], and other similar studies, we consider the dendritic tree of a neuron as a disk of diameter ϕ_d drawn from a Gaussian distribution with mean $\mu_\mathrm{d} = 300\mu$m and standard deviation of $\sigma_\mathrm{d}^2 = 40\mu$m.

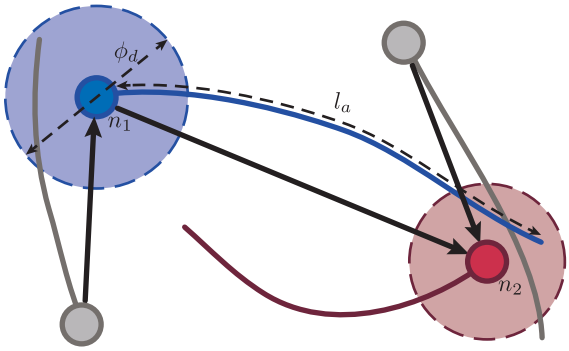

Figure 2.1 | Metric construction of the network. For clarity only four neurons are shown, indicating their somas and axons. The area covered by the dendritic tree is depicted for two neurons (blue and red circular areas). A connection between two neurons (arrow) is allowed whenever the axon of a neuron crosses the dendritic tree of another one.

2.1.4 Connectivity

The growth process described above leads to a geometric construction of the network connectivity based on the following rules. First, a connection can be established only when the axon of a given neuron intersects the dendritic tree of any other

neuron, as illustrated in Figure 2.1. And second, those neurons that fulfill this geometric condition will connect with probability α. This probability of connection is considered to be independent of the overlapping length between the axon and the dendritic tree that is intersected [Wen 2009]. For $\alpha = 1$, any axon that crosses a dendritic tree establishes a connection. In large neuronal structures, e.g. cortex, where the connectivity profiles are known, α is in the range $0.1 - 0.2$. However, in neuronal cultures α is higher due to the reduced connectivity and dimensionality. In our case we consider α in the range 1/3–1. The whole network connectivity that results from this geometric construction is stored in the adjacency matrix A, where $A_{ij} = 1$ identifies a connection[3] $i \to j$.

The typical range of parameters used to generate the networks are presented in Table 2.2.

Table 2.2 | Network parameters. List of parameters used to generate the neuronal networks.

Network Parameters	Value
System-wide parameters	
System size $L \times L$	$L = 5 - 20\,\text{mm}$
Density	$\rho = 10^2 - 10^3\,\text{neu/mm}^2$
Morphological parameters	
Soma size (fixed)	$r_a = 7.5\,\mu\text{m}$
Dendritic tree (Gaussian pdf)	$\mu = 150\,\mu\text{m},\ \sigma = 20\,\mu\text{m}$
Axonal length (Rayleigh pdf)	$\sigma = 800\,\mu\text{m}$
Axonal segment length (fixed)	$l_s = 10\,\mu\text{m}$
Axonal segment angle (G. pdf)	$\mu = 0,\ \sigma = 0.1\,\text{rad}$

More complex and realistic models for network construction exist, like the work by Van Ooyen [Van Ooyen 1995], where they constructed a model for network generation based on self–organization principles of neurite growth and neuronal activity; including axonal overshooting and synapse pruning. Although their model accurately reproduces some dynamical observables, it is of high computational complexity and still misses some key points, like a real asymmetry between input and output connections, and is based on a self–organization mechanism of average activity that is nowadays still unclear. We chose instead to create a non–dynamical model of network generation that matched most of our experimental observables while making as few assumptions as possible.

[3] We only consider monosynaptic connections.

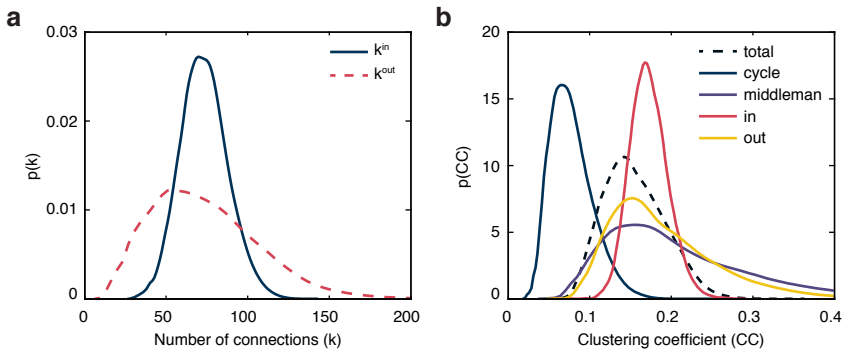

Figure 2.2 | Network connectivity distributions. a, Input and output connectivity distributions for a characteristic network. Although both distributions have the same average, their profiles differ greatly. **b,** All possible clustering coefficient distributions for the same network.

2.1.5 Network properties

All the network properties can be extracted directly from its adjacency matrix A. To study our networks we will focus on connectivity, clustering, triangles and loops, distinguishing between inputs and outputs since the adjacency matrix is not symmetric. Input and output connectivities for neuron i are respectively defined by

$$k_i^{in} = (A^T \mathbf{1})_i = \sum_j A_{ji}, \tag{2.10}$$

$$k_i^{out} = (A\mathbf{1})_i = \sum_j A_{ij}, \tag{2.11}$$

where the sum goes over all the N neurons in the network (we do not allow self–connections) and $\mathbf{1} = (1,\ldots,1)$ is the N–dimensional unit vector. Note that $\langle k^{in} \rangle = \langle k^{out} \rangle$, although their distributions usually differ as we can see in Figure 2.2a. The total number of triangles for neuron i is

$$T_i^T = 1/2(A + A^T)^3_{ii}, \tag{2.12}$$

and the associated clustering coefficient is

$$C_i^T = \frac{(A + A^T)^3}{(k_i^{in} + k_i^{out})(k_i^{in} + k_i^{out} - 1) - 2k_i^{\leftrightarrow}}, \tag{2.13}$$

where $k_i^{\leftrightarrow} = (A^2)_{ii}$ is the number of bidirectional links of neuron i. The clustering coefficient is an important observable that characterizes percolation properties of the network [Serrano 2006], and it is a measure of the number of loops (triangles) a node makes over all its possibilities (based on its connectivity). The above

definitions of triangles and clustering coefficient do not take into account the directed nature of the network links. For directed networks different triangles can be distinguished and the respective clustering coefficients can be defined, and expressed by similar operations as shown in Figure 2.3 (see also [Fagiolo 2007, Ahnert 2008] for details).

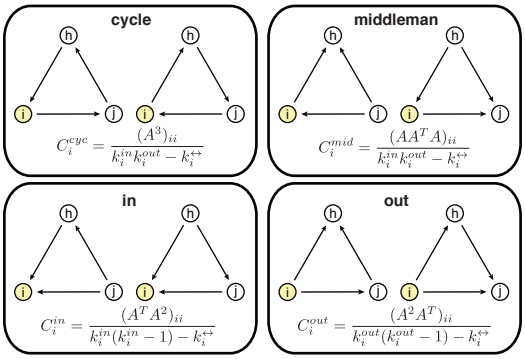

Figure 2.3 | Clustering. All possible connectivity triangles that neuron i can form with its neighbors as well as its clustering coefficient definitions, where $k_i^{\leftrightarrow} = (A^2)_{ii}$ is the number of bidirectional connections. Note that 'cycle' is often called 'feedback loop' and the set of 'middleman', 'in' and 'out' correspond to 'feed-forward loops'.

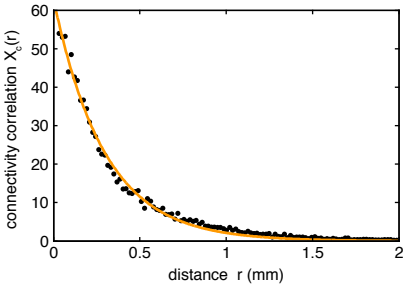

Figure 2.4 | Correlation distance. Correlation distance for a characteristic network according to Equation (2.14). In orange, an exponential fit, resulting in a characteristic length of $\xi_c = 0.26 \pm 0.01$ mm.

Given that our networks have a large number of neurons and are extended in space, instead of working with their individual properties, such as input and output connectivity or triangles, it is better to describe the networks by their *network maps*, a coarse-grained representation of the local observables. These maps are obtained by averaging neuronal properties over a specific kernel[4] with a size given by the average connectivity correlation length ξ_c, which is usually of the order of the size of the dendritic tree, i.e. 300 μm. The precise value of this correlation length is extracted from the decay of the connectivity correlation function $X_c(r)$, defined as the average number of connections that each pair of neurons have in common, as a function of the distance between neurons r

[4] We used a flat, circular kernel.

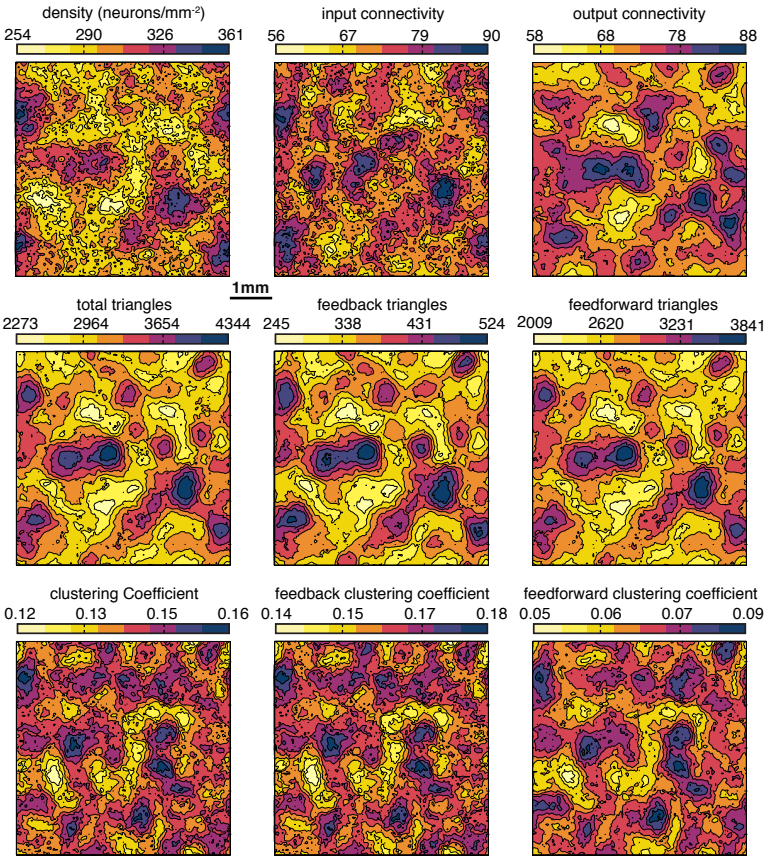

Figure 2.5 | Topological network observables. Network maps obtained from coarse–graining the different topological observables in a network with periodic boundary conditions using the parameters from Table 2.2. The different triangles and clustering observables have been grouped into feedback and feedforward loops.

$$X_c(r) = \sum_{i,j=1}^{N} \sum_{k=1}^{N} \left(A_{ik}A_{jk} + A_{ki}A_{kj}\right) \delta\left(\left|\mathbf{r}_i - \mathbf{r}_j\right| - r\right). \tag{2.14}$$

In general $X_c(r)$ can be fitted by an exponential $\sim \exp(-r/\xi_c)$ which defines the correlation length. The maps for a characteristic network are shown in Figure 2.5.

2.1.6 Connectivity distributions

Based on the connectivity rules from Section 2.1.4 and the respective distributions, the output connectivity of a neuron is easily calculated if we consider the axon to be completely straight. Given a neuron with axon length ℓ, its average output connectivity k^{out} is the number of neurons within range $\langle \phi_d/2 \rangle = \mu/2$ of its axon that form a connection with probability α

$$k^{out} = \left(\pi (\frac{\langle \phi_d \rangle}{2})^2 + \langle \phi_d \rangle \ell \right) \rho \alpha, \tag{2.15}$$

If we now average over all neurons we obtain

$$\langle k^{out} \rangle = \left(\frac{1}{4}\pi\mu^2 + \mu \int_0^\infty \ell p(\ell)\, d\ell \right) \rho\alpha = \left(\frac{1}{4}\pi\mu^2 + \mu \langle \ell \rangle \right) \rho\alpha, \tag{2.16}$$

where $\langle \ell \rangle = \sigma_\ell \sqrt{\frac{\pi}{2}}$. To compute the probability distribution of output connectivity $p(k^{out})$ we need to take into account the distributions of density, dendritic trees and axon lengths. As we have just seen, the output connectivity of a given neuron is defined by its axon length and the sizes of the dendritic trees of the neurons it intersects. These however result in the combination of many independent random variables, and can be approximated by their means. Given that, the probability to have k^{out} connections is the same as having an axon of length

$$\ell = \left(k^{out} - \frac{1}{4}\pi\mu^2\rho\alpha \right) \frac{1}{\mu\rho\alpha}, \tag{2.17}$$

and after changing variables and applying it to the Rayleigh distribution

$$p(k^{out})\, dk^{out} = \frac{k^{out} - \frac{1}{4}\pi\mu^2\rho\alpha}{(\mu\rho\alpha\sigma_\ell)^2} \exp\left(- \frac{\left(k^{out} - \frac{1}{4}\pi\mu^2\rho\alpha \right)^2}{2\left(\mu\rho\alpha\sigma_\ell\right)^2} \right) dk^{out}, \tag{2.18}$$

for $k^{out} > \frac{1}{4}\pi\mu^2\alpha$.

The input connectivity can be calculated in a similar way if we also consider the axons straight, although it is more involved. For a given neuron j with dendritic tree diameter ϕ_d, it will form a connection with another neuron k that is found at a distance r ($r > \phi_d/2$), if its axon initial angle is in the range $\theta_0 \in (-\psi, \psi)$, where

$$\psi = \arcsin\left(\frac{\phi_d}{2r} \right), \tag{2.19}$$

i.e., the axon of k can intersect within the dendritic tree of j. For the axon to intersect, it also needs to have a length of

$$\ell_m = r\cos\theta_0 - \sqrt{\frac{\phi_d}{2}^2 - r^2\sin^2\theta_0}, \tag{2.20}$$

or larger. If we now average over all possible lengths and angles we obtain the probability that the axon of a neuron at a distance ($r > \phi_d/2$) intersects with the dendritic tree of j, which reads

$$P(r > \phi_d/2) = \int_{-\psi}^{\psi} d\theta_0 \int_{\ell_m}^{\infty} p(\theta_0)p(\ell)\,d\ell\,. \tag{2.21}$$

For our choice of distributions it becomes

$$P(r > \phi_d/2) = \frac{1}{2\pi}\int_{-\psi}^{\psi} d\theta_0 \exp\left(-\frac{\ell_m^2}{2\sigma_\ell^2}\right) \equiv \mathscr{P}(r,\phi_d,\sigma_\ell), \tag{2.22}$$

which can not be simplified any further. All the neurons at a distance $r \leq \phi_d/2$ can form a connection, since they are within its dendritic tree. If we now integrate over the whole area and average over realizations, we obtain the average input connectivity of neuron j

$$k^{in} = \left(2\pi\int_0^{\infty} \mathscr{P}(r,\phi_d,\sigma_\ell)d\,dr + \frac{1}{4}\pi\phi_d^2\right)\rho\alpha. \tag{2.23}$$

If we now average over all neurons, given that $\langle k^{in}\rangle = \langle k^{out}\rangle$ and using Equation (2.16) we obtain

$$2\pi\left\langle\int_0^{\infty} \mathscr{P}(r,\phi_d,\sigma_\ell)r\,dr\right\rangle = \mu\langle\ell\rangle, \tag{2.24}$$

which turns into

$$\left\langle\int_0^{\infty} \mathscr{P}(r,\phi_d,\sigma_\ell)r\,dr\right\rangle = \left\langle\frac{\phi_d\langle\ell\rangle}{2\pi}\right\rangle. \tag{2.25}$$

From this relation and Equation (2.23) we now have a relationship between the input connectivity and the dendritic tree size of the form

$$\phi_d = -\sqrt{\frac{2}{\pi}}\sigma_\ell + \sqrt{\frac{\sigma_\ell^2}{2\pi} + 4\frac{k^{in}}{\pi\rho\alpha}}, \tag{2.26}$$

which allows us to express the input connectivity based on the distribution of the dendritic tree as

$$p(k^{in})\,dk^{in} = \frac{1}{\pi\sigma_d\sqrt{(\sigma_\ell\rho\alpha)^2+2k^{in}\rho\alpha}}\times \exp\left\{-\frac{1}{2\sigma_d^2}\left(\sqrt{\frac{2}{\pi}}\left(\frac{1}{\rho\alpha}\sqrt{(\sigma_\ell\rho\alpha)^2+2k^{in}\rho\alpha}-\sigma_\ell\right)-\mu\right)^2\right\}dk^{in}, \tag{2.27}$$

for $k^{in} > 0$.

The comparison between these approximate distributions and the ones obtained from the numerical model are presented in Figure 2.6. The $p(k^{out})$ is almost a perfect match whereas the $p(k^{in})$ differs slightly, because of the fact that axons are not completely straight.

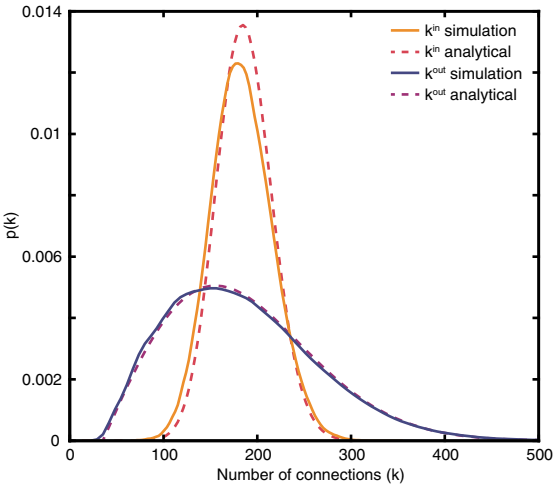

Figure 2.6 | Analytical connectivity distributions. Comparison of the approximated analytical connectivity distributions and the simulated ones for a network with ρ =500 neurons/mm^2, $\alpha = 1$, μ =300 μm, σ_d =150 μm and σ_ℓ =800 μm.

2.1.7 Simulation details

All the source codes used in the simulations are publicly available under an MIT license and are based on the following programs:

- neurongen[5] is the program used to generate the networks. The code is able to generate a neuronal network in any 2D topological configuration by using bitmap images as a mask to tell the neurons where they are able to grow. This feature enables us to use any kind of 2D pattern to modify the connectivity rules.

[5] https://github.com/orlandi/neurongen

- neurondyn[6] is the program used to simulate the dynamics and is implemented to be as efficient as possible. It allows parallelization through OpenMP for the neuronal dynamics and through CUDA for the random number generation. An equivalent code has also been implemented in NEST [Gewaltig 2007], although a new implementation of the Izhikevich model was required (available upon request).

2.2 The emergence of spontaneous activity

Using the parameters from Tables 2.1 and 2.2 the system shows the characteristic activity regime found in neuronal cultures, i.e, collective bursts of spontaneous activity followed by periods of barely any activity (see Figure 2.7a). The bursts are quite periodic, as observed from their inter–burst interval (IBI) distribution (see Figure 2.7d), and each bursts consists of 4–6 spikes per neuron with a frequency of $\sim$ 200Hz. As we have seen in the introduction, several groups have tried to understand the mechanisms underlying the generation of these bursts, but the physical picture is unclear. To tackle this issue we first analyze the activity using data equivalent to the one obtained in classical MEA setups, i.e., a subset of up to 64 neurons within a 1.4x1.4 mm^2 region. By doing so, we are unable to observe any significant similarity between bursts or any sort of internal order. Moreover, the bursts appear suddenly, with no significant changes in activity prior to the burst.

This picture however, changes completely when we analyze the activity of all the neurons simultaneously. By spatially coarse graining the onset time[7] of each neuron in the same way we did to define the *network maps* (see Section 2.1.5), we observe something else; the burst is actually a wave that nucleates in a localized region of the culture and rapidly propagates throughout the system (see Figures 2.7e and 2.7f). The nucleation does not happen in a single point however, but rather on a wide and irregular area. The shape of this area also defines the structure of the propagating front.

This new picture can shed some light in trying to understand why we were unable to see anything significant by observing the activity of a small subset of neurons before. If we calculate the onset time of this subset, and order them with respect to their distance to the nucleation site, we can see that if the nucleation site is close to the region occupied by the neurons, or its shape is highly irregular, then very little correlation between them is found (see Figure 2.7b), whereas if the nucleation site is far from the electrodes a better correlation is observed (see Figure 2.7c). This effect illustrates the difficulty of trying to understand the underlying dynamics by just analyzing the activity of a subset of the system when networks of highly

[6] https://github.com/orlandi/neurondyn

[7] Defined as the mean of spiking times of a neuron within a burst.

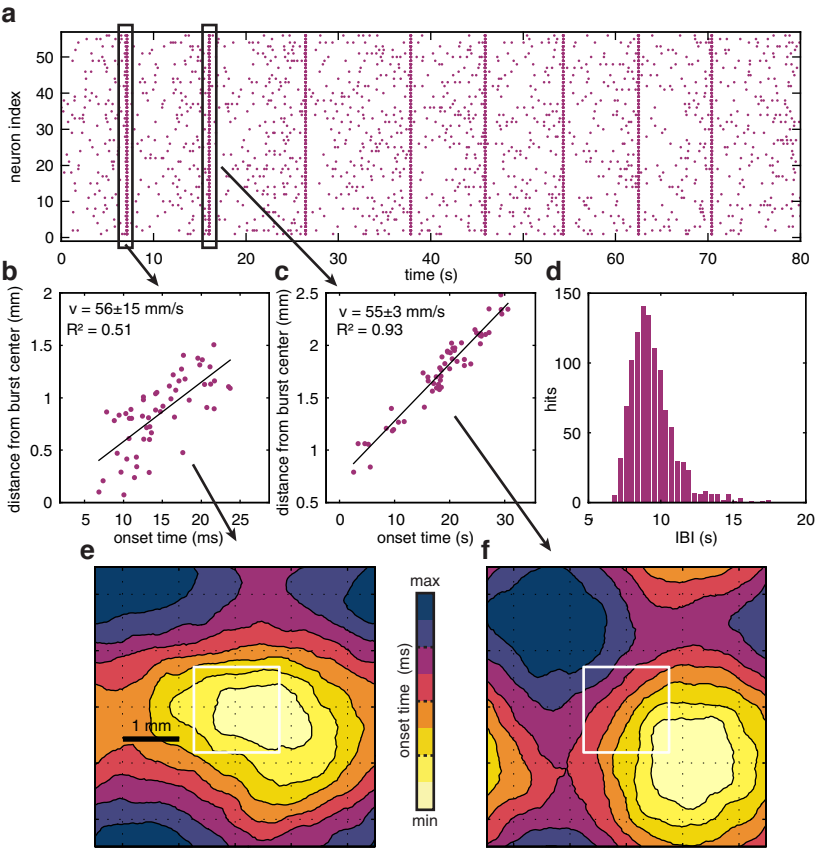

Figure 2.7 | Bursting dynamics. a, Raster plot showing all spikes in a 80 s time window from a selected group of 55 neurons in a region of 1.4x1.4 mm^2 (equivalent to a typical MEA configuration). Bursts are clearly visible as vertical lines where all neurons spike multiple times in a short time span. **b,c,** Onset time (defined as the mean time from the spike train) for each of the 55 neurons from **a,** for two consecutive bursts ordered from their distance to the nucleation point (see main text). In **b,** there is a poor agreement with a constant velocity front given that most neurons are next to the nucleation point. In **c,** the agreement is much better but the data is still quite noisy. **d,** Distribution of inter–burst intervals (IBIs) showing a clear peak at 8 s. The distribution spreads asymmetrically from 6 to 17 s. **e,f,** Wave–profile obtained from the two previous bursts by using the onset time of all neurons in the system. The white square marks the region occupied by the 55 neurons from the raster plot.

non–linear units are involved. Before analyzing the burst structure in detail however, it is insightful to observe how the culture reaches the bursting regime.

2.2.1 Bursting transition

During culture maturation, the network shifts from a state characterized by the spontaneous firing of individual neurons to the reported state of collective firing, composed of bursts of activity. Based on previous studies [Soriano 2008], this transition can be observed within two different but equivalent protocols. First, in a fully formed network that gradually strengthens its connections until bursts appear, and second, in a system that has no connections and forms them until bursts appear.

The first protocol describes a neuron recovering after connectivity blockade with a drug like CNQX, and the later to network maturation during development. These two approaches can be observed in Figure 2.8. If we observe the average firing rate of a neuron as we increase the strength of the connections (g^*, see Figure 2.8a) or the average number of connections ($\langle k \rangle$, see Figure 2.8b) we see a sharp increase in the average firing rate at a specific point ($g^* \sim 6 \cdot 10^{-2}$ and $\langle k \rangle \sim 35$ respectively). If we look at the firing rate distribution we see that the sharp increase in the mean is produced in both cases by the appearance of a high–frequency peak in the distribution, characteristic of the bursting regime (Figures 2.8c and 2.8d).

The appearance of the bursting peak is abrupt, and the transition is better observed if we use the inverse of the bursting rate, the inter–burst interval (IBI), as control parameter. As we can see in Figures 2.9a and 2.9b, for high values of synaptic strength the IBI quickly reaches a plateau whose characteristic value is dominated mostly by the recovery time of synaptic depression τ_D. When the synaptic strength is low, however, the bursting frequency diverges until the point that no bursts can appear in finite time. If we look at the IBI distribution close to the transition (see Figure 2.9c) the distribution is dominated by an exponential tail, characteristic of processes dominated by noise; in this regime, the system has to wait for a sufficiently big fluctuation of spontaneous activity for a burst to form. Far from the transition however, the distribution becomes much more narrow and almost periodic (see Figure 2.9d); in this regime, a burst can develop as soon as the system has recovered from the previous burst.

2.2.2 Macroscopic analysis of bursting dynamics

After characterizing the bursting transition, we can go back and analyze the bursting dynamics in more detail. We begin by trying to identify any pattern within bursts,

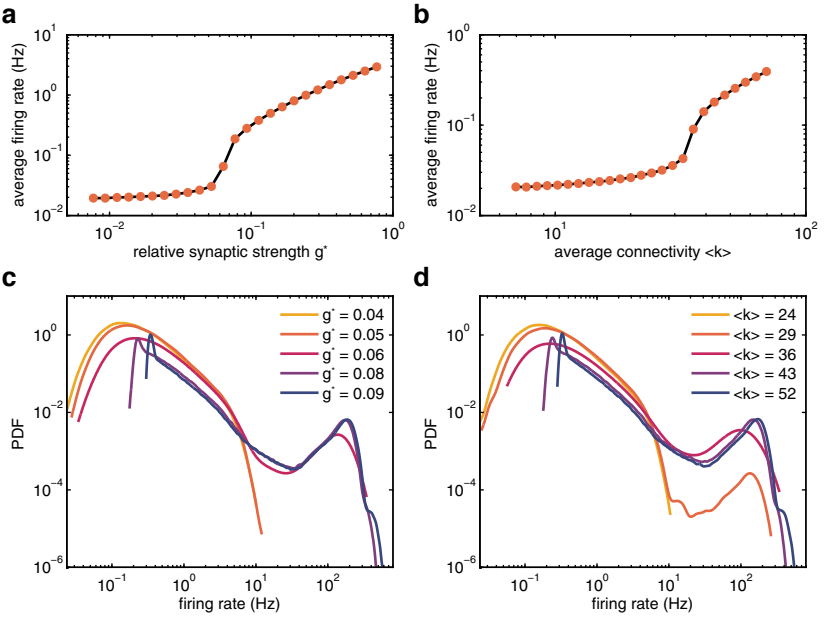

Figure 2.8 | Bursting transition (I). a, Average firing rate in a network with $\langle k \rangle = 75$ for different values of the relative synaptic strength $g^* = g/g^{max}$, where g is the actual synaptic strength and g^{max} the strength required to generate a postsynaptic spike with probability 1. **b,** Average firing rate in a network with $g^* = 0.08$ for different values of the average connectivity. **c,** Probability density function for 5 points from **a,** around the transition. For $g^* < 0.6$ the distribution is unimodal, whereas for $g^* \geq 0.6$ a second maximum appears at a very high frequency ~ 200 Hz, characteristic of the bursting behavior. **d,** Probability density function for 5 points from **b** around the transition. Here the second maximum appears around $\langle k \rangle = 29$. Note that the low–frequency sharp peak that appears in **c, d,** after the bursting transition is due to the last spike in a burst, that is of a much lower frequency.

and define similarity between bursts as follows: we describe each burst by the onset time of every neuron, as we did in Section 2.2. Given a sequence of B bursts, we define the onset vector $O^j = (t_1^j, t_2^j, \ldots, t_N^j)$, where $j = 1 \rightarrow B$, and t_i^j is the onset time of neuron i ($i = 1 \rightarrow N$) within burst j. We now compute the interburst similarity matrix ρ whose entries ρ_{ij} are the Spearman correlation [Hollander 1999] between onset vectors i and j. Spearman correlation is the equivalent of the classical Pearson correlation, but using ranked variables instead. For our onset vector O^j rank 1 is assigned to the first neuron that fires, 2 to the 2nd, and so on, resulting in a new vector $R^j = (r_1^j, r_2^j, \ldots, r_N^j)$ whose entries are the ranks. Using ranks instead of the onset times allows us to establish more robust relationships, specially when non–linear dependencies might exist. Within this framework, the Spearman correlation is defined as

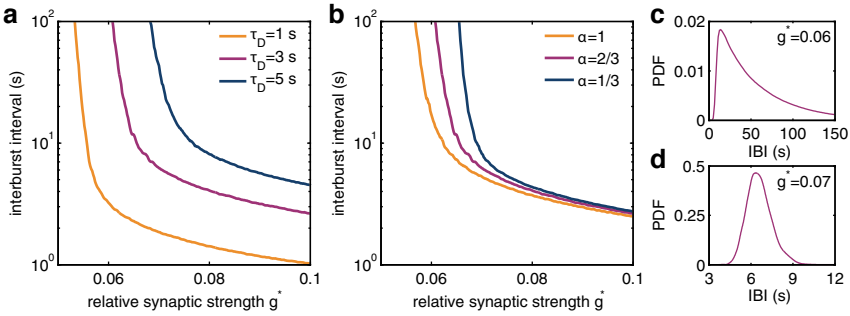

Figure 2.9 | Bursting transition (II). a, Interburst interval dependency with the synaptic strength g^* for different values of the synaptic depression time constant τ_D. For low synaptic strengths the IBI increases rapidly, whereas for high synaptic strengths it slowsly decreases and starts to saturate. **b,** Same but for networks with different clustering (obtained by varying the connection probability α while keeping the average connectivity constant). The bursting transition occurs at very different values of synaptic strengths, while they all saturate to the same value. **c,** Distribution of IBIs close to the transition ($\tau_D = 3$s, $\alpha = 2/3$). The distribution is dominated by an exponential tail, characteristic of processes driven by noise **d,** Distribution of IBIs far from the transition ($\tau_D = 3$s, $\alpha = 2/3$). The distribution is now peaked at its mean with a much narrower distribution.

$$\rho_{ij} = 1 - \frac{6}{N(N^2-1)} \sum_{k=1}^{N} \left(R_k^i - R_k^j \right)^2, \tag{2.28}$$

where $\rho_{ij} = 1$ corresponds to a perfect increasing monotonic relationship between onset vectors i and j, and $\rho_{ij} = -1$ a decreasing one. The data from the Spearman correlation matrix ρ is then used to create an agglomerative hierarchical cluster tree using the shortest distance as metric [Maimon 2010]. After ordering the clusters based on their hierarchy in the tree, we plot ρ with the new order to try to identify similarities between bursts[8]. We can see the results for a particular sample of 256 successive bursts in Figure 2.10, where the first ~ 100 bursts form a clear structure, indicating that these bursts have essentially the same internal structure. The next ~ 25 bursts also form a clear structure, and this one is also almost completely anticorrelated to the first group. Further inspection of some of these bursts shows that each of these two big groups correspond to activity waves initiating at opposite sides of the culture. This analysis tells us that bursts are neither identical nor completely random, but there exists a rich internal structure. It is also important to observe that the groups in the similarity matrix are heterogeneous in size, indicating a preference for specific patterns.

We also checked if there was any temporal correlation between consecutive bursts, i.e., if a burst that belong to a specific group conditioned the group of the next burst. We have not observed any statistical significance in the group of consecutive

[8] Although this procedure appears rather complex, it only involves calling the MATLAB pdist, linkage and dendrogram functions.

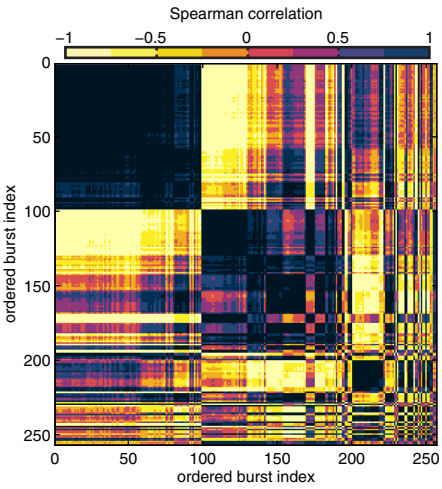

Figure 2.10 | Interburst similarity matrix. The similarity matrix shows the Spearman (rank) correlation between every burst pair onset times. Groups of bursts with similar scores are then grouped together so each color block around the diagonal identifies bursts with a similar structure. The first 100 bursts in the matrix are extremely similar, showing rank correlation of almost 1 to each other, a clear indicator of an underlying pattern. The next 25 bursts also form a similar group, which is also completely anti–correlated with the previous group. Within this framework, each burst pair showing a correlation of 1 corresponds to waves that originate in the same region and propagate in the same direction.

bursts. These results suggest that there are specific patterns occurring in the culture, and without memory. Given that each group in the similarity matrix corresponds to a wave nucleating at a specific region in the culture, most of the information is already contained in the nucleation region and the full information from the onset vector is not really needed.

We now proceed to characterize each wave (burst) by its nucleation point, defined as the geometrical center of the neurons spiking at the beginning of the burst. If we now build a nucleation probability density function by spatially averaging all the nucleation points obtained for a given simulation (usually ~ 1000 bursts), a new picture emerges. As we can see in Figure 2.11a, the original set of nucleation points is far from being homogeneously distributed, they concentrate in specific regions or sites, where the probability to nucleate is relatively high. Outside of these regions, the nucleation probability decays very rapidly. Almost no waves can nucleate outside these sites[9].

To try elucidate the origin of these nucleation sites we tried to correlate this network map with different topological and dynamical observables of the system. None of them show a good correlation. In Figures 2.11b and 2.11c we can see the network maps of triangles and firing frequency respectively. Although the nucleation sites appear in zones of high number of triangles and firing frequency, the opposite is not true. We have many zones of high number of triangles and firing frequency that do not translate into a nucleation site or correlate with its relative intensity. A more comprehensive list of network maps for this specific network was presented in Figure 2.5, and none of the other observables correlate any better with the nucleation sites.

[9] A nucleation point is the origin of a single wave, whereas a nucleation site is a region of high nucleation probability.

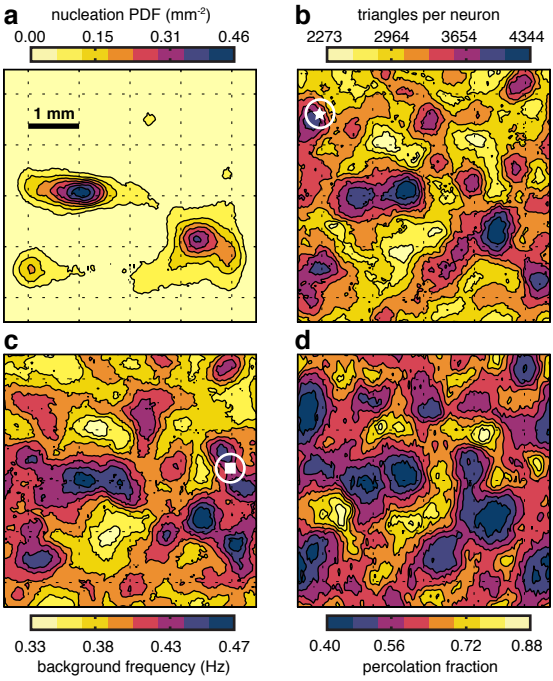

Figure 2.11 | Nucleation statistics and noise focusing. a-d, Contour plots of different observables, coarse–grained over the connectivity correlation length scale of 0.26 mm. The specific network realization contains 7500 neurons with an average of 70 connections per neuron, on a square of 5×5 mm^2 ($\rho = 300$ neurons/mm^2 with a connection probability of $\alpha = 2/3$), with periodic boundary conditions. **a,** Nucleation probability density, identifying 3 nucleation sites. **b,** Number of triangles per neuron (number of neighbors of a neuron that are themselves neighbors). **c,** Background activity. Average number of spikes per second and neuron between bursts. **d,** Local percolation fraction. For every point in the system a region of radius 0.4 mm is selected. The local percolation fraction is the fraction of neurons in the selected region that needs to be activated simultaneously to generate a burst. Comparison of **a-c** shows that high clustering and high background activity do not correlate strongly with high nucleation probability. The latter is much more peaked and selective, as similar values of those observables yield significantly different values of nucleation probability. Looking at the zones denoted by ■ and ★ it is clear that local statistics cannot explain the selection of a site with high nucleation probability. Zones with high clustering (★) may not correspond to high background noise, and vice-versa (■). This mismatch is also identified by the calculation of the Pearson's correlation coefficient between the nucleation map and any other network observable, giving at best values of ~ 0.5.

Given that several studies were able to successfully map collective dynamics in neuronal cultures to a problem of percolation [Breskin 2006, Soriano 2008, Tlusty 2009, Cohen 2010, Eckmann 2010] we have tried a similar approach based on the quorum percolation model. This is explored in detail in Chapter 5, but we include here a short description. Quorum (or bootstrap) percolation, is a generalization of classical percolation to the case where a minimum quorum of m inputs is required for a neuron to fire and f^* describes the critical fraction of neurons needed for the system to percolate. In the case of random graphs [Tlusty 2009] we have that

$$f^* \simeq m/\bar{k}, \tag{2.29}$$

where $\bar{k} = \langle k \rangle$ is the average connectivity. The meaning of this expression is that each neuron has to have at least m of its k neighbors active for percolation to happen. This is only valid for random graph, in the limit of zero loops in the network.For metric networks, however, no equivalent expression exists, and there is a different condition for which the system can percolate.

For a given network embedded in a metric spare, we define an n–sphere[10] of size R, e.g., for a network embedded in two–dimensional euclidean space this corresponds to choosing all the neurons within a circle of size R. Within the n–sphere, there exists a local critical fraction f^*_{local} at which the system can percolate. Note that this critical fraction might not have anything to do with Equation (2.29), but it needs to exist. If f^*_{local} exists, then as long as the condition

$$f^*_{local}\bar{k}/2 \geq m \tag{2.30}$$

is met, the whole system will also percolate. This relationship comes from the fact that any neuron that is at the boundaries of the n-sphere will have of the order of $f^*_{local}k/2$ neurons already active, since half of its neighbors will be inside the n-sphere. If this condition is met for most of the neighbors, this will result in an increase of the original n-sphere volume until the condition can no longer be fulfilled, or the whole system is active and has effectively percolated. Note that in general $\bar{k}/2 \gg m$ so if we are able to reach the critical fraction locally, the system is very likely to percolate.

With the quorum percolation framework in mind, we computed f^*_{local} for our networks in areas with a size given by ξ_c (see Equation (2.14)). The results for a particular network are shown in Figure 2.11d, where we see that the percolation fraction does not correlate with the nucleation sites. The nucleation sites do not correspond to regions of the system where the critical fraction is small. This result, together with the previous ones, already suggests that the nucleation process might not be dominated by local properties of the system, as we will later see.

The relationship between the different observables is better characterized by the use of Lorenz curves[11]. We can map any discretized two–dimensional observable $S_{i,j}$ to the ordered set $S^* = (s_1, s_2, \ldots, s_N)$ such that $s_1 > s_2 > \ldots > s_N$. The corresponding Lorenz curve is a function of the cumulative proportion of S^* mapped onto the corresponding relative size,

$$L(j/N) = \sum_{i=1}^{j} s_i \Big/ \sum_{i=1}^{N} s_i. \tag{2.31}$$

For our particular case, if the observable is the nucleation PDF, $L(0.1)$ is the maximum fraction of the nucleation probability found in 10% of the area. The Lorenz curve is useful to describe the asymmetry of a given observable. A linear

[10] Being n the dimensionality of the system, 2 in our case.

[11] Lorenz curves are mostly used in economics to describe inequalities in a given population.

Lorenz curve from $(0,0)$ to $(1,1)$ indicates a flat distribution, whereas a curve with $L(0) \to 1$ indicates a delta distribution.

Figure 2.12a shows the Lorenz curves for many of our observables computed with extensive statistics. The Lorenz curve for the nucleation PDF is highly asymmetric, indicating a very sharp distribution. 80% of the nucleation probability is already found in 20% of the available area, whereas all the network observables are close to the diagonal. The nucleation probability is indeed much more pronounced than the fluctuations of any simple local observable of the network. We also find that the spatial localization increases with the level of clustering (at equal connectivity), emphasizing the sensitivity of the phenomenon to the metric connectivity correlations. This difference between the curves indicates that the small fluctuations in the local observables must combine in a non–linear way to produce such a sharp nucleation PDF. Figure 2.12b shows the scaling of the Lorenz curve with system size, the fact that the Lorenz curve is invariant with system size shows that the nucleation sites posses a characteristic area. Increasing the system size increases the number of nucleation sites. If the number of nucleation sites and their properties did not depend on system size, the distribution would become sharper and sharper with bigger system size. The dependence of the nucleation sites with system size is also shown in Figure 2.13 for three particular cases.

In Figure 2.12a we also observe the differences in the Lorenz curves for two networks with different α but with the same connectivity distribution. In our networks the average connectivity is proportional to the density, and by keeping the product $\rho\alpha$ constant, we can obtain networks with the same degree distribution but different clustering coefficient distributions. These Lorenz curves show how the networks with higher clustering (higher α) have a faster rise, indicating a sharper distribution. This effect is also shown for two particular cases in Figure 2.14, where we show the nucleation sites for two networks with different clustering coefficient distributions.

2.2.3 Inhibition

We have also performed extensive analysis of the nucleation sites and the burst structure in the presence of inhibitory connections. We generated networks where 20% of the neurons were inhibitory. The inhibitory neurons were modeled with the same dynamical parameters as the excitatory ones, but with the synaptic currents twice as strong and twice as long, consistently with $GABA_A$ currents. We also explored the dynamics with more realistic models of interneurons, but the results remain unaffected.

In our typical parameter ranges, our main results remain essentially unaffected by the presence of inhibition were not significantly affected. A typical example is

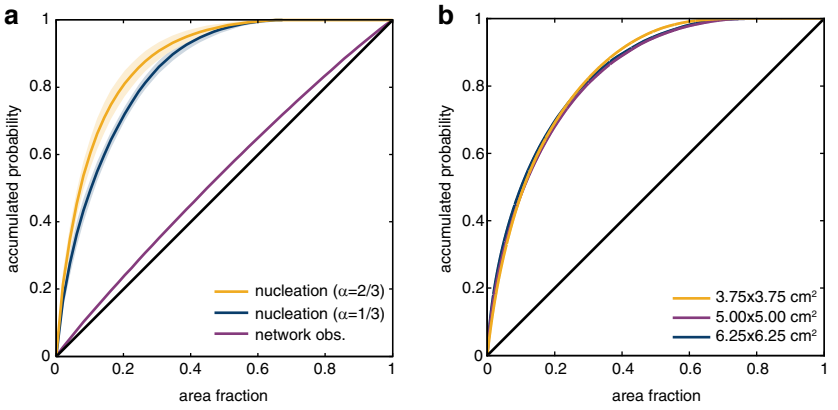

Figure 2.12 | Lorenz curves. a, Lorenz curves of the different observables. The diagonal line (black) corresponds to a flat distribution. Deviations from the diagonal give a clear image of the sharpness of a distribution. For the nucleation (yellow) a 20% of the system area contains the 80% of the probability. Another nucleation curve for networks with $\alpha = 1/3$ but the same average of connections per neuron, is shown (blue). Note how the spatial fluctuations of the other observables (purple) are much smaller. Lines are averaged over 5 different network realizations and the solid regions show the 95% confidence interval. **b,** Lorenz curves for the nucleation PDF for a network embedded in a square substrate with three different sizes. Each curves has been averaged over 10 different network realizations containing $\sim$1000bursts each. The shape of the PDF scales with system size whereas the number of nucleation sites is an extensive property of the system (the bigger the system, the more nucleation sites appear).

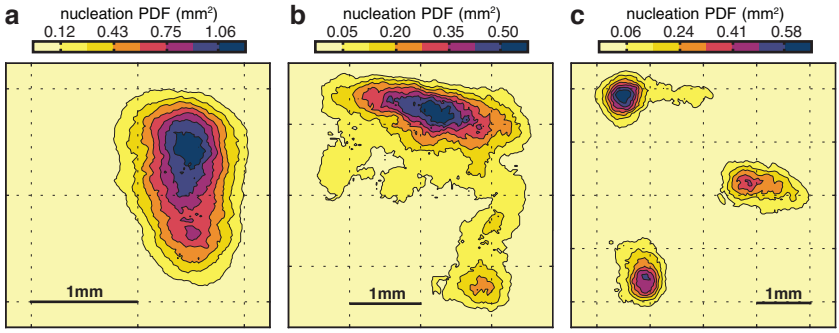

Figure 2.13 | Nucleation sites dependence with system size. Comparison of the nucleation sites for three different networks with the same density ρ =300 neurons/mm^2 and $\alpha = 2/3$ but different system sizes (with periodic boundary conditions) **a,** Square network with size L =3.75 mm **a,** Square network with size L =5 mm **a,** Square network with size L =6.25 mm

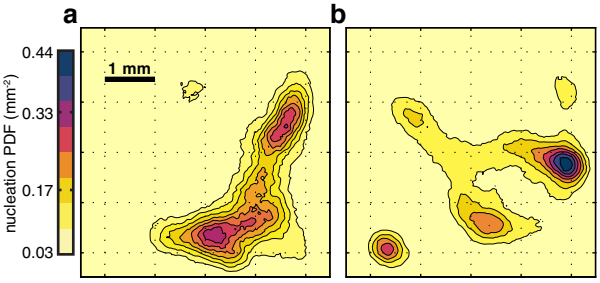

Figure 2.14 | Nucleation sites and clustering. Comparison of the nucleation sites for two networks with the same dynamical parameters and connectivity $\langle k \rangle \sim 70$. **a,** Nucleation sites for a network with $\rho = 500\,\text{neurons}/\text{mm}^2$ and $\alpha = 0.4$. **b,** Nucleation sites for a network with $\rho = 200\,\text{neurons}/\text{mm}^2$ and $\alpha = 1$. The distribution in **b,** is sharper, reaching a local probability of $\sim 0.45\,\text{mm}^{-2}$. The highest peak in **a,** is only $\sim 0.30\,\text{mm}^{-2}$.

shown in Figure 2.15, where we compare the nucleation sites of the same network with and without blocked inhibition. Inhibition is blocked by setting the inhibitory postsynaptic currents to 0, while the neurons themselves remain active, consistently with GABA_A–blocking experiments through the use of bicuculline. In both networks we observe the same nucleation process, but the locations of the nucleation sites have shifted. This shift emphasizes the sensitivity of the nucleation process to the exact wiring of the network, as we will see in the following sections.

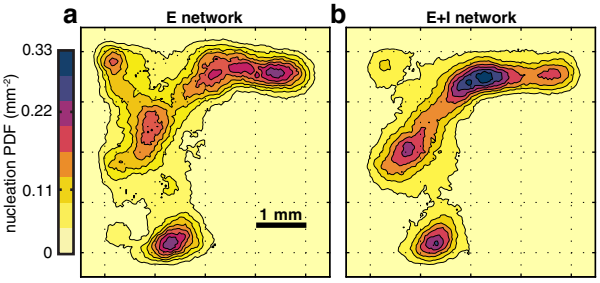

Figure 2.15 | Nucleation sites and inhibition. Map of the nucleation sites for a network equivalent to Figure 2.11 where 20% of the neurons are now inhibitory, in two different realizations. With inhibition blocked (E Network) and without (E+I network). **a,** Nucleation sites when inhibition is blocked. **b,** Nucleation sites when inhibition is active. The structure of the nucleation sites in both realizations is similar, but their relative strength has changed.

2.3 Experimental results

Before delving further in the burst structure, we now proceed to report the set of experiments that were performed to corroborate our findings. To be able to resolve wave propagation in two–dimensional cultures and the presence of nucleation sites, we need to be able to simultaneously track the activity of thousands of neurons with enough temporal resolution to observe propagation. As we reported in

Section 1.3.1, standard MEAs have good temporal resolution, being able to detect single spikes, but they usually lack spatial resolution due to the limited number of electrodes available, which also are too far apart. Traditional calcium imaging on the other hand, allows the simultaneous tracking of many neurons, but its temporal resolution does not allow the observation of any dynamical structure within a burst. To overcome these difficulties we concluded that high–speed calcium imaging was the best choice at the time. Most of the experiments focus on micro–cultures, where the whole culture can be recorded within the field of view and in young cultures, were the connections are still developing and propagation speed is low. All the experiments shown in this chapter were performed by Jordi Soriano and Sara Teller.

2.3.1 Small cultures

To corroborate our numerical findings, the experiments study the initiation and propagation of spontaneous neuronal activity in small, mm–sized cultures of rat cortical neurons that include $1000 - 3000$ neurons (Figure 2.16a, see also Appendix 2.B). Activity was monitored through high–speed, high–resolution calcium fluorescence imaging that provided $5 - 30$ ms recording interval and single–cell resolution (Figures 2.16b and 2.16c). Cultures with both excitation and inhibition (E+I networks), and only with excitation after the blockade of inhibition with 40 μm bicuculline (E networks) were considered. The advantage of working with such small cultures and high–speed calcium imaging is that all the neuronal activity can be recorded simultaneously since they all fit within the microscope field of view. Although it is not possible to detect single spikes, the bursting dynamics at the single cell level can be fully characterized, with enough temporal resolution to observe differences in the bursting transition.

Data was obtained from $30 - 60$ min recordings of the individual neuron activity. About 70 experiments were carried out, exploring different culture sizes, shapes, and maturation. As shown in Figure 2.16d, activity in the cultures was characterized by repeated bursting episodes that encompassed the entire culture. The typical inter–burst interval (IBI) was about 30 s for E+I networks, substantially increasing to about 120 s when inhibition was blocked (Figure 2.16e). The IBIs statistics and their dependence on the presence or absence of inhibitory activity is consistent with previous studies [Cohen 2008, Tabak 2003, Latham 2000, Soriano 2008, Jacobi 2010]. The distribution of IBIs is peaked at a mean value that is set by the synaptic depression time, i.e., the characteristic time of the exponential recovery of synapses after the saturation produced by the global burst [Opitz 2002, Cohen 2011].

The analysis of the individual neuron fluorescence signal allowed us to verify our numerical findings, revealing that the bursting episodes are not synchronous events but are mediated by circular waves originated at well–defined centers or nucleation points. Figures 2.16f to 2.16h show illustrative examples, for both the cases with

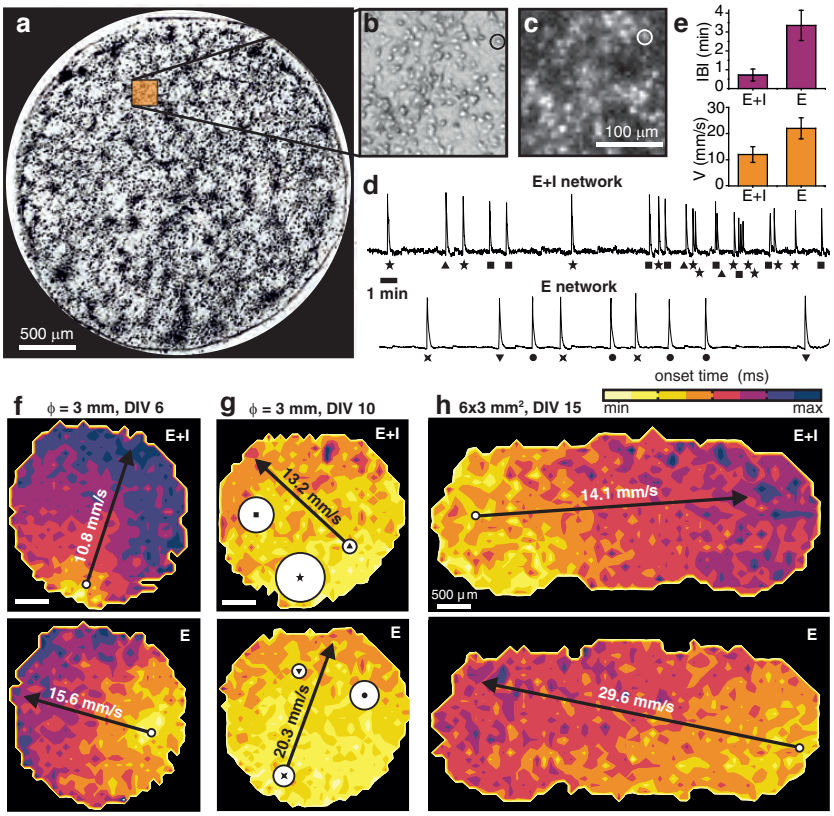

Figure 2.16 | Experimental observation of nucleation and propagation. a, Highly contrasted bright field image of a neuronal culture at *day in vitro* (DIV) 10, grown on glass and confined within a circular cavity 3 mm in diameter. Culture contains $\simeq$ 3000 neurons. **b,** Bright field image showing a detail of the culture and the distribution of neurons. The circle identifies a single neuron. **c,** Corresponding fluorescence image during a spontaneous activity event. Bright spots are firing neurons. The resolution of the image is the same as the actual measurements. **d,** Fluorescence signal from 30 min recording of spontaneous activity in the culture shown in **a,** averaged over the 500 brightest neurons. The top plot corresponds to measurements with both excitation and inhibition active (E+I network); the bottom one corresponds to excitation–only measurements (E network), with inhibitory synapses blocked with 40 μM bicuculline. Fluorescence peaks identify network bursts. The symbols below each burst identify its initiation in a specific area of the culture. **e,** Distribution of inter–burst intervals (IBIs, top) and burst propagation velocities v (bottom) for E+I and E networks. Statistics is based on 6 cultures of identical size and density, at DIV 9-10. On average, E networks are characterized by larger IBIs and propagation velocities. **f,-h,** Examples of the propagation of spontaneous bursts in cultures of different sizes and developmental stages. The analysis of the onset times of neuronal firing provides the average velocity of the advancing front and its initiation point (white circle). E+I and E networks show a qualitatively similar behavior, with a propagation in the form of a circular wave. **g,** also depicts, for the data shown in **d,** the approximate initiation point of each burst. For clarity, nearby initiations are grouped defining the nucleation sites. Three main initiation sites are identified. The size of the circles is proportional to the relative occurrence of nucleation events at each site. Localized nucleation occurs both in E+I and E networks. The location of the nucleation sites and its relative importance is different in the two networks, and illustrates the sensitivity of nucleation to network details.

and without inhibitory action. Although previous works [Maeda 1995] hinted at the presence of activity propagation in large 2D cultures, the existence of such waves was not resolved before, whereas later studies explored different scenarios of synchronization [Shein 2008] and percolation [Eckmann 2010]. The spatial and temporal resolution in these experiments settles this issue and allows measurement of the wave velocity for the first time. As in the simulations, while the precise points where these waves are initiated appear distributed throughout the culture, they are very strongly concentrated in relatively small regions (hereinafter, the *nucleation sites*), as shown in Figure 2.16g.

In addition, the temporal sequence of burst initiations, e.g. Figure 2.16d, appears to be random, with no statistically significant correlation between consecutive events. Statistical significance in the temporal sequence of burst initiations was analyzed by grouping individual bursts in clusters. A cluster is defined by all nucleation points whose distance amongst cluster members is $l < \xi_c$, where $\xi_c \approx 0.26\,\text{mm}$ is the connectivity correlation length (see Equation (2.14) for an illustrative example). Given a sequence of consecutive bursts, we computed the conditional probabilities $P(n+1 = x_i | n = x_j)$, that define the probability that the burst $n+1$ belongs to cluster x_i given that the previous burst happened in cluster x_j. Then we have compared these probabilities to the ones obtained from bootstrapped data with the same statistics and size over many realizations. The results for a particular experiment are shown in Figure 2.17. Although some apparent correlations can be noticed, they are not statistically significant with the limited data set. From all our data we can only conclude that the results are compatible with a very weak (or lack of) correlation between the locations of consecutive bursts, that is, that the origin of the next burst is independent from where the previous one started. On the other hand, the typical experimental average IBI is $\sim 30\,\text{s}$, a time–scale associated to synaptic depression and much larger than any other time–scale involved in the dynamics. Given that neurons start to fire spontaneously again a few seconds after a burst, it is improbable that a correlation between the position of successive bursts really exists. There is no known mechanism that could generate this kind of correlation.

Going back to the nucleation points, a new picture emerges with an appropriate coarse–graining of the data. Given the set of nucleation sites of a given experiment (and their errors), a nucleation probability density (PDF) function can be obtained by smoothing each nucleation site with a Gaussian kernel (whose standard deviation comes from the nucleation site identification error) as shown in Figures 2.18a and 2.18b (see Appendix 2.B for details). These nucleation PDFs show that nucleation point are not uniformly distributed, but concentrate in specific regions of the culture. This localization phenomenon can also be quantified by Lorenz curves as shown in Figure 2.18c. The Lorenz curves show that a small fraction of the culture $\sim 10\%$ already contains 80% of the nucleation probability, clearly indicating the high–localization of the nucleation process. The fact that the Lorenz curves are invariant with system size also, as they were in the simulations, show that the nucleation mechanism involves a region with a finite extent. Indeed, if the whole network was involved in the nucleation process, the number of nucleation

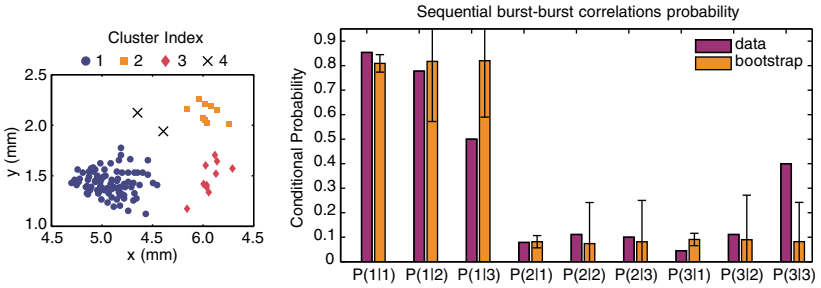

Figure 2.17 | Interburst correlations. Left: the identification of the different clusters based on proximity (3 main clusters and 2 discarded points). Right: experimental conditional probabilities (purple) and bootstrapped data (orange), error bars correspond to the 95% CI. Only on bursts that happen after a burst in cluster 3 ($P(1|3)$ and $P(3|3)$ some correlation could be present, but the result is not statistically significant due to the limited data set.

sites would not increase with system size (and the fraction of area they occupy would decrease). The Lorenz curves however, remain independent of system size, thus indicating that there is a typical length scale that controls the area of influence of a nucleation site. It is reasonable to assume that this scale is given by the average axon length.

The IBI dispersion observed in the experiments (Figure 2.16e) originates at the (exponential) time distribution of nucleation events at the different nucleation sites. We observed that the IBI dispersion decreases for increasingly larger cultures. This reflects the competition between nucleation sites, consistently with the observation that the number of nucleation sites scales with the system size (Figure 2.18).

The existence of initiation areas and their strong localization is a robust experimental result, although the details of the nucleation map vary from culture to culture. Robustness is also exemplified by the similar nucleation scenario with inhibitory synapses either active or blocked. For the cultures studied here, inhibition slows down burst propagation, facilitates burst termination, and leads to richer wave propagation patterns, but the nucleation process remains unaffected. While inhibition is key for more complex activity patterns, like neuronal avalanches, synchronization and self–organization in general, these effects show up in more mature cultures. At the onset of the GABA switch, inhibition has not developed enough to allow a significant change in activity dynamics. Hence, to understand the mechanisms underlying the nucleation process from now on we will focus on excitatory networks.

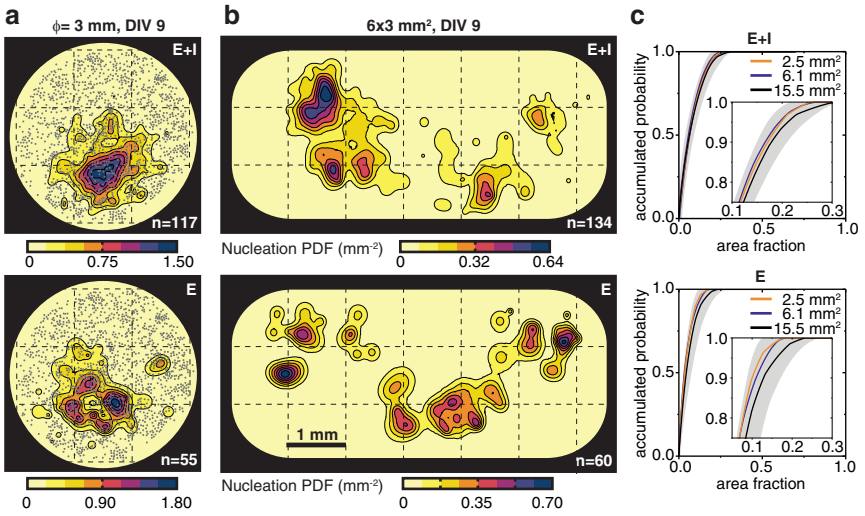

Figure 2.18 | Spatial distribution of nucleation sites in experiments. a,b, Nucleation probability densities for a circular culture and a rectangular one at *day in vitro* (DIV) 9. The top plots correspond to measurements in untreated cultures (E+I networks); the bottom ones correspond to measurements in the same cultures after the blockade of inhibitory synapses with 40 μM bicuculline (E networks). Data is obtained by coarse–graining the burst initiation points of a given measurement. The number of bursts n observed in each measurement is indicated at the bottom–right corner of each plot. The small circles in **a,** are the neurons in the network. Neurons are not shown in **b,** for clarity. The grid lines are a guide to the eye. Nucleation is highly localized in specific regions for both E+I and E measurements. For the circular culture and E+I measurements, nucleation is peaked at the bottom–center of the network. The blockade of inhibition reconfigures the distribution of nucleation probability, but its degree of localization is similar. The larger rectangular culture accommodates a higher number of nucleation sites. The blockade of inhibition changes their location and relative weight while maintaining their strong localization. **c,** Lorenz curves for different culture sizes, and comparing E+I (top) and E networks (bottom). The curves are obtained by plotting the accumulated nucleation probability as a function of the area fraction of the culture, and after averaging over cultures of similar area and developmental stage. For both E+I and E measurements, data corresponds to cultures at DIV 9-11 and areas $A \pm 1$ mm^2, with $A = 2.5$ mm^2 (orange, $N = 4$); 6.1 mm^2 (purple, $N = 8$); and 15.5 mm^2 (black, $N = 5$). The gray area depicts 95 % confidence interval for the data with the highest standard deviation ($A = 15.5$ mm^2). The insets provide a detail of the plots. The sharp increase to 1 of the Lorenz curves illustrates the strong localization of nucleation probability. The different curves collapse within experimental error, evidencing the scaling of nucleation with system size.

2.3.2 Big cultures

The nucleation phenomenon is not specific of small cultures, experiments were also carried with regular–size, 13mm–wide cultures. Figure 2.19 provides an example of activity propagation in a regular culture, studied at DIV 21. Big cultures have the advantage that spontaneous activity is richer and more periodic (Figure 2.19a). Additionally, the entire field of view contains neurons in these experiments (in small cultures the field of view was larger than the culture), see Figures 2.19b and 2.19c, and therefore burst initiation and front propagation can be better resolved (Figures 2.19d and 2.19e). The major disadvantage of big cultures in this experimental setup is that initiation can occur both in the monitored field of view and in regions outside. The statistics of nucleation sites is therefore partial. For this reason big cultures were not used for the study of the nucleation sites distribution.

2.4 Microscopic dynamics and activity avalanches

The experimental results confirm the propagation dynamics and the presence of heterogeneous nucleation sites, however, they are unable to tell us much about the mechanisms behind these processes. To gain insights into the mechanisms of burst initiation, we must go back to our simulation framework.

The strong localization in both time and space, quantified by the small IBI dispersion and the Lorenz curves respectively, are apparently in conflict with an *a priori* scenario of homogeneous nucleation, as the information from the analysis of the bursting transition suggests (see Section 2.2.1). Indeed, for the phenomenon to be truly noise-driven and not controlled by specific leader neurons or network architectures, two puzzles must be solved. First, time localization requires a very fast nucleation mechanism, in a scale comparable to the spontaneous firing rate of a single neuron (around 1 Hz). Second, space localization requires that, effectively, the noise is very unevenly distributed even though the network is fairly homogeneous and the neurons presumably identical. Here we show that these apparently unrelated puzzles are solved at a quantitative level by a single phenomenon that we call *noise focusing* that arises from the presence of activity avalanches in the microscopic dynamics.

The simulations are particularly insightful to unveil the detailed build-up process that leads to nucleation in the form of avalanches of activity. Avalanches in neuronal networks were first identified in cortical slices [Beggs 2003, Beggs 2004] and later observed in other experimental conditions [Mazzoni 2007, Tetzlaff 2010] and used, in particular, in the context of self-organized criticality [Beggs 2003, Beggs 2004, Levina 2007, Levina 2009, Millman 2010], in situations that differ substantially from our problem as we will now see.

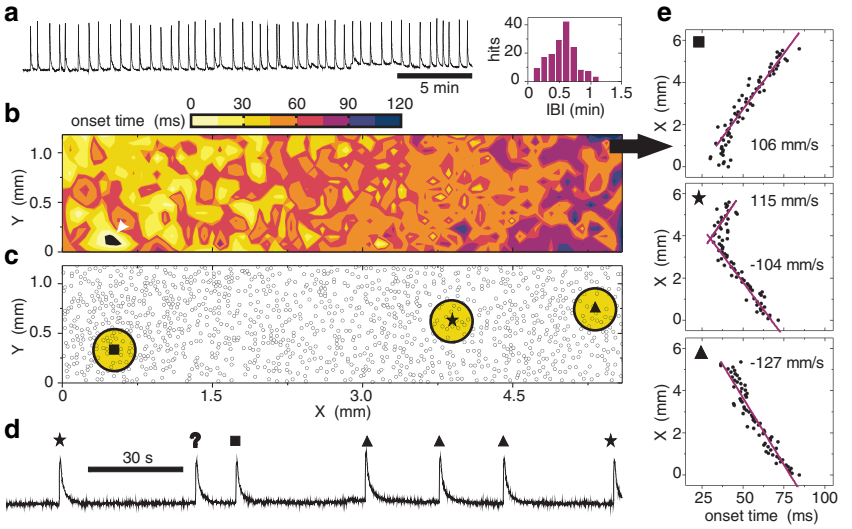

Figure 2.19 | Experiments on big cultures. a, Spontaneous activity in a neuronal network cultured on a 13 mm diameter glass coverslip, studied at DIV 21 and with only excitation active. Data corresponds to the average fluorescence signal of ∼1000 neurons. Fluorescence peaks correspond to network bursts. The histogram shows the distribution of inter–burst intervals (IBIs) along the total 90 min duration of the recording, and provides an average bursting period of 40 s. **b,** High speed (200 frames/s) monitoring of a network burst in a 5.6×1.2 mm^2 region of the culture. Onset times correspond to the occurrence of individual neuronal firing within the burst. Activity initiates in a small area at the bottom-left corner (white arrow) and propagates towards the right edge of the region. **c,** Corresponding spatial distribution of neurons together with the three most frequent nucleation sites of the region, based on the analysis of 10 bursts. **d,** Detail of a train of bursts with their associated nucleation sites. For the burst marked with "?" activity started outside the monitored region. **e,** Onset times (averaged over the Y direction of the region) along X, for the three most frequent nucleation sites. The linearity of the data points reveals the advance of the activity front at a constant velocity, with its value given by the slope of the least squares fit.

Here we use the term avalanche in its more general meaning, referring to any cascade of induced activity, i.e., any group of causally connected spikes, usually initiated by spontaneous firings. These avalanches can be understood as noise being amplified and propagated through the network. Given its spontaneous (noise driven) origin, the avalanche statistics will inform us of possible amplification mechanisms. The spontaneous firing of a given neuron is simultaneously transmitted towards all its output connections k^{out}, and added to the internal noise of these neurons, effectively increasing their firing probability. As a consequence, if the noise in these neurons is above a certain threshold, it can be coherently amplified and be able to produce large sequences of induced firings. Our dynamics will be dominated by these avalanches, and we will distinguish between Ignition Avalanches (IA), as

those that end up nucleating a burst, and Background Avalanches (BA), as those that eventually die out.

Our numerical approach allows to detect all causal interactions between individual spikes, that is, to reconstruct the sequences of induced firings, and hence to identify all avalanches that may be occurring simultaneously, a crucial information that is virtually inaccessible experimentally.

To do so we start with the first detected spike. Next, we scan all its output neurons for the occurrence of spikes in a short time window $\sim 2\tau$, where τ is the characteristic decay time of the post-synaptic current (we chose $\tau \simeq 10$ms). The process is iteratively repeated for all the newly detected spikes until no more spikes are found. When multiple avalanches with different initiation neurons have spikes in common, they are merged into a single, bigger avalanche. This process is equivalent to counting clusters in a problem of classical percolation, with the difference that the time component makes the system effectively infinite.

All avalanches eventually die out, i.e. no more correlated spikes are found with 2τ, and are considered as Background Avalanches (BAs) of size n, with n the number of spikes involved and duration T being T the time difference between the first and the last spike. Any avalanche that recruits over 95% of the population in a very short time window (usually 2τ), however, is considered an ignition avalanche (IA) and is separated from the BA set. This fast recruitment is what defines a burst, hence this avalanche has a completely different structure than the others and can then be separated in two parts: the Ignition Avalanche (IA) (the precursor of the burst) and the burst itself. IAs have the characteristic signature of a steep amplification of activity over time, which is not present in BAs. Note that the separation point between the IA and the burst is arbitrary, and in our case we define it by when the activity rate slope changes from an exponential increase to a quadratic increase, as we will later see.

2.4.1 Background avalanches

In Figure 2.20 we show the distribution of BAs sizes and durations. In Figure 2.20a we observe a clear scaling relation, over 2 decades in size and 6 in frequency, independent of network properties, with an universal exponent close to the one from classical percolation in a Cayley tree, $\sim 5/2$ [Albert 2002]. For larger avalanches however, this scaling relation starts to break down and becomes more sensitive to the specific details of the network. Does that mean that our system is in a critical state? Not quite. To understand what is going on we need to understand how our system evolves during bursts. Right after a burst, synapses are completely depressed, and although the neurons can spontaneously fire, they are unable to transmit any signal to their neighbors. In this regime, the firings are completely uncorrelated,

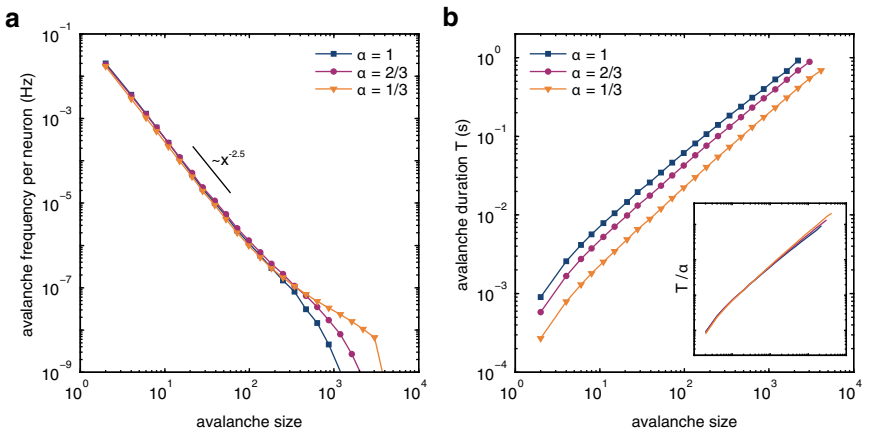

Figure 2.20 | Statistics of Background Avalanches (BAs). a, Statistics of BAs for networks with different connection probability α and different density ρ. The mean connectivity is fixed at $\langle k \rangle \sim 70$. The avalanche size distribution shows power-law statistics for almost three decades. **b,** Relationship between avalanche duration and avalanche size for the same networks as in **a,**. Inset: the curves collapse into a single one when rescaled with the connection probability α, although deviations start to appear at larger sizes. In all cases the calculated exponent is below 1. Each curve from **a,** and **b,** is averaged over 5 different network realizations and over 3 hours of simulated activity.

and if we tried to detect avalanches we would observe a curve consistent with a Poisson process (since the firings are uncorrelated). While the system is recovering, however, the connections are being strengthened, and the neurons are able to induce firings in their neighbors so the system is effectively subcritical. If the connections keep being strengthened, there will be a point when a single spike is able to induce more than one firing in average (characteristic of supercritical behavior), when this happens however, a burst can also develop (which is different from a large avalanche), triggering the nucleation process, wave propagation and complete activity saturation. So our system is continuously evolving from subcritical to supercritical, thus crossing the critical state in between. Averaging all over these phases results in the curve observed in Figure 2.20a, the system is always moving around the critical regime[12] but never being exactly there.

Why is the exponent so similar to that of percolation in a Cayley tree? The defining feature of a Cayley tree is the absence of loops (zero clustering coefficient), and our networks are far from that, as they are highly clustered. As we will see the answer relies in the fact that our process is dynamical, and neurons can fire multiple times in a single avalanche.

[12] This is not SOC.

A Cayley tree (also known as a Bethe lattice) is a loopless network where each node (neuron) has the same number of connections z (coordination number). In a Cayley , the cluster (avalanche) size distribution n_s is calculated as follows. The first node is chosen randomly (since the tree is loopless and infinite they are all equivalent) and ignited with probability p. If it is ignited, the same is performed with its z neighbors. For those neighbors that were ignited, the process is repeated with its $z-1$ neighbors (since one of the nodes is already ignited, the precursor), until no nodes can be ignited. The total number of nodes that were ignited n define the cluster size. It can be shown [Albert 2002] that around the percolation threshold

$$n_s \propto s^{-5/2} e^{-cs} \quad \text{with} \quad c \propto (p - p_c)^2 \tag{2.32}$$

where p_c is the percolation threshold. It is also easy to see that $p_c = 1/(z-1)$. On average, a node will ignite $p(z-1)$ new nodes. So only when $p(z-1) \geq 1$ we can obtain an infinite cluster. Below that the cluster will eventually stop. Above that, however, the cluster size will increase exponentially. Note that a Cayley tree is essentially a random graph with fixed degree, since both show zero clustering in the limit $N \to \infty$.

If we look closely to the way the clusters are computed in a Cayley tree we can see the parallelism with our activity avalanches. If we consider that each iteration in the cluster formation takes a time $\sim \tau$, this becomes equivalent to the time it takes for a given spike to induce another in any of its neighbors. In highly clustered networks, as is our case (usually $\langle \text{CC} \rangle \simeq 0.3$) the percolation transition differs because the number of available neighbors at every iteration is reduced because of the loops. Since our process is dynamical however, given that our degree is large $\langle k \rangle \geq 70$ and we are close to the percolation threshold, after a few iterations the neurons have returned to their resting state and can be activated again, essentially making the system infinite and loopless.

This parallelism helps explain the universal exponent $-5/2$ found for BAs, as shown in Figure 2.20a. The region of interest for wave nucleation, however, is that of large avalanches, where the presence of loops is statistically significant and breaks that scaling. It is also important to compute the distribution of avalanche times (see Figure 2.20b), the fact that the exponent is close to 1 further indicates that the system is close to the percolation transition, and that the internal avalanche structure is self–similar (an avalanche twice as large, lasts twice as long and so on). The exponent, however, is not strictly one (it is slightly smaller) and depends on the clustering of the network, the deviations being more apparent at large avalanches. This indicates that larger avalanches have a smaller duration when the clustering is high, and this is caused by the fact that when the avalanches are large, loops enhance the probability of induced firings, as we will later see.

A typical BA is shown in Figure 2.21. Its spatio–temporal structure is quite complex (see Figure 2.21a) and is better observed when mapped to the unit circle (see Figure 2.21b). In this representation the internal structure of the avalanche is revealed. Almost no neuron spikes twice in the avalanche, which would be represented by

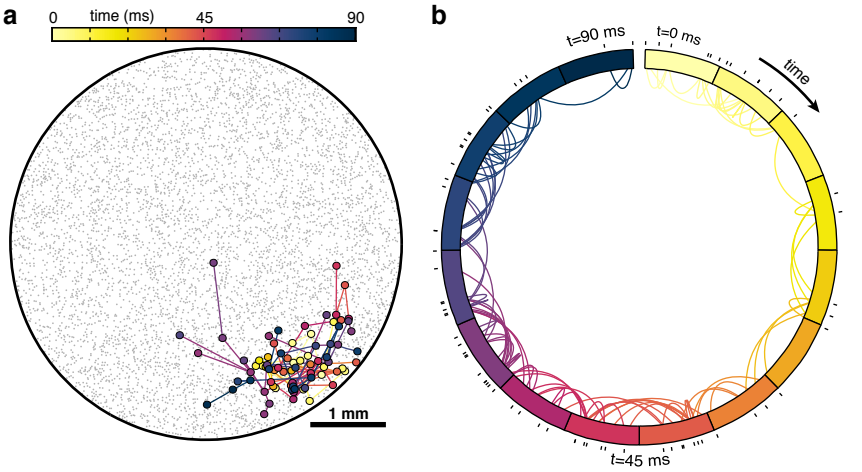

Figure 2.21 | Structure of Background Avalanches. a, Spatio–temporal structure of a background avalanche composed of 91 spikes in a 5 mm–wide circular network with $\langle k \rangle \sim 70$, $\rho = 300\,\text{neurons}/\text{mm}^2$ and $\alpha = 2/3$. Big circles correspond to the neurons that fired during the avalanche (color coded by the first time they fired) and the involved connections. This particular avalanche starts in a small area, spreads out and dies. In gray, all the other neurons that did not participate. **b,** The avalanche structure is mapped to a circular graph where the angle represents firing time. Each neuron is positioned across the circle by the first time they fire (denoted by a small line). Causal interactions are represented by curved paths whose curvature depends on the time difference between the two firings and color–coded by the first.

a backward connection in the graph (a dark line connecting to a light area), and the temporal profile fluctuates greatly. There are many spikes in the first 10 ms, but only a few are able to propagate past that point. Around the 40 ms mark the activity increases again to finally die out 90 ms after the first spike.

2.4.2 Ignition Avalanches

As we have discussed in Section 2.4, the significant difference between BAs and IAs is that the later are responsible for wave nucleation. The initiation of a wave requires the simultaneous excitation of a sufficiently large nucleus to sustain it, typically of the size of the connectivity correlation length. Following Refs. [Cohen 2010, Tlusty 2009], this will be achieved whenever a quorum percolation condition is satisfied in a region of this critical size, requiring the simultaneous excitation of the critical percolation fraction in that region.

We may estimate the quorum percolation condition as follows. If we keep the connectivity correlations of the metric network, and neglect the dynamic correlations between neuron firings, then we do not need to compute the probability of percolation of the entire network. Only the probability to obtain a minimum number of simultaneous firings (the critical fraction) within a spatially correlated area. This area is sufficiently large so that metric correlations will then do the rest and induce percolation in the entire system. This is similar to what we did in Section 2.2.2 to generate the percolation map from Figure 2.11d. This time, however, we want to calculate the time it takes for the system to reach the critical fraction in a given area spontaneously.

Within a correlated area, the network can be treated as a (finite) random graph of N_c neurons, with a critical percolation fraction of the order of $m_0/\langle k\rangle$ or larger, so the number of spontaneous firings that must occur within a Δt in that area must be at least

$$n_c \sim N_c m_0/\langle k\rangle. \tag{2.33}$$

A conservative estimate of the probability of percolation induced by spontaneous firings of frequency ω_0 of a nucleus with N_c neurons would scale as

$$P_{perc} \sim \mathscr{P}(n_c, N_c\omega_0\Delta t) \sim \exp(-N_c\omega_0\Delta t)(N_c\omega_0\Delta t)^{n_c}/n_c! \tag{2.34}$$

where $\mathscr{P}$ is the regularized Gamma function. For typical values in experiments and simulations this estimation is off by many orders of magnitude because of the strong dependence on the small parameter $\omega_0\Delta t$. For a typical example of our simulated cultures, we find that a minimum number of $n_c \sim 20$ neurons must be excited out of the $N_c \sim 85$ contained in a circle of radius 0.26mm. With $\omega_0 \sim 0.4$Hz and $\Delta t \sim 20$ms we have $P_{perc} \sim 10^{-23}$. These extreme values cannot be brought significantly close to realistic ones values by replacing the quorum m_0 and the firing frequency ω_0 by some renormalized values along the lines discussed above. The failure of the percolation estimate dramatically illustrates the importance of dynamic correlations of the neuron firing, that manifest in the form of avalanches. Within our dynamical scenario, the critical event is the occurrence of an IA, that is, an avalanche that excites the local critical percolation fraction. The probability of such an event is much larger, not only because big avalanches occur relatively often, but also because the area that contributes to the formation of such avalanches is much larger than the nucleation sites, where they project the activity.

The statistics of the IAs are shown in Figure 2.22. These avalanches can form and slowly build up their activity for a whole second before a burst is detected. These kind of exponential growth (see Figure 2.22a) in the 'preburst phase' is consistent with previous results with MEA data [Eytan 2006]. When this exponential growth stops and becomes polynomial (defined as $t = 0$) indicates that the wave has formed and starts to propagate. When the wave is propagating, every neuron is receiving a huge amount of inputs, and is firing at its maximum frequency. At this point its temporal evolution is purely dominated by its internal dynamics, and the network

has almost no effect, as observed after $t = 0$ when the plot is normalized by system size (see Figure 2.22b).

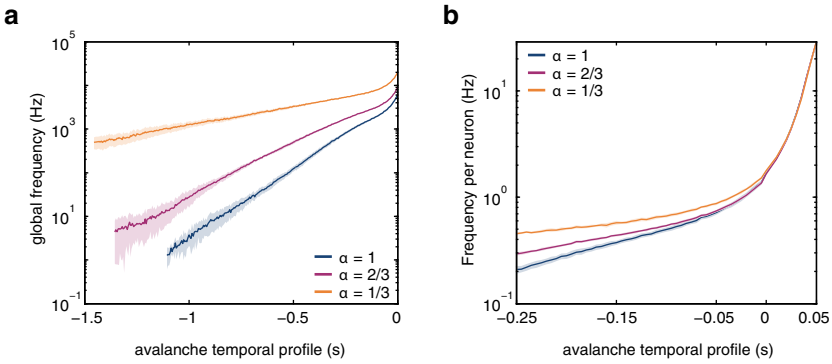

Figure 2.22 | Statistics of Ignition Avalanches (IAs). a, Temporal profile of activity during the IAs. The same set of networks from Figure 2.20 are used. The activity growth during the IAs follows exponential distributions up to the end of the IA that sets the temporal scale origin, moment at which a faster growth describes the formation of the burst. **a,** Activity growth in the region where the IAs transforms into a burst, normalized by system size. The growth during the bursting phase becomes independent on the connectivity probability α, consistent with the fact that the bursting phase is governed by the neuronal dynamics.

Given the size and buildup structure of IAs, their structure becomes more complex and rich than the one observed in BAs. A typical example is shown in Figure 2.23. From the analysis of the IAs structure it is clear that activity travels throughout the system, but is only being amplified at specific regions or paths, whose convergence later defines the nucleation sites. This amplification also happens extremely fast, the fact that most connections and neurons are only triggered once during an avalanche indicates that it is not a build up process where activity is increasing within a subset of neurons. It is actually the convergence of activity, the focalization of noise, what triggers the explosion and posterior wave formation. This mechanism, which we call *noise focusing* explains how a very low level of noise is enough to trigger burst formation in a highly heterogeneous way. It is based on the high anisotropy of the amplification mechanisms, which in turn are enhanced by metric correlations in the network and the non–linearities of neuronal dynamics, as we will now see by analyzing the different mechanisms of noise amplification.

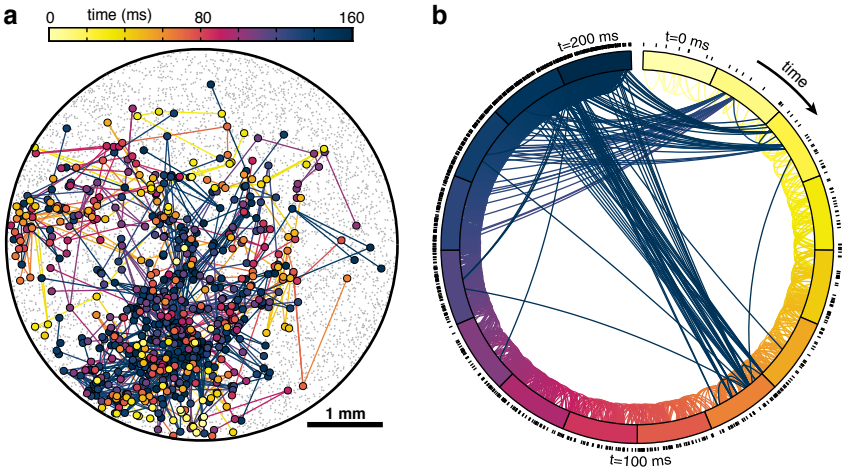

Figure 2.23 | Structure of Ignition Avalanches. a, Spatio–temporal structure of the first 2000 spikes from an Ignition Avalanche in the same network of Figure 2.21. Notice how in this case the avalanche spans almost the whole system, but the activity build up occurs in a smaller region which correlates to the nucleation site. **b,** Mapping of the avalanche structure to a circular graph (see also Figure 2.21b for details). Around $t = 50$ ms activity slowly increases (shown by the accumulation of spikes) but the explosion of activity that will trigger the burst starts at $t = 150$ ms. Until the explosion (ignition), activity travels through different neurons and connections without repetitions. Those only start to occur after $t = 150$ ms, seen by the dark blue lines that cross the circle.

2.5 Noise Amplification

The different mechanisms of noise amplification are better understood within a simplified version of the neuronal dynamics. A neuron is an integrate–and–fire unit, and it fires whenever its membrane potential reaches a given threshold after integrating its input current within a certain time window Δt. The total input current coming from other neurons adds up to the internal noise of the neuron, that in our case are the spontaneous discharges caused by minis (see Section 2.1.1). In the absence of noise, a minimum quorum of m_0 inputs from other neurons is required to fire [Cohen 2010]. In the presence of noise however, a neuron has a finite probability to fire with $m < m_0$ (sub–quorum firing). The case $m = 0$ defines the spontaneous firing rate ω_0. For $m > 0$ (induced firing), the firing probability p_m increases nonlinearly with m as we will now see. This nonlinear growth of the probability of firing in the sub–quorum regime is what we call dynamical noise amplification. Noise can also be amplified by the presence of loops in the network (intrinsic to the metric structure of the network), since any spontaneous firing will induce strong correlations in the probability of firing of its neighbors. We call this mechanism topological noise amplification.

2.5.1 Dynamical noise amplification

To gain quantitative insight, we may assume for simplicity that the noise in each neuron takes the form of a Poisson shot process with frequency λ and that the input from a firing neuron just adds another shot of the same amplitude. The neuron fires whenever it accumulates at least m shots in a time window Δt. Under these assumptions the probability p_m of firing if it receives m inputs from other neurons reads

$$p_m = e^{-\lambda\Delta t} \sum_{i=m_0-m}^{\infty} \frac{(\lambda\Delta t)^i}{i!} = \mathscr{P}(m_0 - m, \lambda\Delta t), \tag{2.35}$$

where $\mathscr{P}(m_0 - m, \lambda\Delta t)$ is the regularized gamma function, a monotonically non-decreasing function of m, that is increasing from the value p_0 that sets the spontaneous firing rate, $\omega_0 \sim p_0/\Delta t$, to $p_m = 1$ for $m = m_0$ (see Figure 2.24a). For $m' > m_0$ the analytical continuation of this function to negative integer values of its first argument yields the correct values $p_{m'} = 1$. $\mathscr{P}(m_0 - m, \lambda\Delta t)$ quantifies in this simplified model how the probability of induced (sub-quorum) firing is enhanced by inputs from other firings. The maximum sensitivity of the firing probability to the addition of a single input occurs for $\varepsilon \equiv \lambda\Delta t/(m_0 - 1) \sim 1$. The parameter ε is an appropriate measure of the noise intensity, and is typically smaller than 1.

If we quantify the importance of sub-quorum firing in terms of the quorum fraction $f(p_c) = m_0^*/m_0$, as the required number of inputs m_0^* that gives a firing probability of p_c, that is, by the implicit equation

$$\mathscr{P}(m_0 - m_0^*, \lambda\Delta t) = p_c, \tag{2.36}$$

then for sufficiently large m_0, $\mathscr{P}(m_0 - m, \lambda\Delta t)$ has a narrow sigmoid shape with fast variation between 0 and 1 centered around $m_0^* \simeq (1-\varepsilon)m_0$ (see Figure 2.24a). Specifically, one can show that

$$\lim_{m_0\to\infty} \mathscr{P}(m_0(1-\eta), \varepsilon(m_0 - 1)) = \Theta(\eta - (1-\varepsilon)), \tag{2.37}$$

where Θ is the Heaviside step function. Therefore, for large m_0 one may unambiguously define an effective quorum fraction $f^* = 1 - \varepsilon$, such that for $m < m_0 f^*$ the firing probability is $p_m \simeq 0$ while for $m > m_0 f^*$ it is $p_m \simeq 1$.

The consequences of this noise amplification mechanism are further studied in Chapter 5.

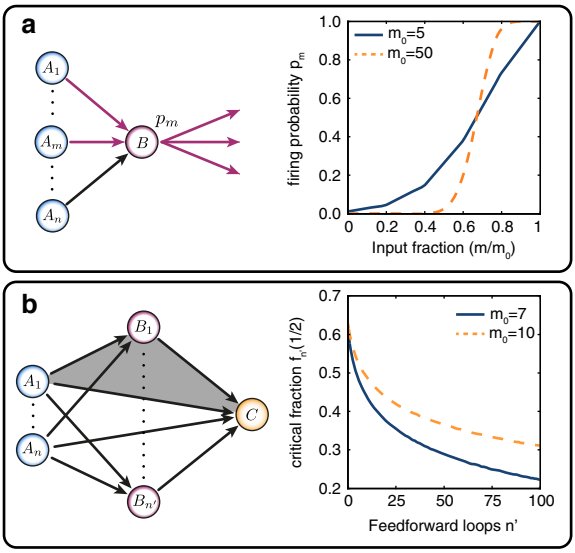

Figure 2.24 | Noise amplification mechanisms. a, Dynamical noise amplification. Left: schematic representation of the mechanism, where a subset of m (from a total of n) firing neurons projecting over neuron B induces a firing probability p_m. Right: dependence of p_m with the input fraction. The firing probability is greatly amplified before the quorum percolation condition m_0 is met. **b,** Topological noise amplification. Left: Schematic representation of the effect of feed-forward loops in the induced firing probability of neuron C. Right: critical fraction $f_{n'}$ of input neurons A_i needed to activate neuron C with a probability $1/2$ as a function of the number of feed-forward loops formed with the intermediate B_j neurons.

2.5.2 *Topological noise amplification*

To pursue the influence of the network wiring in the amplification of the firing probability we can compute the effect of a feed forward motive as that depicted in Figure 2.24b, where n neurons $A_1,...,A_n$ are connected directly to a neuron C, and indirectly through a set of n' intermediate neurons $B_1,...,B_{n'}$, forming n' independent feed-forward loops between A and C. If there are no other connections, the firing probability of C $p_{nn'}$ if the set A_i fires together within a Δt can be expressed as

$$p_{nn'} = \sum_{k=0}^{n'} \binom{n'}{k} p_n^k (1-p_n)^{n'-k} p_{k+n}. \tag{2.38}$$

This 'dressed' probability of induced firing is significantly larger that the 'bare' induced probability p_n. In particular, one may compute the dressed critical fraction $f_{n'}(p_c)$, as the quorum fraction in the presence of n' feed-forward loops, and see that this drops monotonically with n', with the fastest decay for small n', as shown in Figure 2.24b. The extension to more complex wiring however, must be explored numerically.

The effects of the topology on the underlying dynamics are further studied in Chapter 3.

2.6 Noise focusing

The two noise amplification mechanisms discussed before are enhanced by the presence of metric correlations in the network, and are highly sensitive to the local wiring. The growth of avalanches at a given point in the system will be statistically biased towards the directions of stronger amplification. These 'prefered' directions however, are only revealed after time–averaging over many avalanches, resulting in a clear picture in the form of effective networks and activity flows. These two representations allows us to characterize the *noise focusing* mechanism as we will now see.

2.6.1 Effective networks

The complex internal structure of the activity avalanches is revealed after a correct time–averaging. Instead of focusing on the activity of neurons during avalanches, we focus directly on the connections. The information obtained from time–averaging neuronal activity is equivalent to calculating the individual firing rate of the neurons, and we have already seen in Figure 2.11c that they are not a good indicator of the internal dynamics. Instead, we weight each connection by the number of times it participates in an avalanche, i.e., it is involved in two causally–connected firings. This operation creates a new network which is a weighted version of the original (structural) one. If we now apply a certain threshold to only keep the most active connections we obtain an effective network that shows the structure of the most active connections and the subnetwork they might form.

In Figure 2.25a we show the effective network for a particular case which contains the top 1% of most active connections during BAs. These connections only involve about 25% of the neurons. The structure of such a 'dressed' network is remarkably different from the original 'bare' network. Not only is it strongly inhomogeneous in space, but also exhibits a more hierarchical structure, with a fundamentally different degree distribution consistent with a power-law (see Figure 2.25d). A community structure, also appears, as indicated by the different colors in Figure 2.25a. Many of the modules concentrate around the nucleation sites (presented in Figure 2.25c), however, a substantial amount also appear far from the nucleation sites. The construction of this effective network prunes the less active links, effectively filtering the small avalanches, those that are self-similar and essentially homogeneous and isotropic, while keeping the contribution of large avalanches, which grow selectively in more specific locations and directions as a result of the *noise focusing* mechanism.

An equivalent effective network can be constructed with only the IAs, as shown in Figure 2.25b. Notice how the IAs effective network emerges as a subset of the

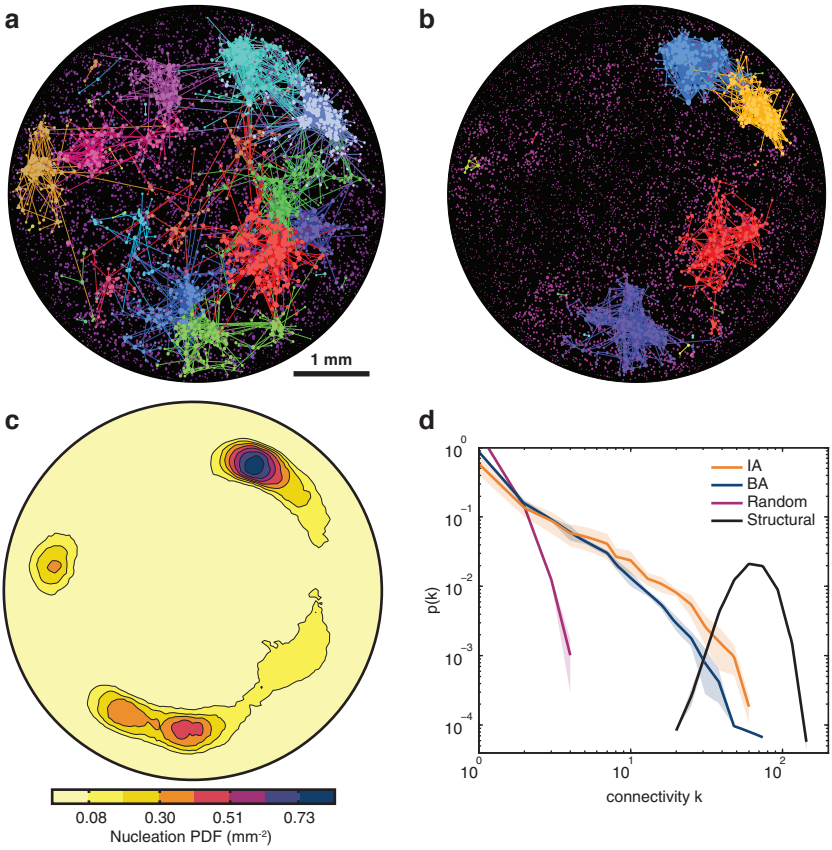

Figure 2.25 | Effective networks. a, Spatial representation of the background avalanche activity in a circular culture 5 mm–wide and density $\rho = 300\,\text{neurons}/\text{mm}^2$, with an average connectivity of $\langle k \rangle \sim 70$. Only the top 1% of the most active connections that participate in the avalanches are shown. Different colors identify communities according to standard community detection algorithms [Blondel 2008]. The background activity forms a subnetwork clustered in specific regions of the culture containing only 25% of the total population. **b,** Spatial representation of the ignition avalanche activity from the same network in **a,**. **c,** Nucleation probability density, coarse–grained over the connectivity correlation length scale of 0.26 mm. Each nucleation point is defined by the geometrical center of the neurons that are the first to fire in a burst. Their distribution is highly localized in specific regions of the system which define the nucleation sites (3 in this case). The nucleation sites are more focused than the IAs activity itself. **d,** Degree probability distribution $p(k)$ of the different networks and subnetworks studied. The distribution of the IA (yellow) and BA (blue) subnetworks is completely different from the structural one (black), and shifts from a Gaussian-like profile to one that is consistent with a scale-free network. The distribution of a randomized version of the original connectivity, with only 1% of the links taken at random, is also shown for comparison (purple).

BA one, more concentrated in fewer modules. All the modules in the IAs effective network are located around the nucleation sites, clearly showing how the activity of IAs concentrate around the nucleation sites. The smallest nucleation site from the left however, is missed out, partially because the activity that concentrates there comes from a wide area and is not as concentrated. This reflects the importance of spatio-temporal correlations in the avalanche dynamics that have been removed by the time-averaging. Remarkably, not even the characterization of these subnetworks is sufficient enough to fully identify the nucleation sites.

Figure 2.25d shows how the effective network structure is shaped by the dynamics. The original network connectivity distribution has a Gaussian profile, while both the BA and IA effective networks resemble a power–law distribution, with a few nodes acting as hubs. These hub neurons are not particularly more active than the other neurons, but they are able to amplify its activity much more effectively.

As a side note, let us point out that the presence of these effective networks also reveals the complexity of the problem of network inference in neuroscience. Any network reconstruction method that is based on activity recordings will be heavily influenced by the presence of these networks, and the resulting reconstruction might be more closely related to this network than to the structural one (even in a system as 'simple' as a neuronal culture).

2.6.2 Activity flow

A new picture emerges if, instead of focusing on the network structure, we identify where the activity flows to during ignition avalanches. Every IA ends up nucleating a wave at a specific point in the system, and we can assign a unit vector to every neuron that participates in the avalanche that points towards the nucleation point. This method overcomes many of the problems from the other analyses, namely heterogeneity and variability. By directly correlating every participating neuron with the final nucleation point we are actually taking into account the long range spatio–temporal correlations and averaging over all possible paths. After iterating over many avalanches, we can finally coarse–grain the resulting vectors to create a flow map (as we did with the other observables and the network maps). Instead of plotting the flow map itself we plot its streamlines, which better describe the flow. In Figure 2.26 we see the streamlines for the same network presented in Figure 2.11. The two nucleation sites now clearly appear as sinks of activity. Activity originating in regions away from the nucleation sites flow, on average, towards them following the corresponding streamlines. This picture also clearly shows the effective basin of attraction of each nucleation site, i.e, its area of effect, which in this particular case appears to be around 2 mm–wide. The small nucleation site in the bottom left creates a perturbation to the streamlines that go to the nucleation site on the right,

and on average, is not strong enough to focalize its activity. Most of the activity around that region will flow towards the other nucleation site.

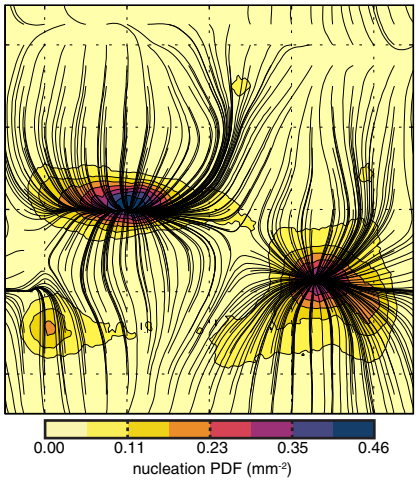

Figure 2.26 | Activity flow. Streamlines of the average flow of Ignition Avalanches (IAs) superimposed on the nucleation PDF from Figure 2.11. For every IA we assign a unitary vector to each participating neuron pointing towards the nucleation point of that IA. Averaging over all the IAs results in a vector field whose streamlines define the basins of attraction of the different nucleation sites. Neurons outside the nucleation sites still have a preferred direction and contribute to the IAs. The basins of attraction also fix the characteristic area of influence of a particular nucleation site, in this case being around 2 mm–wide.

2.7 Discussion and conclusions

The flow pattern of the IAs that emerges after averaging in Figure 2.26 yields the key insight into the new scenario that solves the puzzles mentioned in Section 2.4. Nucleation sites can be pictured as sinks that collect the large–avalanche activity over large basins of attraction. At the root of this flow pattern we identify two mechanisms of noise amplification that are inherent to an integrate-and-fire directed network, and that are enhanced by metric correlations: (i) a dynamical noise amplification, associated to the nonlinear growth of the probability of subquorum firing; and (ii) a topological amplification, related to the growth of the probability of induced firing mediated by connections with other neurons. The high sensitivity of these mechanisms to local details of the network, implies that the growth of avalanches at a given point will be statistically biased towards the directions of stronger amplification. The directionality of avalanches will thus be more pronounced for larger ones. Within this picture, what promotes a given region into a strong nucleation site is the confluence of paths of large amplification. The existence of such a non-local component in the selection of the nucleation sites can be checked experimentally for instance by observing the rearrangement of the nucleation probability distribution after cutting off a distant part of the network (see Section 2.A.2).

The strong spatio-temporal localization of the noise-driven activity due to sensitive noise amplification in integrate-and-fire networks is what we call *noise focusing*. The emerging scenario is opposite to a common view that pictures the local origin of the bursting as a recruitment of activity from the surroundings of highly active neurons or groups of neurons, possibly synchronized through some type of sub-network. In contrast, our nucleation sites do not actively initiate the ignition process, but collect and amplify activity originated elsewhere. Moreover, the effective network that we find emerges as a dynamic, collective phenomenon and neither reflects an inherent heterogeneity of the network nor provides a synchronization mechanism. Interestingly, an effective power-law degree distribution, a feature that has been associated to the burst activity growth [Eckmann 2010], emerges naturally from the dynamics.

The noise focusing effect is a basal phenomenon that should be present to some extent in any neuronal tissue. This should be specially relevant in early stages of neuronal network development when no additional biological traits, such as the presence of specific connectivity layouts, neuronal types or plasticity effects, could eventually mask or tame the noise focusing effect. Regarding this point, we have observed that the presence of nucleation sites and waves could be perfectly characterized in the experiments discussed here (up to 18 DIV). The analysis become more difficult at later stages of development as the network dynamics became gradually more complex, specially in the presence of inhibition. Hence, our description of noise focusing in cultures is especially relevant to young ones, in a stage often referred to as 'initial' in the literature [Wagenaar 2006a, Tetzlaff 2010].

A cultured neuronal network at early stages of development behaves as a homogeneous and isotropic excitable medium with regard to the propagation of large-scale excitation waves. The existence of an underlying network of integrate-and-fire elements however, endows the background spontaneous activity with a complex spatio-temporal structure in the form of avalanches. The scrutiny of the particular avalanches that are capable to ignite the bursts reveals the sensitivity of the noise amplification mechanisms to network details, and leads to a strong spatio-temporal localization of peaks of spontaneous activity, i.e. *noise focusing*.

Noise focusing highlights the complex interplay between structure and dynamics in neuronal systems. A single structural network can entail many functional networks within, and reconstructing these effective networks directly from the dynamics might be more revealing than looking directly at their ground–truth topology. In this context, information–theoretic approaches have been recently introduced to infer effective connectivities directly from spiking data [Ito 2011] and also from calcium imaging data [Stetter 2012].

2.8 Acknowledgments

Part of the computational framework developed in this chapter has been done in collaboration with E. Álvarez–Lacalle. All the experiments presented here were performed by J. Soriano and S. Teller.

Appendix

2.A Additional experiments

A complementary series of experiments that were inspired by the theory were also carried out. They provide direct evidences of the sensitivity of the nucleation process on both network architecture and background neuronal activity. The experiments strengthen the validity of the theoretical framework and the simulation approach. These experiments show that changes in temperature modify the nucleation sites, hinting at the importance of noise in neuronal network dynamics. They also show that a modification of the architecture of the network through ablation of neurons and connections considerably changes the distribution of nucleation sites, revealing the nonlocal nature of the nucleation process and the subtle interplay between connectivity and dynamics.

2.A.1 Influence of temperature

The chamber in the experimental setup that contains the neuronal culture is equipped with a temperature controller in the range 25 °C to 50 °C. To test temperature effects, in a typical experiment activity was first measured for 30 min at 25 °C in a culture with both excitation and inhibition active (E+I network), then switched to 37 °C, and measured again for another 30 min. Next, inhibition was blocked with 40 μM bicuculline (E network) and repeated the measurements at the two temperatures. In total $N = 6$ cultures were investigated with similar size (7.3 mm^2 in area), density (400 neurons/mm^2) and maturation (*day in vitro*, DIV, $16 - 18$).

In general the experiments showed similar results with both temperatures, with no qualitative difference in activity. Global bursts of spontaneous activity appeared at both temperatures, and with similar shapes. Nucleation points and propagation velocities could also be described well. For each experimental condition the analysis consisted of $n = 20 - 60$ bursts, were the inter–burst interval (IBI) and the velocity v of the propagating front were obtained. The results are shown in Figure 2.A.1b. Within experimental error we could not observe any difference in the overall dynamics of the network due to temperature. However, we did obverse a significant

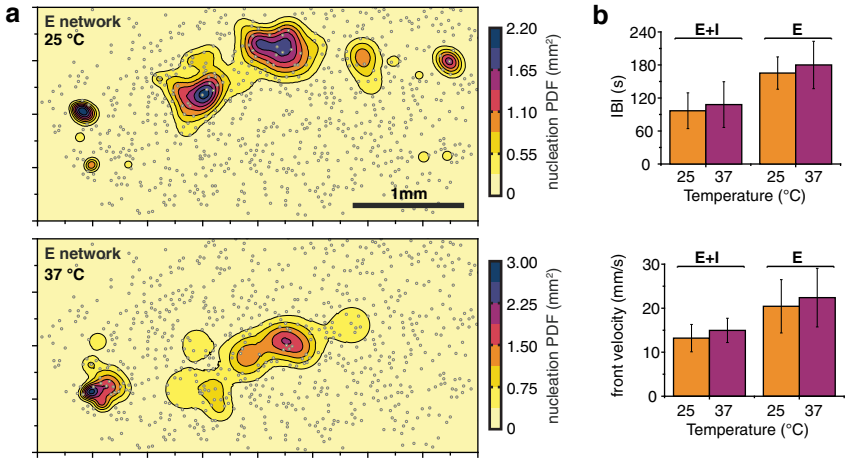

Figure 2.A.1 | Temperature influence. a, Comparison of the values for the inter–burst intervals (IBIs) and front velocity for cultures studied at two temperatures, 25°C and 37°C, and two connectivity conditions, E+I and E. Statistics is based on $N = 6$ cultures of 7.3 mm^2 in area at DIV $16 - 18$, with $n = 20 - 60$ bursts analyzed for each temperature and condition. **b,** Nucleation probability distribution for a culture studied at two temperatures, 25°C and 37°C, at DIV 18 and with only excitatory synapses active. Culture size was 4 mm^2 × 2 mm^2. Small gray–yellow circles are neurons.

variation in the distribution of nucleation sites, as shown in Figure 2.A.1a for a culture with only excitatory synapses active. The foci of nucleation displaced from the top areas of the culture to its left–center areas as the temperature increased. Although temperature has a complex role in neuronal dynamics, we hypothesize that, in the context of our noise focusing model, temperature may increase the spontaneous release of neurotransmitters, therefore increasing the background activity of the network. This, in turn, may modify the frequency and structure of activity avalanches, ultimately modifying the spatial distribution of nucleation events.

2.A.2 Modification of network circuitry through cutting

The alteration in the spatial distribution of nucleation sites was studied by removing of a small region of the neuronal culture. These experiments were carried out in cultures with both excitatory and inhibitory synapses active (E+I network), and at DIV $12 - 13$. E+I networks are convenient since they provide the maximum firing rate and therefore rich nucleation statistics. In a typical experiment spontaneous activity was first measured in 3 mm diameter mini cultures for about 40 min. Next,

with the help of a scalpel, a cut was performed in a small region of the culture and spontaneous activity was measured right after for another 40 min. The cut out region contained about $15-20\%$ of the neurons of the original network. The distribution of nucleation sites was calculated both before and after the damage. The study was carried out for $N = 4$ different cultures of equal size and nominal density. Initiation statistics is based on $n \simeq 50$ bursts per experimental condition.

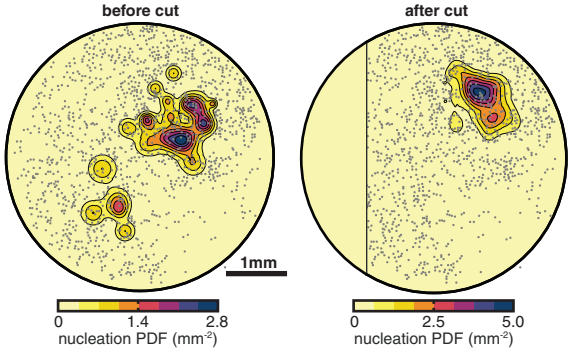

Figure 2.A.1 | Circuitry modification. Comparison of the nucleation probability distribution for a 3 mm diameter culture before and after damaging the network with a sharp blade. Culture was studied at DIV 12 and had both excitatory and inhibitory synapses active. The black lines shows the position and length of the incision. Neurons are shown as small gray–yellow circles. Neurons in the cut out region are shown in a lighter color. Nucleation statistics is based on $n = 30$ bursts before the cut, and on $n = 57$ bursts after. Spontaneous activity recordings lasted 35 min in both cases.

The results for a particular culture are shown in Figure 2.A.1 Before the cut, initiation switched between two well separated nucleation sites, a big one at the top–right of the culture, and a smaller one at the bottom-left. After the cut, the small nucleation site (at the vicinity of the damaged region) disappeared, while the remaining one (located at about 1 mm from the damage) changed its spatial configuration. We note that the cut not only eliminated a number of neurons and associated background activity, but also their input and output connections, effectively remapping the flow of activity in the culture. Interestingly, the average activity of the network increased after the damage, and illustrates the subtle interplay between connectivity and activity. In the framework of the noise focusing phenomena, the spatial modification of the nucleation distribution probability has a clear interpretation: a series of avalanches that originated in the left side of the culture and that possibly ended on its right side were completely eliminated.

2.B Experimental methods

2.B.1 Culture preparation

Rat cortical neurons from 18–19-day-old Sprague-Dawley embryos were used in the experiments. All procedures were approved by the Ethical Committee for Animal Experimentation of the University of Barcelona. Following [Segal 1992, Soriano 2008], dissection was carried out in ice-cold L-15 medium enriched with 0.6% glucose and 0.5% gentamicin (Sigma-Aldrich). Embryonic cortices were isolated from the rest of the brain and neurons dissociated by gently pipetting through gradually narrower pipette tips.

Cortical neurons were plated on 13 mm glass coverslips (#1 Marienfeld-Superior) that contained a pierced PDMS mold, as illustrated in Figure 2.B.1a. Prior to plating, glasses were washed in 70% nitric acid for 2 h, rinsed with double–distilled water (DDW), sonicated in ethanol and flamed. During glass cleaning, several 13 mm diameter layers of PDMS 1 mm thick were prepared and subsequently pierced with biopsy punchers (Integra-Miltex) of diameters in the range $2-5$ mm. Each pierced PDMS mold typically contained 5 to 8 cavities, either circular or quasi–rectangular by overlapping consecutive pierced areas (Figure 2.B.1b)). The PDMS molds were then attached to the glasses and the combined structure autoclaved at 120°C, firmly adhering to one another. Each combination of glass and PDMS was placed in 15 mm diameter culture wells for neuronal plating and maintenance. To facilitate a homogeneous distribution of neurons in the cultures, the PDMS–glass structure was incubated overnight with 0.01% Poly–l–lysine (PLL, Sigma). For each dissection 24 wells were prepared, giving rise to about 100 mini–cultures of areas in the range $2-20$ mm^2. Bigger cultures were also prepared by plating the neurons directly on the 13 mm diameter glass coverslips.

Cultures were incubated at 37°C, 95% humidity, and 5% CO_2 for 4 days in plating medium [90% Eagle's MEM —supplemented with 0.6% glucose, 1% 100X glutamax (Gibco), and 20 μg/ml gentamicin— with 5% heat–inactivated horse serum, 5% heat–inactivated fetal calf serum, and 1 μl/ml B27]. The medium was next switched to changing medium [90% supplemented MEM, 9.5% heat–inactivated horse serum, and 0.5% FUDR (5–fluoro–deoxy–uridine)] for 3 days to limit glia growth, and thereafter to final medium [90% supplemented MEM and 10% heat–inactivated horse serum]. The final medium was refreshed every 3 days by replacing the entire culture well volume. Plating was carried out with a nominal density of 1 million cells/well (5000 neurons/mm^2). The actual density of the neuronal culture was measured at the end of each experiment by counting the number of active neurons, and ranged between 500 and 700 neurons/mm^2. Figure 2.B.1b shows an actual culture 11 days after plating. A detail of the culture depicting the neurons is shown in Figures 2.B.1c to 2.B.1d Although neurons grew both over glass and PDMS, the connectivity between the top and bottom areas was minimal. The PDMS

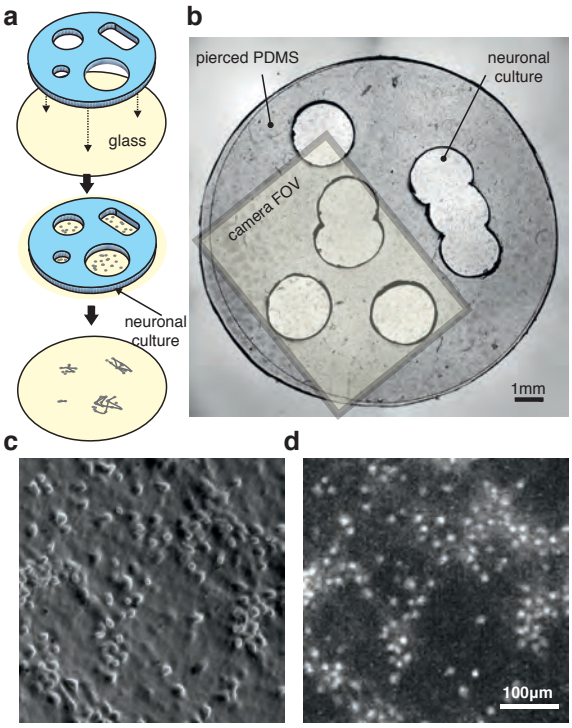

Figure 2.B.1 | Neuronal cultures. a, Schematic representation of the culturing process by using pierced PDMS molds (blue) attached to glass coverslips (yellow). The preparation process (top) included piercing, autoclaving and poly–l–lysine coating; the culturing process (center) yielded to the formation of mini–cultures in the pierced areas; the final process (bottom) consisted in the removal of the PDMS mold and the preparation of the culture for the measurements. **b,** Actual image of combined glass–PDMS structure 11 days after plating. The rectangular area depicts the maximum field–of–view (FOV) of the camera (8.2×6.1 mm). **c,** Bright field image of a small region of a culture. Round objects are neurons' cell bodies. **d,** Corresponding fluorescence image integrated over 200 frames. Bright spots are firing neurons.

was gently removed before measuring, and no substantial damage in the network was detected after PDMS removal.

2.B.2 Experimental setup and imaging

Neuronal activity was studied at day *in vitro* 9–18, which corresponds to a state of development sufficiently mature for the culture to show rich spontaneous activity. Prior to imaging, and after removing the PDMS mold, cultures were incubated for 40 min in External Medium (EM, consisting of 128 mM NaCl, 1 mM $CaCl_2$, 1 mM

$MgCl_2$, 45 mM sucrose, 10 mM glucose, and 0.01 M Hepes; treated to pH 7.4) in the presence of the cell–permeant calcium sensitive dye Fluo-4-AM (4 μl Fluo-4 per ml of EM). The culture was washed with fresh EM after incubation and finally placed in a recording chamber containing 4 ml of EM.

The recording chamber sit on a temperature controller stage that provided stable temperature during recording with an error of 0.1°C. The stage was mounted on a Zeiss inverted microscope equipped with a 2.5X objective and a variable optical zoom in the range 0.32X-0.81X. Neuronal activity was monitored through fluorescence calcium imaging (Figure 2.B.1d)) using a Hamamatsu Orca Flash 2.8 CMOS camera attached to the microscope. Images were acquired with a speed in the range $33.33 - 200$ frames per second (fps) and a spatial resolution in the range $3.44 - 8.51$ μm/pixel (depending on the optical zoom and camera settings). As described later, the recording speed was adjusted in each experiment to balance image quality, minimum photo–damage to the cells, and sufficient temporal resolution. The size of the images was automatically set by the camera to fit the requested acquisition speed. The maximum image size that we could set was 960×720 pixels (width×height), i.e. 8.2×6.1 mm^2 at the lowest resolution and acquisition speed (33.33 fps). At 200 fps, for instance, the maximum image size was 960×144 pixels, corresponding to 8.2×1.2 mm^2. The number of neurons monitored depended on the actual size of the mini–culture and the recording settings, but all experiments contained at least 1000 neurons.

2.B.3 Experimental procedure

Prior to recording, the mini–cultures were carefully inspected to reject those with dead cells or poor distribution of neurons. The selected culture was next placed in the recording chamber and oriented respect to the camera to fit as many cultures as possible in the field of view, as illustrated in Figure 2.B.1b.

In all experiments the spontaneous activity of the neuronal network was monitored at a temperature of 25 °C unless stated otherwise. Experiments were carried out in two steps. In the first step a short image sequence at 100 fps was recorded for about 5 min, containing a few bursts. The data was then pre–analyzed to determine the typical propagation speed of the front. The camera settings were then readjusted to set the maximum image size and recording quality according to this speed. In the experiments it was observed that a front propagating at $v \simeq 10$ mm/s (see Figure 2.16) could be well resolved at speeds of $33.33 - 50$ fps, while propagations at $v \simeq 100$ mm/s (typically for cultures at DIV 14-27) required an acquisition speed of 200 fps.

The second step corresponded to the actual recording of spontaneous activity. A long sequence of typically 45 min in duration was acquired, which contained

several network bursts, on the order of 100. A second recording of $45-60$ min long was also programmed for those experiments in which the neuronal network was manipulated, e.g. to study inhibition or different temperatures. Cultures under continuous recording are healthy for about $2-3$ h, and therefore we limited the experiments to 1.5 h to prevent artifacts in the data due to culture deterioration.

We designed the experiments to explore different culture sizes, the excitatory–inhibitory balance, temperature, as well as the influence of physical damage to the network. The experiments are summarized in Table 2.B.1.

As indicated, experiments carried out at day *in vitro* (DIV) $9-18$ showed rich and sustained spontaneous activity. This activity took the form of bursts. However, for completeness, we also tested (Table 2.B.1)): a) very young cultures at DIV $5-6$, which lack inhibition but do fire [Soriano 2008]; b) maturing cultures at DIV $7-8$, characterized by a low activity and low propagating velocity; and c) relatively old cultures at DIV $20-27$, which are highly active but that may exhibit a more complex bursting dynamics [Wagenaar 2006a]. Data averaging was carried out only with cultures that differed a maximum of 2 days for DIV<9, or 3 days for DIV≥ 9. Although nucleation and front propagation could be observed in all cases, the dynamics of the front depended on culture age, culture size, and the balance between excitation and inhibition.

2.B.4 Pharmacology

Sufficiently mature neuronal cultures (above DIV $6-7$) contain both excitatory and inhibitory neurons. To study the influence of the inhibitory sub–network in the initiation and propagation of the activity front, data was first recorded with both excitatory and inhibitory connections active (E+I networks). Next, the culture was treated with $40\,\mu$M bicuculline methiodide (Sigma), a $GABA_A$ receptor antagonist, to completely block inhibition, and the activity of the excitatory–only culture (E network) was measured again. Bicuculline was applied to the culture 5 min before the actual recording of activity for the drug to take effect.

2.B.5 Data analysis

The recorded image sequences were processed at the end of the experiment to retrieve the fluorescence intensity of $1000-3000$ individual neurons as a function of time. To reconstruct the neurons' ignition sequence, a particular bursting event was isolated from the rest of the sequence. Next, for the fluorescence signal of each neuron, two linear fits were carried out: one fit of the data points preceding the

Table 2.B.1 | Summary of the experiments. 'DIV' is culture days *in vitro*. Cultures were always grown on cover glasses, and the presence of PDMS pierced molds during culture development provided mini–cultures of either circular or rectangular shapes. 'Type' indicates then the nominal size and shape of the circular or rectangular PDMS pierced molds. For those experiments without PDMS, the diameter of the cover glass is provided instead. 'Area' is the actual region covered by the neurons in the mini–culture, measured at the end of the experiment. The 'standard experiments' correspond to measures with excitation and inhibition active (E+I networks), followed by measurements in the same culture with inhibition blocked upon application of 40 μM bicuculline (E networks). Some special experiments were inspired by the theory, and included the removal of a part of the network (cutting experiments) and the exploration of different temperatures. The number in brackets beside the measurements of inter–burst interval (IBI) and average velocity of the propagating front $< v >$ is the standard deviation of the data. IBIs and standard deviations are not computed for those experiments with 5 or less bursts.

Culture properties			Realizations (N)	Experimental condition	Recording time (min)	Observed bursts (n)	Dynamics		Comments
Type	Area (mm^2)	DIV					<IBI> (s)	< V > (mm/s)	
Circ, 2 mm	3.0	10	2	E+I	45	38	83 (96)	3 (1)	Standard experiments on pierced PDMS molds [small size]
				E	45	14	173 (122)	6 (1)	
Circ, 2 mm	2.0	9	2	E+I	30	45	47 (64)	3 (1)	
				E	60	9	360 (208)	6 (1)	
Circ, 3 mm	7.1	5	2	E+I	30	29	62 (23)	3 (1)	Standard experiments on pierced PDMS molds [medium size]
				E	45	(no activity)	-	-	
Circ, 3 mm	7.1	6	2	E+I	40	45	51 (32)	10 (3)	
				E	45	3 (erratic)	-	3 (2)	
Circ, 3 mm	7.1	8	2	E+I	25	111	13 (7)	6 (2)	
				E	45	3 (erratic)	-	9 (2)	
Circ, 3 mm	7.1	9	1	E+I	25	52	23 (11)	13 (2)	
				E	45	3 (erratic)	-	28 (4)	
Circ, 3 mm	6.9	9	5	E+I	45	98	26 (19)	8 (2)	
				E	60	44	78 (114)	16 (3)	
Circ, 3 mm	5.6	10	1	E+I	30	58	30 (23)	16 (5)	
				E	45	5 (erratic)	-	28 (3)	
Circ, 3 mm	5.2	10	1	E+I	45	101	26 (16)	11 (2)	
				E	45	7 (erratic)	270 (72)	24 (3)	
Circ, 3 mm	6.2	10	4	E+I	45	63	44 (46)	20 (5)	
				E	60	21	156 (81)	28 (7)	
Circ, 4 mm	7.4	11	2	E+I	40	68	35 (10)	5 (1)	
				E	60	44	83 (64)	9 (1)	
Circ, 3 mm	8.1	13	2	E+I	40	49	48 (47)	13 (3)	
				E	60	13	265 (172)	21 (5)	
Circ, 3 mm	6.9	12	2	E+I normal	35	24	75 (46)	13 (2)	Cutting experiments
				E+I after cut	35	58	37 (24)	10 (2)	
Circ, 3 mm	7.3	12	2	E+I normal	35	56	31 (24)	12 (3)	
				E+I after cut	45	60	43 (43)	11 (2)	
Rect, 6x3 mm^2	15.8	9	1	E+I	40	134	17 (8)	16 (3)	Standard experiments on pierced PDMS molds [big size]
				E	60	60	53 (36)	18 (3)	
Rect, 6x4 mm^2	16.8	9	2	E+I	40	157	15 (8)	12 (2)	
				E	60	42	79 (62)	16 (2)	
Rect, 7x3 mm	16.9	11	3	E+I	40	148	16 (8)	6 (2)	
				E	60	92	39 (24)	9 (2)	
Rect, 6x3 mm^2	13.8	15	2	E+I	35	34	56 (33)	18 (4)	
				E	55	28	117 (108)	26 (4)	
Rect, 5x3 mm^2	7.3	16 – 18	6	E+I [25 ºC]	40	43	96 (32)	13 (3)	Temperature experiments
				E+I [37 ºC]	40	34	108 (41)	14 (2)	
				E [25 ºC]	40	17	165 (29)	20 (6)	
				E [37 ºC]	40	16	180 (43)	22 (7)	
			1	E [49 ºC]	40	2	-	33 (10)	
13 mm glass	132.7	5	2	E+I	30	38	47 (25)	19 (6)	Standard experiments on 13 mm cover glasses
				E	60	(no activity)	-	-	
13 mm glass	132.7	6	2	E+I	25	81	18 (9)	13 (3)	
				E	45	14 (erratic)	185 (114)	11 (3)	
13 mm glass	132.7	9	3	E+I	20	96	11 (10)	6 (1)	
				E	20	14	13 (9)	26 (3)	
13 mm glass	132.7	12	3	E+I	30	92	19 (23)	13 (2)	
				E	45	19	144 (102)	23 (4)	
13 mm glass	132.7	13	3	E+I	25	64	24 (15)	15 (2)	
				E	45	62	44 (37)	51 (5)	
13 mm glass	132.7	14	3	E+I	30	179	10 (3)	9 (3)	
				E	60	122	29 (19)	13 (2)	
13 mm glass	132.7	15	2	E+I	35	219	9 (4)	17 (3)	
				E	50	91	33 (8)	34 (6)	
13 mm glass	132.7	16	2	E+I	40	72	33 (21)	18 (3)	
				E	45	35	79 (29)	26 (3)	
13 mm glass	132.7	27	2	E+I	35	264	8 (6)	26 (5)	
				E	55	169	19 (6)	43 (6)	
13 mm glass	132.7	20	2	E only	30	51	36 (29)	63 (5)	
13 mm glass	132.7	21	2	E only	30	54	32 (13)	89 (8)	
13 mm glass	132.7	8	2	E+I (before cut)	20	56	21 (10)	23 (5)	Cutting experiment
				E+I (after cut)	20	18 (erratic)	62 (41)	22 (7)	

firing and another one of the points encompassing the fast increase in fluorescence (Figure 2.B.2)). The crossing point of the two lines provided the ignition time of the neuron. This process was repeated for all neurons, and the final activation times data set was ordered to reconstruct the neurons' firing sequence (Figure 2.B.2)). This information, together with the spatial position of the neurons, provided the map of neuronal activation shown in Figure 2.16 (see also Figure 2.19). The first group of neurons to fire determined the position of the nucleation point, i.e., the center of burst initiation. Since the burst propagates as a circular wave, the velocity of the front was calculated as the average radial displacement at different time intervals.

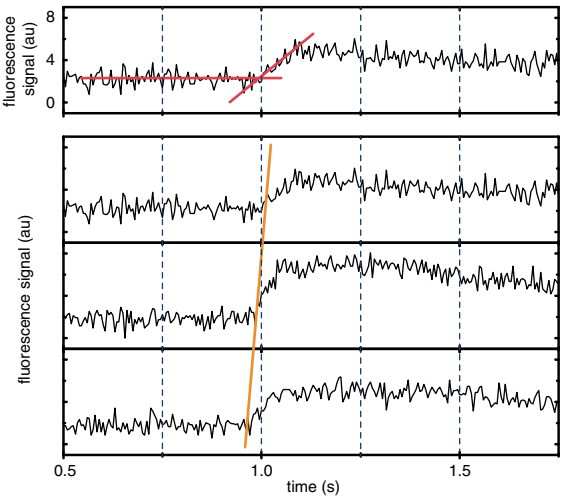

Figure 2.B.2 | Determination of the onset time. Top: Example of the fluorescence signal of an individual neuron, together with the linear fits used to determine the onset time of firing. Bottom: Fluorescence traces of three neurons located (from top to bottom) at the left edge, center, and right edge of the region studied. The thick line connects the measured onset times, and illustrates the propagation of an activity front from right to left.

The reconstruction of the neurons' ignition sequence was slightly sensitive to the signal–to–noise ratio, i.e. fluorescence signal quality, and on the parameters of the linear fits, i.e. the fitting origin and range. The determination of the coordinates of the nucleation point and their associated error took into account the fact that activity propagates as a circular wave, and proceeded as follows. For each activity front, the average position of initiation for the first N firing neurons was calculated with $N = 1, 2, 3, 5$ and 10, considering the standard deviation of these positions as the error ε_{xy} in the location of the nucleation site. This initial calculation was carried out using preset fitting parameters, which were later refined to take those that minimized ε_{xy}. The propagation velocity of the front is measured along consecutive radius, centered at the nucleation site and separated by 200 μm.

Each spontaneous activity measurement provided a set of about $50-200$ nucleation points and associated errors. The number of bursts depended on culture properties, e.g., maturation or size, and network connectivity, e.g. inhibition active or blocked. The corresponding nucleation probability distribution of these nucleation points was calculated as follows. First, the area of the neuronal culture was coarse–grained by applying a grid with a lateral size $s = 10\ \mu$m. This grid was next associated to a matrix initiated with zeros. For each nucleation point, one was added to the matrix element with indexes (i, j) that corresponded to the coordinates (x, y) of the nucleation point. The matrix elements at concentric radius from the nucleation point, and up to the error ε_{xy}, were added with radially decreasing values according to a Gaussian distribution. In this way the spatial distribution of nucleation sites could be weighted by their errors. The matrix was finally normalized and divided by the coarse–graining factor s^2 (in mm^{-2}) to obtain the probability density plotted in the manuscript. A comparison of the distribution of burst initiation points and the final nucleation probability function is shown in Figure 2.B.3.

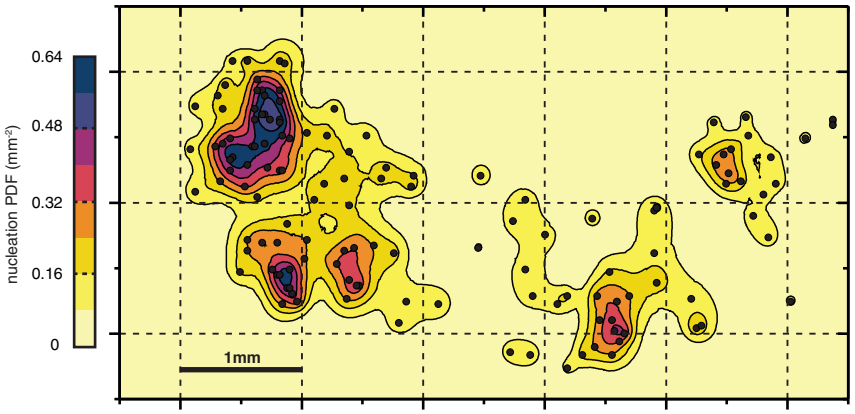

Figure 2.B.3 | Experimental determination of nucleation points and sites. Nucleation probability function for the experiment shown in Figure 2.18 together with the corresponding burst initiation points (black dots). Nucleation probability is obtained by coarse–graining the 134 nucleation points with an algorithm that includes the error in their detection. The data shown corresponds to a measurement with both excitation and inhibition active, and at DIV 9.

Lorenz curves show the cumulated probability of nucleation as a function of their covered area in the culture. Lorenz curves therefore provide a visual aid for the observed small area coverage of nucleation sites. Homogeneously distributed nucleation sites across the culture would result in a straight line along the diagonal of the plots shown in Figure 2.16c since each area unit of the culture would contribute equally to nucleation. Hence, deviations from this line mark the tendency for nucleation to occur in a relatively small area of the culture, as observed both in experiments and simulations.

The Lorenz curves shown in Figure 2.16c were obtained from the probability density of nucleation sites, as follows. The normalized, cross–grained matrix of nucleation sites was computed, and its values p_i ordered in a descending order. Next, the cumulated sum $\sum_i^n p_i$ was plotted as a function of i/n, with n the total number of elements in the matrix.

3

Neuronal dynamics in single–motif periodic networks

The avalanche dynamics described in Section 2.4, and the noise amplification mechanisms from Section 2.5 that lead to the *noise focusing* effect, were presented in the context of metric networks, that inherit their properties from experimental data. In the description so far, neurons were dynamically identical, but not topologically. The slight local differences on the detailed wiring of the network resulting in highly inhomogeneous patterns of activity. To gain further insight into the interplay between dynamics and topology we will now study case in which the neurons are also topologically all identical. This will allow new insights on the effects of different network motifs in the collective activity of the network.

3.1 Generation of single–motif periodic networks

We construct a set of regular networks with N neurons, labeled $M(F,B)$; where F and B are the number of forward and backward connections per neuron respectively. Each neuron is assigned a circular index (imagine that the neurons are positioned in a ring), and each neuron creates an output connection with the next F (clockwise) neurons and the previous B (counterclockwise) neurons. Within this description, the vector $\mathbf{K}_i^{out}$ describing the output connections of neuron i (which correspond to the i-th row of the adjacency matrix A) is described by

$$\mathbf{K}_i^{out} = \Big(\underbrace{0,\ldots,0,\overbrace{1,\ldots,1}^{\text{B}},0}_{\text{i}},\overbrace{1,\ldots,1}^{\text{F}},0,\ldots,0\Big), \tag{3.1}$$

and it is straightforward to see that the input connectivity vector $\mathbf{K}_i^{in}$ is

$$\mathbf{K}_i^{in} = \Big(\underbrace{0,\ldots,0,\overbrace{1,\ldots,1}^{\text{F}},0}_{\text{i}},\overbrace{1,\ldots,1}^{\text{B}},0,\ldots,0\Big). \tag{3.2}$$

If we change F and B while keeping $k = F + B$ constant, we can study the effect of different levels of clustering and triangle types for the same connectivity. It is easy to see that the full forward network $M(k,0)$ only contains feed–forward (T_{FF}) triangles[1], while the network $M(k/2,k/2)$ has the maximum number of feed–back (T_{FB}), feed-forward and total number of triangles T_{TOTAL}. Also note that $M(F,B)$ is the mirror image of $M(B,F)$, so we will restrict our analysis to $F > B$ without loss of generality.

Characteristic examples of the generated networks are shown in Figure 3.1a for $N = 13$ and $k = 4$, where the neurons are positioned in the unit circle and the forward connections correspond to the clockwise direction and backward connections to the counterclockwise one. The network labeled $M_0 = (4,0)$ only presents feedback triangles, whereas the network $M_3 = (2,2)$ has the maximum number of feedback and feedforward triangles. The network labeled $M_1 - M_2$ correspond to cases in-between. The network M_R on the other hand, corresponds to a random graph with the same connectivity. M_R has the minimum possible triangles, $T_{TOTAL} \to 0$ as $N \to \infty$.

3.2 Avalanches and bursting activity

We simulated the dynamics described in Section 2.1 with the same parameters for regular networks with $N = 200$ and $k = 35$ for five different networks: $M_0 = (35,0)$, $M_1 = (30,5)$, $M_2 = (25,10)$, $M_3 = (18,17)$ and M_R being a random graph with fixed $k = 35$. For all the networks we observe the bursting behavior and the presence of both background (BA) and ignition (IA) avalanches, as in the metric networks. Figure 3.1b shows the distribution of BAs for all the studied networks. The BAs distributions for all the regular networks have a similar trend with a reasonable data collapse, although the distribution starts to deviate at large avalanches due to the small size of the system. These networks however, do not posses nucleation sites, or more accurately, the distribution of nucleation sites is homogeneous, since all points in the system are equivalent.

[1] As long as $N > 2k$.

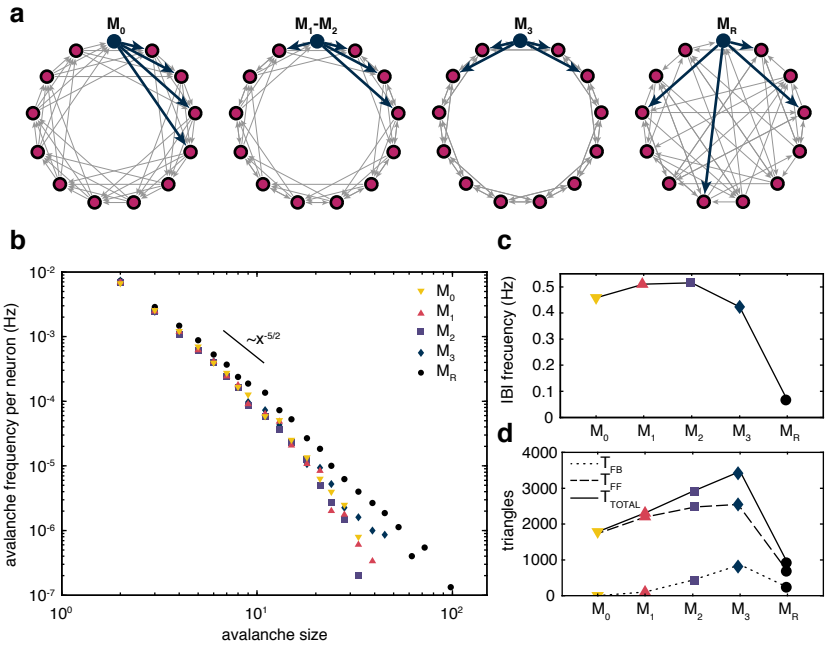

Figure 3.1 | Statistics of Background Avalanches for regular, non-metric networks. a, Four examples of regular networks, with four connections per neuron (the motif in dark color is repeated for all 13 neurons). M_0 designates the case with fully asymmetric (one-sided) connections, while M_3 designates the fully symmetric arrangement. The case depicted as $M_1 - M_2$ describes a generic intermediate case with a non-symmetric arrangement. These network configurations provide scenarios with a different balance between FF and FB triangular loops, with only FFs in M_0 and the maximum number of FBs in M_3, and while keeping the number of input and output connections constant. Finally, M_R designates a random case with the same number of connections per neuron. **b,** Avalanche frequency as a function of the avalanche size for regular networks of 200 neurons, 35 connections per neuron, and different motif arrangements, including: asymmetric $M_0 = (35, 0)$, two intermediate cases $M_1 = (30, 5)$ and $M_2 = (25, 10)$, symmetric $M_3 = (18, 17)$, and random M_R. The values in brackets denote the number of clockwise connections and counterclockwise connections. The dashed horizontal lines correspond to the frequency of IA for the four regular networks (values indistinguishable in this scale) and the random one. The dashed line marks the crossover scale for departure from the power law behavior, with approximate slope $-5/2$. **c,** Nucleation frequency for the different regular and random networks, showing a non-monotonic behavior. **d,** Statistics of FFs, FBs and total number of triangles for the different networks.

The interburst interval (IBI) frequency is highly sensitive to the wiring of the network. This sensitivity becomes clear in Figure 3.1c, where we show the IBI frequency of the four regular networks and the random one. We note that the nucleation time (the inverse of the IBI frequency) for the random network is two orders of magnitude higher than the regular ones. Such a difference is associated to the weaker correlations between neurons in the random network. For the regular cases, however, the difference is associated to the balance between FF and FB

triangles. Indeed, although a larger number of FF triangles initially favors nucleation, the shortest nucleation times are obtained when a finite amount of recurrence (FB triangles) is introduced. For these particular networks, the optimal ratio of FF triangles to the total number of triangles is $R_{FF} \simeq 0.85$. As a reference we note that for an infinite random graph $R_{FF} = 0.75$. It is suggestive that the simulated metric networks presented in Section 2.1.4 yield values close to the above optimum value, with $R_{FF} = 0.87$.

These results indicate that the general structure of avalanches followed by nucleation is a robust scenario and, more importantly, that random graphs would need a much larger time to nucleate once the network has recovered from synaptic depression. This indicates that the metric correlations in the connectivity generated by the growth process of axons leads to much faster nucleation. On the other hand, we can see that the detailed wiring at the level of triangles can introduce significant differences in the characteristic time scale of nucleation. This sensitivity of the nucleation times to the detailed wiring explains why regions of similar average connectivity in the metric networks show significant differences in nucleation probability, as we have seen in Section 2.2.2.

3.3 Multi–layer networks

The regular networks described above are particularly insightful to describe the statistics of avalanches and the relevance of different types of triangles in the collective dynamics. These networks however, can only be used for small N due to their scaling properties. In the realistic networks, the average path length l_G, that defines the number of jumps needed to travel from one side of the network to the other, is dominated by the axon length ℓ and the system size L. For the networks used in Chapter 2 we have $\langle \ell \rangle \sim 1.1$ mm and $L \sim 5$ mm, resulting in $l_G \sim L/\langle \ell \rangle \sim 5$. For the M regular networks however, we have in general $l_G = N/k$. If we go to large networks $N > 10^3$, for the typical connectivity $35 - 70$, the path length quickly becomes very large. The path length is an important characteristic of non–metric networks, since it allows to establish a distance between nodes in the absence of a metric space. In these networks we can define a propagation velocity by the time it takes for a burst to propagate through the entire system, which is proportional to l_G. Although the system is periodic, propagation stops when the wave reaches the original nucleation region because the system is still depressed. For large l_G however, the system enters a periodic regime if it is allowed to recover before the wave can travel the whole system.

This shortcoming can be avoided by using instead multi–layer networks, which are the direct generalization of the previous regular networks. These networks are described by two global parameters, the number of layers L and the neurons per layer N_L, where $N = LN_L$ is the total number of neurons. The connectivity pattern

is described by a single vector **K** of length L that describes the connections a layer makes with the other layers in the same way we did in Equations (3.1) and (3.2). The way in which each neuron connects with the neurons in the other layers also needs to be established, but for simplicity we only consider cases where if a neuron connects to a layer, it connects to all the neurons within that layer. Within this description we can also describe the connectivity pattern between layers by $M_L(F,B)$, and the total connectivity of a neuron is $(F+B)N_L = k$. A schematic representation of a multi–layer network is shown in Figure 3.2. Variant of these types of networks are often used in neuroscience, like feed-forward networks [Kumar 2010] and synfire chains [Ikegaya 2004, Long 2010], often used to describe coding and information transfer.

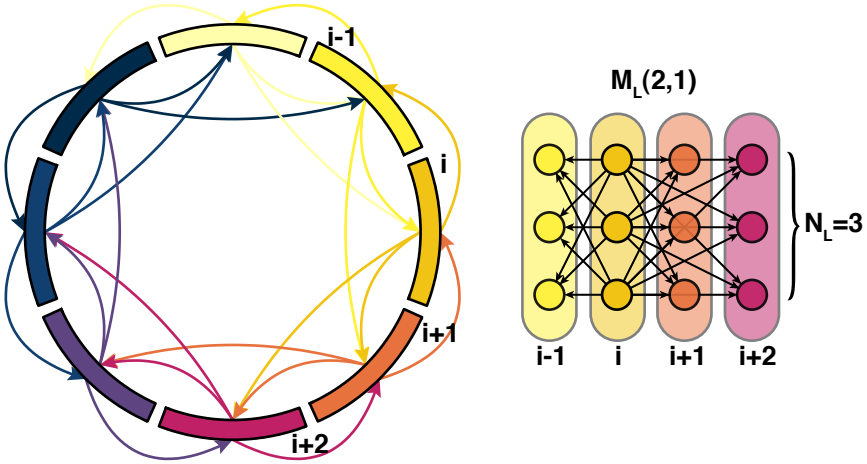

Figure 3.2 | Multi–layer networks structure. Left: ring representation of a multi–layer network. Each of the eight segments represents a layer with N_L neurons, and the arrows represent the connections between layers. For this particular case each layer connects with the next two layers (arrows inside the circle) and with the previous layer (arrows outside the circle), i.e., $M_L = (2,1)$. Connections are not allowed within the same layer. Right: the connectivity pattern for the neurons in layer i for the particular case $N_L = 3$.

It is also easy to see from Figure 3.2 that when a layer only contains a single neuron $N_L = 1$, the multi–layer network is equivalent to the ones described in Section 3.1.

3.4 Statistics and structure of avalanches

We perform a systematic study of many avalanche observables for networks with the same global connectivity k (see Figure 3.3). All the observables shown in Figure 3.3

appear to be independent of the connectivity pattern, from fully feed-forward networks $F = 50$ to undirected networks[2] $F = 25$.

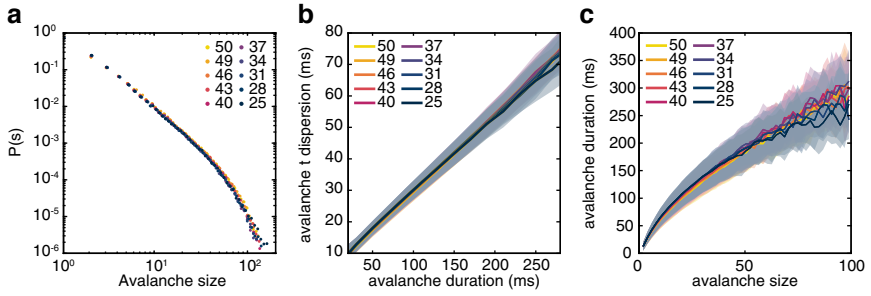

Figure 3.3 | Avalanche statistics in single–layer networks. a, PDF of avalanche sizes in single–layer networks with the characteristic power–law behavior for small avalanches. **b,** Relation between the temporal dispersion and the duration of the avalanches. The temporal dispersion is the standard deviation of spike times within an avalanche. **c,** Relationship between avalanche duration and size which becomes almost linear for large avalanches. The legend indicates the number of forward connections F for each network with $k = 50$ and $L = 250$. Shaded area indicates the standard deviation of each observable. The three observables shown here are invariant to the connectivity pattern.

The only observable that appears to depend on the connectivity pattern is the avalanche radius. The avalanche radius is defined as the standard deviation of the positions of spiking neurons within an avalanche (the position of the neuron is defined by its layer), and defining the unit distance by the distance between consecutive layers. The characteristic radius for different networks in single–layer and multi–layer configurations are shown in Figure 3.4. The avalanche radius increases rapidly with avalanche size, but it saturates for large avalanches.

From the characterization of the avalanches presented in Figures 3.3 and 3.4 a clear picture emerges. Although the statistics of avalanche sizes and lengths remain almost invariant for the different connectivity patterns, the avalanche radius (spatial spreading) indeed does change. This behavior is not directly related to the clustering or triangles, since the networks with $F = B$ have the highest number of triangles (for every motif); or to the path length, since it is the same for all the networks. It is related to how the avalanche can spread to newer areas. Although a network with maximum F does not have the highest number of feed–forward triangles, all these triangles are effectively spreading the activity away from where it started. In a network with lower F (same k) however, activity travels back and forth, and its spread is smaller.

[2] We use the term undirected to denote that there is no preferred direction in the network. Activity spreads equally through the network due to the symmetry between forward and backward layers.

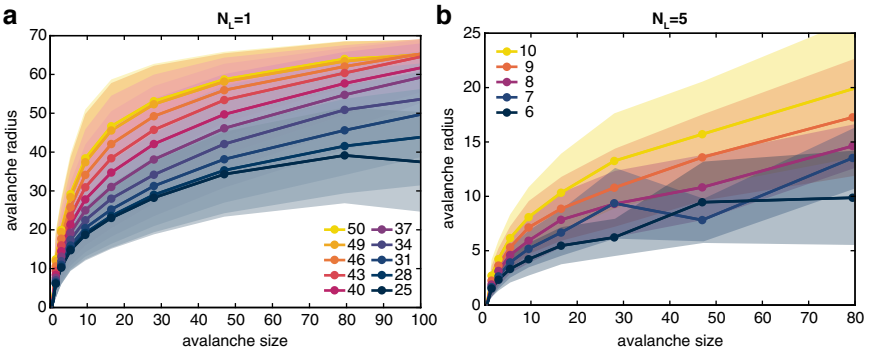

Figure 3.4 | Avalanche radius in multi–layer networks. a, Dependence of the avalanche radius with avalanche size for $N_L = 1$ networks with different connectivity patterns. **b,** Same representation for multi-layer avalanches with $N_L = 5$. The legend indicates the number of forward layers F a given layer connects to. For each network with $k = 50$ and $L = 250$. Shaded area indicates the standard deviation of the observable.

Another characteristic of the avalanches that depends on the specific topology is the average displacement of activity within an avalanche. A moving–window average in time of the positions of the spiking neurons within an avalanche creates a smooth trajectory in space. The end points of the trajectory define the displacement within an avalanche, and also using its duration we can define an average avalanche velocity

$$\langle V(s)\rangle = \left\langle \frac{D(s)}{T(s)} \right\rangle, \tag{3.3}$$

where $D(s)$ and $T(s)$ are the displacement and duration of a given avalanche of size s. The distribution of avalanche sizes for the different networks are shown in Figure 3.5. For $N_L = 1$ (see Figure 3.5a) the distribution shows a non–monotonic behavior for small avalanches, but the velocity of large avalanches quickly stabilizes and appears to be independent of avalanche size. Note that the non–monotonic behavior is not present for $N_L = 5$ (see Figure 3.5b).

Averaging over the distribution of avalanche sizes, results in a well defined velocity

$$\langle V\rangle = \int_0^\infty \langle V(s)\rangle p(s) ds, \tag{3.4}$$

where $p(s)$ is the probability density function of avalanche sizes. The resulting average avalanche velocity quantifies the effect of the network topology on the spreading of the avalanches, and is shown in Figure 3.6. The average avalanche velocity for the symmetric network $F = B$ is 0, and it increases with the asymmetry.

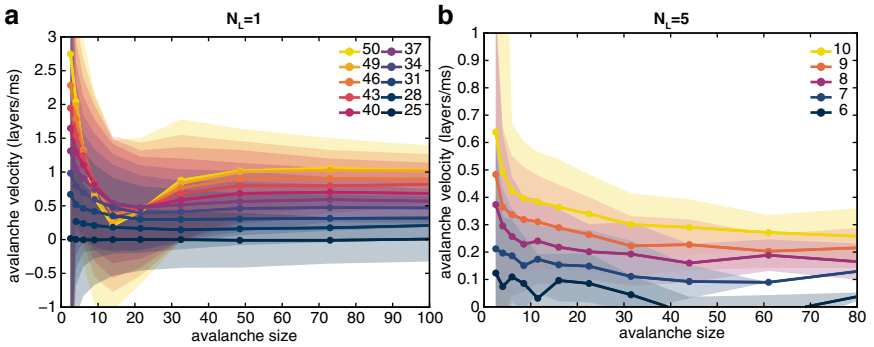

Figure 3.5 | Avalanche velocity. a, Distribution of avalanche velocities for $N_L = 1$. **b,** Distribution of avalanche velocities for $N_L = 5$.

The average velocity establishes a clear connection between the spreading of the avalanches in the network and its topology.

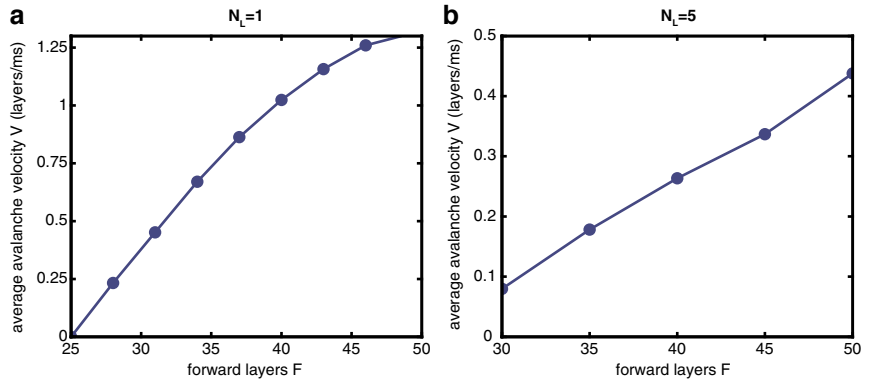

Figure 3.6 | Average avalanche velocity. a, Average avalanche velocities for $N_L = 1$. **b,** Average avalanche velocities for $N_L = 5$.

3.5 Conclusions

The implementation of the neuronal dynamics in regular networks allows us to further identify and quantify the effects of the different network motifs in the avalanche and bursting behavior. The noise amplification mechanism introduced in Section 2.5

is also present in these networks, however, the key ingredient of noise focusing, i.e., the existence of different amplification paths created by inhomogeneities in the network, is not present in regular networks. Since all neurons have the same connectivity, activity flows equally through the network.

Regular networks however, are useful to quantify the effects of topology on the dynamics. The avalanches show the same scaling relations and behavior than those found in metric networks, and although there are no specific, permanent nucleation sites, waves do nucleate homogeneously and propagate. The close relationship between the bursting rate and the topology (shown in Figures 3.1c and 3.1d) further explains why no single observable can be used to identify nucleation sites. The interplay between network and dynamics is such, that it will be extremely difficult for any coarse–grained or mean-field description to accurately capture this relationship.

The characterization of the avalanches by its radius and velocity, which depend on the network structure (shown in Figure 3.4 and Figure 3.5), allows us to define a transport coefficient V that characterizes how activity spreads throughout the network based on the network motifs. In a non–regular metric network however, this coefficient will in general depend on the local network structure, and the propagation will be anisotropic, as we have seen in the activity flow maps from Section 2.6.2. In general we will be able to define a vector coefficient with spatial dependence $\mathbf{V}(x,y)$.

4

Neuronal cultures at the mesoscale

The results presented in Chapter 2 suggest that a coarse–grained representation of the collective dynamics of neuronal cultures could be adequate and possibly insightful to clarify the nature of the collective phenomena involved. Many of the interesting results from the analysis of spontaneous activity in neuronal cultures are only appreciated after an appropriate coarse–graining of the network observables and the network activity. A description at the level of population activity, that takes into account the spatio–temporal structure of the microscopic dynamics, should be possible, and given the features of the metric networks, a description in terms of a continuous, spatially–extended system emerges naturally. Within this description, the system is characterized by a set of continuous variables in space, the network is replaced by spatial couplings, and the microscopic dynamics are characterized by effective transport coefficients [García-Ojalvo 1999, Sagués 2007]. The distinctive feature of the mesoscale level of description is that the microscopic degrees of freedom are incorporated through stochastic noise terms. The challenge is thus to elucidate the way to include the phenomenon of noise focusing in this type of description.

As we have seen in Chapter 2, the population dynamics of neuronal cultures is governed by collective bursts of activity, whose internal structure is that of traveling fronts that nucleate at specific sites of the system and propagate. When it comes to the analysis of activity propagation, the system behaves as a regular excitable system [Lindner 2004], where the network plays little role and the propagation is governed by spiking dynamics. The description of the nucleation process, however, is not so simple to implement as we will now see.

4.1 A coarse–grained model for noise focusing

The propagation dynamics observed in the spontaneous activity of neuronal cultures can be described with almost any reaction-diffusion model [Sagués 2007], like the Oregonator model [Tyson 1980, Field 1972, Sendiña-Nadal 2000] or the Barkley model [Barkley 1991]. The full macroscopic dynamics, however, are those of an excitable system, which can be understood as an extension of the above by the inclusion of a feedback mechanism [Lindner 2004]. Our model of neuronal cultures at the mesoscale starts with the most general version of the FitzHugh–Nagumo (FN) model [Nagumo 1962, Fitzhugh 1961], due to its historical use in neuroscience. The original spatially–extended FN model is described by

$$\dot{u} = f(u) - \kappa v + D\Delta u + \eta, \tag{4.1a}$$

$$\dot{v} = \gamma(u + g - hv), \tag{4.1b}$$

where $f(u) = au^3 + bu^2 + cu + d$. In the original FN model the variable u describes the behavior of a neuron membrane potential and v is a recovery variable that provides a negative feedback to account for the effect of slow currents. The original FN was used to describe the propagation of an action potential through an axon via a diffusive coupling $D\Delta u$. In our case however, the variable u describe the population activity, a coarse–grained version of the single neuron activity. The population activity can also propagate, and is mediated by the same kind of diffusive coupling.

By an appropriate choice of the parameters $a, b, c, d, \kappa, \gamma, g$ and h (see Table 4.1), we effectively constrain the possible trajectories of our system to the region $u \in (0,1)$ and $v \in (0,1)$; we associate $u \sim 0$ to the background activity and $u \sim 1$, to the bursting behavior[1].

Within this parameter range, the system has a single fixed point (see Figure 4.1). The fixed point is stable, but very close to a supercritical Andronov-Hopf bifurcation [Izhikevich 2007], and the presence of a noise term η, allows the system to lose stability and generate large amplitude excursions around a limit cycle attractor. In the two–dimensional system, these excursions can start at any point in the system and propagate by means of the diffusive coupling, giving rise to a traveling front.

The dynamical behavior of this model reproduces the generation and propagation of traveling fronts that are equivalent to the bursts of neuronal cultures, but the mechanisms involved in front termination, however, differ substantially. In the FN model front termination is controlled by the variable v, that plays a role similar to the slow currents and the after–spike hyper–polarization of the membrane. In neuronal cultures, however, synaptic depression plays a key role in wave termination and regulates the periodicity of the fronts. In the neuron model from Chapter 2, synaptic depression is described by Equation (2.6), and the response of this equation to an

[1] Formally this corresponds to a logarithmic mapping between the population activity rate and the variable u.

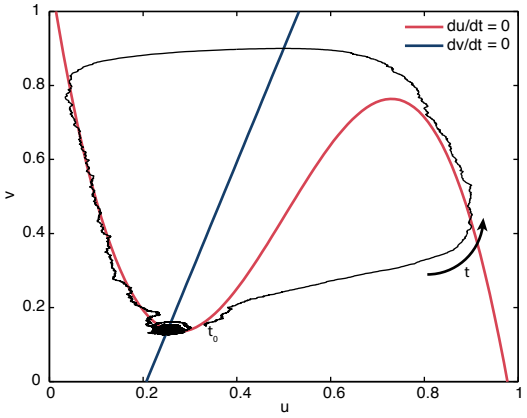

Figure 4.1 | Phase–portrait of the zero–dimensional FN model. Phase–portrait and null-clines for the zero–dimensional FN model in our parameter range. The black line shows the trajectory of an initial perturbation at t_0 that excites the system.

input of varying frequency is shown in Figure 4.2, where w accounts for the level of depression of the synapses. The level of depression w is close to 0 for low values of activity whereas it quickly reaches saturation for high activity values.

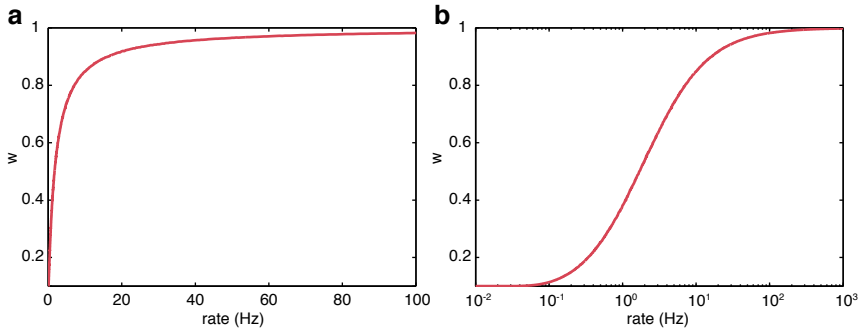

Figure 4.2 | Depression response for a Poisson spike train. a, Steady–state value of the depression of a synapse $w = 1 - D$, governed by Equation (2.6), for a Poisson spike train. **b,** Same plot in logarithmic scale.

Based on these results, we propose to introduce synaptic depression in the FN model by means of the following equation

$$\dot{w} = -\frac{1}{\tau_D} w + \beta u^n (1 - w), \tag{4.2}$$

where w is the level of depression, τ_D the time scale of synaptic recovery, and β and n parameters fitted to obtain a curve like the one presented in Figure 4.2b. Note that the steady–state solution of Equation (4.2) is

$$w_{st} = \frac{u^n}{(\beta\tau_D)^{-1} + u^n}, \tag{4.3}$$

which has the form of a Hill equation, often used to describe cooperative binding dynamics between ligands and their receptors in biochemistry.

The coupling between synaptic depression and the original activity equation has to be introduced with care. Synaptic depression must be able to completely eliminate the spatial coupling, thus preventing activity from spreading, but should not affect the internal dynamics of the system. While the system is recovering from a burst, it is not able to generate a new one, however, it is possible to excite the system externally, and this has to be taken into account. To complete the model, we also include two new transport coefficients that will effectively incorporate the specific features of the noise within an underlying network of excitable elements. Specifically, we will introduce a scalar parameter α that describes the amplification of the noise, and a vector parameter $\mathbf{V}$ that accounts for the directional transport of the noise activity through the network. These are both space dependent fields and will be discussed later in this chapter. The final version of the model reads

$$\dot{u} = f(u) - \kappa v + (1-w)\Big(D\Delta u - \nabla\cdot(u\mathbf{V}) + \alpha u\Big) + \eta, \tag{4.4a}$$

$$\dot{v} = \gamma(u + g - hv), \tag{4.4b}$$

$$\dot{w} = -\frac{1}{\tau_D}w + \beta u^n(1-w), \tag{4.4c}$$

where $f(u) = au^3 + bu^2 + cu + d$ and η is a white noise term. The phase–portrait for the 0D–version of this model is shown in Figure 4.3. The depression from Equation (4.2) is coupled to the activity in Equation (4.4a), but only interacts with the spatial coupling and the new transport coefficients.

The term αu in eq. (4.4a), introduces a local mechanism of activity amplification, representing the effect of network loops within a small area, whose interaction amplifies incoming activity. Although an heterogeneous amplification $\alpha(x,y)$ is also possible, we consider it to be a constant for simplicity. Given that this term accounts for local mechanisms of activity amplification, it has to be coupled to the synaptic depression, since no amplification can take place when the system is fully depressed.

In the zero–dimensional version of the model (see Figure 4.3), the system has a single stable fixed point $p_{st} = (u_{st}, v_{st}, w_{st})$. The nullclines of the model correspond to two–dimensional surfaces, but it is useful to analyze their projections around specific values. One of them corresponds to $w = 1$ (fully depressed system); when the system is fully depressed, the temporal evolution of $w(t)$ is governed by τ_D, which defines a characteristic time scale, orders of magnitude higher than any other scale in the system. Hence u and v can be adiabatically eliminated and substituted with a constant value w_a for the following analysis. For any w the system has a single stable fixed point $p_a = (u_a, v_a, w)$, where

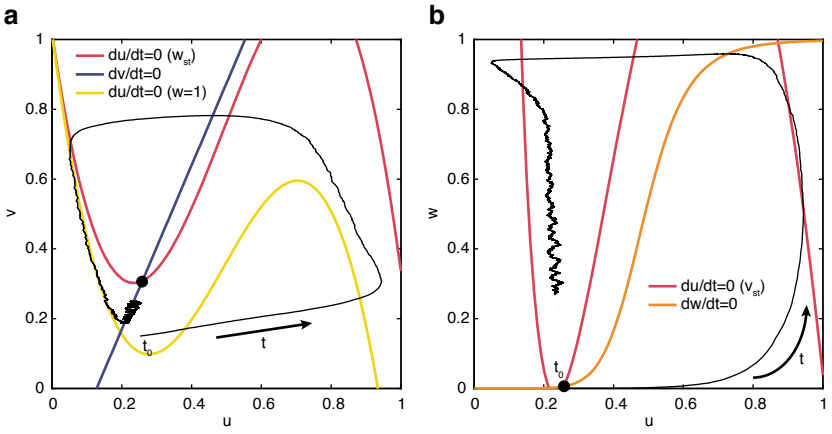

Figure 4.3 | Model phase–portrait and nullclines. Set of nullclines for the full extended model in a 0D–spatial system. The trajectory of a small perturbation at t_0 is also shown (black line). The list of parameter values is shown in Table 4.1. **a,** Projection of the nullclines in the (u,v) coordinates. The system has a single fixed point (black circle), and the nullcline for $\dot{u}=0$ is plotted at the stationary value of $w=w_{st}$ (red line) and also at $w=1$ (yellow line). The nullcline for $\dot{w}=0$ (not shown) corresponds to a horizontal line crossing the fixed point, since it is indendent of v. **b,** Projection of the nullclines in (u,w) coordinates. The $\dot{u}=0$ nullcline is plotted at $v=v_{st}$.

$$f(u_a)+u_a\left(\alpha(1-w_a)-\frac{\kappa}{h}\right)+\kappa g=0, \tag{4.5a}$$

$$v_a=\frac{1}{h}(u_a+g), \tag{4.5b}$$

where u_a is obtained by solving Equation (4.5a), which is a cubic polynomial. The evolution of the system after depression corresponds to the evolution of the fixed point (u_a,v_a,w_a) with time, and during this recovery phase we can further approximate the evolution of $w_a(t)$ by

$$w_a(t)\propto \exp -t/\tau_D, \tag{4.6}$$

since the second term in Equation (4.4c) can de discarded.

This analysis is graphically shown in Figure 4.3a, where we plot the $\dot{u}=0$ nullcline for $w=1$ and w_{st}. Given that $\dot{v}$ does not depend on w, the evolution of the system is determined by the intersection of $\dot{v}=0$, and the nullcline for $\dot{u}=0$ that is slowly evolving in time from the yellow curve to the red one, as shown by the black trajectory. During recovery the system is slowly evolving from p_a, which is stable, towards p_{st}, which is also stable but it is close to the bifurcation point, where a perturbation can easily drive it towards a limit cycle.

Going back to the analysis of the amplification factor αu, the nullcline of $\dot{u}$ for a given w_a can be expressed as $v = \mathscr{F}(u, w_a)$. We have that $\mathscr{F}(u,0) = \mathscr{F}(u,1) + \alpha u$, so in the 0D system term αu is controlling the evolution of the fixed point during recovery. In the 2D model however, there are several other terms that affect the evolution of the system.

In the two–dimensional system, the diffusion term $D\Delta u$, is also coupled to the depression variable, since it accounts for the spreading of activity throughout the system, specially when u is high, which corresponds to the propagation of a wave of activity. The remaining part of Equation (4.4a), $\nabla \cdot (u\mathbf{V})$, is an advective term that describes the effective activity flow due to the underlying network structure and activity avalanches that we saw in Chapter 2. This term attempts to capture ina s imple way the phenomenon of *noise focusing*. The $\mathbf{V}$ field is directly related to the activity flow defined in Section 2.6.2, however, there are many possible ways to describe this field, which we call the *avalanche field*.

Table 4.1 | Mesoscale parameters. List of parameters used to simulate noise focusing at the mesoscale

Dynamics Parameters	**Value**
Activity parameters	
	$a = -12.93\,\mathrm{ms}^{-1}$
	$b = 19.05\,\mathrm{ms}^{-1}$
	$c = -7.6\,\mathrm{ms}^{-1}$
	$d = 1.016\,\mathrm{ms}^{-1}$
Activity–recovery coupling	$\kappa = 1\,\mathrm{ms}^{-1}$
Diffusion coefficient	$D = 0.01\,\mathrm{mm}^2/\mathrm{ms}$
Maximum avalanche velocity	$V_{max} = 0.02\,\mathrm{mm/ms}$
Amplification rate	$\alpha = 0.8\,\mathrm{ms}^{-1}$
White noise strength	$\eta_0 = 3 \times 10^{-8}\,\mathrm{ms}^{-1}$
Avalanche noise strength	$\varepsilon = 5 \times 10^{-10}\,\mathrm{mm}^2/\mathrm{ms}$
Recovery parameters	
	$\gamma = 0.3\,\mathrm{ms}^{-1}$
	$g = -0.13$
	$h = 0.43$
Depression parameters	
Depression recovery constant	$\tau_D = 500\,\mathrm{ms}$
Depression decay constant	$\beta = 4\,\mathrm{ms}^{-1}$
Cooperativity exponent	$n = 8$
Simulation parameters	
Algorithm	Forward Euler
Time step	$\Delta t = 1 \times 10^{-4}\,\mathrm{ms}$
Spatial step	$\Delta x = \Delta y = 1 \times 10^{-4}\,\mathrm{mm}$
Typical Run time	$1 \times 10^2\,\mathrm{s}$
Typical system size	$10\,\mathrm{mm}^2$

4.2 Determination of the avalanche field

The avalanche field $\mathbf{V}$ tries to describe, in a coarse–grained description, all the phenomenology behind the *noise focusing* mechanism and the activity avalanches. Based on our previous study of avalanches in regular networks (see Chapter 3), where we were able to define a characteristic velocity to different network motifs, we know that although there exists a preferred direction of activity flow, their distribution is broad and noisy, so in general we separate our avalanche field in two components

$$\mathbf{V}(\mathbf{r},t) = \mathbf{V}^0(\mathbf{r}) + \boldsymbol{\xi}(\mathbf{r},t), \tag{4.7}$$

where the first term $\mathbf{V}^0$ describes an average, constant component of the field, and $\boldsymbol{\xi} = (\xi^x, \xi^y)$ accounts for the variability in activity propagation, which for simplicity we model as a Gaussian white noise with autocorrelation

$$\langle \xi^i(\mathbf{r},t)\xi^j(\mathbf{r}',t')\rangle = 2\varepsilon\delta(\mathbf{r}-\mathbf{r}')\delta(t-t')\delta^{ij}, \tag{4.8}$$

where ε denotes its strength. $\mathbf{V}^0$, however, has to be modeled taking into account the neuron dynamics and the network topology, and there are different strategies to model it.

4.2.1 Connectivity–based avalanche field

A first approximation to the avalanche field consists on generating the field directly from the connectivity matrix. We associate to each connection A_{ij} a vector $\mathbf{r}_{ij} = \mathbf{r}_j - \mathbf{r}_i$, where r_i is the position of neuron i, and then define the vector field for each neuron by

$$\mathbf{V}_i^A = \sum_{j=1}^{N} A_{ij}\mathbf{r}_{ij} = \sum_{i\in k_i^{out}} \mathbf{r}_{ij}, \tag{4.9}$$

where the last sum goes over all the k_i^{out} connections. The vector $\mathbf{V}_i$ describes the average direction neuron i forms with its output connections, and its modulus is proportional to the distance and number of connections. The vector is not normalized, given that neurons with higher output connectivity must be associated to a higher activity flow. $\mathbf{V}_i$ is associated to each neuron, and it still has to be coarse–grained into a continuum description, with the same procedure we used in Section 2.1.5 to generate *network maps*. The streamlines associated to an avalanche field constructed with this procedure are shown in Figure 4.4a superimposed to the nucleation map of a particular network. Many streamlines concentrate around the nucleation sites,

but there are other regions where streamlines concentrate that do not relate to the nucleation sites.

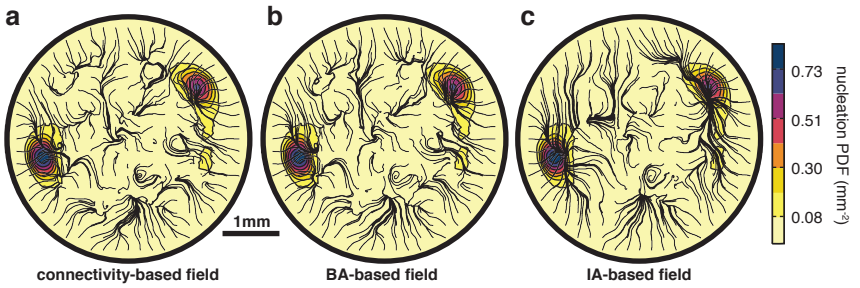

Figure 4.4 | Avalanche fields. Streamlines of three different definitions of the avalanche field for the same circular network, with the nucleation PDF superimposed. **a,** Streamlines from a connectivity–based avalanche field V_i^A (see Equation (4.9)). **b,** Streamlines from a BA–based avalanche field V_i^B (see Equation (4.10)). **c,** Streamlines from an IA–based avalanche field V_i^I (see Equation (4.11)).

4.2.2 BA–based avalanche field

The avalanche field generated above only relies on the connectivity, and is independent of the underlying dynamics. A different field can be generated if we also use the information from the background activity. We can generate a weighted matrix B_{ij} from the information obtained by the analysis of the background avalanches (BAs) in the dynamical system (see Section 2.4.1). Every time a link participates in a BA its weight is increased by a fixed amount. The full weighted matrix is then normalized so it describes the probability that a given link participates in a BA. By using this matrix we can define a new avalanche field as

$$\mathbf{V}_i^B = \sum_{j=1}^{N} B_{ij}\mathbf{r}_{ij}. \tag{4.10}$$

This field is very similar to the one constructed with only the connectivity information, but it now takes into account the structure of the effective network associated to the avalanche dynamics (see Section 2.6.1). The streamlines from this field construction are shown in Figure 4.4b. Comparing the streamlines with the ones obtained with the previous field we observe only a few differences. The reason that the fields differ very little is directly related to the avalanche statistics. Most avalanches are small, and those are isotropic in space, with no preferred directions, these avalanches are the ones that dominate in the construction of the new field, and

they do not reveal any particular feature of the system other than the ones already show by the connectivity structure alone.

4.2.3 IA–based avalanche field

A more refined approach to construct the avalanche field consists in using only the information from the ignition avalanches (IAs), those that end up in the nucleation of a burst. For each IA, we assign to the participating neurons a vector pointing towards the nucleation point of that particular avalanche (see Section 2.6.2),

$$\mathbf{V}_i^I = \sum_{j \in I_i} (\mathbf{r}_j^B - \mathbf{r}_i), \tag{4.11}$$

where I_i is the subset of IAs where neuron i participates, and $\mathbf{r}_j^B$ is the nucleation point of the j–th IA. The streamlines associated to this vector field are shown in Figure 4.4c. Note that the center of mass of all the spiking activity on an IA must be very close to the actual ignition point, so the above procedure is equivalent to defining the vector field as that that unites the origin and the center of mass of the IA, as we did in Section 2.6.2.

In contrast with the two previous definitions, the IA–based field correlates much better with the nucleation sites. Most of the streamlines concentrate in the nucleation sites, and those that do not are regions equidistant to nucleation sites with similar probability, and no temporal average defined at a single point is ever going to achieve any better. The IA–based avalanche field is constructed in such a way that it retains non–local information from the whole region that covers the basin of attraction of a given nucleation site, which has an extension defined by the mean axon length. This information is inaccessible to a connectivity–only construction, or from one that takes into account all avalanches. By using only the IA information, which corresponds to large avalanches, and also by using the information of the nucleation point, i.e., where the IA activity ends up concentrating, we are providing each neuron with information that is not available locally. From now on our avalanche field will always be constructed from the IA information, i.e., $\mathbf{V} = V_{max}\mathbf{V}^I$. Here we introduce a global scale factor V_{max} that controls the relative weight of the avalanche field with respect to other terms in Equation (4.4a).

4.2.4 Avalanche field decomposition

To further refine our understanding of the avalanche field, we decompose it into two different fields through a Helmholtz decomposition, i.e,

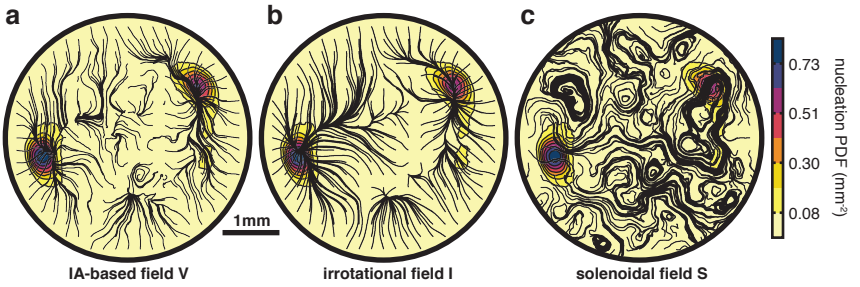

Figure 4.5 | Avalanche field decomposition. Streamlines of three different definitions of the avalanche field for the same circular network, with the nucleation PDF superimposed. **a,** Full IA–based avalanche field. **b,** Irrotational part of the field. It correlates much better with the nucleation sites than the full field. **c,** Solenoidal part of the field. The streamlines form loops with no particular correlation with the nucleation map.

$$\mathbf{V} = \mathbf{I} + \mathbf{S} \tag{4.12}$$

where $\mathbf{I} = -\nabla\phi$ and $\mathbf{S} = \nabla \times \mathbf{A}$. $\mathbf{I}$ is an irrotational field (curl–free) and $\mathbf{S}$ is a solenoidal (divergence–free) one. Applying the divergence operator to both sides of Equation (4.12) results in the Poisson equation

$$\Delta\phi = -\nabla \cdot \mathbf{V}. \tag{4.13}$$

which we can solve to obtain ϕ. When ϕ is known, $\mathbf{I}$ and $\mathbf{S}$ are straightforward to obtain. In Figure 4.5 we show the resulting decomposition for the IA field we showed in Figure 4.4c. The irrotational field $\mathbf{I}$ shown in Figure 4.5b is a very good predictor of the nucleation sites. Most of the streamlines converge in the nucleation sites, showing clearly the preferred paths of activity flow. The irrotational field is similar to the original field, but the removal of the solenoidal part improves the matching with the nucleation sites. The solenoidal field $\mathbf{S}$, on the other hand, does not correlate with the nucleation sites. In fact, the average ratio between the two components

$$\langle \left\| V^I \right\| / \left\| V^S \right\| \rangle \approx 2, \tag{4.14}$$

shows that the irrotational part plays a much greater role in the whole flow.

Since $\nabla \cdot \mathbf{V} = \nabla \cdot \mathbf{I}$, all the information of the irrotational field is already contained in the divergence of the whole field. In Figure 4.6 we show the divergence of the avalanche field $-\nabla \cdot \mathbf{V}$ for all the different field definitions from Section 4.2. The divergence map of the IA–based field is a very good predictor of the nucleation map, whereas the other two definitions are not. This result indicates that a great part of the information contained in the complex interplay between the dynamics and the network topology can be captured within a continuous description, something

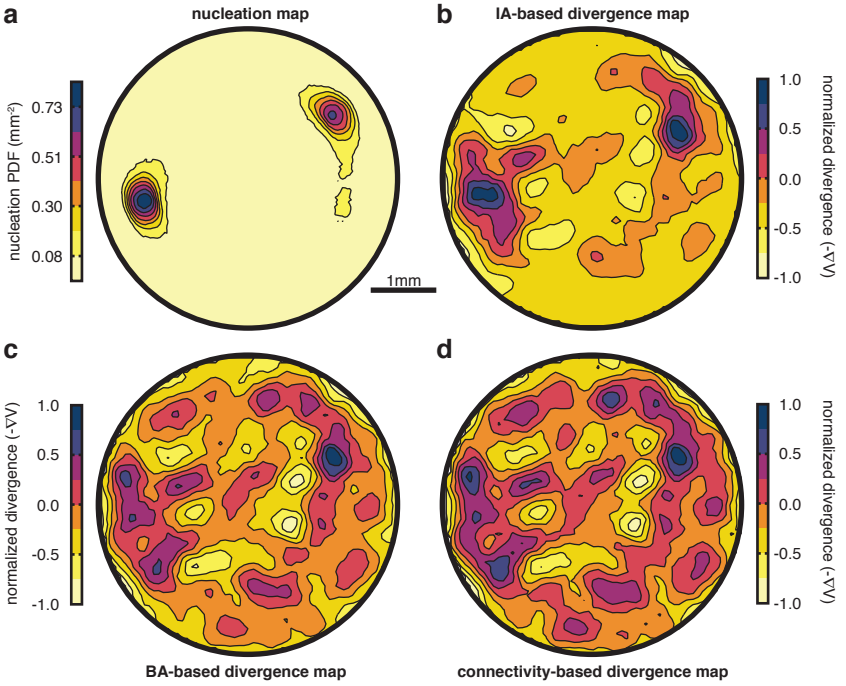

Figure 4.6 | Divergence maps. Divergence maps for each of the avalanche field definitions from Section 4.2. **a,** Nucleation PDF of the network for reference. **b,** Divergence map from the IA–based avalanche field ($-\nabla \cdot \mathbf{V}^I$). **c,** Divergence map from the BA–based avalanche field ($-\nabla \cdot \mathbf{V}^B$). **d,** Divergence map from the connectivity–based avalanche field ($-\nabla \cdot \mathbf{V}^A$). The correlation between the IA–based avalanche field divergence map and the nucleation sites is clear, where the zones of maximum (negative) divergence indicate the nucleation sites. The other maps show many regions of maximum divergence that do not correlate with the nucleation sites.

that was not possible using only the network information or the dynamics at the single neuron level, as we already showed in Chapter 2.

Although the irrotational part of the avalanche field is the best predictor of the nucleation sites, the whole vector is necessary to describe the avalanche dynamics accurately. The full avalanche field $\mathbf{V}^I$ is the vector field that we will plug into Equation (4.7) to define the velocity field, i.e.,

$$\mathbf{V}(\mathbf{r},t) = \mathbf{V}^I(\mathbf{r}) + \boldsymbol{\xi}(\mathbf{r},t). \tag{4.15}$$

4.3 Simulation details

After obtaining a good description of the avalanche field, we can proceed to integrate numerically the original model from Equation (4.4), which can now be written as

$$\dot{u} = \overbrace{f(u) - \kappa v + (1-w)\left(D\Delta u - \nabla\cdot(u\mathbf{V}^I) + \alpha u\right)}^{\text{Deterministic}} \overbrace{-(1-w)\nabla\cdot(u\boldsymbol{\xi}) + \eta}^{\text{Stochastic}} \quad (4.16a)$$

$$\dot{v} = \gamma(u + g - hv) \quad (4.16b)$$

$$\dot{w} = -\frac{1}{\tau_D}w + \beta u^n(1-w), \quad (4.16c)$$

where we have separated the deterministic and stochastic terms from Equation (4.16a). This separation is useful for the algorithmic implementation of the model, however, it is important to remember that the terms $\mathbf{V}^I$ and α that appear in the deterministic part also have an stochastic origin. The stochastic part of Equation (4.16a) has an additive term η and also a multiplicative one $u\boldsymbol{\xi}$ that is coupled in space through the ∇ operator, and has to be treated with care [García-Ojalvo 1999]. After the system is discretized in space, the first equation can be expressed as

$$\dot{u}_{ij} = F_{ij} + \sum_{kl}\left(g^x_{ijkl}\xi^x_{kl} + g^y_{ijkl}\xi^y_{kl} + \delta_{ik}\delta_{jl}\eta_{kl}\right), \quad (4.17)$$

where the index i corresponds to the discretization on x and j on y. F_{ij} is the discretized version of the deterministic part from Equation (4.16a) which is straightforward. The second term of the equation runs over all elements k,l, and the g^d_{ijkl} for $d \in (x,y)$ are functions that will depend on the exact implementation of the discretization of the ∇ operator. If we use central differences for the first and second derivatives we can finally write

$$g^x_{ijkl} = -(1-w_{ij})\frac{1}{2\Delta x}\left(u_{ij}\left(\delta_{i+1,k} - \delta_{i-1,k}\right) + \left(u_{i+1,j} - u_{i-1,j}\right)\delta_{ik}\right)\delta_{jl}, \quad (4.18a)$$

$$g^y_{ijkl} = -(1-w_{ij})\frac{1}{2\Delta y}\left(u_{ij}\left(\delta_{j+1,l} - \delta_{j-1,l}\right) + \left(u_{i,j+1} - u_{i,j-1}\right)\delta_{jl}\right)\delta_{ik}, \quad (4.18b)$$

where Δx and Δy are the spatial discretization steps. The discretization of Equations (4.16b) and (4.16c) is direct, since they are deterministic and not spatially coupled.

This formulation makes it easy to apply any of the stochastic algorithms for solving multiplicative Langevin equations, since each of the multiplicative terms can be treated independently. We chose the Heun algorithm [García-Ojalvo 1999] to simulate the dynamics of the system in the Stratonovich interpretation.

The implementation of this model is usually computationally more expensive than simulating the full dynamics, however, it scales much better with system size and

density. The primary bottleneck is due to the presence of the ∇^2 operator, that imposes heavy restrictions on the choice of Δt, Δx and Δy in order for the system to be stable. In our typical system of size $5\,\mathrm{mm}^2 \times 5\,\mathrm{mm}^2$ we usually discretize each spatial dimension into 64 or 128 bins, which sets an upper bound on $\Delta t < 10^{-3}$ ms, whereas for the single neuron simulations $\Delta t = 10^{-1}$ ms is already good enough. Also, for densities $\rho < 500\,\mathrm{neurons/mm}^2$ we might be simulating more points in space than actual neurons. The coupling however in the extended system, however, is much faster to compute since we only consider interactions between nearest neighbors in a square lattice, which is much faster than looking at entries in the adjacency matrix, specially when the connectivity is high $k > 10^2$.

Given that most of the temporal evolution of the system is spent on the recovery phase, i.e., going from $w \approx 1$ to $w \approx 0$ after a burst, we implement a hack in the simulation, and during this regime we simulate the evolution of $u(t)$ with the spatial coupling disabled ($D = 0$, $\mathbf{V}^I = 0$ and $\boldsymbol{\xi} = 0$), and only recover it when $w \approx 0$. We have performed extensive comparison and it does not affect the overall dynamics, whereas it reduces computational time by a factor of 3.

4.4 Nucleation and bursting dynamics

Taking all of this into account we proceed to simulate the full system in two dimensions with an avalanche field obtained from the neuron dynamics. The single–point results are summarized in Figure 4.7, where we show the trajectories in state–space and in time for two different points (solid and dashed lines) in the system for one cycle (from one burst to the next). In Figures 4.7a to 4.7c we show the projections of the trajectories in the u, v, w coordinates, where we observe that both points follow similar trajectories. Most of the cycle excursion in u, v, which corresponds to the wave propagation, is done in a very short time $\sim$50 ms, whereas the remaining part of the cycle, corresponding to the slow recovery from depression, takes much longer. In this particular case we have set τ_D =75 ms to speed-up the simulations, but in the experiments usually $\tau_D \approx$500 ms to 5000 ms.

In Figures 4.7d and 4.7e we show the trajectories in time of the u and w variables respectively (the dynamics of v are equivalent to the ones from u but shifted in time). The evolution of $u(t)$ has the characteristic form of excitable systems, whereas the evolution of $w(t)$ shows the same behavior as the neuron model of synaptic depression. In the inset of Figure 4.7d we zoom–in around a burst, where we see that the two different points do not evolve synchronously, and in fact, the delay is due to the (expected) presence of a propagating front. The presence of the small oscillations before a burst is characteristic of the supercritical Andronov-Hopf bifurcation of the model, and could easily be avoided by a small change in the feedback mechanism $\dot{v}$ to obtain a saddle–node bifurcation [Izhikevich 2007].

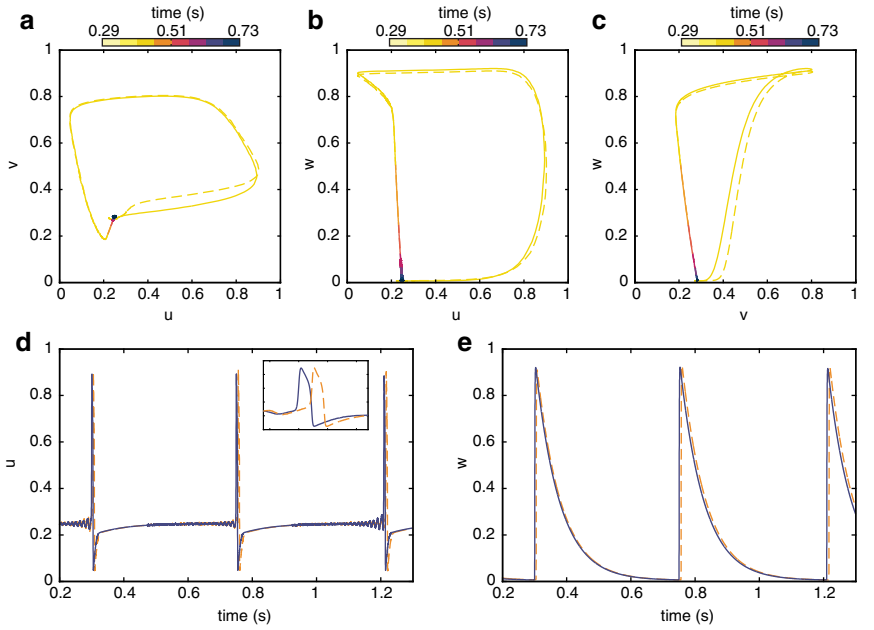

Figure 4.7 | 2D trajectories. Trajectories from the full simulation of Equation (4.16) for two different spatial points in the system. **a,** Projection of the trajectory in (u, v). **b,** Projection of the trajectory in (u, w). **c,** Projection of the trajectory in (v, w). **d,** Evolution of u in time. Inset: zoom in on the first burst. **e,** Evolution of w in time.

Next, we focus on the spatio–temporal structure of each burst. We define the onset time for each point in the system as the first time its activity crosses an arbitrary (high) threshold ($u_{ij}(t) \geq 0.8$ in our case). From the analysis of the onset times we observe that the bursts are indeed traveling fronts that nucleate at specific points in the system. In Figure 4.8 we show two examples for a system with periodic boundary conditions. The traveling front is almost perfectly circular, indicating that the propagation is governed by the diffusive part of the spatial coupling, whereas the avalanche field $\mathbf{V}^I$ plays very little role during propagation. On the other hand, the avalanche field is the one governing the nucleation process as we will now see.

The analysis of the set of nucleation points allows us to generate the nucleation PDF, in the same way we did in Chapter 2, i.e., we define the nucleation site as the point with the smallest onset time for a given burst. The results for a particular network are shown in Figure 4.9, where we compare the map obtained with the extended system (Figure 4.9a), with the one from the full neuron dynamics (Figure 4.9b). Both maps are very similar, showing the same main nucleation sites and overall shape. Only some of the intermediate nucleation sites differ between the two, information that is lost in the construction of the avalanche field.

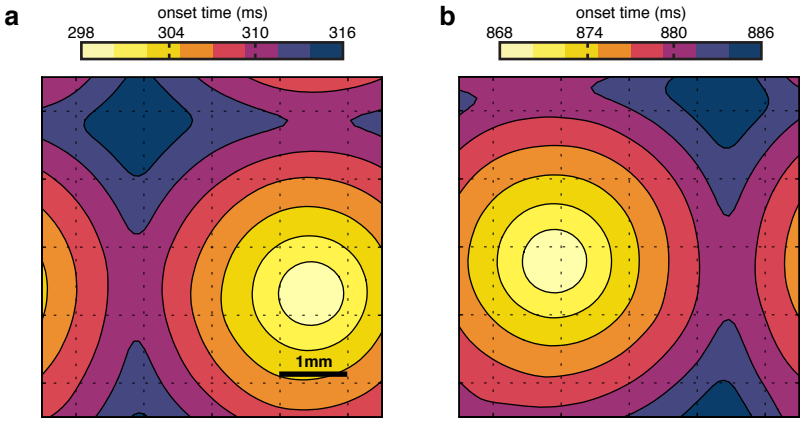

Figure 4.8 | Traveling pulses. Two examples of traveling pulses for a system with periodic boundary conditions and $S = 5\,\mathrm{mm}^2 \times 5\,\mathrm{mm}^2$. The onset time is defined as the first time a point crosses an arbitrary threhold $u_{th} = 0.8$. **a,** Pulse that originates in the middle right area. **a,** Pulse that originates in the middle left area. The waves present an average velocity of $\langle V \rangle = (120 \pm 20)\,\mathrm{mm/s}$.

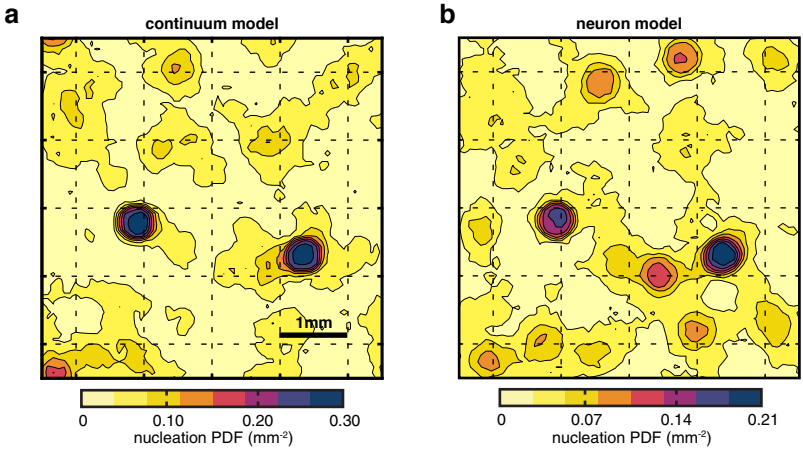

Figure 4.9 | Nucleation maps. Nucleation maps obtained with the two models based on the same original system with $S = 4\,\mathrm{mm}^2 \times 4\,\mathrm{mm}^2$, $\rho = 400\,\mathrm{neurons/mm}^2$ and periodic boundary conditions. **a,** Nucleation PDF generated from the nucleation points in the extended system. **b,** Nucleation PDF obtained from the full neuron dynamics.

The analysis of the different nucleation points also shows that they are uncorrelated in time, i.e., the location of nucleation point is independent of the location of the previous one.

4.5 Conclusions

In this chapter we have developed a coarse–grained approach to neuronal cultures at the mesoscale, where the whole activity of the culture is encoded in field variables. We show that modeling the intrinsic noise requires a nontrivial form in order to reflect the inner network structure and thus account for the phenomenon of *noise focusing* identified in Chapter 2. The model is based on the original Fitzhugh-Nagumo model, and incorporates the minimum ingredients required to describe the behavior of spontaneous activity in neuronal cultures. The model is able to replicate the phenomenon of heterogeneous nucleation, i.e., bursts develop in specific sites of the system and propagate in a wave–like fashion. It also reproduces the characteristic time scales associated to wave propagation and synaptic depression.

This description formalizes the global physical picture observed in Chapter 2 regarding the *noise focusing* phenomena. The emergence of a vector field at the coarse–grained level, that reflects the dynamical properties of the underlying avalanche dynamics at the microscopic level, is the key element behind the heterogeneous nucleation. The direction and modulus of the vector field reflect the directionality of the large avalanches. The field, however, must have a stochastic component itself at the mesoscale, to guarantee the randomness of the nucleation events.

To model the stochastic part of the avalanche field we chose a white noise in time and space for simplicity, which is already sufficient to obtain the heterogeneous nucleation behavior. However, it cannot capture the richness of the self–similar structure of the avalanche dynamics.

This theoretical approach clearly reflects the idea that the nucleation sites in this problem do collect the activity from large basins of attraction, as it is advected by the vector avalanche field. Interestingly, this mesoscale description reproduces to some extent the integrate-and-fire dynamics of the microscopic elements, but now for nucleation sites, as they collect the spontaneous activity around them to the point that they fire global bursts.

5

Stochastic quorum percolation

In Chapter 2 we have drawn several parallelisms to try to explain the mechanisms behind burst generation within the framework of of quorum percolation (QP), however, several differences exist between the two. Quorum percolation [Cohen 2010], which is similar to bootstrap [Tlusty 2009] and k-core percolation [Dorogovtsev 2006], is an extension of percolation theory in which a node (neuron) requires a minimum quorum of m simultaneous inputs to fire.

The original QP model was developed to understand the collective dynamics of neuronal networks under external stimulation [Soriano 2008]. In these experiments, the network connectivity is weakened with different drugs and an external current is applied to the system to study their response. It was found that for specific values of the applied current and drug concentration, the system undergoes a discontinuous phase transition, where a small increase in the current is able to generate a wide response in the system, where all the neurons are excited. The QP model is able to accurately describe this transition and predict some of the properties of the underlying network.

Several groups have tried to extend the concept of QP to include dynamics [Tlusty 2009, Renault 2013] and spontaneous activity [Eckmann 2010], with varying levels of success. In this chapter we analyze our networks under the QP formalism and develop a dynamical protocol for our simulation framework that further connects QP with the real dynamics. Finally, we introduce a generalization of QP called *subquorum percolation*, that includes the dynamics in a natural way and also describes the effects of noise in the neuron dynamics.

5.1 Introduction to quorum percolation

We summarize the basic formalism of QP following the description from [Tlusty 2009] and [Cohen 2010] (see the references for more details). In the QP model, a neuron can be either in an active or inactive state, whose evolution is described by an iterative process, where the state of a neuron s_i can be expressed as

$$s_i(t+1) = s_i(t) + (1 - s_i(t)\Theta\left(\sum_{j=1}^{N} A_{ij}s_j - m\right), \tag{5.1}$$

where $s_i = 1$ if the neuron is active and 0 otherwise. Θ is the heaviside step function, N the total number of neurons, A_{ij} the (binary) adjacency matrix of the network and m the minimum inputs required to fire. We can see from Equation (5.1) that a neuron only changes to active when $\sum_j A_{ij}s_j \geq m$, i.e., at least m of its inputs are active. The iterative process runs until no more state changes are detected within an iteration. Note that a neuron that is turned 'on', stays 'on' forever.

The characteristic observable of the iterative process described in Equation (5.1) is the fraction of active nodes at any given time $f(t)$, where the initial condition $f(0)$, i.e., the initial fraction of lit nodes, acts as a control parameter. Performing an ensemble average of Equation (5.1) results in the self-consistency equation

$$\Phi = f + (1-f)\Psi(m,\Phi), \tag{5.2}$$

where $\Phi = \lim_{t\to\infty} f(t)$ and $f = f(0)$. The function $\Psi(m,\Phi)$ describes the probability that there is a quorum of m inputs to fire, and for the case of directed random graphs[1] can be expressed as

$$\Psi(m,\Phi) = \sum_{k=m}^{\infty} p_k \sum_{l=m}^{k} \binom{k}{l} \Phi^l (1-\Phi)^{k-l}, \tag{5.3}$$

where p_k is the input degree distribution of the network. Note that Equation (5.2) can be expressed as

$$\frac{\phi - \Psi}{1 - \Psi} = f, \tag{5.4}$$

and solved numerically. In the limit of large $\bar{k} = \langle k \rangle$ and m, $\Psi(m,\Phi)$ can be approximated by

$$\Psi(m,\Phi) = \Psi(m/\Phi) \sim \int_{k=m/\Phi}^{\infty} p_k\, d_k, \tag{5.5}$$

[1] In the limit of zero clustering.

and in the case of a Gaussian degree distribution $p_k = (2\pi\sigma_k^2)^{-1/2}\exp(-(k-\bar{k})^2/(2\sigma_k^2))$ we can write

$$\psi(m/\Phi) \simeq \frac{1}{2}\,\mathrm{erfc}\left(\frac{m/\Phi - \bar{k}}{\sqrt{2\sigma_k^2}}\right), \tag{5.6}$$

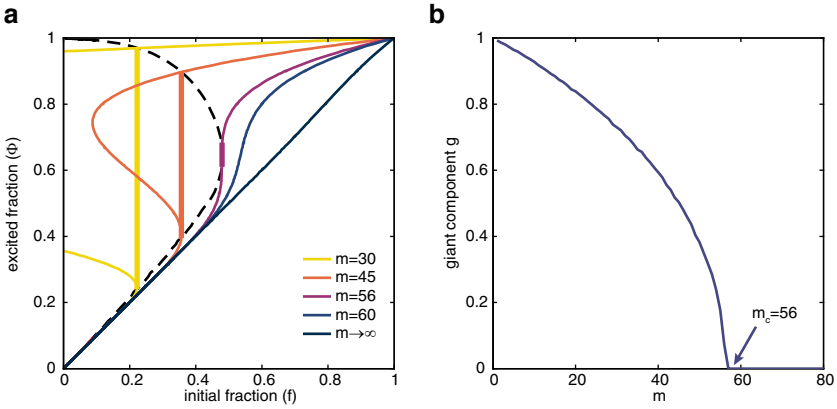

Figure 5.1 | Quorum percolation. a, Numerical solution of Equation (5.2) for different values of m in a network with Gaussian degree distribution and $\bar{k} = 50$, $\sigma_k = 15$. The solid vertical line identifies the size of the giant component g, and the dashed line shows the envelop of the different giant components. **b,** Size of the giant component g for different values of m. The largest m with non–zero giant component defines the critical point m_c.

where erfc is the complementary error function. For this particular approximation the solution of Equation (5.2) is shown in Figure 5.1a. For large m the solution is a single–valued curve, where the excited fraction starts to differ from the initial fraction only for large values of f, i.e., the system barely reacts to the initial perturbation. For small m, however, the curve shows a multi–valued region, with a characteristic S shape, characteristic of a first order phase transition. The upper and lower branch solutions are stable, whereas the middle one is unstable. For a finite system, the multi–valued region indicates bi–stability[2], and for a given initial fraction the system has two stable solutions. To be consistent with previous studies [Cohen 2010, Renault 2013] we define the giant component g as the difference between the two stable solutions of Φ at the largest f, i.e., where (where $d\Phi/df \to \infty$). g is the difference between the excited fraction of the two stable states[3] (marked in Figure 5.1a with a thick line), and its dependence with m is shown in Figure 5.1b. There exists a critical m_c at which the giant component disappears and the system

[2] For an infinite system, this corresponds to the coexistence region.

[3] For an infinite system, the giant component is the infinite cluster.

undergoes a second order phase transition. At the vicinity of the critical point, the size of the giant component can be described with a typical power–law scaling

$$g(m) \propto \left(\frac{m_c - m}{m_c} \right)^{\beta}, \tag{5.7}$$

for $m \to m_c^-$ and β being the characteristic scaling exponent. The exponent β, however, is not universal, and depends on the specific details of the network structure [Renault 2014].

The fact that the critical exponent β changes with the network structure, already suggests that the whole $g(m)$ curve might also change. Hence, it is possible to exploit it from an experimental point of view, where the curve $g(m)$ might be much simpler to obtain than the network structure itself. This was already done by J. Soriano and coworkers to observe differences in network structure between pre and postnatal hippocampal cultures, as well as to study the effects of inhibition in the network [Soriano 2008].

5.2 Quorum percolation in metric networks

Within the quorum percolation formalism, we proceed to study the structure of the QP transition using the metric networks we generated in Chapter 2 and compare them with their random graph counterparts. Given that our networks are far from being tree–like, we cannot use any of the approximations shown above, and have to simulate the whole iterative process described in Equation (5.1). Also, to obtain the characteristic curves observed in the experiments [Soriano 2008] we assign an arbitrary threshold R_i to each node, drawn from a Gaussian distribution with mean $\bar{R} = 10$ and standard deviation $\sigma_R = 2.5$. Hence, the initial fraction f is mapped to a new control parameter V, where

$$f(V) = \frac{1}{N} \sum_{i=1}^{N} \Theta(V - R_i), \tag{5.8}$$

where Θ is the Heaviside step function. Within this description, for a given value of V, only the neurons with R_i smaller than V are ignited. This way, the functional form of $\Phi(V)$ when $m \to \infty$ is that of an error function, similar to the experimental one. Also, the control parameter corresponds to the applied voltage in the experiments.

The characteristic curves $\Phi(V)$ for one of the metric networks used in Chapter 2 are shown in Figure 5.2, where we observe the same behavior as in the original QP with random graphs. This is to be expected, given that in [Cohen 2010] they already reported a good match between simulations in finite random graphs and the theory, even though a finite random graph has finite clustering coefficient. Even

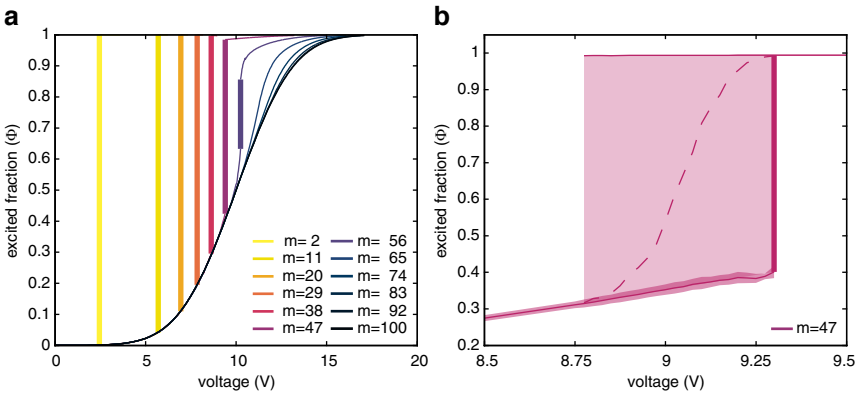

Figure 5.2 | Quorum percolation in metric networks. a, Set of $\Phi(V)$ curves for the QP model run on a network with $\rho = 100\,\text{neurons}/\text{mm}^2$ on a $4\,\text{mm}^2 \times 4\,\text{mm}^2$ area with periodic boundary conditions. Main network observables: $\langle k \rangle = 74$, $\sigma_k = 14$, $\langle CC \rangle = 0.23$. The legend shows the m used for each curve. Giant component g is represented by a thick vertical line (it disappears for $m > 56$). **b,** Zoom in around the transition zone for the $m = 47$ curve. The region of bi–stability is represented by the solid area and the giant component g by the vertical thick line. In this region the two solutions coexist (which correspond to the stable solutions of Equation (5.2)), and the average over many realizations $\langle \phi \rangle$ is shown as a dashed line. The shaded area around the lower branch denotes its standard deviation.

though the metric networks we have used have a much higher clustering coefficient $\langle CC \rangle \approx 0.26$, their in–degree distribution is Gaussian (see Equation (2.23)), and the in–degree distribution is almost all that matters in QP.

The changes in the QP transition are better observed in Figure 5.3, where we compare the QP curves of a metric network and its random graph counterpart (accomplished by randomly shuffling the connections while keeping the same $p(k)$). In Figure 5.3a we see that for very small m, the transition appears for a lower voltage in the random network. For all other values of m, however, the transition fist occurs in the metric network, although the differences between the two are always small. In Figure 5.3b we show the dependence of the giant component g with m, where we observe that both networks have the same m_c. Note that m is an integer by definition, hence we cannot appreciate differences in m_c below the unity (unless we extended the QP formalism to allow $m \in \mathbb{R}$ [Renault 2014]).

In finite systems, it is difficult to obtain an accurate value of m_c and of g when $m \to m_c$, specially if we are interested in a protocol that can be replicated experimentally. By definition g is the relative size of the largest cluster at the end of the bistable region (largest V), and in QP this corresponds to obtaining the largest k–shell. To obtain the k–shell, we need the adjacency matrix, and this information is inaccessible in an experimental setup. However, we can approximate the size of g with different realizations of the initial fraction. In the bistable region, each realization of V will trigger the formation of the infinite cluster with a given

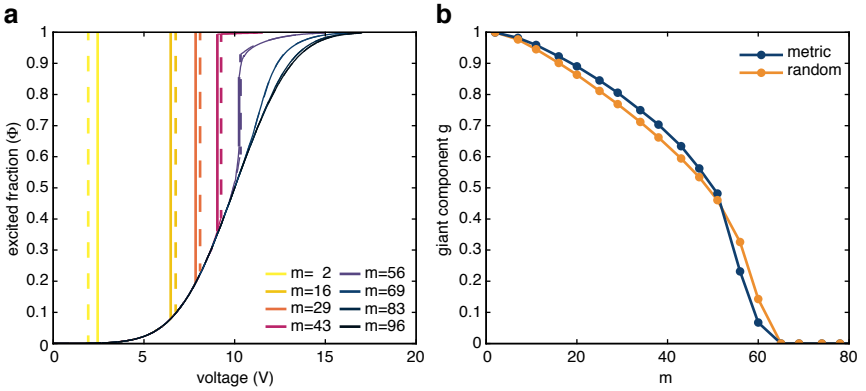

Figure 5.3 | Differences in QP between metric and random networks. a, Set of $\Phi(V)$ curves for metric networks (solid lines) and their random graph equivalents (dashed lines) for the same network used in Figure 5.2. Note that for $m = 2$ the transition on the random graph occurs at a lower voltage, whereas for higher values of m the order is inverted. **b,** Size of the observed giant component $g(m)$ for the same network. The critical point m_c, is the same for both the metric and the randomized network, however, the shape of the curve differs.

probability. However, sometimes it might not. Indeed, in the bistable region we observe a bimodal distribution of excited fractions Φ for each V, and its difference corresponds to g, as we have seen in Figure 5.3b. This definition, however, becomes problematic when we are close to m_c, given that g is extremely small. For small g, the bimodal distribution of Φ can not be observed, since the distributions around each 'mode' overlap.

To overcome this effect, and to have a systematic calculation of g we proceed as follows. We first compute the system response for $m \to \infty$, and obtain the curve for the excited fraction as well as its variance $\sigma_\Phi(\infty, V)$ for each value of the external stimulation. Then, for each of the $\Phi(m,V)$ curves we also compute its variance $\sigma_\Phi(m,V)$, and define the transition region where $\sigma_\Phi(m,V) \geq 2.5\sigma_\Phi(\infty,V)$, i.e., when the standard deviation of the excited fraction is much larger than the corresponding standard deviation of the disconnected network. Indeed, what we observe is that in the region where the infinite cluster appears, the variance of the excited fraction increases substantially. Within the transition region, we try to separate the different realizations of Φ in two groups with a k–means clustering algorithm [Lloyd 1982]. If there is no significant overlap between the two groups, i.e., $|\mu_1 - \mu_2| \geq 3\sqrt{\sigma_1^2 + \sigma_2^2}$, where μ and σ are the mean and standard deviation of each cluster respectively, we consider that a finite g exists.

The characterization of the giant component g for different metric networks and their randomized counterparts is shown in Figure 5.4. In Figure 5.4a we show the $g(m)$ curves for five different densities. We observed systematic differences between the metric and the randomized networks in every case, specially when the

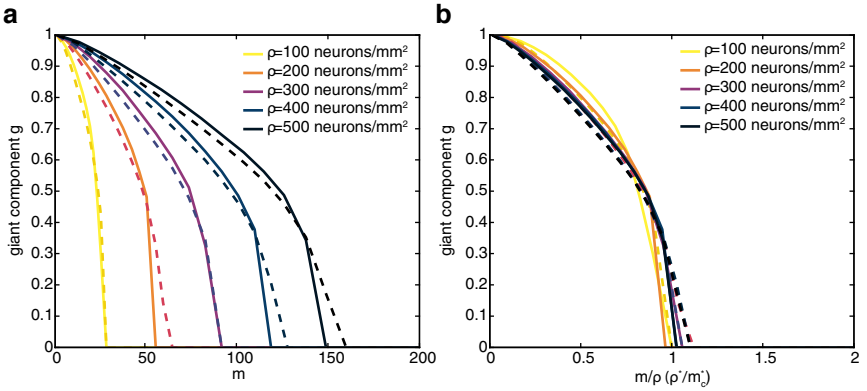

Figure 5.4 | Giant component in metric networks. a, Sizes of the giant component $g(m)$ for five different densities in metric networks (solid lines) and their randomized counterpart (dashed lines). **b,** Collapse of the $g(m)$ curves when m is rescaled by $m/\rho(\rho^*/m_c^*)$, where ρ is the density, and ρ^* and m_c^* the density and m_c for $\rho = 100\,\text{neurons}/\text{mm}^2$ respectively.

giant component is large. It appears that for the same m the giant component in the metric network is systematically bigger. m_c, however, appears to be larger for the random network in most cases. In Figure 5.4b we show the collapse of the same g curves when we rescale m by $m/\rho(\rho^*/m_c^*)$, where ρ is the density, and ρ^* and m_c^* the density and m_c for $\rho = 100\,\text{neurons}/\text{mm}^2$ respectively. For large densities there is a reasonable data collapse (one for the metric networks and another for the randomized versions), and the differences in the $g(m)$ are consistent.

The QP formalism makes several assumptions on the underlying system, namely that the networks are tree–like, and that each neuron stays 'always on' for the duration of the stimulation. We have already checked the effects of network structure in the previous section, and now we explore the possible effects the real neuronal dynamics might have on the stimulation process. We devise a stimulation protocol, using the neuronal dynamics model presented in Section 2.1.1, where we inject an input current to each neuron of the form

$$I_i(t) = \frac{V}{R_i}\left(\Theta(t-t_f) - 2\Theta(t-(t_f-\frac{1}{2}\Delta)) + \Theta(t-(t_f+\Delta))\right), \tag{5.9}$$

which corresponds to a bipolar pulse at $t = t_f$ with amplitude V/R_i and period Δ, where Θ is the Heaviside step function and R_i the internal resistance of each neuron, which has the same role as the threshold we defined in Section 5.2.

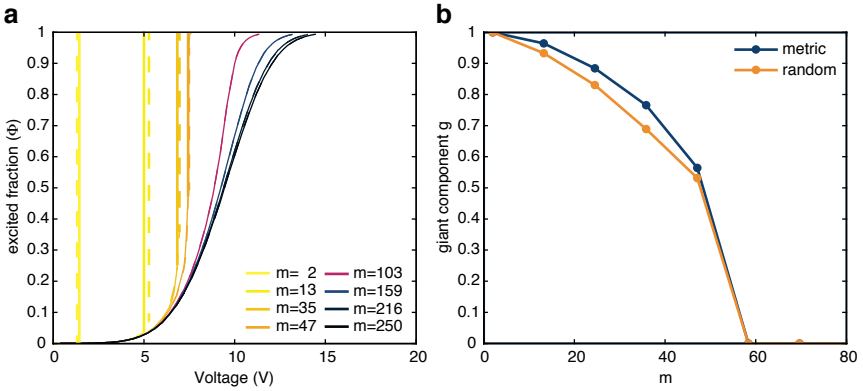

Figure 5.5 | Stimulation protocol with neuronal dynamics. a, Set of $\Phi(V)$ curves for metric networks (solid lines) and their random graph equivalents (dashed lines) for the same network used in Figure 5.2 but simulating the stimulation protocol with the full neuronal dynamics. The differences between the two networks appear to be smaller than in the QP model. **b,** Size of the observed giant component $g(m)$ for the same network. The critical point m_c, is the same for both the metric and the randomized network, however, the shape of the curve differs.

5.3 Stochastic modeling of subquorum percolation

We now introduce a generalization of quorum percolation, called stochastic quorum percolation (SQP), that takes into account some of the underlying dynamics and is capable of explaining both a protocol of external stimulation as well as spontaneous activity.

In the original QP a neuron either fires when it receives m inputs or it does not, however, real neurons are driven by noise, and always have a finite probability of firing. For simplicity, we assume that the internal noise of the neuron is characterized by a Poisson process with a given rate λ (a shot noise). This noise model is inspired on minis (spontaneous miniature post synaptic currents), which in dense cultures have the same strength as evoked currents. Hence, each time a mini arrives is equivalent to receiving one input. Within this description, the probability that a neuron fires spontaneously within a time Δt is

$$p_0 = e^{-\lambda \Delta t} \sum_{i=m}^{\infty} \frac{(\lambda \Delta t)^i}{i!} = \mathscr{P}(m, \lambda \Delta t), \tag{5.10}$$

where $\mathscr{P}$ is the regularized gamma function, and we chose Δt as the characteristic integration time of synaptic currents $\Delta t \approx 20ms$. Hence, the spontaneous firing frequency of a neuron is $\omega_0 \approx p_0/\Delta t$. Within this model, the neuron spontaneously fires when it receives the required m inputs from a Poisson process with rate λ within Δt. Hence, we easily generalize to the case where the neuron is receiving

external inputs from other neurons, which is equivalent to lowering the requirement to fire from m to $m-k$, where k is the number of external inputs the neuron receives within Δt, i.e.,

$$p_k = \mathscr{P}(m-k, \lambda\Delta t), \tag{5.11}$$

and in the limit of large m and low noise $\lambda\Delta t \ll 1$, we recover the QP model $p_k = \Theta(m-k)$. To simulate the dynamics of the system no extra ingredient is required.

With this model we can study the same type of transition as in the QP model, where now p_0 plays the role of the initial fraction f, and instead of an iterative process we now have a Markov process (memoryless) that models the dynamics with discrete time, where each neuron can fire with probability p_k at every step. Instead of characterizing the response of the system to an initial perturbation f, in the SQP model we analyze the steady state of the system. Note that if the system undergoes the equivalent of the first–order QP transition, activity becomes self–sustained and a k–shell $(k > m)$ forms, i.e., a subgroup of active neurons that share k inputs between them. This model has only two parameters (for a given network), the required number of inputs to fire m and $x = \lambda\Delta t$, a dimensionless parameter denoting the noise strength.

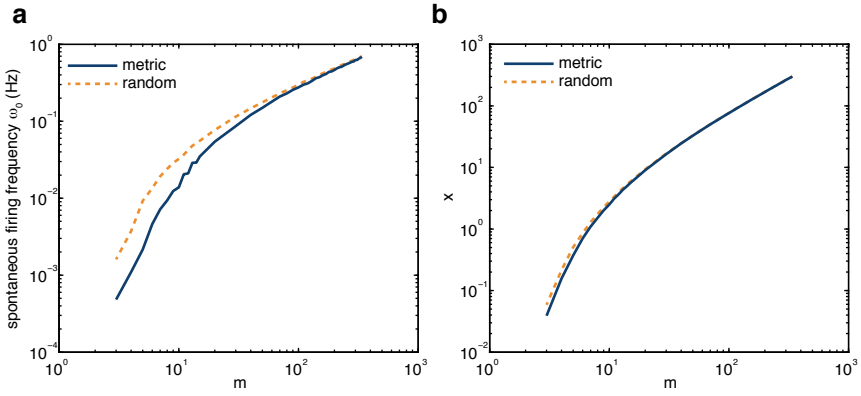

Figure 5.6 | Subquorum percolation transition. a, Characterization of the SQP transition for one of the networks used in Figure 5.4 ($\rho = 500\,\text{neurons}/\text{mm}^2$) and its randomized counterpart. The differences between the transition due to the network structure are maximal for low m. **b,** Same characterization as in Figure 5.6a, but using the 'raw' noise strength x instead.

In Figure 5.6 we characterize the SQP transition by checking, for a given m, the lowest level of noise required for the system to percolate in finite time[4], for both

[4] In infinite time there will always be a non–zero probability of the system to spontaneously percolate, however, we define an upper–bound to the percolation time of 5000 s.

metric networks and their randomized counterpart. Given that $\omega_0 = \mathscr{P}(m,x)$, we can characterize the transition with either ω_0 (Figure 5.6a) or x (Figure 5.6b). We observe that the differences in the percolation point due to the network structure are always small in x, and become almost non–existent for large m. When we look at ω_0, however, given its non–linear dependence on x, the differences are much greater. Indeed, for small values of m the difference in ω_0 might be up to half an order of magnitude.

Given that this is a dynamical model, we can also compute the characteristic time it takes for the system to percolate, called the *ignition time* (IT), which, when coupled with the characteristic time of synaptic depression, is the equivalent to the IBI in a neuronal culture. This dependence is shown in Figure 5.7a, where we compare the IT distribution for $m = 15$ between a metric network and its randomized counterpart. Note that the profiles between the two are completely different, even though they both converge to the same value for large noise. This effect clearly indicates that the differences in the network topology are greatly amplified (close to the transition point) when we take into account the underlying dynamics, something that cannot be observed in analyses that do not take into account the dynamics. For a given noise, the differences in the average IT might be orders of magnitude depending on the network topology. In Figure 5.7b we also show the characteristic distribution of ITs in the metric network. Its profile is consistent with the characteristic exponential decay of a nearly Poissonian process with a constant time rate. It differs from the characteristic profile observed in real networks because there is no recovery variable (STD) in this model (see Section 2.2.1). It is this recovery component which dominates the IBI time scale, typically much larger than the IT.

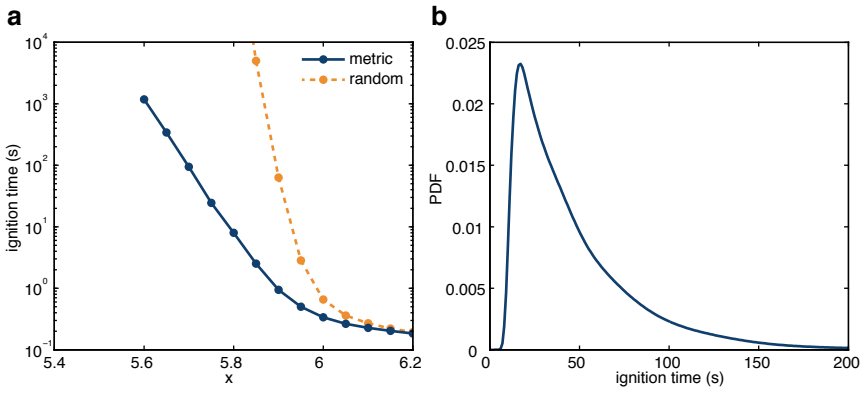

Figure 5.7 | Characterization of ITs in SQP. a, Average ignition time (IT) for the SQP model in the same metric networks used in Figure 5.6 at $m = 15$. Note that the dependence of the IBI on x is extremely different between the two networks. **b,** Distribution of ITs in the metric network for $x = 5.9$.

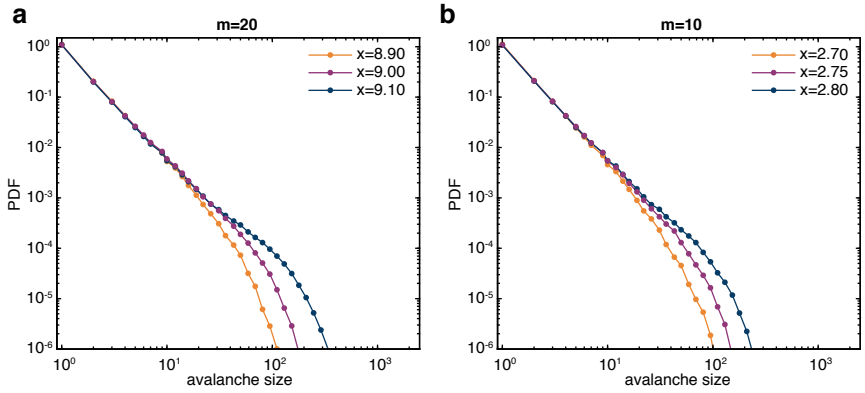

Figure 5.8 | Avalanche dynamics. a, Distribution of avalanche sizes in the SQP model for $m = 20$, using the same metric network as in Figure 5.5. The three curves are chosen to show the transition from sub to supercritical. **b,** Same as Figure 5.8a but using $m = 10$. The characteristic slope on the first decade is the same for both values of m and its exponent is $\sim 2.2 \pm 0.1$.

Within the SQP model we can also study the dynamic structure, which is also characterized by activity avalanches, as in the full model (see Section 2.4). However, there is an important difference. In the full model, the background avalanches structure was evolving in time due to the recovery from synaptic depression. In this model, the distribution of avalanches is fixed and we can study its profile for different values of x. The distribution of avalanche sizes is shown in Figure 5.8, and we observe that the distribution approaches a power–law for a given x with an exponent of $\sim 2.2 \pm 0.1$ (see Figure 5.8), similar to the one observed in the full dynamics in Chapter 2. For smaller x the distribution decays faster, whereas for higher x the distribution shows a characteristic 'bump' for large avalanche sizes. The structure of these avalanches resembles the characteristic behavior of a second order phase transition, with the avalanche distribution being either sub, critical or supercritical.

Note that for the avalanche distributions shown in Figure 5.8 we have discarded the percolation events, which would correspond to an avalanche with size bigger than the system size. These percolation events start to appear near the critical 'x', but they usually happen before. It is as if both types of transitions coexist, a discontinuous one, equivalent to QP, and a continuous one, equivalent to classical percolation transition. Note that in QP a continuous transition also exists, but only at m_c. In the SQP model it exists at any m. An in–depth study of these questions is deferred to future work.

5.4 Conclusions

In this chapter, we have explored the collective behavior of neuronal cultures within the framework of quorum percolation, with the goal of uncoupling the effects of the network structure from the dynamics. We have observed that differences in network topology play little role in the characteristic transition of quorum percolation. However, these differences can be measured and observed. In particular, the shape of the curve of the giant component $g(m)$ can be used to distinguish between different topologies.

We have also generalized the simulation framework presented in Chapter 2 to include a stimulation protocol that mimics the QP model and the experimental details. Within this model, the differences on the QP transition due to the network structure appear to be even smaller than in the original QP model, however, differences in the $g(m)$ curve can still be observed.

Finally, we have generalized the QP model into a stochastic, dynamic model, called *stochastic quorum percolation*, which takes into account the effects of the noise as well as the mechanisms of noise amplification shown in Chapter 2. This simple model reproduces most of the observed dynamical features of the original neuron model and shows that noise plays a very important role in the system behavior. This model confirms some of the underlying hypothesis developed in Chapter 2, showing that small differences in network structure are greatly amplified when noise and the integrate–and–fire dynamics are combined, which cannot be observed as clear within a static description. These effects are inherently dynamic, and thus missed by previous approaches.

6

Network inference

As we have discussed in Section 1.5, network inference is of paramount importance in neuroscience. Neuronal dynamics are fundamentally constrained by the underlying structural network architecture, yet much of the details of this synaptic connectivity are still unknown even in neuronal cultures *in vitro*. Possessing a fully detailed map of the connectome, and knowing the set of rules that govern network connectivity is essential to understanding brain dynamics and behavior. Although the field of network and causal inference has developed greatly in the last century, there are still many challenges to overcome, specially in neuroscience, where data is extremely noisy, and the number of neurons and possible causal relations is vast. The development of new reconstruction techniques and protocols that can be tested on well controlled environments is a major challenge for the field.

For this reason, different studies have focused on *in vitro* neuronal cultures of dissociated neurons [Eckmann 2007, Wheeler 2010]. As we have previously seen, neuronal cultures are highly versatile and easily accessible in the laboratory. Unlike in naturally formed neuronal tissues, the structural connectivity in cultures can be dictated to some extent [Wheeler 2010], and even neuronal dynamical processes can be regulated using pharmacological agents or optical or electrical stimulation. These features have made neuronal cultures particularly attractive for unveiling the processes shaping spontaneous activity, including its initiation [Maeda 1995], synchronization [Eytan 2006] and plasticity [Wagenaar 2006a, Cohen 2008], as well as self-organization [Pasquale 2008] and criticality [Tetzlaff 2010]. Moreover, some studies also showed that spontaneous activity in *in vitro* preparations shares several dynamical traits with the native, naturally formed neuronal tissues [Mazzoni 2007].

Neuronal cultures also provide the most straightforward and natural environment for the development and testing of tools and techniques that identify directed functional interactions between neurons in a complex network. Here we present an approach based on the Generalized Transfer Entropy (GTE) method [Stetter 2012], to the reconstruction of connectivity of simulated neuronal networks of both excitatory and inhibitory neurons.

Inhibition is a major player in regulating neuronal network dynamics, and the regulation of the excitatory-inhibitory balance is crucial for optimal circuit function [Poil 2012, Lombardi 2012]. In the brain, inhibition shapes cortical activity [Isaacson 2011], dominates sensory responses [Haider 2013], and regulates motor behavior [Arber 2012]. Severe behavioral deficits in psychiatric diseases such as autism and schizophrenia have been ascribed to an imbalance of the excitatory and inhibitory circuitry [Yizhar 2011b]. Despite the importance of inhibition, functional connectivity studies often disregard it because of the difficulty in its identification. Hence, unraveling inhibitory connections, and their interplay with the excitatory ones in shaping network dynamics, is of major interest. We show here that the GTE-based approach that was previously used for the inference of excitatory connectivity can be extended with virtually no modifications to networks including as well inhibitory interaction, whose dynamics is once again reproduced by realistic computational models for which the ground-truth connectivity is known. We reveal that the most difficult inference problem is not the identification of a link, be it excitatory or inhibitory, but rather the correct labeling of its type. We show that an elevated accuracy of labeling of both excitatory and inhibitory links can be obtained by combining the analysis of network activity in two conditions, a first one where both excitation and inhibition are active, and a second one where inhibition is pharmacologically removed. We show as well, however, that the inference of link types remain extremely uncertain with current experimental protocols. As a perspective solution, we foresee, based on extensive simulations, that significant improvements in both reconstruction and labeling performance can be achieved by enhancing the spontaneous firing of a culture through a weak external stimulation.

6.1 Introduction to generalized transfer entropy

In a previous work [Stetter 2012], Stetter and coworkers investigated the assessment of excitatory-only structural connectivity from neuronal activity data (with inhibitory synaptic transmission blocked). For this purpose they have developed an extension of transfer entropy (TE), termed Generalized Transfer Entropy (GTE) to test the accuracy of the connectivity reconstruction method by considering realistic computational models that mimics the characteristically bursting dynamics of spontaneously active neuronal cultures. When Comparing diverse reconstruction approaches, GTE performs superiorly, even when systematic artifacts such as light

scattering are explicitly added to the surrogate data. Besides the inclusion of corrections coping with the poor temporal resolution of typical calcium fluorescence recordings, a key ingredient making GTE successful is dynamical state selection, i.e. the restriction of the analysis to a dynamical regime in which functional interactions are largely determined by the underlying hidden structural connectivity. In particular they show that it is necessary to restrict the analysis to inter-burst regimes, while consideration of bursting epochs leads to inference of exceedingly clustered structural topologies [Stetter 2012].

Transfer Entropy (TE) [Schreiber 2000] is an information theoretic measure that quantifies the statistical coherence between different signals evolving in time. It is non–symmetric and is a better predictor than mutual information (MI), since it can filter out information due to a common history and shared inputs. Transfer entropy is equivalent to Granger Causality for Gaussian variables [Barnett 2009], but can instead be used with almost any input signal.

Following [Schreiber 2000], almost any process I can be described by a corresponding Markov process of order k where

$$p(i_{n+i}|i_n^{(k)}) = p(i_{n+i}|i_n^{(k+1)}), \tag{6.1}$$

i.e., the probability to find I in state $p(i_{n+1})$ only depends on its last k-th values, where we have used the shorthand notation $i_n^{(k)} = (i_n, \ldots, i_{n-k+1})$.

We can define the entropy rate of the process I as

$$h_I = -\sum p(i_{n+1}, i_n^{(k)} \log p(i_{n+1}|i_n^{(k)})), \tag{6.2}$$

which measures the average number of bits needed to encode the state $p(i_{n+1})$ if its past is known.

If we generalize to two processes (I,J), we can measure the deviation from the following Markov property

$$p(i_{n+1}|i_n^{(k)}) = p(i_{n+1}|i_n^{(k)}, j_n^{(l)}), \tag{6.3}$$

which will only be valid when the evolution of I does not depend on the past of J, i.e., when there is no information flow from J to I. Transfer Entropy measures the deviation from this assumption by computing the corresponding Kullback entropy

$$T_{J\to I} = \sum p(i_{n+1}, i_n^{(k)}, j_n^{(l)}) \log \frac{p(i_{n+1}|i_n^{(k)}, j_n^{(l)})}{p(i_{n+1}|i_n^{(k)})}. \tag{6.4}$$

We can see that when Equation (6.3) holds, the logarithm in Equation (6.4) is zero, denoting statistical independence between the two processes, i.e., the knowledge of the past values of J has no effect on the predictability of I.

Generalized Transfer Entropy (GTE)[1] [Stetter 2012] is an extension of the original Transfer Entropy formulation, where the signals are also conditioned on the global dynamical state of the system and same–bin interactions are allowed. In the case of fluorescence signals, this state selection is achieved by conditioning the analysis to the regime where the population average of the time series G is lower than a given threshold $\tilde{g}$. Same bin interactions are included due to the limitations of the temporal resolution of calcium imaging. Since time bins are usually $\sim$20 ms, "instantaneous" interactions between different signals need to be considered. GTE can be expressed as

$$\mathrm{GTE}_{J\to I} = \sum P(i_n, i_{n-1}^{(k)}, j_{n-1+S}^{(k)} | g_n < \tilde{g}) \log \frac{P(i_n | i_{n-1}^{(k)}, j_{n-1+S}^{(k)}, g_n < \tilde{g})}{P(i_n | i_{n-1}^{(k)}, g_n < \tilde{g})}. \quad (6.5)$$

where g_n is the average population firing at step n and the shift variable $S \in \{0,1\}$ denotes the aforementioned inclusion of same-bin (instantaneous) interactions for $S = 1$, which is also called the Instantaneous Feedback Term (IFT) correction. Furthermore, the time-series of calcium fluorescence are high-pass filtered by mean of a discrete difference operator, as a straightforward attempt to enhance the visibility of firing events drowned in noise. Note that GTE reduces to conventional Transfer Entropy for $S = 0$ and $\tilde{g} \to \infty$, i.e. when same-bin interactions are excluded and when the selected state encompasses the whole observed dynamics. The Markov order of the underlying process is here somewhat arbitrarily set to $k = 2$, after extensively checking its effect on the reconstructions. $k = 2$ results to be the lowest dimensionality in the probability distribution allowing to separate actual interactions from signal artifacts like light scattering.

Note that for our datasets there is no need to perform any delay embedding of the time-series to reach satisfying performance levels. Methodological developments along the lines of [Wibral 2011, Vicente 2011] would be however desirable for future applications to real experimental data. Also, if we are interested in reconstructing networks from experimental data, where the truth is not known, a method to establish statistical significance based on the bootstrapping of the original data, is also required.

6.2 Theoretical and computational description

The networks and neuron models used in this chapter differ from those used in Chapter 2 and we include their description here for completeness. The main reason for these differences is due to trying to decouple the reconstruction methods from specific dynamical models. Even though the model presented in Chapter 2

[1] Code for the Generalized Transfer Entropy method is publicly available at https://github.com/olavolav/TE-Causality.

accurately predicts most of the dynamical observables of neuronal cultures, for the task of network inference, we are interested in methods that are independent of the underlying dynamics. Hence the use of a different model. The methods presented here also describe the dynamics of neuronal cultures however, there are some key differences. The model presented here does not predict the onset of bursting dynamics and wave nucleation (the networks are essentially random) and the neuronal dynamics are as simple as possible (linear integrate–and–fire with short–term synaptic depression).

Although the use of a random network might seem questionable, here we are dealing with the dynamics of a small population (from 100 to 1000 neurons). For such a small population, the network can indeed be approximated by a random graph, since this corresponds to a region with a size of the order of a nucleation site (see Chapter 2).

6.2.1 Network generation

We randomly distribute $N = 100$ neurons over a square area of 1 mm^2. Neurons are labeled as either excitatory with probability $p_E = 0.8$ or inhibitory with $p_I = 0.2$. A directed connection (link) is created between any pair of neurons with fixed probability $p = 0.12$, giving rise to a directed Erdős-Rényi network[Albert 2002]. The resulting network is defined by the adjacency matrix A, whose entries $a_{ji} = 1$ denote a connection from neuron j to neuron i ($j \to i$). The average full clustering coefficient of the network [Fagiolo 2007] is given by

$$\mathrm{CC} = \left\langle \frac{\left(A + A^{\mathrm{T}}\right)^3_{ii}}{2T_i} \right\rangle_i , \tag{6.6}$$

where A^{T} is the transpose of A and $\langle\rangle_i$ denotes average over index i. T_i is defined as

$$T_i = d_i^t \left(d_i^t - 1\right) - 2d_i^{\leftrightarrow}, \tag{6.7}$$

where d_i^t is the total degree of node i (the sum of its in– and out–degree) and $d_i^{\leftrightarrow}$ is the number of bidirectional links of node i. The clustering coefficient of the network after its construction is ~ 0.12, a value that is then raised up to a target one of 0.5 by following the Bansal *et al.* construction [Bansal 2009]: Two existing links a_{ij} and a_{kl} are first chosen at random, with $i \neq j \neq k \neq l$. These links are then replaced by a_{il} and a_{kj}, given that they do not already exist. This step is repeated until the desired clustering coefficient is finally reached within a tolerance of 0.1%.

This above-chance clustering level is generated to account for experimental observations of clustered connections in neuronal local circuits [Perin 2011]. We do not

perform here a systematic study of the impact of CC on reconstruction performance, which was already performed in [Stetter 2012].

6.2.2 Network dynamics

Neurons in the simulated culture are modeled by simple integrate-and-fire units, of the form

$$\tau_m \frac{dV_i}{dt} = -(V_i - V_r) + \frac{1}{g_l}\left(I_i^A + I_i^G + \eta\right), \tag{6.8}$$

where V_i is i-th neuron's membrane potential and $V_r = -70$mV its resting value, $\tau_m = 20$ms is the membrane time constant, $g_l = 50$pS is the leak conductance, I^A and I^G the excitatory (AMPA) and inhibitory ($GABA_A$) input currents respectively, and η a noise term. When the membrane potential reaches the threshold value $V_t = -50$mV the neuron fires and its membrane potential is reset to a value $V_r = -70$mV, which is maintained for a refractory time $\tau_r = 2$ms during which the neuron is prevented from firing.

Neurotransmitters are released as a response to a presynaptic action potential fired at time t_k, binding to the corresponding receptors at the postsynaptic side of its output neurons. The binding of neurotransmitters at the receptors triggers the generation of postsynaptic currents I^A or I^G, depending on the presynaptic neuronal type. The total input current received by a given neuron is described by

$$I_i^x(t) = g^x \sum_{j=1}^{N} \sum_{t_j^k} A_{ij} E_j^x(t) \alpha(t - t_j^k - t_d^x), \tag{6.9}$$

where t_d^x is a transmission delay (mimicking axonal conduction), with $t_d^A = 1.5$ms and $t_d^G = 4.5$ms. g^x is the synaptic strength, which is adjusted to obtain the desired bursting rate. The value of $g^A = 7.75$pA in a network with inhibition silenced provided a bursting rate of $\sim$0.1 Hz. When inhibition is active, a comparable bursting rate of of $\sim$0.12 Hz is obtained by setting $g^G = -2g^A$. $E_j^x(t)$ is a term accounting for short–term synaptic depression, and $\alpha(t)$ is an alpha shaped function of the form

$$\alpha(t) = \exp\left(1 - t/\tau_s\right) \frac{t}{\tau_s} \Theta(t), \tag{6.10}$$

where $\tau_s = 2$ms represents the synaptic rise time and $\Theta(t)$ is the Heaviside step function.

Short–term synaptic depression accounts for the depletion of available neurotransmitters at the presynaptic terminals due to repeated activity [Zucker 2002]. The

neurotransmitters dynamics at the synapses of neuron i is described by the set of equations [Tsodyks 1997]:

$$\begin{aligned}\frac{dR_i^x}{dt} &= \frac{1-R_i^x-E_i^x}{\tau_r^x} - U\sum_{t_k} R_i^x(t_i^k)\,\delta(t-t_i^k),\\ \frac{dE_i^x}{dt} &= -\frac{E_i^x}{\tau_i} + U\sum_{t_k} R_i^x(t_i^k)\,\delta(t-t_i^k),\end{aligned} \tag{6.11}$$

where R_i^x and E_i^x are the fraction of available neurotransmitters in the recovered and active states, respectively. τ_r^x is the characteristic recovery time with $\tau^A =_r 5000$ ms and $\tau_r^G = 100$ ms. $\tau_i = 3$ ms is the inactivation time and $U = 0.3$ describes the fraction of activated synaptic resources after an action potential.

6.2.3 Simulating calcium fluorescence signals

Based on the simulated spike data, synthetic calcium fluorescence signals are generated according to a model that incorporates the calcium dynamics in the neurons and experimental artifacts. The former describes the saturating nature of calcium concentration bound to the calcium dye inside the cells, while the latter treats the noise of the recording camera as well as light scattering due to anisotropies in the recording medium [Stetter 2012].

Each action potential of a neuron i at time t leads to the intake of $n_{i,t}$ calcium ions through the cell membrane, raising the calcium concentration inside the cell. A fraction $[Ca^{2+}]_{i,t}$ of the Calcium ions bind the fluorescence dye by a fixed amount $A_{\mathrm{Ca}} = 50\mu$M, and are slowly freed with a time scale $\tau_{\mathrm{Ca}} = 1$s. This process is described by the equation

$$[Ca^{2+}]_{i,t} - [Ca^{2+}]_{i,t-1} = -\frac{\tau_{\mathrm{image}}}{\tau_{\mathrm{Ca}}}[Ca^{2+}]_{i,t-1} + A_{\mathrm{Ca}}\, n_{i,t}, \tag{6.12}$$

where τ_{image} is the simulated image acquisition frame rate.

The level of calcium fluorescence $F_{i,t}^0$ emitted by a cell is modeled by a Hill function of the bound calcium concentration (with saturation level $K_d = 300\mu$M) together with an additive Gaussian noise term $\eta_{i,t}$ characterized with a standard deviation $\sigma_{\mathrm{noise}} = 0.03$ [Mishchenko 2011b], i.e.

$$F_{i,t}^0 = \frac{[Ca^{2+}]_{i,t}}{[Ca^{2+}]_{i,t} + K_d} + \eta_{i,t}. \tag{6.13}$$

The level of fluorescence recorded by the camera at a given neuron is *not* independent of neighboring cells due to the introduction of simulated light scattering. We incorporate this artifact by adding to the monitored cell a fraction $A_{\mathrm{sc}} = 0.15$ of the

fluorescence from neighboring cells, which is weighted according to their mutual distance d_{ij} by a Gaussian kernel of width $\lambda_{sc} = 0.05$mm. The total fluorescence captured in a neuron was then given by:

$$F_{i,t} = F^0_{i,t} + A_{sc} \sum_{j=1, j\neq i}^{N} F^0_{j,t} \exp\left\{ -\left(d_{ij}/\lambda_{sc}\right)^2 \right\}. \tag{6.14}$$

6.2.4 Optimal binning

The probability distributions in GTE as defined in Equation (6.5) are estimated based on discretized values of the temporal difference signal of the observed fluorescence. To cope with potential under–sampling artifacts —since the probability distributions to estimate have an elevated dimensionality, as large as $2k+1$— we symbolize the signals into a binary sequence by applying a sharp threshold. The optimal threshold value $\hat{x}$ for this conversion is obtained from the following analysis.

We first ignore the exponential decay of the fluorescence signal since it has a small influence on discretely differentiated signals, and assume a sufficiently low firing rate so that the occurrence of more than one spike per frame of a given neuron is negligible. Under these simplification hypotheses, the probability distribution of the signal can be cast as a combination of Gaussian functions, with mean values given by the offset associated to the number of action potentials encountered in the current time bin. Additionally, to preserve information about spiking events when projecting the time-series into a binary representation, we compute the optimal mapping by determining the probability P that the mapping is correct at any given time step (provided the parameters of the model ϑ and a threshold value x), i.e.,

$$P(\text{correct mapping} \,|\, \vartheta) = P(x_t \geq x, s_t = 1 |\, \vartheta) + P(x_t < x, s_t = 0 |\, \vartheta),$$

where $s_t \in \{0,1\}$ denotes the occurrence of a firing event at time frame t, and ϑ refers to unspecified but frozen parameters of the analyzed system, which have a potential influence on the estimated probability. In particular, the probability that a neuron fires at a given image frame is a function of the firing rate and the length of the image frame, $p_{sp} = f_{sp}\, \tau_{image}$. For a normally distributed camera noise with standard deviation σ_{noise} and an expected variation Δx in fluorescence due to a single spike, a straightforward solution for the optimal separation value $\hat{x}$ that yields the maximum of the correct mapping probability can be derived,

$$\hat{x} = \frac{1}{2}\Delta x + \frac{\sigma^2_{noise}}{\Delta x} \log\left(\frac{1-p_{sp}}{p_{sp}}\right). \tag{6.15}$$

GTE scores are robust against the selection of a separation value above the optimal $\hat{x}$. Indeed, for $x > \hat{x}$ the total number of samples above the separating value is reduced,

but the fraction of samples that correspond to real spikes is actually increased. The resulting network reconstructions do not show any notable decrease of quality for values of x up to a 30% above the optimal value.

This optimal binning procedure is a fast and straightforward way to do spike inference. More advanced methods of spike inference exist, and might also be used if additional information about the system is known, e.g., [Vogelstein 2009, Mishchenko 2011b].

6.2.5 Network reconstruction

In order to reconstruct a whole network, GTE is computed for each directed pair of neurons i, j from Equation (6.5), resulting in a matrix M of directed causal influences where $M_{ji} = GTE_{J\to I}$. A new binary matrix $T(z)$ is created from the GTE scores, where $T_{ji} = 1$ if M_{ji} is amongst the fraction z of links with the highest GTE score (thresholding).

The quality of the reconstruction is quantified through a Receiver Operating Characteristic (ROC) analysis. The ROC is a parametric curve that establishes a relationship between the true and the false positive links found in $T(x)$ for the different thresholded levels. If A denotes the binary connectivity matrix of the real network, then the true positive ratio (TPR) is defined as the number of links in T that are present in A respect to the total number of existing links. The false positive ratio (FPR) is the fraction of links in T that do not match original links, i.e.,

$$\mathrm{TPR}(z) = \sum_{\forall i,j} T_{ji}(z) A_{ji} \Big/ \sum_{\forall i,j} A_{ji}, \tag{6.16}$$

$$\mathrm{FPR}(z) = \sum_{\substack{\forall i,j \\ i\neq j}} T_{ji}(z) \hat{A}_{ji} \Big/ \sum_{\substack{\forall i,j \\ i\neq j}} \hat{A}_{ji}, \tag{6.17}$$

where $\hat{A}$ is the negation of the binary connectivity matrix A ($0 \leftrightarrow 1$). Thus $\mathrm{TPR}(z)$ and $\mathrm{FPR}(z)$ constitute, respectively, finite-size estimates of the probabilities $P(\text{reconstruction} = 1 | \text{true} = 1, z)$ and $P(\text{reconstruction} = 1 | \text{true} = 0, z)$, for any given link across the network. Confidence intervals for ROC curves are estimated based on 5 different network realizations.

6.3 Dynamics of biological and simulated networks

Dissociated neurons grown *in vitro* self-organize and connect to one another, giving rise to a spontaneously active neuronal network within a week (see Figure 6.1a) [Eckmann 2007, Soriano 2008, Chiappalone 2006, Cohen 2008]. About 70–80% of the grown connections are excitatory, while the remaining 20–30% are inhibitory [Soriano 2008]. Activity in neuronal cultures is characterized by a bursting dynamics, where the whole network is active and displays quasi-synchronous, high frequency firing within 100–200 ms windows [Cohen 2008]. The timing of the bursts themselves is irregular, with average inter-burst intervals on the order of 10 s in a typical preparation. Between different bursts, firing across the network has a low-frequency and can be described as asynchronous.

Neuronal dynamics in cultures may be monitored using calcium fluorescence imaging [Eckmann 2007, Grienberger 2012], which enables the recording of the activity of thousands of individual neurons simultaneously. Figure 6.1a shows example traces illustrating the characteristic fluorescence signal of individual neurons *in vitro*. The fluorescence signal is characterized by a fast onset as a result of neuronal activation and the binding of Ca^{2+} ions to the fluorescence probe, followed by a slow decay back to the baseline due to the slow unbinding rate. This behavior is apparent in the population average of the signal, as shown in Figure 6.1b, where bursts are clearly identified by the fast rise of the fluorescence signal.

To appraise the role of inhibition on dynamics, we monitor neuronal network activity in two different conditions: A first one, with only excitatory connections active, where inhibitory connections have been completely blocked (denoted as "E–only" networks); and a second one, where both excitatory and inhibitory connections are functionally active (herein after denoted as "E+I" networks). In experiments, inhibitory synapses are silenced through the application of saturating levels of bicuculline, a $GABA_A$ receptor antagonist (see Methods). An example trace of the population average signal of such an excitatory-only system is shown in the top left panel of Figure 6.1b, whereas the dynamic behavior in presence of inhibition is shown in the bottom left panel of Figure 6.1b. In the "E–only" condition, bursts are more pronounced and more regular in amplitude than in the "E+I" condition, an effect also seen in other studies [Cohen 2008, Jacobi 2009, Tibau 2013].

These recordings in neuronal cultures provide a comparison reference for our simulated networks of model neurons. We build a computational model of a culture whose dynamics capture its major qualitative features. These include a high variability in the inter-burst intervals, a low ~ 0.1 Hz inter-burst firing rate, and, in presence of inhibition, an increase in bursting frequency as well as a general decay in the amplitudes of the fluorescence signal, paired by an increase in their heterogeneity. More specifically, we consider networks with $N = 100$ leaky integrate-and-fire nodes with depressive synapses in combination with a model for the calcium fluorescence. Network connectivity is random and sparse, with links rewired in order to reach an above-chance level of clustering. Each node receives inputs from its

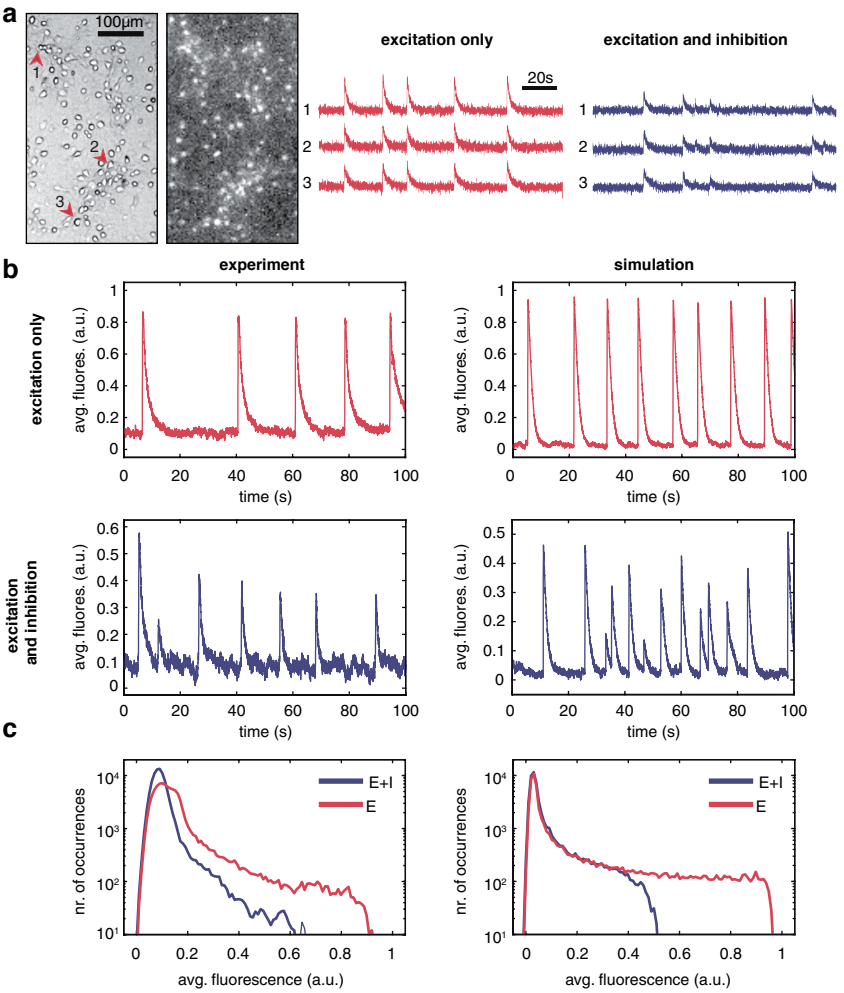

Figure 6.1 | Neuronal network dynamics. a, Top: Bright field and fluorescence images of a small region of a neuronal culture at day *in vitro* 12. Bright spots correspond to firing neurons. Bottom: Representative time traces of recorded fluorescence signals of 3 individual neurons. The numbers beside each trace identify the neurons on the images. Data shows, for the same neurons, the signal in recordings with only excitation active ("E") and the signal with both excitation and inhibition active ("E+I"). **b,** Population-averaged fluorescence signals in experiments (left) and simulations (right), illustrating the semi-quantitative matching between *in vitro* and *in silico* data. Top: excitatory-only traces ("E–only" data). For the experiments, inhibition was silenced through application of saturating concentrations of bicuculline. For the simulations, inhibitory synapses were silenced by setting their efficacy to zero. Bottom: traces for both excitation and inhibition active ("E+I" data). Network bursts appear as a fast increase of the fluorescence signal followed by a slow decay. Bursts are more frequent and display lower and more heterogeneous amplitudes in the presence of inhibitory connections. **c,** Histogram of population-averaged fluorescence intensity for a 1 h recordings in experiments (left) and simulations (right). Data is shown in semilogarithmic scale for clarity. Red curves correspond to the "E–only" condition, and the blue curves to the "E+I" one.

pre-synaptic neighbors as well as from independent external sources to mimic spontaneous single neuron activity due to noise fluctuations in the ionic current through its membrane. Free model parameters, such as the homogeneous conductance weights of recurrent connections, were calibrated such as to yield dynamics comparable to the biological recordings, with a bursting rate of 0.1Hz and realistic decay time constants of the calcium fluorescence (see the bottom right panels of Figure 6.1b). The blocking of inhibitory connections (top right panel of Figure 6.1b) is simulated by setting the synaptic weight of all inhibitory connections to zero (note, therefore, that the firing itself of inhibitory neurons is not suppressed, but just its postsynaptic effects).

As discussed more in depth in [Stetter 2012], a hallmark of bursting dynamics is the right-skewed histogram of the population average of the calcium fluorescence signal (see Figure 6.1c). Low fluorescence amplitudes are associated to the non-bursting regime, which is noise dominated, and the right tail of the distribution reflects bursting events. The range spanned by this right tail is distinctly shortened in presence of inhibition. This difference in the large fluorescence amplitude distribution can be ascribed to the dynamics at the synapse level: For purely excitatory networks, the neurotransmitters resources of a given synapse are depleted during a bursting event [Cohen 2011]. Neurons experience high frequency discharge, but require a longer time to recover, giving rise to long inter-burst intervals. Inhibition lowers this release of neurotransmitters by suppressing neuronal firing before complete depletion, therefore providing a faster recovery, shorter inter-burst periods and lower firing activity inside the bursts.

6.4 Connectivity reconstruction from directed functional links

Based on simulations of the calcium dynamics in the network, a network of (directed) functional connectivity is reconstructed by computing the Generalized Transfer Entropy (GTE) for each (directed) pair of links. GTE is an extension of Transfer Entropy, a measure that quantifies predictive information flow between stationary systems evolving in time [Schreiber 2000]. As an information theoretical implementation of the Granger Causality concept [Granger 1969], a positive TE score assigned to a directed link from a neuron i to a neuron j indicates that the future fluorescence of j can be better predicted when considering as well the past fluorescence of i in addition to the past of j itself.

6.4.1 Conditioning as state selection

A central observation that motivated the definition of GTE was the existence of different dynamical states in the switching behavior from asynchronous firing to synchronous bursting activity. The distribution of fluorescence amplitudes (see Figure 6.1c) provides a visual guide to the relative weight of the single activity events and the bursting episodes. A functional reconstruction in this bursting regime shows a very clustered connectivity due to the tightly synchronized firing of large communities of neurons. We can understand intuitively this finding, by considering that, in the bursting regime, the network is over-excitable and the firing of a single neuron can trigger the firing of a large number of other neurons not necessarily linked to it by a direct synaptic link. On the other hand, the neuronal activity in the non-bursting regime is sparse and dominated by pairwise interactions, and thus, a reconstruction in this regime identifies directed functional interactions that more closely match the structural connectivity, i.e., high GTE might signal direct pre- to post-synaptic coupling in this regime, as previously discussed thoroughly for "E–only" networks [Stetter 2012].

A rough segmentation of the population signal into time sequences of bursting and non-bursting events is simply achieved by defining a fixed *conditioning level* on the population average fluorescence. This simple modification with respect to the original TE formulation, makes GTE suitable for an analysis of functional interactions which distinguish different dynamical regimes, as illustrated for purely excitatory networks in the left panel of Figure 6.2a. The network is indeed considered to be in a bursting regime when the network-averaged fluorescence exceeds the chosen conditioning level (dotted line in Figure 6.2a), and in an inter-burst regime otherwise. The value of the conditioning level itself is obtained through the analysis of the fluorescence signal histogram and set close to the transition from the Gaussian-like profile shown for low fluorescence values to the long tail characteristic of the population bursts.

Note that, while our approach works by restricting the analysis to epochs of inter-burst activity only, other complementary methods exploit detailed information about typical burst build-up sequences in order to infer structure, with potentially superior results when the required time resolution is accessible [Pajevic 2009].

6.4.2 Connectivity reconstruction of simulated "E–only" networks

Reconstruction performances from the GTE computation are quantified in the form of *receiver operating characteristic* (ROC) curves (see section 6.2.5). ROC curves show the fraction of true positives, i.e., inferred connections which really exist, as a function of the fraction of false positives, i.e., wrongly inferred connections.

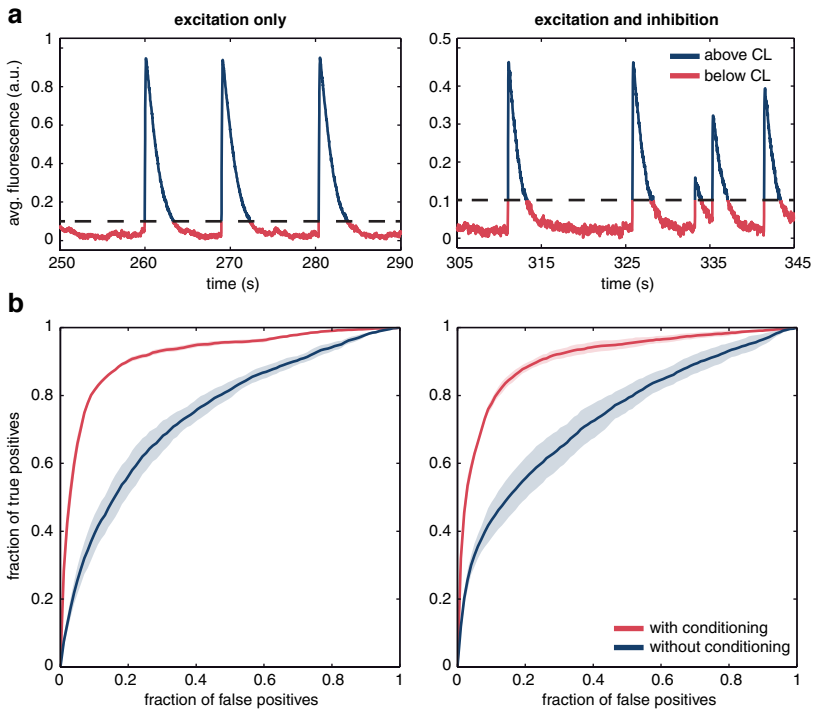

Figure 6.2 | Signal conditioning. a, Separation of the signal in two regimes according to the conditioning level (dotted line), a first one that encompasses the low activity events (red curves), and a second one that includes the bursting regimes only (blue). The same conditioning procedure is applied in both "E–only" networks (left) and in "E+I" ones (right). **b,** *Receiver Operating Characteristic* (ROC) curves quantify the accuracy of reconstruction and its sensitivity on conditioning. Functional networks are generated by including links with a calculated GTE score exceeding an arbitrary threshold. ROC curves plot then the fraction of true and false positives in the functional networks inferred for every possible threshold. For "E–only" networks (left) and "E+I" networks (right), the red curves show the goodness of the reconstruction after applying the conditioning procedure. Blue curves illustrate the reconstruction performance without conditioning. The ROC curves show that the conditioning procedure significantly improves reconstruction performance. ROC curves were averaged over different network realizations (95% confidence intervals shown).

The ROC curves of the reconstruction performance, with and without conditioning, for the case of simulated "E–only" networks are shown in the left panel of Figure 6.2b. Without conditioning (blue ROC curves), the reconstruction quality of excitatory connections — to both excitatory and inhibitory neurons confounded — is significantly better than a random choice (which would correspond to a diagonal line in the ROC curve). The reconstruction is, however, hindered by the fact that the analysis effectively averages over data from multiple dynamical regimes as described above. The reconstruction performance thus significantly increases by

applying a conditioning (red ROC curves) which selects uniquely the inter-burst regime.

It was also shown for simulations comparable to the ones presented here, that the reconstructed networks using GTE are approximately unbiased regarding bulk network properties, such as the mean clustering coefficient, or the average length of connections in the network [Stetter 2012].

6.4.3 Connectivity reconstruction of simulated "E+I" networks

An important aspect of Transfer Entropy, and by extension of GTE, is its model-free nature. Thus, during the process of identifying causal influences between neurons, there is no need to define a generative model for neuronal firing or calcium dynamics, as in the case of Bayesian inference approaches [Mishchenko 2011b]. It follows that we can apply GTE without modifications to the case in which both excitatory and inhibitory links are active, provided that the inter-burst network state can be identified in an analogous way. Indeed we observe that while the presence of inhibition does change the dynamics of the system to some extent, the bursting behavior remains robustly present (see the right panel of Figure 6.2a), allowing the straightforward identification of a performing conditioning level.

Remarkably, the reconstruction performance of "E+I" networks remains at high levels after conditioning, of about 80% true positives at 10% false positives, as shown in the right panel of Figure 6.2b. Thus the model-independence of GTE allows the reconstruction of both excitatory and inhibitory links. As a further self-consistency check, we have simulated the dynamics of a neuronal culture with a topology identical to the inferred one and compared it with the dynamics of the network with the original ground-truth topology. The resulting bursting and firing rates, for both the "E-only" and the "E+I" cases, are not statistically significantly different from the case of perfect reconstruction, while they markedly differ from the case of a randomized topology (not shown). Nevertheless, given the phenomenon of structural degeneracy, a large number of even very different structural circuits could give rise to equivalent dynamical regimes [Stetter 2012]. Therefore, passing this self-consistency check is not a sufficient condition to prove high reconstruction quality, though it is a necessary one.

Note, finally, that we have disregarded, until now, the identification of the specific type, i.e. excitatory or inhibitory, of each link, focusing uniquely on whether a link is present or absent in the ground-truth structural network, whatever is its nature. As previously mentioned, correctly labeling a link turns out to be a more elaborated task than just inferring its existence.

6.5 Differentiation of excitatory and inhibitory connections

GTE probes the existence of unspecified influences between signals, but cannot identify the type of occurring interaction *a priori*. Its versatility also means that very different types of interactions can give the same GTE score if their influence in terms of predictability is the same. Hence, to separate between excitatory and inhibitory connections we have to either introduce *ad hoc* information on neuronal types or combine different reconstructions together to single out the different connectivity types.

Such *ad hoc* information might come from dye impregnation, fluorescence labeling or immunostaining [Lichtman 2008]. These techniques identify cell bodies and processes according to some specific traits, for instance membrane proteins or neurotransmitters' receptors. According to Dale's principle [Kandel 1967], a neuron shows the same distribution of neurotransmitters along its presynaptic terminals. Hence, if a neuron is labeled as either excitatory or inhibitory, we can assume that all its output connections are of the same matching type. Thus by combining the type of information provided by some extrinsic labeling technique with the unspecific causal information provided by GTE, the overall set of inferred links can be separated into two non–overlapping subsets of excitatory and inhibitory links.

Being able to identify the type of a neuron — even with perfect accuracy — does not guarantee *a priori* that excitatory and inhibitory links can be inferred equally well. On the contrary, different reconstruction performances have to be expected in general, since the interaction mechanism of excitatory links is inherently different from the inhibitory ones, the former promoting the activity of the target neuron, whereas the latter restrain it. We have tested the accuracy of this *ad hoc* approach through numerical simulations. GTE is applied to the "E+I" data, and the reconstruction quality is assessed separately for the connections originating from neurons of different types (see Methods). Non trivially, the results of this analysis indicate that both types of connections are reconstructed with high accuracy (see Figure 6.3a). At a fraction of 10% of false positives, excitatory links are detected at a true positive rate of 80%. Inhibitory links show a lesser but still high detection accuracy, of about 60% of true positives.

6.6 Reconstruction and labeling from spontaneous dynamics

In the absence of information on neuronal types, an alternative approach consists in a direct combination of the reconstructions procured by the "E–only" and "E+I" data on the same neurons. By adding together the GTE scores from the two reconstructions we can assume that the higher scores come from links that show a high score in both reconstructions. This procedure is thus expected to highlight the

pool of excitatory connections, since they are the only ones present in both network conditions. Similarly, we can subtract the "E–only" scores from the "E+I" ones. High scores will then now highlight those links that are present in the "E+I" but not in the "E–only" network, i.e. the pool of inhibitory connections.

The performance of this first two-step reconstruction approach is shown in Figure 6.3b. The reconstruction of excitatory connections has a quality as good as the one obtained with *a priori* knowledge of neuronal type based on extrinsic labeling (see Figure 6.3a). However, the performance markedly deteriorates for the reconstruction of inhibitory links, since only 40% of the inhibitory connections are correctly identified at 10% of false positives.

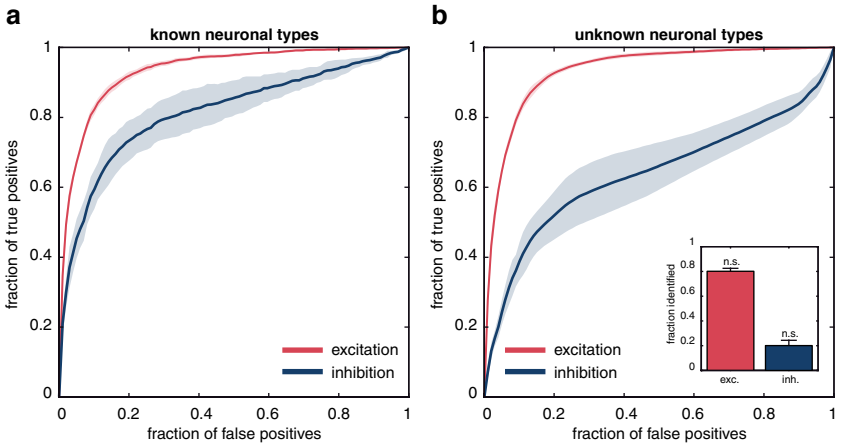

Figure 6.3 | Optimal network reconstruction. a, ROC curves for the reconstruction of a network with both excitatory and inhibitory connections active, supposing to know *a priori* information about neuronal type. GTE is first applied to the "E+I" data. Next, following Dale's principle and exploiting the available information on neuronal type, links are classified according to their excitatory (red) or inhibitory (blue) nature. **b,** ROC curves for the best possible identification of excitatory and inhibitory connections, when information on neuronal type is unaccessible. Excitatory links (red) are identified by adding together the Transfer Entropy scores of simulations run in "E–only" and "E+I" conditions, and later thresholding them. Inhibitory links (blue) are identified by computing the difference in Transfer Entropy scores between the runs with inhibition present and blocked. Inset: fraction of excitatory and inhibitory neurons correctly identified from these ROC curves. Results were not significantly different from random guess (see Methods). All the results were averaged over different network realizations. The shaded areas in the main plots, as well as the error bars in the inset, correspond to 95% confidence intervals.

Note that an additional complication arises with the described two-steps pipeline. A given link might be attributed a combined score above the inclusion threshold, both when considering the sum *and* the difference of original GTE scores. In this case, the link would be labeled as "both excitatory and inhibitory", a fact which is excluded by Dale's principle. Despite this problem, we might still try to combine

the "E–only" and "E+I" reconstructions to infer the nature of each neuron. To test the accuracy of such identification we try to label neurons as excitatory or inhibitory based on a highly "pure" structural network reconstruction. To do so, we select a very high GTE threshold for link, in such a way that in the inferred subnetwork —including, correspondingly, very few links only— the fraction of false positives remains small (with a maximally tolerable ratio of 5%). We first sum and subtract "E–only" and "E+I" scores to obtain putative excitatory and inhibitory links, as just discussed. We next compute the output degrees of the neurons for each subnetwork, k_E and k_I, respectively. Finally, we rank each neuron according to the difference $k_E - k_I$. Following Dale's principle, the set of neurons with the highest (positive) ranking would be labeled as excitatory, and those with the lowest (negative) ranking as inhibitory. The results, however, as shown in the inset of Figure 6.3b, indicate that this approach does not provide better results than a random guessing of neuronal type (see Methods for details on significance testing) and a different approach is required.

6.7 Reconstruction and labeling from stimulated dynamics

As a matter of fact, the major challenge for an accurate reconstruction and precise labeling of neuronal types is the identification of inhibitory links, and this for the following reason. To estimate GTE, we need to evaluate the probability of each given neuron to be active in a short time window of a duration $\Delta t = (k+1)\,\tau_{\text{image}}$, where $k = 2$ is the order of an assumed Markov approximation (see Methods) and $\tau_{\text{image}} = 20$ms is the image acquisition interval. With these parameter choices, we obtain then $\Delta t = 60$ms. Neurons in a culture spike with an average inter-burst frequency of $\nu \sim 0.1$Hz, resulting in a low firing probability within each time bin. Continuing this reasoning, the probability that two unconnected neurons spike at random in the same time window is given by $(\nu\,\Delta t)^2 \sim 4 \cdot 10^{-5}$. The number of coinciding events N_{events} expected in a recording is thus:

$$N_{\text{events}} \sim N_{\text{samples}}\,(\nu\,\Delta t)^2, \tag{6.18}$$

where N_{samples} is the number of independent samples in a recording. In a typical recording session lasting $\sim$ 1h, one gets $N_{\text{samples}} \sim 1.8 \cdot 10^5$ independent samples and therefore $N_{\text{events}} \sim 6$. Hence, one can expect to observe, on average, just six concurrent spikes between any pair of unconnected neurons. If an excitatory link exists between two neurons, the conditional probability of firing rises above this random level and more coincidence events are observed, turning into an appreciable contribution to the GTE calculation. However, if an inhibitory link is present, the number of simultaneous spikes gets further reduced with respect to the already very small chance level, making any accurate statistical assessment very difficult. Nevertheless, we note that the number of detected events scales as ν^2 with the

frequency of firing, and even a slight increase in spiking frequency would enhance considerably the reconstruction performance.

A promising approach to increase neuronal firing consists in forcing the neuronal network through external stimulation. Several studies on neuronal cultures have used external drives, typically in the form of electrical stimulation, to act on neuronal network activity, for instance to investigate connectivity traits [Breskin 2006, Soriano 2008], modify or control activity patterns [Wagenaar 2005, van Pelt 2005], or explore network plasticity [Madhavan 2006, Wagenaar 2006a]. Such *in vitro* approaches are reminiscent of *in vivo* clinically relevant techniques such as deep brain stimulation, used in the treatment of epilepsy and movement disorders [McIntyre 2004, Durand 2001].

External stimulation in neuronal cultures has been employed to increase neuronal firing [van Pelt 2005] as well as to reduce network bursting [Wagenaar 2005, Madhavan 2006]. Factors that, in the GTE reconstruction context, improve the accuracy in the identification of the network architecture. To explore potential improvements in reconstruction, we simulate the effect of an applied external drive in a purely phenomenological way by increasing the frequency parameter of the Poisson process that drives spontaneous activity. This additional drive never increases the spontaneous firing frequency beyond 3 Hz, being meant to represent the effects of a rather weak external stimulation. Due to this contained increase of firing rate, the collective bursting activity of the simulated network continues to be shaped dominantly by network interactions, rather than by the drive itself.

The performance of our GTE algorithm combined with a weak network stimulation is illustrated in Figure 6.4a, where we show the fraction of true positives in the reconstruction of "E–only" networks at 5% false positives. The presence of even very small external drives substantially enhances reconstruction based on GTE. For higher drives, reconstruction performance reaches a plateau that quantifies the range of optimum stimulation. Performance later decays due to the excess of stimulation, which substantially perturbs spontaneous activity and alters qualitatively the global network dynamics. We incidentally remark that the incorporation of the external drive makes unnecessary — actually, even deleterious — the instantaneous feedback term correction (IFT, see Methods), i.e., an *ad hoc* modification to the original formulation of TE which was introduced in [Stetter 2012] to cope with the poor frame rate of calcium fluorescence recordings, definitely slower than the time-scale of monosynaptic interaction delays. The IFT correction allows to encompass interactions occurring in the same temporal bin of the recording for TE estimation, a feature useful to enhance reconstruction results when the time-scale of pre-postsynaptic neuron interactions is fast relative to the time resolution of the recording. However, same–bin interactions also result in an overestimation of bidirectional connections, since one cannot establish directionality within a single time bin. When the firing rate is enhanced with respect to spontaneous conditions these negative effects of the IFT corrections become predominant.

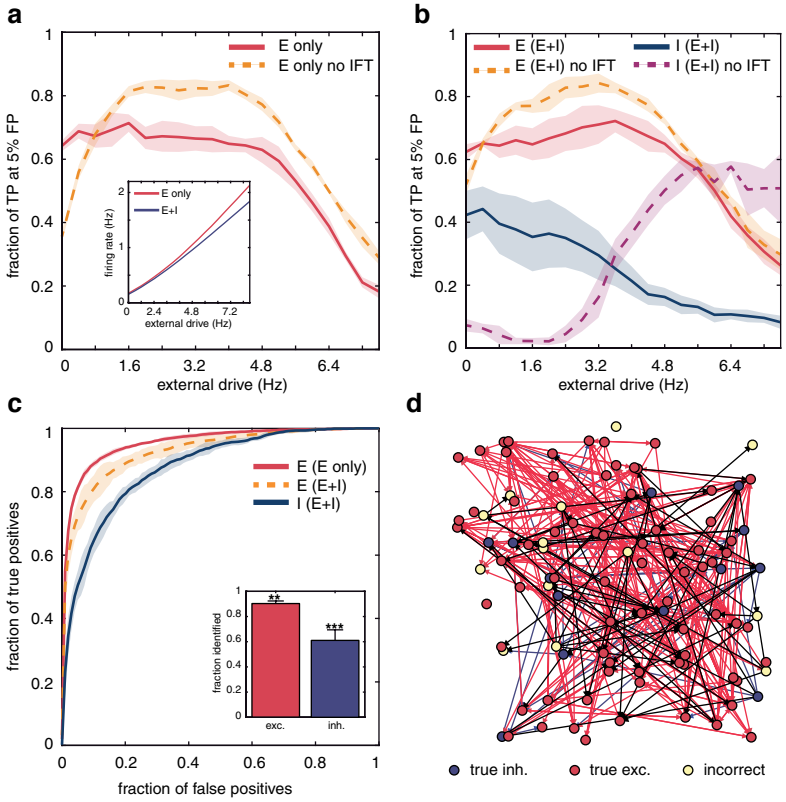

Figure 6.4 | Reconstruction improvement through external stimulation. a,b,, fraction of true positives from the reconstructions at the 5% false positive mark for the studied networks. "E–only" networks are shown in **a,**; "E+I" networks in **b,**. Inset: dependence of the spontaneous firing rate on the applied external drive, emulated here by increasing the rate of the background drive to the culture *in silico*. All the excitatory reconstructions reach a stable plateau in the reconstruction after removal of the instantaneous feedback term (IFT) correction (see Methods). The inhibitory reconstruction is accurate only for higher values of the external drive. **c,** ROC curves extracted from **a,b,** with an external stimulation of 4 Hz. Inset: fraction of excitatory and inhibitory neurons correctly identified from these reconstructions. Identification was statistically significant compared to random guessing. For excitatory neurons, $p < 0.01$ (**); for inhibitory neurons, $p < 10^{-4}$ (***). **d,** Example of an actual reconstruction after identification of neuronal type.Identified excitatory neurons are shown in red and inhibitory ones in blue. Incorrectly identified neurons are shown in gray. Correctly identified excitatory and inhibitory links are shown in red and blue, respectively, and wrongly identified links are shown in black. For clarity in the representation of the links, a threshold value lower than the optimal has been applied.

The same reconstruction analysis for "E+I" networks is shown in Figure 6.4b, for excitatory and inhibitory links separately. The identification of excitatory links greatly improves with moderate drives and, again, IFT becomes unnecessary. For inhibitory links, performance is optimum at low drives, when IFT is used. Without IFT, however, performance is better at relatively high drives, and one can observe the existence of an optimal stimulation range (leading to a firing rate of $\sim$ 5Hz) that maximizes inhibition reconstruction while preserving a relatively good excitatory identification.

We note as well that, for "E+I" networks, bursts disappear in general at higher values of the external drive. In general, as depicted in the inset of Figure 6.4a, the dependence of the spontaneous firing frequency on the external drive is quantitatively different from "E–only" networks, requiring typically a stronger drive to achieve a comparable firing rate.

With the external drive the overall ROC curves are also improved. In Figure 6.4c we show the reconstruction performance for medium values of stimulation. In this new regime, we can again try to determine the neuronal type based on the labeling procedure used in the previous section (inset of Figure 6.4c). Now excitatory neurons are correctly identified with 90% accuracy, whereas the fraction of inhibitory neurons correctly identified rises conspicuously to 60%. This marked improvement is now statistically significant (see Methods).

In Figure 6.4d we show an actual reconstruction of a portion of the original network with this procedure. Correctly inferred excitatory and inhibitory neurons are shown in red and blue respectively, and mismatches in yellow. Correctly identified excitatory and inhibitory links are also shown in red and blue respectively, and false positives are shown in black. It is visually evident that for this thresholding level a very high purity is achieved, and only a small fraction of the reconstructed links are false positives.

We conclude that the addition of a weak external stimulation to the "bare" network dynamics results in an overall improvement on the reconstruction of both excitatory and inhibitory links. Moreover, by combining the reconstructions of "E–only" and "E+I" networks, we also become able to infer the neuronal type by just analyzing the dynamics, with no *a priori* knowledge of the system and without resorting to extrinsic information of any sort.

6.8 Discussions and outlook

A systematic extrinsic labeling of neuronal types might be difficult to achieve in large culture experiments. When *a priori* information is unavailable, our results show that the combination of the reconstructions for "E–only" and "E+I" spontaneous activity data fails at identifying robustly the inhibitory interactions.

Nevertheless, we find that the reconstruction performance of excitatory links remains almost unchanged when inhibition is present, despite the fact that inhibition may substantially alter excitatory interactions, and in turn network dynamics, for instance through feedback and feedforward inhibitory loops. The observation that excitatory links are still correctly reconstructed in "E+I" data shows the robustness of the algorithm to the presence of different interactions in the system. We remark that the main factor determining the poor identification of inhibitory links is the weak firing rate during inter-burst epochs. Since, in a nearly asynchronous regime of inter-burst firing, the action of a direct inhibitory link manifests itself by reducing below the already small chance level the probability of firing coincidence between the two connected neurons, the recording of a larger amount of inhibitory firing would be required to improve the reconstruction of inhibitory couplings. Although the recording duration can be increased at will in numeric simulations, this is not the case for real experimental recordings, to which our algorithm aims at being applied.

In our simulations, we naturally achieved to increase single neuronal firing activity, and therefore reconstruction statistics through a weak external stimulation of the network, with neither a significant disturbance in neuronal network dynamics nor the need for substantially longer recordings. In many previous works resorting to external drives to stimulate network activity, both experimental and theoretical, the applied stimulation was supra-threshold, i.e. the stimulation triggered directly neuronal firing [Breskin 2006, Soriano 2008, Jacobi 2009, Cohen 2010, Linaro 2011]. Our approach raises instead network excitability by a weak external drive that effectively increases activity without modifying the network intrinsic behavior, in the direction of other experimental studies that stimulated multiple sites of a neuronal culture via a multi-electrodes array, to either increase network firing, reduce the occurrence of bursting episodes, or investigate plasticity [van Pelt 2005, Wagenaar 2006a]. Interestingly, these works observed that a weak stimulation along few hours did not induce plastic effects, i.e. did not change network behavior, thus making our reconstruction strategy of immediate applicability in experimental recordings.

In the present work we have exhibited experimental data only for qualitative comparison with fluorescence traces obtained from the numerical model. The experimental data could be analyzed in principle without need of any modification to the GTE formulation, but we found our present knowledge of the experimental recordings insufficient to get reliable reconstructions. In particular, we are lacking good estimates of the neuronal firing rate during the inter-burst periods, as well as the amount of fluorescence change caused by an action potential. The former does not allow to determine whether we expect enough events to make the reconstruction of inhibitory links feasible (see Equation (6.18)), while the latter prevents the application of an optimal data discretization strategy that would reduce the minimal recording length needed for accurate results. Our study intends therefore to foster the future application of the workaround strategies here explored in experiments *in silico*, i.e., most notably: (i) a weak external stimulation to increase spontaneous activity; and (ii) the extrinsic labeling of excitatory and inhibitory neuronal cell bodies after the

recording (to provide at least a partial source of *a priori* information) to be used in synergy with our algorithmic approach.

Finally, our reconstruction algorithm has the potential to be immediately applied to the analysis of fluorescence data in experimental recordings that are not affected by the aforementioned limitations. In particular, *in vivo* recordings and brain slice measurements [Mao 2001, Brustein 2003, Dombeck 2007] display a much richer activity at the individual neuron level than in the *in vitro* counterparts. Recent works have highlighted the ability of high speed multi-neuron calcium imaging to access neuronal circuits *in vivo* [Stosiek 2003, Kerr 2008, Grewe 2010]. Our methodology can thus be directly applied to these data, particularly in those investigations that target the role of inhibition [Bonifazi 2009, Marissal 2012], although systematic verification of the inferred connectivity (in absence of a known ground-truth structure) remains currently out of reach and validation is only possible at the statistical level.

6.9 Conclusions

Living neuronal networks contain both excitatory and inhibitory neurons. Although the interplay between excitation and inhibition gives rise to the rich dynamical traits and operational modes of brain circuits, inhibition is often neglected when analyzing functional characteristics of neuronal circuits, mostly because of its difficult identification and treatment. In this work we have made a first step towards filling this gap, and introduced a new algorithmic approach to infer inhibitory synaptic interactions from multivariate activity time-series. In the framework of a realistically simulated neuronal network that mimics in a semi-quantitative way key features of the behavior of neuronal cultures, we applied Generalized Transfer Entropy (and Dale's principle) to identify excitatory as well as inhibitory connections and neurons.

In a previous work [Stetter 2012], the GTE framework was developed and applied to extract topological information from the dynamics of purely excitatory networks, but left as an open question the treatment of inhibition. Here we have shown that GTE has the potential to be applied without substantial modifications to recordings relative to cultures with active inhibition ("E+I" cultures). This data is characterized by an irregular bursting dynamics with overall lower — but distinctly fluctuating — fluorescence amplitudes as well as higher bursting frequencies than purely excitatory ("E–only") signals. In general, GTE provided an overall good reconstruction of the "E+I" simulated data, hinting at the robustness and general applicability of the algorithm. This is a highly non trivial achievement of the algorithm, given the profoundly different functional profile of inhibitory actions. The GTE reconstruction alone performed well in identifying the existence of links between pairs of neurons, however, it was not sufficient to resolve their excitatory or inhibitory nature. Yet,

we provided evidence through numerical experiments that this additional goal could be fulfilled by retrieving *a priori* information about the types of different neurons (e.g. through immunostaining or selective fluorescent dyes), or by combining the reconstructions obtained from both "E+I" and "E–only" recordings from a same network (thus, again relying uniquely on time-series analysis).

When *a priori* information about the type of each neuron is available, Dale's principle proves to be, at least in our simulations, a solid yet simple approach that allows the identification of the major connectivity traits of the neuronal network. However, when applying Dale's principle to actual, living neuronal networks recordings (see later), one has to consider its possible limitations, like the existence of (rare) exceptions to it [Jonas 1998]. We also remark that, in a more realistic context, other types of *a priori* information beyond the nature of the neurons and their processes could be considered, like, e.g. information about their spatial distribution.

6.10 Acknowledgments

The work presented in this chapter has been done in collaboration with D. Battaglia, O. Stetter, T. Geisel and J. Soriano. In particular, O. Stetter first developed the GTE formulation and J. Soriano performed the experiments.

Appendix

6.A Experimental Methods

All procedures were approved by the Ethical Committee for Animal Experimentation of the University of Barcelona, under order DMAH-5461.

Experimental traces of fluorescence calcium signals were obtained from rat cortical cultures at day *in vitro* 12, following the procedures described in [Stetter 2012] and in other studies [Segal 1992, Soriano 2008, Orlandi 2013]. Briefly, rat cortical neurons from 18–19-day-old Sprague-Dawley embryos were dissected, dissociated and cultured on glass coverslips previously coated with poly–l–lysine. Cultures were incubated at 37°C, 95% humidity, and 5% CO_2. Each culture gave rise to a highly connected network within days that contained on the order of 500 neurons/mm^2. Sustained spontaneous bursting activity appeared by day *in vitro* $6-7$. Prior to imaging, cultures were incubated for 40 min in recording medium containing the cell–permeant calcium sensitive dye Fluo-4-AM. The culture was washed with fresh medium after incubation and finally placed in a recording chamber for observation. The recording chamber was mounted on a Zeiss inverted microscope equipped with a Hamamatsu Orca Flash 2.8 CMOS camera. Fluorescence images were acquired with a speed of 50 frames per second and a spatial resolution of 3.4 μm/pixel.

In a typical measurement, spontaneous activity was first recorded as a long image sequence 60 min long. Both excitatory and inhibitory synapses were active in this first measurement ("E+I" network). Next, inhibitory synapses were fully blocked with 40 μM bicuculline, a $GABA_A$ antagonist, so that activity was solely driven by excitatory neurons ("E–only" network). Activity was next measured again for another 60 min. At the end of the measurements, images were analyzed to to retrieve the evolution of the fluorescence signal for each neuron as a function of time.

Note once again that, in this study, experimental fluorescence traces were used only as a guiding reference for the design of synthetic data in "E–only" and "E+I" conditions, and were not analyzed to provide network reconstructions, given the limitations of current experimental protocols, highlighted in Section 6.8.

6.B Numerical recipes

6.B.1 Combining two reconstruction results

To distinguish between excitatory and inhibitory neurons, we combined the information of the reconstructions obtained from the "E+I" and "E–only" data, namely M^{E+I} and M^{Eonly}. We assumed that excitatory links are present in both datasets, while inhibitory ones appear only in the "E+I" reconstruction, and proceeded by defining new matrices of putative excitatory M^{exc} and putative inhibitory influences M^{inh}, of the form:

$$M^{\text{exc}} = M^{E+I} + M^{Eonly}, \tag{6.19}$$

$$M^{\text{inh}} = M^{E+I} - M^{Eonly}. \tag{6.20}$$

To obtain the effective connectivity reconstruction only the rank ordering of GTE values is relevant. Therefore no rescaling of these matrices is necessary, and the final set of links could be obtained by thresholding the matrices as described above.

To label the neurons as either excitatory or inhibitory, we first removed all links that were present in both reconstructions, and then ranked the neurons according to the difference between excitatory and inhibitory links, $l_i = \sum_j T^{\text{exc}}_{ji} - \sum_j T^{\text{inh}}_{ji}$. We next used the prior information that a fraction $f_E = 80\%$ of the neuronal population is excitatory, therefore identifying as excitatory neurons the f_E fraction with the highest l_i score, and labeling the rest as inhibitory.

6.B.2 Statistical tests

Statistical significance on the inference of excitatory and inhibitory neuronal types was performed as follows. Assuming that the fraction of excitatory and inhibitory neurons (f_E and f_I respectively) is known with good precision in a population of N cells, the probability to correctly identify by chance a given set of neurons n_E and n_I in a given trial X follows a binomial distribution:

$$P(X = n) = \binom{Nf_x}{n} f_x^n (1 - f_x)^{Nf_x - n}. \tag{6.21}$$

Let suppose that a labeling method provides a fraction n_{guess} of correctly labeled links. We considered this labeling result as statistically significant if the probability of outperforming by chance this success rate was $P(X \geq n_{\text{guess}}) < p$, with a standard choice of $p = 0.05$.

7

General conclusions and perspectives

The main purpose of this thesis has been to untangle the complex interplay between noise, coherent activity and network structure in neuronal cultures, with focus on dynamics. To fully understand and characterize this interplay we modeled and characterized the spontaneous activity of neuronal cultures at different scales, from the microscopic structure of the single–neuron dynamics and the associated macroscopic observables, to a mesoscale description as an excitable medium with nontrivial fluctuations.

The work presented here comprises a full picture in the study of spontaneous activity in neuronal cultures. We start by showing how patterns of coherent activity emerge spontaneously due to a highly heterogeneous mechanism of noise propagation and amplification in a metric network called *noise focusing*, and circle back to show a reliable method to characterize the properties of the network structure based on the observed dynamics.

7.1 Summary of results and conclusions

Chapter 2 contains the most salient results of this thesis. We develop an accurate model of the network structure and the dynamics of neuronal cultures in their early stages of development and show that their collective spontaneous activity is

dominated by activity bursts which take the form of propagating fronts that nucleate at specific sites of the system, i.e., nucleation sites.

We show that the underlying neuronal activity in the system is characterized by avalanches of activity that originate in the spontaneous noise and propagate through the system. The activity in the avalanches is amplified due to the clustered topology of the network (inherited from its metric structure) and the non–linear behavior of the neuronal dynamics. This results in the emergence of effective paths in the network where this amplification is maximal. The convergence of these paths is what ultimately concentrates the activity in specific sites, a phenomenon that we call *noise focusing*. These sites act as sinks of an effective average flow with large basins of attraction, explaining the highly heterogeneous nucleation maps, observed in experiments done in collaboration with the group of J. Soriano.

We also show that the amplification paths that arise from the *noise focusing* mechanism dynamically generate an effective subnetwork with scale–free topology.

In Chapter 3 we study how the avalanche dynamics and the noise amplification mechanisms depend on network topology by using regular networks with very simple motifs. We are able to characterize the avalanches by their propagation velocity and their radius and relate this quantities to the different network motifs. This analysis clarifies the directional nature of the amplification mechanisms, thus providing a microscopic explanation of the highly anisotropic nature of the noise flow in the system.

In Chapter 4 we develop a coarse–grained model of a neuronal culture as a continuous excitable medium, able to capture the physical picture emerging from Chapter 2. We have also characterized the structure of the amplification paths caused by the *noise focusing* mechanism with the introduction of a new vector field and an amplification coefficient. The inclusion of these terms, in combination with the effect of synaptic depression, is sufficient to account for the heterogeneous nucleation. This approach formalizes the intuitive ideas of anisotropic noise flow that characterize the *noise focusing phenomenon*, by emphasizing the need of a nontrivial anisotropic structure of the noise at the mesoscopic level of description.

Chapter 5 studies the spontaneous activity in neuronal cultures within the framework of quorum percolation (QP). We show that network structure has a mild effect on the QP transition and in the formation of the giant component. We also show an equivalent description of QP based on the neuron model introduced in Chapter 2 and how it compares to QP. Finally, we present a new model, called *stochastic quorum percolation* (SQP) that takes into account the finite probability of subquorum firing. It extends the QP model into a dynamical description that includes the presence of noise in the system. We show that when noise and the dynamics are taken into account, the metric structure of the network plays a much greater role in the actual nucleation times.

Finally, in Chapter 6 we introduce a network inference method, based on information theory, tailored to the study of spontaneous activity in neuronal cultures. The

method, called Generalized Transfer Entropy (GTE), was previously developed by O. Stetter, and in here we extend it to the study of spontaneous activity when both excitatory and inhibitory connections are present. We show that under normal experimental conditions is almost impossible to detect inhibitory connections when the neuronal type is now know. To overcome this fact, we propose an experimental protocol, based on already developed methods for external stimulation, where we are able to detect and reliably infer inhibitory connections (and distinguish them from excitatory connections), when a small external stimulation is added to the system.

7.2 Publications

The work presented in this thesis has spanned two main peer–reviewed publications:

- [Orlandi 2013] Orlandi, J. G., Soriano, J., Alvarez-Lacalle, E., Teller, S. and Casademunt, J. "Noise focusing and the emergence of coherent activity in neuronal cultures." **Nature Physics** 9, 582–590 (2013).
- [Orlandi 2014] Orlandi, J. G., Stetter, O., Soriano, J., Geisel, T. and Battaglia, D. "Transfer entropy reconstruction and labeling of neuronal connections from simulated calcium imaging." **PLOS ONE** 9, e98842 (2014).

And two more are currently under preparation:

- Orlandi J.G. and Casademunt, J. "Noise focusing at the mesoscale: a coarse–grained view of neuronal cultures."
- Orlandi, J.G. and Casademunt, J. "Stochastic quorum percolation in metric networks."

7.3 Perspectives

The work presented here is highly interdisciplinary, spanning various disciplines in physics and neuroscience, hence there is still much that can be done within this framework, and in here we proceed to name a few.

The results presented in Chapter 2 have implications in the study of dynamics on complex networks in general. We have shown that, based on the statistics of avalanche size at different scales, one may define different effective networks that decompose the dynamics in different layers. Avalanches at different scales may exhibit different spatio-temporal structure, eventually breaking the statistical self-similar structure. The relationship between avalanche dynamics at different

scales and their interplay with the network structure might have interesting uses in other dynamical systems and network structures. Within the context of avalanche dynamics, it is also important to fully characterize the avalanche shape, preliminary studies show that its shape (avalanche size in time) is asymmetric which can be related to other systems [Laurson 2013].

An example from a different context where the results from Chapter 2 may be directly applied is that of rumor propagation in social networks, where the role of the integrate-and-fire response is played by the so-called 'illusion-of-truth' effect, i.e. the requisite of repeated inputs to grant credibility, prior to propagation [Moons 2009]. Accordingly, not only the rumor activity network will differ from the underlying social network, but the points of rumor 'ignition' [Kitsak 2010] will in general depart from the actual community structure of both the social and the effective networks.

The study of how different topologies affect the underlying dynamics also deserves more work. In fact, the software presented in Chapter 2 is already capable of generating networks in confined geometries, like the patterns presented in Section 1.3.5, where we have observed that the front dynamics can have dramatic changes. In a similar direction, several results in the context of criticality deserve more attention. For instance, it is still unclear whether the exponents have some degree of universality, or rather they always depend on network structure, a fact that could be related to griffiths phases, which have already been proposed within the context of brain networks [Moretti 2013].

Several results regarding the *noise focusing* mechanism depend on the underlying structure of the noise. For example, the spontaneous activity of individual neurons depend on the different ionic concentrations in the medium, and small changes in ionic concentration could completely change the behavior of the system. Although we have already explored this by introducing variability in the neuron model, more needs to be done, for example by including endogenously active neurons. This is also related to the concept of leader neurons, which seem to exist in neuronal cultures. These neurons might be intrinsically different from other neurons and form a subpopulation. However, its existence might also be be the result of a collective effect, namely they are neurons that are present in the paths of high amplification described in Chapter 2. Another possible study, from an experimental point of view, would be to change the structure of the noise, for example by modifying the spontaneous quantal release of neurotransmitters by using several different chemicals [Bouron 2001].

Another possible extension to this work is within the context of plasticity. The bursting behavior observed in young cultures appears to change as the network matures [Wagenaar 2006a], and several groups have associated the new dynamical regime to self–organized criticality (SOC) [Tetzlaff 2010, Pu 2013]. This could be explored by including a simple mechanism of plasticity, like spike–timing–dependent plasticity (STDP), and study the evolution of the synaptic connections to see if the evolves into a state of SOC. It could very well be that the effective

subnetwork that we have observed is potentiated by the plasticity mechanisms. On the other hand, it could also be possible that a homeostatic mechanism is smoothing the differences.

Several of the results presented in Chapter 5 are preliminary, and still more work is required, specially regarding the SQP model. The original QP model is a powerful tool that extends the classical framework of percolation to neuronal networks, where individual links have very limited role and the system needs to be characterized by an ensemble of them (m in the QP model). In the same direction, many useful concepts of network theory need to be modified to be applicable to neuronal networks. The identification of influential spreaders in complex networks [Kitsak 2010], or competitive percolation, where single links have a very important role [Nagler 2011], as well as explosive percolation [Achlioptas 2009], are all useful tools within the context of complex networks. Their application to neuronal networks is not straightforward[1], yet they could prove valuable tools.

The results on network inference presented in Chapter 6 show that providing an accurate description of the network structure based on the underlying dynamics is extremely difficult, and a lot of work is still required in this context. For example, spike trains could be inferred from the fluorescence dynamics through Monte Carlo approaches [Mishchenko 2011a] or peeling [Lütcke 2013]. The results from GTE could also be improved by network deconvolution [Feizi 2013], which we have already tried, and the preliminary results are promising.

[1] At the single neuron level.

A

Resum en Català

Aconseguir una completa comprensió del funcionament del cervell i de la ment, així com el descobrir noves formes d'identificar, tractar, prevenir i curar trastorns com Alzheimer, esquizofrènia, epilèpsia i autisme és un dels grans reptes científics d'aquest segle. Aquest repte és altament multidisciplinari i només es podrà avançar mitjançant una estreta col·laboració entre científics de moltes disciplines, neurociència, medicina, biologia, química, informàtica, física, etc. En aquesta tesi aportem el nostre petit granet de sorra a aquesta tasca com millor sabem fer els físics en un entorn multidisciplinari, aïllant els problemes i revelant mecanismes bàsics i fonamentals que s'amaguen dins la complexitat del mon biològic. En aquest treball s'han estudiat els mecanismes fonamentals que regeixen l'activitat espontània en el sistema neuronal més elemental i controlat que podem tenir, un cultiu neuronal.

Un cultiu neuronal primari consisteix en la dissociació de neurones en fase embrionària i la seva posterior deposició en una placa de petri al laboratori. Aquestes neurones inicialment són cèl·lules aïllades, però ja 24h després de la deposició comencen a estendre les seves neurites i a connectar-se amb altres neurones. Durant aquesta fase, les neurones comencen a mostrar activitat de forma espontània, i.e., generen potencials d'acció, tot i que de forma aïllada, sense correlació. En canvi, quan ja porten prop d'una setmana en cultiu, aquestes comencen a mostrar activitat, també espontània, però de forma coordinada, on sembla que totes elles s'activin simultàniament. En aquesta tesi estudiant des de un punt de vista físic, els mecanismes fonamentals que hi ha darrera d'aquest fenòmen, de com les neurones passen d'actuar com a elements individuals a fer-ho col·lectivament.

Aquesta tesi comença en el Capítol 1 amb una visió força personal de la ciència en el segle XXI, fent especial èmfasi en el seu caràcter interdisciplinari i de com, en aquest cas la neurociència, ha d'aprofitar aquest fet si espera assolir una completa comprensió del funcionament del cervell. Aquesta introducció també inclou una revisió històrica, força detallada, de tota la feina que s'ha fet anteriorment en cultius neuronals, principalment des del punt de vista d'un físic. A més a més, també s'inclou un resum detallat dels mecanismes fisiològics principals per poder entendre el comportament d'un cultiu neuronal.

En el Capítol 2 mostrem, mitjançant simulacions numèriques i teoria, com l'activitat espontània en cultius joves (entre una i tres setmanes) es pot caracteritzar per fronts d'activitat que es formen, per un procés de nucleació, en punts concrets del sistema i es propaguen. Els punts on l'activitat pot nuclear no són aleatoris (tot i que la seva seqüència ho és), i es concentren en zones específiques que anomenem zones de nucleació. Aquestes zones es poden determinar per la interacció entre l'estructura de la xarxa i la pròpia dinàmica de les neurones, que hem aconseguit caracteritzar com a un nou mecanisme, que anomenem focalització del soroll. Aquest mecanisme descriu com l'activitat individual de les neurones es propaga per la xarxa en forma d'allaus, les quals es veuen amplificades quan recorren camins específics de la xarxa. Justament és la confluència d'aquests camins el que genera les zones de nucleació, actuen com a centres d'atracció de l'activitat. A més a més, aquestes zones de nucleació tenen una mida característica, així com un domini d'atracció, que ve determinat principalment per la longitud dels axons.

Aquests camins d'alta amplificació que són conseqüència del mecanisme d'amplificació del soroll formen una subxarxa amb una estructura totalment diferent de la xarxa original. La xarxa original, la que descriu les connexions entre les neurones, ve descrita per una distribució pràcticament Gaussiana, on totes les neurones tenen pràcticament les mateixes connexions. En canvi, la subxarxa associada als camins d'amplificació presenta una estructura molt més heterogènia, i s'assimila a una distribució tipus ´scale-free´, sense una escala característica, en la qual s'observen 'hubs', neurones per on passa gran part de l'activitat. Un detall important és que aquestes neurones no tenen cap propietat especial, ni són més actives, ni tenen connexions més fortes, simplement la seva posició a la xarxa fa que tota l'activitat que passa a través d'ella acabi sent amplificada. No actuen com a líders, sinó com a missatgeres.

En el mateix capítol també mostrem confirmació experimental de la existència de les zones de nucleació i de la propagació de l'activitat en forma de fronts.

En el Capítol 3 tractem des d'un punt de vista més abstracte, els efectes que l'estructura de la xarxa té en el mecanisme d'amplificació i propagació del soroll. Mitjançant xarxes regulars, on cada neurona presenta el mateix patró de connexions, estudiem l'estructura interna de les allaus d'activitat. Aquest anàlisi ens permet caracteritzar amb ple detall l'estructura de les allaus, i associar-hi una velocitat i grandària característica, que depèn de la topologia de la xarxa.

El Capítol 4 conté una descripció de l'activitat dels cultius neuronals a la mesoescala. Mitjançant el formalisme de sistemes dinàmics i medis excitables, introduïm un nou model continu (estès a l'espai) que incorpora, a un altre nivell de detall, el mecanisme de focalització del soroll i presenta la mateixa dinàmica observada en els cultius neuronals, sense la necessitat d'introduir una xarxa. Això és possible mitjançant la introducció de nous coeficients de transport. Un d'ells, α, està directament associat a l'amplificació del soroll, i un altre, $\mathbf{V}$, de caràcter vectorial, està íntimament relacionat amb la estructura de les allaus observades en el model microscòpic, de neurones individuals.

El Capítol 5 està dedicat a introduir el concepte de percolació de quòrum estocàstica. La percolació de quòrum s'havia fet servir anteriorment per descriure el comportament d'un cultiu neuronal sota una pertorbació externa (estimulació elèctrica). El model de percolació de quòrum es basa únicament en el fet que una neurona necessita un mínim de m veïns actius per disparar. Experimentalment, aquest nombre m es pot manipular mitjançant fàrmacs que debiliten la força de les connexions sinàptiques. El model de percolació de quòrum permet descriure com respon el cultiu a l'estimulació elèctrica en funció de la quantitat del fàrmac aplicat, i permet caracteritzar-ho com una transició de fase de primer ordre, equivalent a la transició de fase líquid-gas del model de Van der Waals. A més a més, el sistema també presenta un punt crític m_c on la transició esdevé contínua. En aquest capítol mostrem primer com el procés de percolació de quòrum depèn de l'estructura de la xarxa del sistema, i com aquesta afecta a l'estructura de la transició.

També mostrem com es pot generalitzar el model de percolació de quòrum per incloure la dinàmica real del sistema i els efectes del soroll. Introduïm el model estocàstic de percolació de quòrum, que associa una probabilitat de disparar a cada neurona en funció del nombre de veïns que es troben actius. Aquesta descripció ve motivada pels resultats del Capítol 2, on les neurones disparen espontàniament, i sempre presenten una probabilitat finita d'activar-se, inclòs quan les veïnes no estan actives. Aquest nou model és capaç de descriure els observables de la percolació de quòrum i les seves transicions de fase, i a més permet definir temps de nucleació i allaus d'activitat, ja que el model és ara dinàmic. A més a més, mostrem com la incorporació de la dinàmica i del soroll en el model amplifica enormement els efectes de la topologia de la xarxa.

En el Capítol 6 fem un canvi de perspectiva. Fins ara ens hem dedicat a mostrar, entre d'altres, com l'estructura de la xarxa influeix en la dinàmica dels cultius neuronals. Ara en canvi, mostrem com es pot inferir l'estructura de la xarxa observant simplement la dinàmica. El nostre estudi s'engloba dins el marc de la teoria de la informació, i més concretament, de la transferència d'entropia. La transferència d'entropia és una mesura que permet identificar la influència que un procés temporal té en un altre procés. És una mesura d'informació, de com el coneixement d'un senyal ens ajuda a predir el comportament d'un altre. En aquest capítol mostrem com aquesta tècnica ens permet inferir la connectivitat en un cultiu neuronal a partir de l'anàlisi de les senyals de fluorescència que s'obtenen en els experiments. En

concret, ens centrem en explorar si amb aquesta tècnica som capaços de distingir entre diferents tipus de connexions (si són excitadores o inhibidores). Demostrem que en el cas dels cultius, aquesta distinció entre el tipus de connexions només és possible si tenim un coneixement a priori del tipus neuronal que estem mirant. Tot i això, també demostrem que mitjançant un protocol d'estimulació externa del cultiu (equivalent al descrit en el capítol anterior), és possible distingir entre els diferents tipus de connexions sense el coneixement del tipus neuronal.

Acronyms

AMPA	α-amino-3-hydroxy-5-methyl-4-isoxazolepropionic acid
APV	2-amino-5-phosphonovaleric acid
BA	Background avalanche
BDNF	Brain–derived neurotrophic factor
CCD	Charge–coupled device
CMOS	Complementary metal-oxide-semiconductor
CNQX	6-cyano-7-nitroquinoxaline-2,3-dione
DIV	Days in vitro
EPSC	Excitatory postsynaptic current
EPSP	Excitatory postsynaptic potential
IA	Ignition avalanche
IBI	Interburst interval
IPSC	Inhibitory postsynaptic current
IPSP	Inhibitory postsynaptic potential
ISI	Interspike interval
GABA	γ-aminobutyric acid
GC	Granger causality
GFP	Green fluorescent protein
GTE	Generalized transfer entropy
HBP	Human brain project
LFP	Local field potential
MEA	Multi–electrode array
MI	Mutual information
NC	Neuronal culture

NF	Noise focusing
NMDA	N-Methyl-D-aspartic acid
QP	Quorum percolation
SA	Spontaneous activity
SQP	Stochastic quorum percolation
STDP	Spike–timing–dependent plasticity
TE	Transfer entropy
TTX	Tetrodotoxin
XC	Cross–Correlation

List of Figures

List of Tables

References

[Abbott 2013a] Abbott, A. "Brain-simulation and graphene projects win billion-euro competition". *Nature* (2013). Cited on pages: 4, 33.

[Abbott 2013b] Abbott, A. "Neuroscience: Solving the brain". *Nature*, **499**, 272–274 (2013). Cited on page: 4.

[Achlioptas 2009] Achlioptas, D., D'Souza, R. M., & Spencer, J. "Explosive percolation in random networks". *Science*, **323**, 1453–1455 (2009). Cited on page: 165.

[Ahnert 2008] Ahnert, S. E. & Fink, T. M. A. "Clustering signatures classify directed networks". *Phys Rev E Stat Nonlin Soft Matter Phys*, **78**, 36112 (2008). Cited on page: 46.

[Ahrens 2013] Ahrens, M. B., Orger, M. B., Robson, D. N., Li, J. M., & Keller, P. J. "Whole-brain functional imaging at cellular resolution using light-sheet microscopy". *Nat Met*, **10**, 413–420 (2013). Cited on pages: 13, 14.

[Albert 2002] Albert, R. & Barabási, A.-L. "Statistical mechanics of complex networks". *Rev Mod Phys*, **74**, 47–97 (2002). Cited on pages: 4, 69, 71, 139.

[Alivisatos 2012] Alivisatos, A. P., Chun, M., Church, G. M., et al. "The brain activity map project and the challenge of functional connectomics". *Neuron*, **74**, 970–974 (2012). Cited on page: 33.

[Alivisatos 2013] Alivisatos, A. P., Chun, M., Church, G. M., et al. "Neuroscience The brain activity map". *Science*, **339**, 1284–1285 (2013). Cited on page: 33.

[Alvarez-Lacalle 2009] Alvarez-Lacalle, E. & Moses, E. "Slow and fast pulses in 1-D cultures of excitatory neurons". *J Comput Neurosci*, **26**, 475–493 (2009). Cited on pages: 16, 17, 19, 39, 41.

[Arber 2012] Arber, S. "Motor circuits in action: specification, connectivity, and function". *Neuron*, **74**, 975–989 (2012). Cited on page: 136.

[Arenas 2009] Arenas, A., Fernández, A., & Gómez, S. "An optimization approach to the structure of the neuronal layout of C elegans". In Handbook on Biological Networks, 243–257. World Scientific (2009). Cited on page: 7.

[Ashley 1968] Ashley, C. C. & Ridgway, E. B. "Simultaneous Recording of Membrane Potential, Calcium Transient and Tension in Single Muscle Fibres". *Nature*, **219**, 1168–1169 (1968). Cited on page: 12.

[Bak 1987] Bak, P., Tang, C., & Wiesenfeld, K. "Self-organized criticality: An explanation of the 1/f noise". *Phys Rev Lett*, **59**, 381–384 (1987). Cited on page: 25.

[Bansal 2009] Bansal, S., Khandelwal, S., & Meyers, L. A. "Exploring biological network structure with clustered random networks". *BMC Bioinformatics*, **10**, 405 (2009). Cited on page: 139.

[Barabási 1999] Barabási, A.-L. & Albert, R. "Emergence of Scaling in Random Networks". *Science*, **286**, 509–512 (1999). Cited on page: 4.

[Bardy 2015] Bardy, C., van den Hurk, M., Eames, T., et al. "Neuronal medium that supports basic synaptic functions and activity of human neurons in vitro". *Proc Natl Acad Sci USA*, 201504393–10 (2015). Cited on page: 27.

[Barkley 1991] Barkley, D. "A model for fast computer simulation of waves in excitable media". *Phys D*, **49**, 61–70 (1991). Cited on page: 108.

[Barnett 2009] Barnett, L., Barrett, A. B., & Seth, A. K. "Granger Causality and Transfer Entropy Are Equivalent for Gaussian Variables". *Phys Rev Lett*, **103**, 238701 (2009). Cited on page: 137.

[Baruchi 2008] Baruchi, I., Volman, V., Raichman, N., Shein, M., & Ben-Jacob, E. "The emergence and properties of mutual synchronization in in vitro coupled cortical networks". *Eur J Neurosci*, **28**, 1825–1835 (2008). Cited on pages: 8, 21, 38.

[Battaglia 2012] Battaglia, D., Witt, A., Wolf, F., & Geisel, T. "Dynamic effective connectivity of inter-areal brain circuits". *PLoS Comput Biol*, **8**, e1002438 (2012). Cited on page: 34.

[Beggs 2003] Beggs, J. M. & Plenz, D. "Neuronal avalanches in neocortical circuits". *J Neurosci*, **23**, 11167–11177 (2003). Cited on pages: 7, 8, 9, 10, 11, 23, 67.

[Beggs 2004] Beggs, J. M. & Plenz, D. "Neuronal avalanches are diverse and precise activity patterns that are stable for many hours in cortical slice

cultures". *J Neurosci*, **24**, 5216–5229 (2004). Cited on pages: 7, 11, 23, 67.

[Beggs 2008] Beggs, J. M. "The criticality hypothesis: how local cortical networks might optimize information processing". *Phil Trans R Soc A*, **366**, 329–343 (2008). Cited on page: 23.

[Beggs 2012] Beggs, J. M. & Timme, N. "Being critical of criticality in the brain". *Front Physiol*, **3** (2012). Cited on page: 27.

[Besserve 2010] Besserve, M., Schölkopf, B., Logothetis, N. K., & Panzeri, S. "Causal relationships between frequency bands of extracellular signals in visual cortex revealed by an information theoretic analysis". *J Comput Neurosci*, **29**, 547–566 (2010). Cited on page: 35.

[Bettencourt 2007] Bettencourt, L. M. A., Stephens, G. J., Ham, M. I., & Gross, G. W. "Functional structure of cortical neuronal networks grown in vitro". *Phys Rev E Stat Nonlin Soft Matter Phys*, **75**, 21915 (2007). Cited on page: 35.

[Blankenship 2010] Blankenship, A. G. & Feller, M. B. "Mechanisms underlying spontaneous patterned activity in developing neural circuits". *Nat Rev Neurosci*, **11**, 18–29 (2010). Cited on pages: 22, 37.

[Blondel 2008] Blondel, V. D., Guillaume, J.-L., Lambiotte, R., & Lefebvre, E. "Fast unfolding of communities in large networks". *J Stat Mech*, **10**, 008 (2008). Cited on page: 79.

[Bock 2011] Bock, D. D., Lee, W.-C. A., Kerlin, A. M., et al. "Network anatomy and in vivo physiology of visual cortical neurons". *Nature*, **471**, 177–182 (2011). Cited on pages: 29, 33.

[Bonifazi 2009] Bonifazi, P., Goldin, M., Picardo, M. A., et al. "GABAergic hub neurons orchestrate synchrony in developing hippocampal networks". *Science*, **326**, 1419–1424 (2009). Cited on page: 157.

[Boudreau 2005] Boudreau, C. E. & Ferster, D. "Short-term depression in thalamocortical synapses of cat primary visual cortex". *J Neurosci*, **25**, 7179–7190 (2005). Cited on page: 30.

[Bouron 2001] Bouron, A. "Modulation of spontaneous quantal release of neurotransmitters in the hippocampus". *Prog Neurobiol*, **63**, 613–635 (2001). Cited on page: 164.

[Breskin 2006] Breskin, I., Soriano, J., Moses, E., & Tlusty, T. "Percolation in Living Neural Networks". *Phys Rev Lett*, **97**, 188102 (2006). Cited on pages:

8, 57, 153, 156.

[Briggman 2011] Briggman, K. L., Helmstaedter, M., & Denk, W. "Wiring specificity in the direction-selectivity circuit of the retina". *Nature*, **471**, 183–188 (2011). Cited on page: 29.

[Brustein 2003] Brustein, E., Marandi, N., Kovalchuk, Y., Drapeau, P., & Konnerth, A. ""In vivo" monitoring of neuronal network activity in zebrafish by two-photon Ca(2+) imaging". *Pflügers Archiv*, **446**, 766–773 (2003). Cited on page: 157.

[Bullmore 2009] Bullmore, E. & Sporns, O. "Complex brain networks: graph theoretical analysis of structural and functional systems". *Nat Rev Neurosci*, **10**, 186–198 (2009). Cited on pages: 33, 37.

[Buzsáki 2004] Buzsáki, G. & Draguhn, A. "Neuronal oscillations in cortical networks". *Science*, **304**, 1926–1929 (2004). Cited on page: 37.

[Cajal 1906] Cajal, S. R. "The Structure and Connexions of Neurons". *Nobel prize in physiology or medicine lecture Nobel Foundation* (1906). Cited on page: 5.

[Caporale 2008] Caporale, N. & Dan, Y. "Spike timing-dependent plasticity: a Hebbian learning rule". *Annu Rev Neurosci*, **31**, 25–46 (2008). Cited on page: 30.

[Chialvo 2004] Chialvo, D. R. "Critical brain networks". *Phys A*, **340**, 756–765 (2004). Cited on page: 23.

[Chialvo 2010] Chialvo, D. R. "Emergent complex neural dynamics". *Nat Phys*, **6**, 744–750 (2010). Cited on page: 37.

[Chiappalone 2006] Chiappalone, M., Bove, M., Vato, A., Tedesco, M., & Martinoia, S. "Dissociated cortical networks show spontaneously correlated activity patterns during in vitro development". *Brain Research*, **1093**, 41–53 (2006). Cited on page: 144.

[Chicurel 2000] Chicurel, M. "Databasing the brain". *Nature*, **406**, 822–825 (2000). Cited on page: 33.

[Cohen 2008] Cohen, E., Ivenshitz, M., Amor-Baroukh, V., Greenberger, V., & Segal, M. "Determinants of spontaneous activity in networks of cultured hippocampus". *Brain Research*, **1235**, 21–30 (2008). Cited on pages: 32, 38, 62, 135, 144.

[Cohen 2009] Cohen, D. & Segal, M. "Homeostatic presynaptic suppression of neuronal network bursts". *J Neurophysiol*, **101**, 2077–2088 (2009). Cited on pages: 32, 39.

[Cohen 2010] Cohen, O., Keselman, A., Moses, E., et al. "Quorum percolation in living neural networks". *Europhys Lett*, **89**, 18008 (2010). Cited on pages: 38, 57, 72, 75, 123, 124, 125, 126, 156.

[Cohen 2011] Cohen, D. & Segal, M. "Network bursts in hippocampal microcultures are terminated by exhaustion of vesicle pools". *J Neurophysiol*, **106**, 2314–2321 (2011). Cited on pages: 18, 20, 31, 41, 62, 146.

[Collingridge 2004] Collingridge, G. L., Isaac, J. T. R., & Wang, Y. T. "Receptor trafficking and synaptic plasticity". *Nat Rev Neurosci*, **5**, 952–962 (2004). Cited on page: 18.

[Compte 2003] Compte, A., Sanchez-Vives, M. V., McCormick, D. A., & Wang, X.-J. "Cellular and network mechanisms of slow oscillatory activity (<1 Hz) and wave propagations in a cortical network model". *J Neurophysiol*, **89**, 2707–2725 (2003). Cited on page: 11.

[Corbetta 2008] Corbetta, M., Patel, G., & Shulman, G. L. "The reorienting system of the human brain: from environment to theory of mind". *Neuron*, **58**, 306–324 (2008). Cited on page: 33.

[Corral 1995] Corral, Á., Pérez, C., Díaz-Guilera, A., & Arenas, A. "Self-organized criticality and synchronization in a lattice model of integrate-and-fire oscillators". *Phys Rev Lett*, **74**, 118–121 (1995). Cited on page: 23.

[Crivellato 2007] Crivellato, E. & Ribatti, D. "Soul, mind, brain: Greek philosophy and the birth of neuroscience". *Brain Res Bull*, **71**, 327–336 (2007). Cited on page: 5.

[Cuntz 2010] Cuntz, H., Forstner, F., Borst, A., & Häusser, M. "One rule to grow them all: a general theory of neuronal branching and its practical application". *PLoS Comput Biol*, **6**, e1000877 (2010). Cited on page: 28.

[Cuntz 2012] Cuntz, H., Mathy, A., & Häusser, M. "A scaling law derived from optimal dendritic wiring". *Proc Natl Acad Sci USA*, **109**, 11014–11018 (2012). Cited on page: 29.

[Czarnecki 2012] Czarnecki, A., Tscherter, A., & Streit, J. "Network activity and spike discharge oscillations in cortical slice cultures from neonatal rat". *Eur J Neurosci*, **35**, 375–388 (2012). Cited on pages: 8, 10, 11.

[De Carlos 2007] De Carlos, J. A. & Borrell, J. "A historical reflection of the contributions of Cajal and Golgi to the foundations of neuroscience". *Brain Res Rev*, **55**, 8–16 (2007). Cited on page: 5.

[De Simoni 2003] De Simoni, A., Griesinger, C. B., & Edwards, F. A. "Development of rat CA1 neurones in acute versus organotypic slices: role of experience in synaptic morphology and activity". *J Physiol*, **550**, 135–147 (2003). Cited on page: 7.

[Deco 2011] Deco, G., Jirsa, V. K., & McIntosh, A. R. "Emerging concepts for the dynamical organization of resting-state activity in the brain". *Nat Rev Neurosci*, **12**, 43–56 (2011). Cited on pages: 7, 33, 37.

[Deco 2012] Deco, G. & Jirsa, V. K. "Ongoing cortical activity at rest: criticality, multistability, and ghost attractors". *J Neurosci*, **32**, 3366–3375 (2012). Cited on page: 34.

[Desai 1999] Desai, N. S., Rutherford, L. C., & Turrigiano, G. G. "Plasticity in the intrinsic excitability of cortical pyramidal neurons". *Nat Neurosci*, **2**, 515–520 (1999). Cited on page: 30.

[Deuchars 1996] Deuchars, J. & Thomson, A. M. "CA1 pyramid-pyramid connections in rat hippocampus in vitro: dual intracellular recordings with biocytin filling". *Neuroscience*, **74**, 1009–1018 (1996). Cited on page: 30.

[Dichter 1978] Dichter, M. A. "Rat cortical neurons in cell culture: culture methods, cell morphology, electrophysiology, and synapse formation". *Brain Research*, **149**, 279–293 (1978). Cited on page: 14.

[Dombeck 2007] Dombeck, D. A., Khabbaz, A. N., Collman, F., Adelman, T. L., & Tank, D. W. "Imaging large-scale neural activity with cellular resolution in awake, mobile mice". *Neuron*, **56**, 43–57 (2007). Cited on page: 157.

[Dorogovtsev 2006] Dorogovtsev, S. N., Goltsev, A. V., & Mendes, J. F. F. "k-Core Organization of Complex Networks". *Phys Rev Lett*, **96**, 040601 (2006). Cited on page: 123.

[Dranias 2013] Dranias, M. R., Ju, H., Rajaram, E., & Vandongen, A. M. J. "Short-term memory in networks of dissociated cortical neurons". *J Neurosci*, **33**, 1940–1953 (2013). Cited on page: 11.

[Durand 2001] Durand, D. M. & Bikson, M. "Suppression and control of epileptiform activity by electrical stimulation: a review". *Proc IEEE*, **89**, 1065–1082 (2001). Cited on page: 153.

[Eckmann 2007] Eckmann, J.-P., Feinerman, O., Gruendlinger, L., et al. "The physics of living neural networks". *Physics Reports*, **449**, 54–76 (2007). Cited on pages: 16, 37, 135, 144.

[Eckmann 2008] Eckmann, J.-P., Jacobi, S., Marom, S., Moses, E., & Zbinden, C. "Leader neurons in population bursts of 2D living neural networks". *New J Phys*, **10**, 5011 (2008). Cited on pages: 23, 38.

[Eckmann 2010] Eckmann, J.-P., Moses, E., Stetter, O., Tlusty, T., & Zbinden, C. "Leaders of neuronal cultures in a quorum percolation model". *Front Comput Neurosci*, **4** (2010). Cited on pages: 23, 38, 57, 64, 82, 123.

[El Hady 2013] El Hady, A., Afshar, G., Bröking, K., et al. "Optogenetic stimulation effectively enhances intrinsically generated network synchrony". *Front Neural Circuits*, **7**, 167 (2013). Cited on page: 27.

[Erickson 2008] Erickson, J., Tooker, A., Tai, Y. C., & Pine, J. "Caged neuron MEA: a system for long-term investigation of cultured neural network connectivity". *J Neurosci Methods*, **175**, 1–16 (2008). Cited on page: 21.

[Eurich 2002] Eurich, C. W., Herrmann, J. M., & Ernst, U. A. "Finite-size effects of avalanche dynamics". *Phys Rev E Stat Nonlin Soft Matter Phys*, **66**, 066137 (2002). Cited on page: 23.

[Eversmann 2003] Eversmann, B., Jenkner, M., Hofmann, F., et al. "A 128×128 CMOS biosensor array for extracellular recording of neural activity". *Solid-State Circuits, IEEE Journal of*, **38**, 2306–2317 (2003). Cited on page: 11.

[Eversmann 2011] Eversmann, B., Lambacher, A., Gerling, T., et al. "A neutral tissue interfacing chip for in-vitro applications with 32k recording/ simulation channels on an active aera of 26 mm²". 211–214. Proceedings 2011 (ESSCIRC) (2011). Cited on page: 10.

[Eytan 2006] Eytan, D. & Marom, S. "Dynamics and Effective Topology Underlying Synchronization in Networks of Cortical Neurons". *J Neurosci*, **26**, 8465–8476 (2006). Cited on pages: 23, 38, 73, 135.

[Fagiolo 2007] Fagiolo, G. "Clustering in complex directed networks". *Phys Rev E Stat Nonlin Soft Matter Phys*, **76**, 26107 (2007). Cited on pages: 46, 139.

[Failor 2015] Failor, S., Chapman, B., & Cheng, H.-J. "Retinal waves regulate afferent terminal targeting in the early visual pathway". *Proc Natl Acad Sci USA*, 201506458 (2015). Cited on page: 22.

[Fedirchuk 1999] Fedirchuk, B., Wenner, P., Whelan, P. J., et al. "Spontaneous network activity transiently depresses synaptic transmission in the embryonic chick spinal cord". *J Neurosci*, **19**, 2102–2112 (1999). Cited on page: 22.

[Feinerman 2003] Feinerman, O. & Moses, E. "A picoliter 'fountain-pen' using co-axial dual pipettes". *J Neurosci Methods*, **127**, 75–84 (2003). Cited on page: 15.

[Feinerman 2005] Feinerman, O., Segal, M., & Moses, E. "Signal propagation along unidimensional neuronal networks". *J Neurophysiol*, **94**, 3406–3416 (2005). Cited on pages: 8, 15, 16, 17.

[Feinerman 2006] Feinerman, O. & Moses, E. "Transport of information along unidimensional layered networks of dissociated hippocampal neurons and implications for rate coding". *J Neurosci*, **26**, 4526–4534 (2006). Cited on page: 16.

[Feinerman 2007] Feinerman, O., Segal, M., & Moses, E. "Identification and dynamics of spontaneous burst initiation zones in unidimensional neuronal cultures". *J Neurophysiol*, **97**, 2937–2948 (2007). Cited on pages: 16, 21, 38.

[Feinerman 2008] Feinerman, O., Rotem, A., & Moses, E. "Reliable neuronal logic devices from patterned hippocampal cultures". *Nat Phys*, **4**, 967–973 (2008). Cited on pages: 8, 9, 16, 38.

[Feizi 2013] Feizi, S., Marbach, D., Médard, M., & Kellis, M. "Network deconvolution as a general method to distinguish direct dependencies in networks". *Nat Biotechnol*, **31**, 726–733 (2013). Cited on page: 165.

[Fenwick 1982] Fenwick, E. M., Marty, A., & Neher, E. "A patch-clamp study of bovine chromaffin cells and of their sensitivity to acetylcholine". *J Physiol*, **331**, 577–597 (1982). Cited on page: 10.

[Field 1972] Field, R. J., Koros, E., & Noyes, R. M. "Oscillations in chemical systems II Thorough analysis of temporal oscillation in the bromate-cerium-malonic acid system". *J Am Chem Soc*, **94**, 8649–8664 (1972). Cited on page: 108.

[Fitzhugh 1961] Fitzhugh, R. "Impulses and Physiological States in Theoretical Models of Nerve Membrane". *Biophys J*, **1**, 445–466 (1961). Cited on page: 108.

[Frega 2012] Frega, M., Pasquale, V., Tedesco, M., et al. "Cortical cultures coupled to micro-electrode arrays: a novel approach to perform in vitro excitotoxicity testing". *Neurotoxicol Teratol*, **34**, 116–127 (2012). Cited on

page: 8.

[Frega 2014] Frega, M., Tedesco, M., Massobrio, P., Pesce, M., & Martinoia, S. "Network dynamics of 3D engineered neuronal cultures: a new experimental model for in-vitro electrophysiology". *Sci Rep*, **4**, 5489 (2014). Cited on page: 27.

[Fregnac 2014] Fregnac, Y. & Laurent, G. "Neuroscience: Where is the brain in the Human Brain Project?". *Nature*, **513**, 27–29 (2014). Cited on pages: 4, 6.

[Frey 2009] Frey, U., Egert, U., Heer, F., Hafizovic, S., & Hierlemann, A. "Microelectronic system for high-resolution mapping of extracellular electric fields applied to brain slices". *Biosens Bioelectron*, **24**, 2191–2198 (2009). Cited on page: 10.

[Friedman 2012] Friedman, N., Ito, S., Brinkman, B. A. W., et al. "Universal Critical Dynamics in High Resolution Neuronal Avalanche Data". *Phys Rev Lett*, **108**, 208102 (2012). Cited on pages: 23, 26.

[Friston 2003] Friston, K. J., Harrison, L., & Penny, W. "Dynamic causal modelling". *NeuroImage*, **19**, 1273–1302 (2003). Cited on page: 35.

[Friston 2011] Friston, K. J. "Functional and effective connectivity: a review". *Brain Connect*, **1**, 13–36 (2011). Cited on page: 33.

[Gaillard 2009] Gaillard, R., Dehaene, S., Adam, C., et al. "Converging intracranial markers of conscious access". *Plos Biol*, **7**, e61 (2009). Cited on page: 33.

[Ganguly 2001] Ganguly, K., Schinder, A. F., Wong, S. T., & Poo, M. "GABA itself promotes the developmental switch of neuronal GABAergic responses from excitation to inhibition". *Cell*, **105**, 521–532 (2001). Cited on page: 22.

[García-Ojalvo 1999] García-Ojalvo, J. & Sancho, J. M. "Noise in spatially extended systems". Institute for Nonlinear Science. Springer, New York, NY (1999). Cited on pages: 107, 118.

[Garcia-Perez 2008] Garcia-Perez, E., Lo, D. C., & Wesseling, J. F. "Kinetic isolation of a slowly recovering component of short-term depression during exhaustive use at excitatory hippocampal synapses". *J Neurophysiol*, **100**, 781–795 (2008). Cited on pages: 31, 41.

[Garofalo 2009] Garofalo, M., Nieus, T., Massobrio, P., & Martinoia, S. "Evaluation of the performance of information theory-based methods and cross-correlation to estimate the functional connectivity in cortical networks".

PLoS ONE, **4**, e6482 (2009). Cited on page: 35.

[Gasparini 2004] Gasparini, S., Migliore, M., & Magee, J. C. "On the initiation and propagation of dendritic spikes in CA1 pyramidal neurons". *J Neurosci*, **24**, 11046–11056 (2004). Cited on page: 32.

[Gee 2000] Gee, K. R., Brown, K. A., Chen, W. N., et al. "Chemical and physiological characterization of fluo-4 Ca(2+)-indicator dyes". *Cell Calcium*, **27**, 97–106 (2000). Cited on page: 12.

[Gewaltig 2007] Gewaltig, M.-O. & Diesmann, M. "NEST (NEural Simulation Tool)". *Scholarpedia*, **2**, 1430 (2007). Cited on page: 51.

[Golding 1998] Golding, N. L. & Spruston, N. "Dendritic sodium spikes are variable triggers of axonal action potentials in hippocampal CA1 pyramidal neurons". *Neuron*, **21**, 1189–1200 (1998). Cited on page: 32.

[Golomb 1997] Golomb, D. & Amitai, Y. "Propagating neuronal discharges in neocortical slices: computational and experimental study". *J Neurophysiol*, **78**, 1199–1211 (1997). Cited on pages: 17, 41.

[Gourévitch 2007] Gourévitch, B. & Eggermont, J. J. "Evaluating information transfer between auditory cortical neurons". *J Neurophysiol*, **97**, 2533–2543 (2007). Cited on page: 35.

[Granger 1969] Granger, C. W. "Investigating causal relations by econometric models and cross-spectral methods". *Econometrica*, 424–438 (1969). Cited on page: 146.

[Grewe 2010] Grewe, B. F., Langer, D., Kasper, H., Kampa, B. M., & Helmchen, F. "High-speed in vivo calcium imaging reveals neuronal network activity with near-millisecond precision". *Nat Met*, **7**, 399–405 (2010). Cited on page: 157.

[Grienberger 2012] Grienberger, C. & Konnerth, A. "Imaging calcium in neurons". *Neuron*, **73**, 862–885 (2012). Cited on pages: 11, 144.

[Grillner 2006] Grillner, S. & Graybiel, A. M. "Microcircuits". The Interface Between Neurons and Global Brain Function. MIT Press (2006). Cited on page: 6.

[Gross 1995] Gross, C. G. "Aristotle on the brain". *Neuroscientist*, **1**, 245–250 (1995). Cited on page: 5.

[Grynkiewicz 1985] Grynkiewicz, G., Poenie, M., & Tsien, R. Y. "A new generation of Ca2+ indicators with greatly improved fluorescence properties". *J Biol Chem*, **260**, 3440–3450 (1985). Cited on page: 12.

[Habets 1987] Habets, A. M. M. C., Van Dongen, A. M. J., Van Huizen, F., & Corner, M. A. "Spontaneous neuronal firing patterns in fetal rat cortical networks during development in vitro: a quantitative analysis". *Exp Brain Res*, **69**, 43–52 (1987). Cited on page: 14.

[Hagmann 2008] Hagmann, P., Cammoun, L., Gigandet, X., et al. "Mapping the structural core of human cerebral cortex". *Plos Biol*, **6**, e159 (2008). Cited on page: 33.

[Haider 2013] Haider, B., Häusser, M., & Carandini, M. "Inhibition dominates sensory responses in the awake cortex". *Nature*, **493**, 97–100 (2013). Cited on page: 136.

[Ham 2008] Ham, M. I., Bettencourt, L. M., McDaniel, F. D., & Gross, G. W. "Spontaneous coordinated activity in cultured networks: analysis of multiple ignition sites, primary circuits, and burst phase delay distributions". *J Comput Neurosci*, **24**, 346–357 (2008). Cited on page: 38.

[Hamill 1981] Hamill, O. P., Marty, A., Neher, E., Sakmann, B., & Sigworth, F. J. "Improved patch-clamp techniques for high-resolution current recording from cells and cell-free membrane patches". *Pflügers Archiv*, **391**, 85–100 (1981). Cited on page: 10.

[Hamilton 2010] Hamilton, N. B. & Attwell, D. "Do astrocytes really exocytose neurotransmitters?". *Nat Rev Neurosci*, **11**, 227–238 (2010). Cited on page: 33.

[Hammond 2001] Hammond, C. "Cellular and Molecular Neurobiology". Academic Press, San Diego (2001). Cited on page: 32.

[Hammond 2008] Hammond, C. "Cellular and Molecular Neurophysiology". Academic Press, San Diego (2008). Cited on page: 32.

[Harris 1963] Harris, T. E. "The Theory of Branching Processes". Springer-Verlag (1963). Cited on page: 25.

[Hernández-Machado 2001] Hernández-Machado, A., Soriano, J., Lacasta, A. M., et al. "Interface roughening in Hele-Shaw flows with quenched disorder: Experimental and theoretical results". *Europhys Lett*, **55**, 194–200 (2001). Cited on page: 21.

[Hirano 1986] Hirano, T. & Ohmori, H. "Voltage-Gated and Synaptic Currents in Rat Purkinje Cells in Dissociated Cell Cultures". *Proc Natl Acad Sci USA*, **83**, 1945–1949 (1986). Cited on page: 10.

[Hollander 1999] Hollander, M. & Wolfe, D. A. "Nonparametric Statistical Methods". Wiley-Interscience (1999). Cited on page: 54.

[Honey 2009] Honey, C. J., Sporns, O., Cammoun, L., et al. "Predicting human resting-state functional connectivity from structural connectivity". *Proc Natl Acad Sci USA*, **106**, 2035–2040 (2009). Cited on page: 33.

[Huang 2012] Huang, Y. & Mucke, L. "Alzheimer mechanisms and therapeutic strategies". *Cell*, **148**, 1204–1222 (2012). Cited on page: 8.

[Huberman 2006] Huberman, A. D., Speer, C. M., & Chapman, B. "Spontaneous retinal activity mediates development of ocular dominance columns and binocular receptive fields in v1". *Neuron*, **52**, 247–254 (2006). Cited on page: 22.

[Ikegaya 2004] Ikegaya, Y., Aaron, G., Cossart, R., et al. "Synfire chains and cortical songs: temporal modules of cortical activity". *Science*, **304**, 559–564 (2004). Cited on page: 101.

[Isaacson 2011] Isaacson, J. S. & Scanziani, M. "How inhibition shapes cortical activity". *Neuron*, **72**, 231–243 (2011). Cited on page: 136.

[Ito 2011] Ito, S., Hansen, M. E., Heiland, R., et al. "Extending transfer entropy improves identification of effective connectivity in a spiking cortical network model". *PLoS ONE*, **6**, e27431 (2011). Cited on pages: 35, 82.

[Ito 2014] Ito, S., Yeh, F.-C., Hiolski, E., et al. "Large-scale, high-resolution multielectrode-array recording depicts functional network differences of cortical and hippocampal cultures". *PLoS ONE*, **9**, e105324 (2014). Cited on page: 10.

[Ivenshitz 2010] Ivenshitz, M. & Segal, M. "Neuronal density determines network connectivity and spontaneous activity in cultured hippocampus". *J Neurophysiol*, **104**, 1052–1060 (2010). Cited on pages: 29, 30, 32.

[Izhikevich 2003] Izhikevich, E. M. "Simple model of spiking neurons". *IEEE Trans Neural Netw*, **14**, 1569–1572 (2003). Cited on pages: 17, 39, 40.

[Izhikevich 2007] Izhikevich, E. M. "Dynamical Systems in Neuroscience". MIT Press, Cambridge, Massachusetts (2007). Cited on pages: 17, 18, 39, 108, 119.

[Jacobi 2007] Jacobi, S. & Moses, E. "Variability and corresponding amplitude-velocity relation of activity propagating in one-dimensional neural cultures". *J Neurophysiol*, **97**, 3597–3606 (2007). Cited on pages: 10, 11.

[Jacobi 2009] Jacobi, S., Soriano, J., Segal, M., & Moses, E. "BDNF and NT-3 increase excitatory input connectivity in rat hippocampal cultures". *Eur J Neurosci*, **30**, 998–1010 (2009). Cited on pages: 30, 144, 156.

[Jacobi 2010] Jacobi, S., Soriano, J., & Moses, E. "BDNF and NT-3 increase velocity of activity front propagation in unidimensional hippocampal cultures". *J Neurophysiol*, **104**, 2932–2939 (2010). Cited on page: 62.

[Jimbo 1999] Jimbo, Y., Tateno, T., & Robinson, H. P. "Simultaneous induction of pathway-specific potentiation and depression in networks of cortical neurons". *Biophys J*, **76**, 670–678 (1999). Cited on page: 30.

[Jonas 1998] Jonas, P., Bischofberger, J., & Sandkühler, J. "Corelease of two fast neurotransmitters at a central synapse". *Science*, **281**, 419–424 (1998). Cited on page: 158.

[Kaiser 2002] Kaiser, A. & Schreiber, T. "Information transfer in continuous processes". *Phys D*, **166**, 43–62 (2002). Cited on page: 35.

[Kandel 1967] Kandel, E. R. "Dale's principle and the functional specificity of neurons". In Electrophysiological Studies in Neuropharmacology, 385–398. Springfield, Ill.: CC Thomas (1967). Cited on page: 150.

[Kavalali 2015] Kavalali, E. T. "The mechanisms and functions of spontaneous neurotransmitter release". *Nat Rev Neurosci*, **16**, 5–16 (2015). Cited on page: 32.

[Keller 2008] Keller, P. J., Schmidt, A. D., Wittbrodt, J., & Stelzer, E. H. K. "Reconstruction of Zebrafish Early Embryonic Development by Scanned Light Sheet Microscopy". *Science*, **322**, 1065 (2008). Cited on page: 12.

[Kerr 2008] Kerr, J. N. D. & Denk, W. "Imaging in vivo: watching the brain in action". *Nat Rev Neurosci*, **9**, 195–205 (2008). Cited on page: 157.

[Kitsak 2010] Kitsak, M., Gallos, L. K., Havlin, S., et al. "Identification of influential spreaders in complex networks". *Nat Phys*, **6**, 888–893 (2010). Cited on pages: 164, 165.

[Kobayashi 2013] Kobayashi, R. & Kitano, K. "Impact of network topology on inference of synaptic connectivity from multi-neuronal spike data simulated by a large-scale cortical network model". *J Comput Neurosci*, **35**, 109–124

(2013). Cited on page: 35.

[Kudo 1986] Kudo, Y. & Ogura, A. "Glutamate-induced increase in intracellular Ca2+ concentration in isolated hippocampal neurones". *Br J Pharmacol*, **89**, 191–198 (1986). Cited on page: 12.

[Kumar 2010] Kumar, A., Rotter, S., & Aertsen, A. "Spiking activity propagation in neuronal networks: reconciling different perspectives on neural coding". *Nat Rev Neurosci*, **11**, 615–627 (2010). Cited on page: 101.

[Lambacher 2011] Lambacher, A., Vitzthum, V., Zeitler, R., et al. "Identifying firing mammalian neurons in networks with high-resolution multi-transistor array (MTA)". *Applied Physics A*, **102**, 1–11 (2011). Cited on page: 10.

[Lander 2001] Lander, E. S., Linton, L. M., Birren, B., et al. "Initial sequencing and analysis of the human genome". *Nature*, **409**, 860–921 (2001). Cited on page: 4.

[Latham 2000] Latham, P. E., Richmond, B. J., Nirenberg, S., & Nelson, P. G. "Intrinsic dynamics in neuronal networks II experiment". *J Neurophysiol*, **83**, 828–835 (2000). Cited on pages: 32, 62.

[Laurson 2013] Laurson, L., Illa, X., Santucci, S., et al. "Evolution of the average avalanche shape with the universality class". *Nat Commun*, **4**, 2927 (2013). Cited on page: 164.

[Levina 2007] Levina, A., Herrmann, J. M., & Geisel, T. "Dynamical synapses causing self-organized criticality in neural networks". *Nat Phys*, **3**, 857–860 (2007). Cited on pages: 25, 67.

[Levina 2009] Levina, A., Herrmann, J. M., & Geisel, T. "Phase Transitions towards Criticality in a Neural System with Adaptive Interactions". *Phys Rev Lett*, **102**, 118110 (2009). Cited on pages: 25, 67.

[Lewicki 1998] Lewicki, M. S. "A review of methods for spike sorting: the detection and classification of neural action potentials". *Network*, **9**, R53–78 (1998). Cited on page: 10.

[Lichtman 2008] Lichtman, J. W., Livet, J., & Sanes, J. R. "A technicolour approach to the connectome". *Nat Rev Neurosci*, **9**, 417–422 (2008). Cited on page: 150.

[Lichtman 2014] Lichtman, J. W., Pfister, H., & Shavit, N. "The big data challenges of connectomics". *Nat Neurosci*, **17**, 1448–1454 (2014). Cited on pages: 6, 28.

[Lin 2002] Lin, Y.-C., Huang, Z.-H., Jan, I.-S., et al. "Development of excitatory synapses in cultured neurons dissociated from the cortices of rat embryos and rat pups at birth". *J Neurosci Res*, **67**, 484–493 (2002). Cited on page: 30.

[Linaro 2011] Linaro, D., Storace, M., & Mattia, M. "Inferring network dynamics and neuron properties from population recordings". *Front Comput Neurosci*, **5**, 43 (2011). Cited on page: 156.

[Lindner 2004] Lindner, B., García-Ojalvo, J., Neiman, A., & Schimansky-Geier, L. "Effects of noise in excitable systems". *Physics Reports*, **392**, 321–424 (2004). Cited on pages: 107, 108.

[Litke 2004] Litke, A. M., Bezayiff, N., Chichilnisky, E. J., et al. "What Does the Eye Tell the Brain?: Development of a System for the Large-Scale Recording of Retinal Output Activity". *IEEE Transactions on Nuclear Science*, **51**, 1434–1440 (2004). Cited on page: 10.

[Lloyd 1982] Lloyd, S. "Least squares quantization in PCM". *IEEE Trans Inform Theory*, **28**, 129–137 (1982). Cited on page: 128.

[Logothetis 2008] Logothetis, N. K. "What we can do and what we cannot do with fMRI". *Nature*, **453**, 869–878 (2008). Cited on page: 34.

[Lombardi 2012] Lombardi, F., Herrmann, H. J., Perrone-Capano, C., Plenz, D., & de Arcangelis, L. "Balance between Excitation and Inhibition Controls the Temporal Organization of Neuronal Avalanches". *Phys Rev Lett*, **108**, 228703 (2012). Cited on pages: 26, 136.

[Long 2010] Long, M. A., Jin, D. Z., & Fee, M. S. "Support for a synaptic chain model of neuronal sequence generation". *Nature*, **468**, 394–399 (2010). Cited on page: 101.

[Lütcke 2013] Lütcke, H., Gerhard, F., Zenke, F., Gerstner, W., & Helmchen, F. "Inference of neuronal network spike dynamics and topology from calcium imaging data". *Front Neural Circuits*, **7** (2013). Cited on page: 165.

[Lynall 2010] Lynall, M.-E., Bassett, D. S., Kerwin, R., et al. "Functional connectivity and brain networks in schizophrenia". *J Neurosci*, **30**, 9477–9487 (2010). Cited on page: 33.

[Madhavan 2006] Madhavan, R., Chao, Z. C., Wagenaar, D. A., Bakkum, D. J., & Potter, S. M. "Multi-site stimulation quiets network-wide spontaneous bursts and enhances functional plasticity in cultured cortical networks". In Conf Proc IEEE Eng Med Biol Soc, 1593–1596 (2006). Cited on page: 153.

[Maeda 1995] Maeda, E., Robinson, H. P., & Kawana, A. "The mechanisms of generation and propagation of synchronized bursting in developing networks of cortical neurons". *J Neurosci*, **15**, 6834–6845 (1995). Cited on pages: 11, 14, 15, 31, 38, 64, 135.

[Maeda 1998] Maeda, E., Kuroda, Y., Robinson, H. P. C., & Kawana, A. "Modification of parallel activity elicited by propagating bursts in developing networks of rat cortical neurones". *Eur J Neurosci*, **10**, 488–496 (1998). Cited on page: 30.

[Magee 2000] Magee, J. C. & Cook, E. P. "Somatic EPSP amplitude is independent of synapse location in hippocampal pyramidal neurons". *Nat Neurosci*, **3**, 895–903 (2000). Cited on page: 29.

[Maimon 2010] Maimon, O. & Rokach, L., editors. "Data Mining and Knowledge Discovery Handbook". Springer US, Boston, MA (2010). Cited on page: 55.

[Mao 2001] Mao, B. Q., Hamzei-Sichani, F., Aronov, D., Froemke, R. C., & Yuste, R. "Dynamics of spontaneous activity in neocortical slices". *Neuron*, **32**, 883–898 (2001). Cited on page: 157.

[Marconi 2012] Marconi, E., Nieus, T., Maccione, A., et al. "Emergent Functional Properties of Neuronal Networks with Controlled Topology". *PLoS ONE*, **7**, 34648 (2012). Cited on page: 35.

[Marissal 2012] Marissal, T., Bonifazi, P., Picardo, M. A., et al. "Pioneer glutamatergic cells develop into a morpho-functionally distinct population in the juvenile CA3 hippocampus". *Nat Commun*, **3**, 1316 (2012). Cited on page: 157.

[Markram 2012] Markram, H., Gerstner, W., & Sjöström, P. J. "Spike-timing-dependent plasticity: a comprehensive overview". *Front Syn Neurosci*, **4**, 2 (2012). Cited on page: 5.

[Marom 2002] Marom, S. & Shahaf, G. "Development, learning and memory in large random networks of cortical neurons: lessons beyond anatomy". *Q Rev Biophys*, **35**, 63–87 (2002). Cited on pages: 29, 32, 38.

[Mazzoni 2007] Mazzoni, A., Broccard, F. D., Garcia-Perez, E., et al. "On the dynamics of the spontaneous activity in neuronal networks". *PLoS ONE*, **2**, e439 (2007). Cited on pages: 25, 67, 135.

[McIntyre 2004] McIntyre, C. C., Savasta, M., Kerkerian-Le Goff, L., & Vitek, J. L. "Uncovering the mechanism(s) of action of deep brain stimulation: activation, inhibition, or both". *Clin Neurophysiol*, **115**, 1239–1248 (2004).

Cited on page: 153.

[McKinney 1999] McKinney, R. A., Capogna, M., Dürr, R., Gähwiler, B. H., & Thompson, S. M. "Miniature synaptic events maintain dendritic spines via AMPA receptor activation". *Nat Neurosci*, **2**, 44–49 (1999). Cited on page: 32.

[Millman 2010] Millman, D., Mihalas, S., Kirkwood, A., & Niebur, E. "Self-organized criticality occurs innon-conservative neuronal networks during'up' states". *Nat Phys*, **5**, 1–5 (2010). Cited on pages: 26, 67.

[Minta 1989] Minta, A., Kao, J. P., & Tsien, R. Y. "Fluorescent indicators for cytosolic calcium based on rhodamine and fluorescein chromophores". *J Biol Chem*, **264**, 8171–8178 (1989). Cited on page: 12.

[Mishchenko 2011a] Mishchenko, Y. & Paninski, L. "Efficient methods for sampling spike trains in networks of coupled neurons". *Ann Appl Stat*, **5**, 1893–1919 (2011). Cited on page: 165.

[Mishchenko 2011b] Mishchenko, Y., Vogelstein, J. T., & Paninski, L. "A Bayesian approach for inferring neuronal connectivity from calcium fluorescent imaging data". *Ann Appl Stat*, **5**, 1229–1261 (2011). Cited on pages: 141, 143, 149.

[Moneta 2005] Moneta, A. & Spirtes, P. "Graph-based search procedure for vector autoregressive models". *LEM Working Paper Series* (2005). Cited on page: 35.

[Moons 2009] Moons, W. G., Mackie, D. M., & Garcia-Marques, T. "The impact of repetition-induced familiarity on agreement with weak and strong arguments". *J Pers Soc Psychol*, **96**, 32–44 (2009). Cited on page: 164.

[Moretti 2013] Moretti, P. & Munoz, M. A. "Griffiths phases and the stretching of criticality in brain networks". *Nat Commun*, **4**, 2521 (2013). Cited on page: 164.

[Müller 1997] Müller, T. H., Swandulla, D., & Zeilhofer, H. U. "Synaptic connectivity in cultured hypothalamic neuronal networks". *J Neurophysiol*, **77**, 3218–3225 (1997). Cited on page: 29.

[Murphy 1992] Murphy, T. H., Blatter, L. A., Wier, W. G., & Baraban, J. M. "Spontaneous synchronous synaptic calcium transients in cultured cortical neurons". *J Neurosci*, **12**, 4834–4845 (1992). Cited on page: 14.

[Murthy 2001] Murthy, V. N., Schikorski, T., Stevens, C. F., & Zhu, Y. "Inactivity produces increases in neurotransmitter release and synapse size". *Neuron*, **32**,

673–682 (2001). Cited on page: 30.

[Nagler 2011] Nagler, J., Levina, A., & Timme, M. "Impact of single links in competitive percolation". *Nat Phys*, **6**, 1–6 (2011). Cited on page: 165.

[Nagumo 1962] Nagumo, J., Arimoto, S., & Yoshizawa, S. "An active pulse transmission line simulating nerve axon". In Proceedings of the IRE, 2061–2070 (1962). Cited on page: 108.

[Nakai 2001] Nakai, J., Ohkura, M., & Imoto, K. "A high signal-to-noise Ca2+ probe composed of a single green fluorescent protein". *Nat Biotechnol*, **19**, 137–141 (2001). Cited on page: 12.

[Nakanishi 1998] Nakanishi, K. & Kukita, F. "Functional synapses in synchronized bursting of neocortical neurons in culture". *Brain Research*, **795**, 137–146 (1998). Cited on page: 30.

[Neher 1976] Neher, E. & Sakmann, B. "Single-channel currents recorded from membrane of denervated frog muscle fibres". *Nature*, **260**, 799–802 (1976). Cited on page: 10.

[Nelson 1975] Nelson, P. G. "Nerve and muscle cells in culture". *Physiol Rev*, **55**, 61 (1975). Cited on page: 8.

[Nicosia 2013] Nicosia, V., Vértes, P. E., Schafer, W. R., Latora, V., & Bullmore, E. T. "Phase transition in the economically modeled growth of a cellular nervous system". *Proc Natl Acad Sci USA*, **110**, 7880–7885 (2013). Cited on page: 7.

[Nolte 2010] Nolte, G. & Müller, K.-R. "Localizing and estimating causal relations of interacting brain rhythms". *Front Hum Neurosci*, **4**, 209 (2010). Cited on page: 35.

[Ogura 1987] Ogura, A., Iijima, T., Amano, T., & Kudo, Y. "Optical monitoring of excitatory synaptic activity between cultured hippocampal neurons by a multi-site Ca2+ fluorometry". *Neurosci Lett*, **78**, 69–74 (1987). Cited on pages: 12, 13, 14.

[Olami 1992] Olami, Z., Feder, H., & Christensen, K. "Self-organized criticality in a continuous, nonconservative cellular automaton modeling earthquakes". *Phys Rev Lett*, **68**, 1244–1247 (1992). Cited on page: 25.

[Opitz 2002] Opitz, T., de Lima, A. D., & Voigt, T. "Spontaneous development of synchronous oscillatory activity during maturation of cortical networks in vitro". *J Neurophysiol*, **88**, 2196–2206 (2002). Cited on pages: 14, 31, 32, 38,

62.

[Orlandi 2013] Orlandi, J. G., Soriano, J., Alvarez-Lacalle, E., Teller, S., & Casademunt, J. "Noise focusing and the emergence of coherent activity in neuronal cultures". *Nat Phys*, **9**, 582–590 (2013). Cited on pages: 8, 12, 159, 163.

[Orlandi 2014] Orlandi, J. G., Stetter, O., Soriano, J., Geisel, T., & Battaglia, D. "Transfer entropy reconstruction and labeling of neuronal connections from simulated calcium imaging". *PLoS ONE*, **9**, e98842 (2014). Cited on page: 163.

[Osan 2004] Osan, R., Curtu, R., Rubin, J., & Ermentrout, B. "Multiple-spike waves in a one-dimensional integrate-and-fire neural network". *J Math Biol*, **48**, 243–274 (2004). Cited on page: 16.

[Otsu 2003] Otsu, Y. & Murphy, T. H. "Miniature transmitter release: accident of nature or careful design?". *Sci STKE*, **2003**, pe54 (2003). Cited on page: 32.

[Pajevic 2009] Pajevic, S. & Plenz, D. "Efficient network reconstruction from dynamical cascades identifies small-world topology of neuronal avalanches". *PLoS Comput Biol*, **5**, e1000271 (2009). Cited on page: 147.

[Pampaloni 2007] Pampaloni, F., Reynaud, E. G., & Stelzer, E. H. K. "The third dimension bridges the gap between cell culture and live tissue". *Nat Rev Mol Cell Biol*, **8**, 839–845 (2007). Cited on page: 27.

[Pasquale 2008] Pasquale, V., Massobrio, P., Bologna, L. L., Chiappalone, M., & Martinoia, S. "Self-organization and neuronal avalanches in networks of dissociated cortical neurons". *Neuroscience*, **153**, 1354–1369 (2008). Cited on pages: 11, 25, 135.

[Pearl 2000] Pearl, J. "Causality: models, reasoning, and inference". Cambridge University Press (2000). Cited on page: 34.

[Perin 2011] Perin, R., Berger, T. K., & Markram, H. "A synaptic organizing principle for cortical neuronal groups". *Proc Natl Acad Sci USA*, **108**, 5419–5424 (2011). Cited on page: 139.

[Pine 1980] Pine, J. "Recording action potentials from cultured neurons with extracellular microcircuit electrodes". *J Neurosci Methods*, **2**, 19–31 (1980). Cited on page: 10.

[Pinto 2001] Pinto, D. J. & Ermentrout, G. B. "Spatially structured activity in synaptically coupled neuronal networks: I Traveling fronts and pulses". *SIAM*

journal on Applied Mathematics, **62**, 206–225 (2001). Cited on page: 16.

[Poil 2012] Poil, S.-S., Hardstone, R., Mansvelder, H. D., & Linkenkaer-Hansen, K. "Critical-state dynamics of avalanches and oscillations jointly emerge from balanced excitation/inhibition in neuronal networks". *J Neurosci*, **32**, 9817–9823 (2012). Cited on pages: 26, 136.

[Popescu 2013] Popescu, E. b., Popescu, F., & Guyon, I., editors. "Causality in Time Series", volume 5 of *Challenges in Machine Learning*. Microtome Publishing (2013). Cited on page: 34.

[Popiel 2009] Popiel, M. R. "Experiments on Patterned Neural Networks". Master's thesis, Universitat de Barcelona (2009). Cited on page: 22.

[Power 2011] Power, J. D., Cohen, A. L., Nelson, S. M., et al. "Functional network organization of the human brain". *Neuron*, **72**, 665–678 (2011). Cited on page: 33.

[Priesemann 2009] Priesemann, V., Munk, M. H. J., & Wibral, M. "Subsampling effects in neuronal avalanche distributions recorded in vivo". *BMC Neuroscience*, **10**, 40 (2009). Cited on page: 27.

[Priesemann 2013] Priesemann, V., Valderrama, M., Wibral, M., & Le Van Quyen, M. "Neuronal avalanches differ from wakefulness to deep sleep–evidence from intracranial depth recordings in humans". *PLoS Comput Biol*, **9**, e1002985 (2013). Cited on page: 26.

[Priesemann 2014] Priesemann, V., Wibral, M., Valderrama, M., et al. "Spike avalanches in vivo suggest a driven, slightly subcritical brain state". *Front Syst Neurosci*, **8** (2014). Cited on page: 26.

[Provine 1972] Provine, R. R. "Ontogeny of bioelectric activity in the spinal cord of the chick embryo and its behavioral implications". *Brain Research*, **41**, 365–378 (1972). Cited on page: 22.

[Pruessner 2012] Pruessner, G. "Self-Organised Criticality". Theory, Models and Characterisation. Cambridge Univ Press (2012). Cited on page: 25.

[Pu 2013] Pu, J., Gong, H., Li, X., & Luo, Q. "Developing neuronal networks: Self-organized criticality predicts the future". *Sci Rep*, **3**, 1081 (2013). Cited on pages: 8, 9, 25, 164.

[Raizada 2003] Raizada, R. D. S. & Grossberg, S. "Towards a theory of the laminar architecture of cerebral cortex: computational clues from the visual

system". *Cereb Cortex*, **13**, 100–113 (2003). Cited on page: 33.

[Reig 2006] Reig, R., Gallego, R., Nowak, L. G., & Sanchez-Vives, M. V. "Impact of cortical network activity on short-term synaptic depression". *Cereb Cortex*, **16**, 688–695 (2006). Cited on pages: 18, 31.

[Renault 2013] Renault, R., Monceau, P., & Bottani, S. "Memory decay and loss of criticality in quorum percolation". *Phys Rev E Stat Nonlin Soft Matter Phys*, **88**, 062134 (2013). Cited on pages: 123, 125.

[Renault 2014] Renault, R., Monceau, P., Bottani, S., & Métens, S. "Effective non-universality of the quorum percolation model on directed graphs with Gaussian in-degree". *Phys A*, **414**, 352–359 (2014). Cited on pages: 126, 127.

[Rizzoli 2005] Rizzoli, S. O. & Betz, W. J. "Synaptic vesicle pools". *Nat Rev Neurosci*, **6**, 57–69 (2005). Cited on pages: 18, 31.

[Robinson 1993] Robinson, H. P., Kawahara, M., Jimbo, Y., et al. "Periodic synchronized bursting and intracellular calcium transients elicited by low magnesium in cultured cortical neurons". *J Neurophysiol*, **70**, 1606–1616 (1993). Cited on pages: 11, 14, 32.

[Ruiz-Mejias 2011] Ruiz-Mejias, M., Ciria-Suarez, L., Mattia, M., & Sanchez-Vives, M. V. "Slow and fast rhythms generated in the cerebral cortex of the anesthetized mouse". *J Neurophysiol*, **106**, 2910–2921 (2011). Cited on pages: 26, 37.

[Ryali 2012] Ryali, S., Chen, T., Supekar, K., & Menon, V. "Estimation of functional connectivity in fMRI data using stability selection-based sparse partial correlation with elastic net penalty". *NeuroImage*, **59**, 3852–3861 (2012). Cited on page: 35.

[Sagués 2007] Sagués, F., Sancho, J. M., & García-Ojalvo, J. "Spatiotemporal order out of noise". *Rev Mod Phys*, **79**, 829–882 (2007). Cited on pages: 107, 108.

[Sanchez-Vives 2000] Sanchez-Vives, M. V. & McCormick, D. A. "Cellular and network mechanisms of rhythmic recurrent activity in neocortex". *Nat Neurosci*, **3**, 1027–1034 (2000). Cited on page: 37.

[Sanchez-Vives 2010] Sanchez-Vives, M. V., Mattia, M., Compte, A., et al. "Inhibitory modulation of cortical up states". *J Neurophysiol*, **104**, 1314–1324 (2010). Cited on page: 26.

[Schreiber 2000] Schreiber, T. "Measuring information transfer". *Phys Rev Lett*, **85**, 461–464 (2000). Cited on pages: 35, 137, 146.

[Schwab 2014] Schwab, D. J., Nemenman, I., & Mehta, P. "Zipf's law and criticality in multivariate data without fine-tuning". *Phys Rev Lett* (2014). Cited on page: 26.

[Seeley 2009] Seeley, W. W., Crawford, R. K., Zhou, J., Miller, B. L., & Greicius, M. D. "Neurodegenerative diseases target large-scale human brain networks". *Neuron*, **62**, 42–52 (2009). Cited on page: 33.

[Segal 1992] Segal, M. & Manor, D. "Confocal microscopic imaging of [Ca2+]i in cultured rat hippocampal neurons following exposure to N-methyl-D-aspartate". *J Physiol*, **448**, 655–676 (1992). Cited on pages: 88, 159.

[Segev 2002] Segev, R., Benveniste, M., Hulata, E., et al. "Long Term Behavior of Lithographically Prepared In Vitro Neuronal Networks". *Phys Rev Lett*, **88**, 118102 (2002). Cited on page: 14.

[Segev 2003] Segev, R., Benveniste, M., Shapira, Y., & Ben-Jacob, E. "Formation of Electrically Active Clusterized Neural Networks". *Phys Rev Lett*, **90**, 168101 (2003). Cited on page: 20.

[Segev 2004] Segev, R., Baruchi, I., Hulata, E., & Ben-Jacob, E. "Hidden Neuronal Correlations in Cultured Networks". *Phys Rev Lett*, **92**, 118102 (2004). Cited on pages: 14, 38.

[Sejnowski 2014] Sejnowski, T. J., Churchland, P. S., & Movshon, J. A. "Putting big data to good use in neuroscience". *Nat Neurosci*, **17**, 1440–1441 (2014). Cited on page: 5.

[Sendiña-Nadal 2000] Sendiña-Nadal, I., Alonso, S., Pérez-Muñuzuri, V., et al. "Brownian motion of spiral waves driven by spatiotemporal structured noise". *Phys Rev Lett*, **84**, 2734–2737 (2000). Cited on page: 108.

[Serra 2010] Serra, M., Guaraldi, M., & Shea, T. B. "Inhibitory neurons modulate spontaneous signaling in cultured cortical neurons: density-dependent regulation of excitatory neuronal signaling". *Phys Biol*, **7**, 026009 (2010). Cited on pages: 32, 33.

[Serrano 2006] Serrano, M. A. & Boguñá, M. "Clustering in complex networks II Percolation properties". *Phys Rev E Stat Nonlin Soft Matter Phys*, **74**, 56115 (2006). Cited on page: 45.

[Seung 2013] Seung, S. "How the Brain's Wiring Makes Us Who We Are". Mariner Books (2013). Cited on page: 28.

[Shahaf 2001] Shahaf, G. & Marom, S. "Learning in networks of cortical neurons". *J Neurosci*, **21**, 8782–8788 (2001). Cited on page: 30.

[Sharp 1993] Sharp, A. A., O'Neil, M. B., Abbott, L. F., & Marder, E. "Dynamic clamp: computer-generated conductances in real neurons". *J Neurophysiol*, **69**, 992–995 (1993). Cited on page: 18.

[Shein 2008] Shein, M., Volman, V., Raichman, N., Hanein, Y., & Ben-Jacob, E. "Management of synchronized network activity by highly active neurons". *Phys Biol*, **5**, 036008 (2008). Cited on page: 64.

[Shen 2013] Shen, H. "NIH serves up wide menu for US brain-mapping initiative". *Nature* (2013). Cited on pages: 4, 14.

[Shimomura 1962] Shimomura, O., Johnson, F. H., & SAIGA, Y. "Extraction, purification and properties of aequorin, a bioluminescent protein from the luminous hydromedusan, Aequorea". *J Cell Comp Physiol*, **59**, 223–239 (1962). Cited on page: 12.

[Shimono 2014] Shimono, M. & Beggs, J. M. "Functional Clusters, Hubs, and Communities in the Cortical Microconnectome". *Cerebral Cortex* (2014). Cited on pages: 8, 11, 35.

[Sjöström 2008] Sjöström, P. J., Rancz, E. A., Roth, A., & Häusser, M. "Dendritic excitability and synaptic plasticity". *Physiol Rev*, **88**, 769–840 (2008). Cited on page: 5.

[Snider 2010] Snider, J., Pillai, A., & Stevens, C. F. "A universal property of axonal and dendritic arbors". *Neuron*, **66**, 45–56 (2010). Cited on page: 28.

[Soriano 2002] Soriano, J., Ramasco, J. J., Rodríguez, M. A., Hernández-Machado, A., & Ortín, J. "Anomalous Roughening of Hele-Shaw Flows with Quenched Disorder". *Phys Rev Lett*, **89**, 026102 (2002). Cited on page: 21.

[Soriano 2008] Soriano, J., Rodríguez Martínez, M., Tlusty, T., & Moses, E. "Development of input connections in neural cultures". *Proc Natl Acad Sci USA*, **105**, 13758–13763 (2008). Cited on pages: 8, 9, 21, 38, 40, 53, 57, 62, 88, 91, 123, 126, 144, 153, 156, 159.

[Sorkin 2006] Sorkin, R., Gabay, T., Blinder, P., et al. "Compact self-wiring in cultured neural networks". *J Neural Eng*, **3**, 95–101 (2006). Cited on page: 20.

[Sorkin 2009] Sorkin, R., Greenbaum, A., David-Pur, M., et al. "Process entanglement as a neuronal anchorage mechanism to rough surfaces". *Nanotechnology*, **20**, 015101 (2009). Cited on page: 20.

[Soto 2012] Soto, F., Ma, X., Cecil, J. L., et al. "Spontaneous activity promotes synapse formation in a cell-type-dependent manner in the developing retina". *J Neurosci*, **32**, 5426–5439 (2012). Cited on page: 37.

[Spitzer 2006] Spitzer, N. C. "Electrical activity in early neuronal development". *Nature*, **444**, 707–712 (2006). Cited on page: 37.

[Sporns 2012] Sporns, O. "Discovering the Human Connectome". The MIT Press (2012). Cited on page: 28.

[Spruston 2008] Spruston, N. "Pyramidal neurons: dendritic structure and synaptic integration". *Nat Rev Neurosci*, **9**, 206–221 (2008). Cited on page: 29.

[Staley 1998] Staley, K. J., Longacher, M., Bains, J. S., & Yee, A. "Presynaptic modulation of CA3 network activity". *Nat Neurosci*, **1**, 201–209 (1998). Cited on page: 30.

[Stetter 2012] Stetter, O., Battaglia, D., Soriano, J., & Geisel, T. "Model-free reconstruction of excitatory neuronal connectivity from calcium imaging signals". *PLoS Comput Biol*, **8**, e1002653 (2012). Cited on pages: 8, 12, 13, 34, 35, 82, 136, 137, 138, 140, 141, 146, 147, 149, 153, 157, 159.

[Stevens 2003] Stevens, C. F. "Neurotransmitter release at central synapses". *Neuron*, **40**, 381–388 (2003). Cited on page: 18.

[Stosiek 2003] Stosiek, C., Garaschuk, O., Holthoff, K., & Konnerth, A. "In vivo two-photon calcium imaging of neuronal networks". In Proceedings of the National Academy of Science, 7319–7324 (2003). Cited on page: 157.

[Stumpf 2012] Stumpf, M. P. H. & Porter, M. A. "Mathematics Critical truths about power laws". *Science*, **335**, 665–666 (2012). Cited on page: 26.

[Su 2001] Su, H., Alroy, G., Kirson, E. D., & Yaari, Y. "Extracellular calcium modulates persistent sodium current-dependent burst-firing in hippocampal pyramidal neurons". *J Neurosci*, **21**, 4173–4182 (2001). Cited on page: 32.

[Sutton 2007] Sutton, M. A., Taylor, A. M., Ito, H. T., Pham, A., & Schuman, E. M. "Postsynaptic decoding of neural activity: eEF2 as a biochemical sensor coupling miniature synaptic transmission to local protein synthesis". *Neuron*, **55**, 648–661 (2007). Cited on page: 32.

[Svoboda 2006] Svoboda, K. & Yasuda, R. "Principles of two-photon excitation microscopy and its applications to neuroscience". *Neuron*, **50**, 823–839 (2006). Cited on page: 12.

[Tabak 2001] Tabak, J., Rinzel, J., & O'Donovan, M. J. "The role of activity-dependent network depression in the expression and self-regulation of spontaneous activity in the developing spinal cord". *J Neurosci*, **21**, 8966–8978 (2001). Cited on page: 31.

[Tabak 2003] Tabak, J. & Latham, P. E. "Analysis of spontaneous bursting activity in random neural networks". *Neuroreport*, **14**, 1445–1449 (2003). Cited on page: 62.

[Teller 2014] Teller, S., Granell, C., De Domenico, M., et al. "Emergence of assortative mixing between clusters of cultured neurons". *PLoS Comput Biol*, **10**, e1003796 (2014). Cited on pages: 8, 9, 21.

[Tetzlaff 2010] Tetzlaff, C., Okujeni, S., Egert, U., Wörgötter, F., & Butz, M. "Self-organized criticality in developing neuronal networks". *PLoS Comput Biol*, **6**, e1001013 (2010). Cited on pages: 8, 11, 25, 67, 82, 135, 164.

[Thomas 1972] Thomas, C. A., Springer, P. A., Loeb, G. E., Berwald-Netter, Y., & Okun, L. M. "A miniature microelectrode array to monitor the bioelectric activity of cultured cells". *Exp Cell Res*, **74**, 61–66 (1972). Cited on page: 10.

[Tibau 2013] Tibau, E., Valencia, M., & Soriano, J. "Identification of neuronal network properties from the spectral analysis of calcium imaging signals in neuronal cultures". *Front Neural Circuits*, **7** (2013). Cited on page: 144.

[Tlusty 2009] Tlusty, T. & Eckmann, J.-P. "Remarks on bootstrap percolation in metric networks". *J Phys A*, **42**, 205004 (2009). Cited on pages: 57, 72, 123, 124.

[Tscherter 2001] Tscherter, A., Heuschkel, M. O., Renaud, P., & Streit, J. "Spatiotemporal characterization of rhythmic activity in rat spinal cord slice cultures". *Eur J Neurosci*, **14**, 179–190 (2001). Cited on pages: 11, 37.

[Tsodyks 1997] Tsodyks, M. V. & Markram, H. "The Neural Code between Neocortical Pyramidal Neurons Depends on Neurotransmitter Release Probability". 719–723 (1997). Cited on pages: 18, 41, 141.

[Tsodyks 2000] Tsodyks, M., Uziel, A., & Markram, H. "Synchrony generation in recurrent networks with frequency-dependent synapses". *J Neurosci*, **20**, RC50 (2000). Cited on page: 41.

[Turrigiano 2004] Turrigiano, G. G. & Nelson, S. B. "Homeostatic plasticity in the developing nervous system". *Nat Rev Neurosci*, **5**, 97–107 (2004). Cited on page: 30.

[Turrigiano 2011] Turrigiano, G. "Too many cooks? Intrinsic and synaptic homeostatic mechanisms in cortical circuit refinement". *Annu Rev Neurosci*, **34**, 89–103 (2011). Cited on page: 30.

[Tyson 1980] Tyson, J. J. & Fife, P. C. "Target patterns in a realistic model of the Belousov-Zhabotinskii reaction". *J Chem Phys*, **73**, 2224–2237 (1980). Cited on page: 108.

[Van Huizen 1987] Van Huizen, F., Romijn, H. J., & Habets, A. "Accelerated neural network formation in rat cerebral cortex cultures chronically disinhibited with picrotoxin". *Exp Neurol*, **97**, 280–288 (1987). Cited on page: 30.

[Van Ooyen 1995] Van Ooyen, A., Van Pelt, J., & Corner, M. A. "Implications of activity dependent neurite outgrowth for neuronal morphology and network development". *J Theor Biol*, **172**, 63–82 (1995). Cited on page: 44.

[van Ooyen 2011] van Ooyen, A. "Using theoretical models to analyse neural development". *Nat Rev Neurosci*, **12**, 311–326 (2011). Cited on page: 30.

[Van Pelt 2004a] Van Pelt, J., Corner, M. A., Wolters, P. S., Rutten, W. L. C., & Ramakers, G. J. A. "Longterm stability and developmental changes in spontaneous network burst firing patterns in dissociated rat cerebral cortex cell cultures on multielectrode arrays". *Neurosci Lett*, **361**, 86–89 (2004). Cited on pages: 11, 23.

[van Pelt 2004b] van Pelt, J., Wolters, P. S., Corner, M. A., Rutten, W. L. C., & Ramakers, G. J. A. "Long-term characterization of firing dynamics of spontaneous bursts in cultured neural networks". *IEEE Trans Biomed Eng*, **51**, 2051–2062 (2004). Cited on page: 23.

[van Pelt 2005] van Pelt, J., Vajda, I., Wolters, P. S., Corner, M. A., & Ramakers, G. J. "Dynamics and plasticity in developing neuronal networks in vitro ". *Prog Brain Res*, **147**, 171–188 (2005). Cited on pages: 8, 153, 156.

[Varela 2001] Varela, F., Lachaux, J. P., Rodriguez, E., & Martinerie, J. "The brainweb: phase synchronization and large-scale integration". *Nat Rev Neurosci*, **2**, 229–239 (2001). Cited on page: 33.

[Vicente 2011] Vicente, R., Wibral, M., Lindner, M., & Pipa, G. "Transfer entropy–a model-free measure of effective connectivity for the neurosciences".

J Comput Neurosci, **30**, 45–67 (2011). Cited on pages: 35, 138.

[Virmani 2006] Virmani, T., Atasoy, D., & Kavalali, E. T. "Synaptic vesicle recycling adapts to chronic changes in activity". *J Neurosci*, **26**, 2197–2206 (2006). Cited on page: 31.

[Vogelstein 2009] Vogelstein, J. T., Watson, B. O., Packer, A. M., et al. "Spike Inference from Calcium Imaging Using Sequential Monte Carlo Methods". *Biophys J*, **97**, 636–655 (2009). Cited on page: 143.

[Wagenaar 2005] Wagenaar, D. A., Madhavan, R., Pine, J., & Potter, S. M. "Controlling bursting in cortical cultures with closed-loop multi-electrode stimulation". *J Neurosci*, **25**, 680–688 (2005). Cited on page: 153.

[Wagenaar 2006a] Wagenaar, D. A., Pine, J., & Potter, S. M. "An extremely rich repertoire of bursting patterns during the development of cortical cultures". *BMC Neuroscience*, **7**, 11 (2006). Cited on pages: 11, 14, 23, 24, 31, 38, 82, 91, 135, 153, 156, 164.

[Wagenaar 2006b] Wagenaar, D. A., Pine, J., & Potter, S. M. "Searching for plasticity in dissociated cortical cultures on multi-electrode arrays". *J Negat Results Biomed*, **5**, 16 (2006). Cited on page: 30.

[Waldrop 2012] Waldrop, M. M. "Computer modelling: Brain in a box". *Nature*, **482**, 456–458 (2012). Cited on page: 4.

[Wang 2013] Wang, Z., Chen, L. M., Négyessy, L., et al. "The relationship of anatomical and functional connectivity to resting-state connectivity in primate somatosensory cortex". *Neuron*, **78**, 1116–1126 (2013). Cited on page: 33.

[Watt 2010] Watt, A. J. & Desai, N. S. "Homeostatic Plasticity and STDP: Keeping a Neuron's Cool in a Fluctuating World". *Front Syn Neurosci*, **2**, 5 (2010). Cited on page: 30.

[Watts 1998] Watts, D. J. & Strogatz, S. H. "Collective dynamics of 'small-world' networks". *Nature*, **393**, 440–442 (1998). Cited on page: 4.

[Welberg 2010] Welberg, L. "Neuron–glia interactions: Astrocytes in the air". *Nat Rev Neurosci*, **11**, 610–610 (2010). Cited on page: 33.

[Wen 2009] Wen, Q., Stepanyants, A., Elston, G. N., Grosberg, A. Y., & Chklovskii, D. B. "Maximization of the connectivity repertoire as a statistical principle governing the shapes of dendritic arbors". *Proc Natl Acad Sci USA*, **106**, 12536–12541 (2009). Cited on pages: 28, 43, 44.

[Wheeler 2010] Wheeler, B. C. & Brewer, G. J. "Designing Neural Networks in Culture: Experiments are described for controlled growth, of nerve cells taken from rats, in predesigned geometrical patterns on laboratory culture dishes". *Proc IEEE*, **98**, 398–406 (2010). Cited on page: 135.

[White 1986] White, J. G., Southgate, E., Thomson, J. N., & Brenner, S. "The Structure of the Nervous System of the Nematode Caenorhabditis elegans". *Phil Trans R Soc B*, **314**, 1–340 (1986). Cited on page: 28.

[Wibral 2011] Wibral, M., Rahm, B., Rieder, M., et al. "Transfer entropy in magnetoencephalographic data: quantifying information flow in cortical and cerebellar networks". *Prog Biophys Mol Biol*, **105**, 80–97 (2011). Cited on pages: 35, 138.

[Williams 2002] Williams, S. R. & Stuart, G. J. "Dependence of EPSP efficacy on synapse location in neocortical pyramidal neurons". *Science*, **295**, 1907–1910 (2002). Cited on page: 29.

[Yizhar 2011a] Yizhar, O., Fenno, L. E., Davidson, T. J., Mogri, M., & Deisseroth, K. "Optogenetics in neural systems". *Neuron*, **71**, 9–34 (2011). Cited on page: 27.

[Yizhar 2011b] Yizhar, O., Fenno, L. E., Prigge, M., et al. "Neocortical excitation/inhibition balance in information processing and social dysfunction". *Nature*, **477**, 171–178 (2011). Cited on page: 136.

[Yoo 2011] Yoo, S. J., Kim, J., Lee, C.-S., & Nam, Y. "Simple and novel three dimensional neuronal cell culture using a micro mesh scaffold". *Exp Neurobiol*, **20**, 110–115 (2011). Cited on page: 27.

[Yu 2014] Yu, S., Klaus, A., Yang, H., & Plenz, D. "Scale-invariant neuronal avalanche dynamics and the cut-off in size distributions". *PLoS ONE*, **9**, e99761 (2014). Cited on page: 27.

[Yuste 1996] Yuste, R. & Tank, D. W. "Dendritic integration in mammalian neurons, a century after Cajal". *Neuron*, **16**, 701–716 (1996). Cited on page: 6.

[Zhang 2009] Zhang, Q., Li, Y., & Tsien, R. W. "The dynamic control of kiss-and-run and vesicular reuse probed with single nanoparticles". *Science*, **323**, 1448–1453 (2009). Cited on page: 31.

[Zhou 2012] Zhou, J., Gennatas, E. D., Kramer, J. H., Miller, B. L., & Seeley, W. W. "Predicting regional neurodegeneration from the healthy brain functional connectome". *Neuron*, **73**, 1216–1227 (2012). Cited on page: 33.

[Zucker 2002] Zucker, R. S. & Regehr, W. G. "Short-term synaptic plasticity". *Annu Rev Physiol*, **64**, 355–405 (2002). Cited on pages: 18, 30, 140.

Revision History

Revision	Date	Author(s)	Description
1.0	02.05.2015	JO	Submitted version (dipòsit)
1.1	10.05.2015	JO	Online version (added hyperlinks and minor corrections)
1.2	24.05.2015	JO	Printed version (minor graphical corrections)
1.3	26.05.2015	JO	Errata: Figure 5.8: fixed x values shown in both legends.
1.4	03.09.2015	JO	Erratas: Figure 2.5: fixed missing scale. Switched feedback and feedforward definitions. Extended caption. Figure 2.9: fixed τ symbol in the caption. Figure 2.11d: inverted colorbar. Figure 2.13: fixed α symbol in the caption. Figure 4.6: fixed ∇ symbol in the y axis labels.